June 2003 • NREL/SR-520-33997

Subcontractor Report

Future CIS Manufacturing Technology Development

Final Report
8 July 1998–17 October 2001

T.J. Anderson, O.D. Crisalle, S.S. Li, and P.H. Holloway
University of Florida
Gainesville, Florida

National Renewable Energy Laboratory

1617 Cole Boulevard
Golden, Colorado 80401-3393

NREL is a U.S. Department of Energy Laboratory
Operated by Midwest Research Institute • Battelle • Bechtel

Contract No. DE-AC36-99-GO10337

June 2003 • NREL/SR-520-33997

Future CIS Manufacturing Technology Development

Final Report
8 July 1998–17 October 2001

T.J. Anderson, O.D. Crisalle, S.S. Li, and P.H. Holloway
University of Florida
Gainesville, Florida

NREL Technical Monitor: B. von Roedern

Prepared under Subcontract No. XAF-8-17619-32

National Renewable Energy Laboratory

1617 Cole Boulevard
Golden, Colorado 80401-3393

NREL is a U.S. Department of Energy Laboratory
Operated by Midwest Research Institute • Battelle • Bechtel

Contract No. DE-AC36-99-GO10337

NOTICE

Available electronically at http://www.osti.gov/bridge

Available for a processing fee to U.S. Department of Energy
and its contractors, in paper, from:

U.S. Department of Energy
Office of Scientific and Technical Information
P.O. Box 62
Oak Ridge, TN 37831-0062
phone: 865.576.8401
fax: 865.576.5728
email: reports@adonis.osti.gov

Available for sale to the public, in paper, from:

U.S. Department of Commerce
National Technical Information Service
5285 Port Royal Road
Springfield, VA 22161
phone: 800.553.6847
fax: 703.605.6900
email: orders@ntis.fedworld.gov
online ordering: http://www.ntis.gov/ordering.htm

Printed on paper containing at least 50% wastepaper, including 20% postconsumer waste

Executive Summary

The University of Florida subcontract entitled "Future CIS Manufacturing Technology Development" served as the basis for educating 12 graduate students in the area of photovoltaics engineering and research with a focus on thin-film CIS manufacturing technologies, and resulted in 23 research publications and presentations. Further details are given in Part 1 of this report.

A critical assessment of the thermodynamic data and of the phase diagram for the Cu-Se binary system was carried out. It was determined that the compounds of this I-VI system exhibit a wide variety of properties. For example, $Cu_{2-x}Se$ behaves as mixed conductor, showing both ionic and electronic conduction, and it is often present in $CuInSe_2$-based solar cells as an undesirable secondary phase. In contrast, the $CuSe_2$ phase is a low-temperature superconductor. Knowledge of the thermochemistry and phase diagram of the Cu-Se system is essential for understanding the ternary Cu-In-Se system and its subsequent use in developing new CIS processes. In producing a critical assessment of the Cu-Se system we used an association model to describe the liquid phase, and a three-sublattice compound energy formalism to describe the $Cu_{2-x}Se$ phase. The remaining intermediate solid phases (Cu_3Se_2, CuSe, $CuSe_2$) were modeled as line compounds. As a result, a self-consistent set of phase diagram and thermodynamic data was obtained. Further details are given in Part 2 of this report.

In addition, a critical assessment of the thermodynamic data and of the phase diagram for the In-Se binary system was also carried out. The In-Se system is a member of the III-VI group and contains several semiconducting compounds (such as In_4Se_3, InSe, In_6Se_7, In_2Se_3) with possible applications to electronic devices. The understanding of the thermochemistry and phase diagram the In-Se system is motivated as a step towards predicting the behavior of the Cu-In-Se ternary system. We carried out an assessment of the In-Se system using all the relevant phase diagram and thermochemical data available in the literature, plus a published unary assessment for indium, and one for selenium. Nine intermediate solid phases (In_4Se_3, InSe, In_6Se_7, In_9Se_{11}, In_5Se_7, α-In_2Se_3, β- In_2Se_3, γ- In_2Se_3, and δ-In_2Se_3) are modeled as line compounds. An association model was used to describe the liquid phase. The key results that we obtained by coupling the thermochemical and the phase diagram data, are optimized expressions for the Gibbs free energy with respect to the stable element reference for the solid compounds and for the liquid phase, along with those for the major vapor phase species (in particular Se_n for n=1 to 8, In, InSe, In_2Se, and In_2Se_2). The temperature-composition and pressure-temperature projections of the phase diagram were assessed. Further details are given in Part 3 of this report.

We investigated the use of two novel precursor structures that used stacked In-Se and Cu-Se binary layers instead of conventional elemental layers, followed by rapid thermal processing (RTP) to produce CIS films. The first test structure was composed of 3 layers, namely an In_4Se_3/$CuInSe_2$/CuSe stack, while the second structure considered consisted of 2 layers, namely an InSe/CuSe stack. The ramp rate, anneal temperature, and anneal time were varied and the resulting films analyzed for formation of CIS using XRD, AES, ICP, and Raman measurements. The results show that relatively larger grain $CuInSe_2$ could be formed. Further details are given in Part 4 of this report.

We investigated the evolution of electrical and microstructural properties of sputter-deposited ZnO:Al thin films. To gauge the influence of the interface on the performance of sputter-deposited ZnO:Al transparent electrodes, the structure and electrical properties of the interfacial region was investigated during the nucleation and growth of the thin films. RF magnetron sputter deposited films with thickness values ranging from ~20 to 1580Å were

characterized using Atomic Force Microscopy (AFM), Auger Electron Spectroscopy (AES), Hall measurements, and four point probe. AES spectra of the films with thickness between ~20 and 60Å exhibited clear Si (1619eV) peaks suggesting the thin films were discontinuous islands on the substrate. AFM micrographs indicated a distribution of hillocks on the surface, which agrees with AES results, and suggest a Volmer-Webber nucleation and growth mechanism. Hall measurements indicated that the films had electron carrier concentrations on the order of 10^{19} to 10^{20} cm^{-3}, mobilities lower than $10cm^2/V{\cdot}s$, and resistivities on the order of 10^{-2} to 10^{-3} $\Omega{\cdot}cm$ depending on the film thickness. Further details are given in Part 5 of this report.

An assessment of the thermodynamics of the pseudobinary Cu_2Se-Ga_2Se_3 was done making use of available experimental data, as well as use of an empirical method for estimating interactions in semiconductor solid solutions. Four phases were considered in this work, namely a liquid, a Cu_2Se-rich solid solution (ss1), a non-stoichometric chalcopyrite compound $CuGaSe_2$ (ch(ss)), and a Ga_2Se_3-rich solid solution (ss2) which melts congruently at 1112°C with a composition of 28.5% Ga. The thermodynamic description began with the Cu_2Se-rich solid solution, where the interaction between Cu_2Se and Ga_2Se_3 is estimated using the delta lattice parameter model. This estimation is modified to a sub-regular solution model considering the asymmetric deviation from regular solution of the Cu_2Se-rich solid solution phase. A sublattice model is used or the non-stoichometric chalcopyrite compound $CuGaSe_2$ and the Ga_2Se_3-rich solid solution, where the Gibbs energy of the pure compounds are obtained from the reported values. The liquid phase is modeled as an associated solution using the Redlich-Kister expression for the Gibbs energy. The final results obtained show that the calculated phase boundaries and the calculated points for all the invariant equilibria are in good agreement with the available experimental data. Further details are given in Part 6 of this report.

Optimization studies were conducted to characterize the rapid thermal processing (RTP) of binary bilayer precursors for CIS synthesis using a newly acquired AG Associates Heatpulse furnace. In addition, two susceptor designs were conceived and tested, along with a variety of target temperatures, soak times, and temperature-ramp rates, leading to improved understanding of the RTP processing operation. Further details are given in Part 7 of this report.

Progress was made on the calculation of the 500ºC isothermal section of the phase diagram of the ternary Cu-In-Se system. A preliminary though comprehensive thermodynamic model was developed to describe each phase in the Cu-In-Se system. The calculated phase diagram is in reasonable agreement with experimental results reported in the literature. Further details are given in Part 8 of this report.

The pursuit of developing alternative buffer layers for Cd-free CIS-based solar cells using a chemical bath deposition (CBD) process has resulted in specific recipes for deposition. We have performed structural and optical analysis of CdS, (Cd,Zn)S, ZnS, and $In(OH)_xS_y$ films deposited by the CBD process on glass substrates. CIS-based solar cells deposited with the CdS, (Cd,Zn)S, ZnS, and $In(OH)_xS_y$ buffer layers by the CBD process were fabricated and characterized. In addition, a comparative study of the performance of the CIS-based cells deposited with the CdS, (Cd,Zn)S, ZnS, and $In(OH)_xS_y$ buffer layers by the CBD process was carried out. Further details are given in Part 9 of this report.

A rigorous model has been derived to predict the metal mass fluxes produced by conical thermal effusion sources. The model predicts the spatial flux distribution and the deposition rates. A companion two-dimensional model that estimates the temperature of the substrates in the plasma-enhaced migration-enhanced (PMEE) reactor has been developed to estimate the temperature at the site where the films grow. New instrumentation has been added to the PMEE reactor to allow for more effective data acquisition and control, and a cascade controller has been designed and tuned to deliver improved control of the indium-to-copper flux ratios. Further details are given in Part 10 of this report.

A two-dimensional model of the heat transfer was developed to model the substrate temperature distribution in the UF PMEE Reactor that features a rotating platen/substrates and effusion sources. Time-varying view factors were calculated and employed to solve the problem dynamically accounting for the fact that the platen rotates at a given angular speed. The correlation between actual temperature on the substrates and the thermocouple reading due to the indirect measurement was modeled. The poor thermal contact between the platen and the substrates was simulated embedding a thin thermal break-region. The modeling study shows that the existence of the contact resistance improves the temperature uniformity in the substrate region. The effects of rotation speed and rotation direction were also investigated. The modeling results predict the temperature distribution in the substrate regions to be fairly uniform under certain conditions. Fairly good agreement with experimental validation result was obtained without using any model-fitting parameter. Further details are given in Part 11 of this report.

We gave grown and characterized polycrystalline CIS epitaxial films have been established on single-crystal GaAs substrates under conditions that enhance the influence of surface effects on the resulting films and their properties. We have found that there is a pronounced morphological contrast between indium-rich and copper-rich films. In addition, epilayers with nominally identical compositions and morphologies can exhibit fundamentally different ordering of the lattice in either the equilibrium chalcopyrite (CH) or the metastable CuAu (CA) structures. The polycrystalline CIS thin films grown in the University of Florida PMEE system reveal features that seem to lend experimental support to the hypothesis of a vapor-liquid-solid growth mechanism. Droplet-like structures reproducibly appear on the surface of as-grown Cu-rich polycrystalline CIS films when certain conditions are fulfilled, namely when a Cu-rich composition is attained and using a sufficiently high Se flux during the growth and cooling-stages. Other features of the samples and corresponding process suggest that the droplet structure is closely related to the presence of a Cu-Se liquid phase during growth process. The results are significantly affected by the substrate type, temperature, as well as by the final thickness of the film. Finally, progress in developing a process for deposition of precursor films that are used for rapid thermal process is discussed. Further details are given in Part 12 of this report.

Progress was made on the study of CIS and CGS single-crystal growth, along with accompanying morphological and compositional characterizations. The work focused on CIS thin films grown on GaAs substrates in the University of Florida PMEE reactor under different ratios of copper to indium mass flow rates. Characterizations were performed by SEM, AFM, EDS and AES. It was established that the films developed two distinct regions of with different morphologies. Furthermore, the adoption of different source-flux ratios and of different substrate temperature appears to affect the growth mechanism or crystal quality of the final CIS films. Further details are given in Part 13 of this report.

We have developed physical models and performed numerical simulations using AMP-1D program to predict the performance of the CIS-based solar cells constructed with different buffer layers (such as CdS and Cd-free materials) and to compare the results with experimental data. The goal is to produce a device model to guide the design of high-efficiency CIS and CIGS cells with optimized cell parameters, and to gain a better understanding of the basic physics underlying the cell's performance. Further details are given in Part 14 of this report.

A new computer-controlled automated measurement system for the characterization of the solar cell performance parameters has been developed, allowing the characterization of dark- and photo- current-voltage and spectral responses. The new measurement system is currently being used for routine measurements of the performance parameters in the CIS-based cells fabricated at the University of Florida. Further details are given in Part 15 of this report.

The plasma-enhanced migration-enhanced epitaxial reactor (PMEE) available at the University of Florida is used for the deposition of a wide variety of thin CIS films, supporting device manufacturing based on polycrystalline co-deposited CIS, as well as are variety of studies such as single-crystal growth, nucleation effects, and bi-layers precursor design for RTP studies. The custom designed reactor provides for this flexibility. Significant effort is spent on operating and maintaining the UF PMEE reactor, a few significant operational hurdles had to be overcome during the period of this contract, including performance problems related to the load luck pump system and the substrate temperature sensors. Furthermore a new source was purchased for deposition of Ga in addition to the existing sources. Finally four new graduate assistants were trained to take over operations after the graduation of the current students responsible for the operation of the reactor to ensure continuity in the project. Further details are given in Part 16 of this report.

A new instrumentation and control interface for the plasma-enhanced migration-enhanced reactor available at the University of Florida has been designed and deploy to enable the implementation of advanced control strategies envisioned for the local sources as well as the supervisory control structure. This section of the report outlines the hardware and the software that has been purchased and installed the system to achieve these goals. The section concludes with the documentation of the success of initial attempts to set-up a supervisory control scheme, namely a ratio control algorithm for the control of the metal fluxes. Further details are given in Part 17 of this report.

TABLE OF CONTENTS

PART 1
Introduction

Abstract

This section summarizes the accomplishments of the research and development efforts during the period of the University of Florida subcontract, includes a list of graduate assistants who have participated in the projects, and presents the list of publications that have been produced.

Section Contents

1.1 Summary of Accomplishments

A brief summary of accomplishments during the period of this contract is given in the list below:

1. A critical assessment of the thermodynamics and phase-diagram of the Cu-Se and of the In-Se binary systems was carried out, and a self-consistent set of phase diagrams were developed.

2. Rapid thermal processing for CIS thin-film formation was investigated as a low thermal-budget annealing technique for precursor layers. The three-layer structure $In_4Se_3/CuInSe_2/Cu_2Se$ and the two-layer structure InSe/CuSe were investigated as precursors.

3. The influence interface on the electrical performance of sputter deposited ZnO:Al transparent electrodes has been investigated. A Volmer-Webber nucleation and growth mechanism is suggested by the AFM and AES results.

4. Developed a recipe for depositing CdS, (Cd,Zn)S, ZnS, and $In(OH)_xSy$ buffer layers on CIS-based cells by the CBD process on glass substrates, and performed a structural and optical characterization of the films.

5. Fabricated and characterized the CIS cells deposited with alternative buffer layers and the CdS buffer layer by CBD process, and performed a comparative study of the performance of these cells.

6. Constructed a semi-automatic computer-controlled I-V and spectral response (QE) measurement system with the LabView software program for electrical and optical characterization of CIS-based solar cells.

7. Conducted numerical simulation of ZnO/CdS/CIS-based solar cells deposited with different CdS buffer layer and absorber layer thickness.

8. Conducted numerical simulation of ZnO/CdS/CIS-based solar cells by taking into account the effects of defects and doping concentration in the CdS buffer layer and ZnO layer.

9. Conducted numerical simulation of the $ZnO/Cd_{1-x}ZnxS$/CIS-based solar cells.

10. Developed a comprehensive model for simulating the mass flux produced by conical thermal effusion sources commonly used for Cu, In, and Ga deposition in low-pressure environments for molecular-beam processing.

11. A two-dimensional model was developed to assess the temperature distribution of substrates in the plasma-enhanced molecular-beam epitaxial reactor at the University of Florida.

12. Epitaxial CIS films were grown on single-crystal GaAs substrates using a bilayer-precursor recipe followed by rapid thermal processing. The resulting films also provide experimental evidence that may lend support to the vapor-liquid-solid growth hypothesis.

13. A preliminary study of the effect of the copper-to-indium ratio on the morphology and composition of single-crystal CIS films was carried out.

14. A new instrumentation and data-acquisition interface for the PMEE reactor was developed and installed to support advanced control strategies for flux control. A new cascade system for metal-flux control was shown to deliver improved copper-to-indium ratios.

15. A total of 23 journal and conference papers, have been published under the sponsorship of this contract research, and three additional publications are in preparation (see Section 1.3 for a comprehensive publications list).

1.2 Graduate Student Training

This contract has provided an environment that supported the education of 12 graduate students of three different disciplines who are likely to join the photovoltaics industry upon graduation. The list of participating graduate students and their departmental affiliations at the University of Florida is given below:

1. Chia-Hua Huang, Computer and Electrical Engineering
2. Chih-Hung "Alex" Chang, Chemical Engineering
3. Muhsin Ider, Chemical Engineering
4. J. Wayne Johnson, Chemical Engineering
5. Suku Kim, Chemical Engineering
6. Serkan Kincal, Chemical Engineering
7. Lei Li Kerr, Chemical Engineering
8. Lauren Rieth, Materials Science and Engineering
9. Jiyon Song, Computer and Electrical Engineering
10. Billy J. Stanbery, Chemical Engineering
11. Seokhyun Yoon, Chemical Engineering
12. Xuege Wang, Computer and Electrical Engineering

1.3 List of Publications

The following list of publications have been produced under the auspices of this contract:

1. S.S. Li, B. Stanbery, C.H Huang, C.-H. Chang, Y.S. Chang and T.J. Anderson, " Effects of Buffer Layer Processing on CIGS Excess Carrier Lifetime: Application of Dual-beam Optical Modulation to Process Analysis". *25th IEEE Photovoltaic Specialist Conference*, Washington, DC, p.821-824, 1996.
2. C.-H. Chang, A. Davydov, B. Stanbery and T.J. Anderson, "Thermodynamic Assessment of the Cu-In-Se System and Application to Thin Film Photovoltaics" *25th IEEE Photovoltaic Specialist Conference*, Washington, DC, p.849-852, 1996.
3. B. Stanbery, C.-H. Chang, A. Davydov, T.J. Anderson, "Reaction Engineering and Precursor Film Deposition for CIS Synthesis". *AIP Conference Proceedings* 394, p.579-588, 1997.
4. C.-H. Chang, B.J. Stanbery, A. Morrone, A. Davydov and T.J. Anderson, "Novel Multilayer Process for CuInSe2 Thin Films Formation by Rapid Thermal Processing", in *Thin-film Structures for Photovoltaics*, MRS Symposium Proceedings, Vol. 485, p.163-168, 1997.
5. S.S. Li, B.J. Stanbery, C.H Huang, C.-H Chang, T.J. Anderson "Investigation of Buffer Layer Processes on CIS Solar Cells by Dual Beam Optical Modulation Technique", *Conference Record of the 26th IEEE Photovoltaic Specialist Conference*, p.407-410, 1997.
6. C.H. Huang, Sheng S. Li, B.J. Stanbery, C.H. Chang, and T.J. Anderson, "Investigation of buffer layer process on CIGS solar cells by Dual Beam Optical Modulation technique," *Conference Record of the 26th IEEE Photovoltaic Specialist Conference*, pp. 407-410, 1997.
7. B.J. Stanbery, C.-H. Chang, T.J. Anderson, "Engineered Phase Inhomogeneity for CIS Device Optimization", *Inst. Phys. Conf.*, Ser. No 152, p.915-922, ICTMC-11, 1998.
8. C.-H. Chang, A.A. Morrone, B.J. Stanbery, C. McCreary, M. Huang, C.-H. Huang, Sheng S. Li, and T.J. Anderson, "Growth and Characterization of CdS Buffer Layers by CBD and MOCVD," *AIP Conference Proceedings* No. 462, pp. 114-119, 1999.
9. B.J. Stanbery, C.H. Huang, C.H. Chang, Sheng S. Li, and T.J. Anderson, "Characterization and processing of CuInSe2 solar cells," *Conf. Record of the 2nd World Conference on Photovoltaic Solar Energy Conversion*, Vienna, Austria, pp. 529-532, 1998.
10. C.H. Huang, C.-H. Chang, J.W. Johnson, S. Kim, B.J. Stanbery, Sheng S. Li, and T.J. Anderson, "Study of Cd-free Buffer Layers Using Inx(OH,S)y on CIGS Solar Cells", *11th International Photovoltaic Science and Engineering Conference*, Sapporo City, Hokkaido, Japan, September 20-24, 1999.
11. S. Kincal, and O. D. Crisalle, "A Modeling and Control Approach for Molecular Beam Sources", Control of Microelectronics Manufacturing Session, Paper 192e, *AIChE Annual Meeting*, Dallas, Texas, 1999.
12. C.H. Huang, Sheng S. Li, W.N. Shafarman, C.-H. Chang, J.W. Johnson, L. Rieth, S. Kim, B.J. Stanbery, and T.J. Anderson, "Study of Cd-free Buffer Layers Using Inx(OH,S)y on CIGS Solar Cells," *Technical Digest of 11th International Photovoltaic Science and Engineering Conference*, Hokkaido, Japan, pp. 855-856, 1999.

13. L. Rieth, P. Holloway, "Nucleation and growth of ZnO:Al thin films on soda-lime glass substrates", Multicomponent oxide films for electronics, Vol. 574, pp. 205-210, 1999.

14. B.J. Stanbery, C.-H. Chang, S. Kim, S. Kincal, G. Lippold, S.P. Ahrenkiel, L. Li, T.J. Anderson, M.M. Al-Jassim, "Epitaxial Growth of CuAu-Ordered $CuInSe_2$ Structural Polytypes by Migration Enhanced Epitaxy", in Self Organized Processes in Semiconductor Alloys, *MRS Symposium Proceedings*, Vol. 583, 195-200, 2000.

15. B.J. Stanbery, S. Kincal, S. Kim, T.J. Anderson, O.D. Crisalle, S.P. Ahrenkiel, and G. Lippold, "Role of Sodium In The Control of Defect Structures in CIS", *Proceedings 28th IEEE PVSC*, Anchorage, 2000.

16. C.-H. Chang, J.W. Johnson, B.J. Stanbery, S.-H. Wei, R.N. Bhattacharya, R. Duran, and G. Bunker, "Composition Effects on the Local Structure of CuInSe2: X-ray Absorption Fine Structure Investigations and First-Principles Calculations", *J. Applied Physics*, 2001.

17. C.-H. Chang, S.H. Wei, J.W. Johnson, R.N. Bhattachcharya, B.J. Stanbery, R. Duran, and T.J. Anderson, "Long Range and Short Range Ordering of Chalcopyrite CuInSe2", *Jap. J. Appl. Phys.*, Vol. 39, Supplement 39-1, pp411-412, 2000.

18. C.H. Huang, Sheng S. Li, L. Rieth, A. Halani, Jiyong Song, T.J. Anderson, and P.H. Holloway, "A Comparative Study of Chemical-bath-deposited CdS, (Cd,Zn)S, ZnS, and In(OH)xSy Buffer Layers for CIS-based Solar Cells," *NCPV Program Review Meeting*, Denver, CO, USA, pp. 229-230, 2000.

19. C.H. Huang, Sheng S. Li, L. Rieth, A. Halani, M.L. Fisher, Jiyong Song, T.J. Anderson, and P.H. Holloway, "A Comparative Study of Chemical-Bath-Deposited CdS, (CdZn)S, ZnS, and In(OH)xSy Buffer Layers for CIS-based Solar Cells," *27th IEEE Photovoltaic Specialists Conference*, 2000.

20. S. Kincal and O. D. Crisalle, "Thermal Effusion Source Modeling for Control in Molecular Beam Epitaxy Applications", *American Control Conference*, Chicago pp. 4401-4405, 2000.

21. C.-H. Chang, S.-H. Wei, S. P. Ahrenkiel, J. W. Johnson, B. J. Stanbery, T. J. Anderson, S. B. Zhang, M.M. Al-Jassim, G. Bunker, E. A. Payzant, and R. Duran, "Structure Investigations of Several In-rich $(Cu_2Se)x(In_2Se_3)_{1-x}$ Compositions: From Local Structure to Long-Range Order", H. 4.3, *MRS Symposium Proceedings*, "II-VI Compound Semiconductor Semiconductor Materials, 2001.

22. B.J. Stanbery, S. Kincal, S. Kim, C.H. Chang, S.P. Ahrenkiel, G. Lippold, H. Nuemann, T.J. Anderson, and O.D. Crisalle, "Epitaxial Growth and Characterization of $CuInSe_2$ Crystallographic Polytypes", accepted for publication in *Journal of Applied Physics*, to appear in 2002.

23. W. Zhuang, C.-H. Chang, J.Y. Shen, T.J. Anderson, "A Critical Assessment of Phase Diagram and Thermodynamic Data for the Cu-Se Binary System", in preparation for *CALPHAD*.

24. C.-H. Chang, A. Davydov, B.J. Stanbery, and T.J. Anderson, "Thermodynamic Assessment of Selenium Unary System", in preparation for *CALPHAD*.

25. C.-H. Chang, Su-Huai Wei, N. Leyarovska, J.W. Johnson, S.B. Zhang, B.J. Stanbery, T.J. Anderson, G. Bunker, R. Duran, "Local Structure of $CuIn_3Se_5$: An X-ray Absorption Fine Structure Study and First Principle Calculation", in preparation for *Physical Review B*.

PART 2

A Critical Assessment of the Thermodynamic Data and Phase Diagram for the Cu-Se Binary System

Abstract

The Cu-Se system, a member of the I-VI family, produces compounds that exhibit a wide variety of properties. For example, $Cu_{2-x}Se$ is a mixed conductor, showing both ionic and electronic conduction, and is often present in $CuInSe_2$-based solar cells as an undesirable secondary phase. In contrast, the $CuSe_2$ phase is a low-temperature superconductor. Knowledge of the thermochemistry and phase diagram of the Cu-Se system is essential for understanding the full Cu-In-Se system and its subsequent use in developing new CIS processes. A critical assessment of the Cu-Se system was performed using an association model to describe the liquid phase, while a three-sublattice compound energy formalism was used for the $Cu_{2-x}Se$ phase. The remaining intermediate solid phases (Cu_3Se_2, CuSe, $CuSe_2$) were modeled as line compounds. The approach produced a self-consistent set of phase diagram and thermodynamic data.

Section Contents

2.1 Brief Overview

2.1.1 Participants

Faculty Adviser: Prof. Timothy J. Anderson

Research Assistant: Chih-Hung "Alex" Chang

2.1.2 Objectives

The objectives of this project are to elucidate the thermochemistry and phase diagram of the Cu-Se system, and make progress towards the understanding of the full Cu-In-Se system by carrying out a critical assessment of the literature phase diagram and thermodynamic data for the Cu-Se system.

2.2 Phase Diagram Data

The Cu-Se liquid phase exhibits two miscibility gaps, one on the Cu-rich side of the phase diagram and the other for Se-rich side. Four intermediate phases were reported in the literature, including Cu_2Se ($Cu_{2-x}Se$), Cu_3Se_2, CuSe, and $CuSe_2$. The Cu_2Se ($Cu_{2-x}Se$) phase is the most stable phase in this system with a broad homogeneity range extending towards the Se side to form a defect compound. $Cu_{2-x}Se$ has two polytypes: α-$Cu_{2-x}Se$ and β-$Cu_{2-x}Se$. CuSe has three polytypes: α-CuSe, β-CuSe, and γ-CuSe. Extensive studies have been carried out for the Cu-Se phase diagram using DTA (Differential Thermal Analysis), XRD (X-Ray Diffraction), microscopy, and microhardness techniques. Earlier work covered the copper-rich side at high temperature as reviewed by Hansen and Anderko [1]. Later, Chakrabarti and Laughlin [2] critically reviewed the phase diagram and thermodynamic data for the system, but did not perform an optimized assessment. Subsequent to their review, Abrikosov and coworkers [3] and [4] further studied the $Cu_{2-x}Se$ phase using DTA and DSC (Differential Scanning Calorimetry). Glazov and Kim [5] studied the miscibility gap on the Cu-rich side by the acoustic method. All the phase diagram data are shown in Figures 2.2 a and b. The invariant equilibria are listed in Table 2.11.

2.3 Enthalpy, Entropy and Heat Capacity Data

2.3.1 Phase α-$Cu_{2-x}Se$

The standard enthalpy of formation, $\Delta H^o_{f,298.15K,}$ value for α-Cu_2Se was measured by several authors using a variety of techniques as summarized in Table 2.1. Gattow and Schneider [6] reported a value of $\Delta H^o_{f,298.15K}$= -59.3 (kJ/mol), by direct synthesis calorimeter. Several investigators have used solid state galvanic cells to measure the Gibbs energy of formation of

Cu_2Se phase at various temperatures. Valverde [7] reported $\Delta G^o_{573.15K}$= -85.0 (kJ/mol) using the following cell;

Pt | C | Pb | $PbCl_2$+KCl | Cu_2Se+PbSe+Cu | C | Pt

The standard enthalpy of formation, $\Delta H^o_{f,298.15K}$ =-69.9 (kJ/mol), was evaluated by Mills [12] from the available literature data using the third law method. Rau and Rabenau [8] measured the equilibrium Se_2 vapor pressure in the Cu+Cu_2Se two-phase domain and estimated the enthalpy and entropy values using the heat capacity data reported by Kubaschewski [9]. Mills re-evaluated the data using a third law analysis, $\Delta H^o_{f,298.15K}$ =-65.3 (kJ/mol), and the more accurate heat capacity and phase transition data reported by Kubascheswki and Nölting [10]. Askerov *et al.* [11] reported a value, $\Delta H^o_{f,298.15K}$ =-65.7 (kJ/mol) and $\Delta S^o_{f,298.15K}$=28.9 (J/mol K), from their EMF measurements. The value derived from Skeoch and Heyding's liquid bismuth calorimetric measurements is substantially lower than other reported values. Part of this discrepancy is likely related to the assumption that the dissolved liquid mixture is an ideal solution. The entropy values, $S^o_{298.15k,}$ were reported by Rau and Rabenau [8] from vapor pressure measurement and Askerov *et al.* [11] from EMF measurements. Their data together with the third law re-evaluation by Mills [12] are listed in Table 2.7. The heat capacity measured by Kubascheswki and Nölting [10] is listed in Table 2.8.

Table 2.1. Standard heat of formation of α-Cu_2Se(s) at 298.15 K.

Author	Method	$-\Delta H^o_{f,298.15K}$ (kJ/mol)
Tubandt and Reinhold [13]*	Reaction calorimetry Cu_2S (s) +Ag_2Se (s) = Ag_2S (s) + Cu_2Se (s)	69.0
Gattow and Schneider [6]	Calorimetry	59.3
Valverde [7]*	EMF	69.9
Rau [8]*	Vapor pressure	65.3
Askerova [11]	EMF	65.7
Skeoch and Heyding [14]**	Liquid bismuth calorimetry	23.3
Mills [12]	Evaluation	65.3

*Calculated in [12], ** calculated in this work.

2.3.2 Phase β-$Cu_{2-x}Se$

The values of the standard enthalpy of formation for β-Cu_2Se as determined by different authors are listed in Table 2.2. Gattow and Schneider [6] reported a value, $\Delta H^o_{f,298.15K}$ =-55.4 (kJ/mol), by direct synthesis calorimetry. Again the values derived from Skeoch and Heyding's liquid bismuth calorimetric measurements are too low.

Table 2.2. Standard enthalpy of formation of β-$Cu_{2-x}Se$(s) at 298.15 K.

Composition	Reference	Method	$\Delta H^{o}_{f,298.15K}$(kJ/mol)
Cu_2Se	[6]	Calorimetry	54.4
$Cu_{1.8}Se$	[6]	Calorimetry	55.4
$Cu_{1.75}Se$	[8]	Estimation	57.5
$Cu_{1.8}Se$	[14]**	Liquid bismuth calorimetry	34.8
$Cu_{1.85}Se$	[14]**		34.1
$Cu_{1.9}Se$	[14]**		26.2
$Cu_{1.95}Se$	[14]**		23.6
$Cu_{1.8}Se$	[12]	Evaluation	58.6
$Cu_{1.75}Se$	[12]	Evaluation	54.0

** Calculated in this work

A value of the standard entropy of β-$Cu_{2-x}Se$ value, S^{o} 298.15 K, was calculated by [8] from vapor pressure measurements. Their data together with that of Mills [12] evaluation value are listed in Table 2.7. The heat capacity measured by Kubascheswki and Nölting [10] is listed in Table 2.8, while the values of ΔH^{trans} (α→β) from various authors are listed in Table 2.3.

Table 2.3 Enthalpy of transition for α-Cu_2Se(s)→β-Cu_2Se.

Author	Method	Transition Temperature	ΔH^{trans} α→β (kJ/mol)
[15]	DTA	404 K	20.5
[16]	DTA	403 K	2.09
[Kub 72]	Adiabatic calorimetry	395 K	6.83
[17]	DTA	396 K	6.40
[18]	DTA	413 K	6.83
[4]	DTA	413 K	7.89

2.3.3 Cu_3Se_2

Reported values of the standard enthalpy of formation, $\Delta H^{o}_{f,298.15K,}$ of Cu_3Se_2 are listed in

Table 2.4. Gattow and Schneider [6] reported the value, $\Delta H^{o}_{f,298.15K}$ =-98.9 (kJ/mol), by direct synthesis calorimetry. Askerov *et al.* [11] reported the value, $\Delta H^{o}_{f,298.15K}$ =-94.6 (kJ/mol), from their EMF measurements. The enthalpy change of the peritectoid reaction, $0.75Cu_3Se_2(s) \rightarrow Cu_{1.75}Se(s)+0.5CuSe(s)$, was reported by several authors [15, 19, 17] and the values are listed in Table 2.4. The absolute entropy value, $S^{o}_{298.15K,}$ was reported by [11] from EMF measurements. Their data together with that of Mills [12] evaluation value are listed in Table 2.7.

2.3.4 CuSe

Reported values of the standard enthalpy of formation, $\Delta H^{o}_{f,298.15K,}$ for CuSe are listed in Table 2.5. Value of the absolute entropy, $S^{o}_{298.15K,}$ was reported by [8] from their vapor pressure measurements and by [11] from their EMF measurements. Their data together with that of Mills [12] evaluated value are listed in Table 2.7.

Table 2.4. Standard heat of formation of Cu_3Se_2 (s) at 298.15 K.

Author	Method	$-\Delta H^{o}_{f,298.15K}$ (kJ/mol)
[6]	Solution calorimetry	98.9
[11]	Vapor pressure	94.6
[15]*	From reaction $0.75Cu_3Se_2(s) \rightarrow Cu_{1.75}Se(s)+0.5CuSe(s)$	124.3
[19]**	From reaction $0.75Cu_3Se_2(s) \rightarrow Cu_{1.75}Se(s)+0.5CuSe(s)$	112.1
[17]**	From reaction $0.75Cu_3Se_2(s) \rightarrow Cu_{1.75}Se(s)+0.5CuSe(s)$	115.0
[12]	Evaluation	104.6

*Calculated by [12]**, calculated in this work

Table 2.5 Standard heat of formation of CuSe (s) at 298.15 K.

Author	Method	$-\Delta H^{o}_{f,298.15K}$ (kJ/mol)
[6]	Solution calorimetry	39.3
[7]*	EMF	46.0
[8]*	Vapor pressure	40.6

[11]	EMF	32.6
[15]*	from reaction 1.75CuSe(s)→ $Cu_{1.75}Se(s)+0.75Se(l)$	41.8
[19]**	from reaction 1.75CuSe(s)→ $Cu_{1.75}Se(s)+0.75Se(l)$	42.3
[12]	Evaluation	41.8

*Calculated in [12], **calculated in this work.

2.3.5 $CuSe_2$

Reported values of the $\Delta H^o_{f,298.15K}$ from various investigators are listed in Table 2.6, while the reported values of $S^o_{298.15K}$ are listed in Table 2.7.

Table 2.6 Standard heat of formation of $CuSe_2$ (s) at 298.15 K.

Author	Method	$-\Delta H^o_{f,298.15K}$ (kJ/mol)
[6]	Calorimetry	43.1
[8]*	Vapor pressure	48.1
[11]	EMF	39.3
[15]*	from reaction $CuSe_2$ (s)→ CuSe(s)+Se(l)	46.9
[19]**	from reaction $CuSe_2$ (s)→ CuSe(s)+Se(l)	48.1
[12]	Evaluation	48.1

*Calculated in [12], **calculated in this work.

Table 2.7 Standard entropy of solid Cu-Se compounds at 298.15 K.

Compound	Author	Method	$S^o_{298.15K}$ (J/mol K)
α-Cu_2Se	[8]	Vapor pressure	157.3
	[11]	EMF	80.2
	[Mil 80]	Evaluation	129.7

β-Cu_2Se	[8]	Vapor pressure	162.3
Cu_3Se_2	[11]	EMF	184.9
	[Mil 80]	Evaluation	207.1
CuSe	[8]	Vapor pressure	72.0
	[11]	EMF	74.1
	[Mil 80]	Evaluation	78.2
$CuSe_2$	[8]	Vapor pressure	120.5
	[11]	EMF	98.4
	[Mil 80]	Evaluation	107.5

Table 2.8 Heat capacity data for Cu_2Se.

Compound	C_p (J/ mol K)	Temperature Range
Cu_2Se	$59.0572 + 75.0191 \times 10^{-3} T$	298-395 K
	$84.2783 - 2.0290 \times 10^{-3} T$	395-1000 K

2.4 Gibbs Energy Data

2.4.1 EMF measurements

Mostafa et al. [21] investigated the $Cu_{2-x}Se$ phase, using the solid state galvanic cell, Pt/Cu/CuBr/$Cu_{2-x}Se$/graphite, in the temperature range 350 to 450°C. The electromotive force was measured as function of the stoichiometry of the selenide compound and temperature. The composition of the solid solution ($Cu_{2-x}Se$) was varied by coulometric titration. The chemical potential of copper, μ_{Cu}, in $Cu_{2-x}Se$ is given by,

$$\mu_{Cu} = \mu^{o}_{Cu} + FE$$

where F is the Faraday constant, E is the open circuit potential, and μ^{o}_{Cu} is the chemical potential of pure Cu. The measured values are plotted in Figure 2.4.

2.4.2 Vapor Pressure Measurement

The following gas species were reported to exist in the Cu-Se system, Se_n (n=1-8), Cu, Cu_2, CuSe, and Cu_2Se, with Se_2 the most prominent one in the temperature range studied. Rau and Rabenau [8] studied the Se_2 equilibrium pressures for Cu-Se system as shown in Figure 2.2. The partial pressure data have been converted into partial Gibbs energy data and used in the assessment. Blachnik and Bolte [22] determined the activities of selenium in molten mixture of copper and selenium by a modified dew-point method at 1373 K. Azakami and Yazawa [23] measured the selenium activities in copper-selenium melt at 1200°C by the transportation method.

2.5 Thermodynamic Models

2.5.1 Pure Elements and Stoichiometric Compound Phases

The Gibbs energy of Cu is from Dinsdale [24], and that of Se is from Chang et al. [25]. The three-term equation given below is used to represent the temperature dependence of the Gibbs energies of stoichiometric compound phases,

$$^{\circ}G=a+bT+cT\ln T \tag{2.1}$$

Where °G is the standard Gibbs energy, T is the absolute temperature, and a, b and c are constants whose values need to be determined from experimental data.

2.5.1.1 Terminal Solid Solutions

A limited solubility of Se in Cu has been measured [26, 27], while negligible solubility of Cu in Se has been proposed [2]. In this work, the solubility of Cu in Se was also considered negligible, whereas the solubility of Se in Cu is modeled. The Gibbs energy (G^{fcc}) of the terminal solid solution based on face-centered cubic (fcc) Cu is expressed as

$$G^{fcc} = {}^{ref}G^{fcc} + {}^{id}G^{fcc} + {}^{E}G^{fcc} \tag{2.2}$$

with

$${}^{ref}G^{fcc} = x_{Cu}\,{}^{\circ}G^{fcc}_{Cu} + x_{Se}\,{}^{\circ}G^{fcc}_{Se} \tag{2.3}$$

$${}^{id}G^{fcc} = RT(x_{Cu}\ln x_{Cu} + x_{Se}\ln x_{Se}) \tag{2.4}$$

${}^{E}G^{fcc}$ is the excess Gibbs energy, and expressed by the Redlich-Kister polynomial [28]:

$${}^{E}G^{fcc} = x_{Cu}x_{Se}\sum_{i=0}^{n} {}^{i}L^{fcc}_{Cu,Se}(x_{Cu}-x_{Se})^{i} \tag{2.5}$$

where L is the binary interaction parameter to be optimized in the present work. The temperature dependence of L may be expressed as

$${}^{i}L^{fcc}_{Cu,Se} = a_i + b_iT \tag{2.6}$$

2.5.1.2 Liquid Phase

The association model [29] was used to describe the Gibbs energy of the liquid phase. $Cu_{2-x}Se$ is the most stable compound in this system, which is stable to 1403 K and congruently melts at that temperature, while the other compounds peritectically decompose below 650 K. It is thus reasonable to select Cu_2Se as an associate species for the modeling of the liquid phase

$$(Cu, Cu_2Se, Se)_l \tag{2.7}$$

The Gibbs energy of this phase (per mole of atoms) can also be expressed by equation (2.2), where fcc should be replaced by l (l=liquid). The term ${}^{ref}G^l$ is equal to

$${}^{ref}G^l = y_{Cu}\,{}^{\circ}G^l_{Cu} + y_{Cu_2Se}\,{}^{\circ}G^l_{Cu_2Se} + y_{Se}\,{}^{\circ}G^l_{Se} \tag{2.8}$$

where y_i refers to the site fractions of the species i, $y_{Cu} + y_{Cu_2Se} + y_{Se} = 1$. The terms ${}^{\circ}G^l_i$ represent the Gibbs energies of the pure liquid phase of species i.

The ideal mixing Gibbs energy ${}^{id}G^l$ is equal to

$${}^{id}G^l = RT(y_{Cu}\ln y_{Cu} + y_{Cu_2Se}\ln y_{Cu_2Se} + y_{Se}\ln y_{Se}), \tag{2.9}$$

and the excess Gibbs energy ${}^{E}G^l$ is by Redlich-Kister

$$\begin{aligned} {}^{E}G^l = {} & y_{Cu}y_{Cu_2Se}({}^0L^l_{Cu,Cu_2Se} + {}^1L^l_{Cu,Cu_2Se}(y_{Cu} - y_{Cu_2Se})) \\ & + y_{Cu_2Se}y_{Se}({}^0L^l_{Cu_2Se,Se} + {}^1L^l_{Cu_2Se,Se}(y_{Cu_2Se} - y_{Se})). \end{aligned} \tag{2.10}$$

where the four L terms represent the interactions between the indicated species. They can be expressed as a function of temperature.

2.5.1.3 Ordered Nonstoichiometric Compound Phases

The high temperature modification of $Cu_{2-x}Se$, β-$Cu_{2-x}Se$, is related to the B4 (ZnO) or C1(CaF_2) fcc structure. It has been suggested that β-$Cu_{2-x}Se$ is the ZnO-type structure with the space group $F\bar{4}3m$ [30, 31, 32]. In this structure, four Se atoms occupy the 4(a) sites, four Cu atoms occupy the 4(c) sites, and the other Cu atoms are statistically distributed in the interstitial sites (four tetrahedral (d), four octahedral (b), and sixteen trigonal (e) positions). [56] and the later investigators [33, 34, 35, 36] suggested another structure model based on the space group Fm3m. Each of these investigators agreed that the Se atoms occupy the 4(a) sites and form a fcc sublattice. While Oliveria et al. [34] proposed that all Cu atoms occupy the trigonal 32(f) sites, and other investigators [33, 35, 36] proposed that Cu atoms lie on two different sites. Based on the structural data, the ordered nonstoichiometric β-$Cu_{2-x}Se$ phase was divided into three sublattices: one occupied by Se atoms, and the other two occupied by Cu atoms. The structural data suggested the nonstoichiometry is due to the formation of vacancies on the Cu sublattice. The energetics of the two Cu-sublattices are different. The Cu atoms can lie more easily on one sublattice with lower energy than the other one. Therefore, vacancies form more easily on the sublattice with higher energy, and thus assume one of the two Cu sublattices is always fully occupied by Cu atoms. As a result, the β-$Cu_{2-x}Se$ phase was described using the sublattice model with three sublattices after the formula [37, 38]:

$$(Cu,Va)_1(Se,Va)_1(Cu)_1 \tag{2.11}$$

where Va represents a vacancy on that site. Including the possibility of vacancies in the Se sublattice introduces flexibility in the modeling of the Gibbs energy, but does not imply that the Se sublattice contains a high concentration of vacancies. From the assessment results given later, it is found find that the vacancy concentration in the Se sublattice is very small, which is in good agreement with the structural information.

The low-temperature modification of $Cu_{2-x}Se$, α-$Cu_{2-x}Se$, exhibits a complex diffraction pattern and makes it difficult to identify. The structure of α-$Cu_{2-x}Se$ has been described as cubic [30, 39, 36], pseudo-cubic [40], tetragonal [31, 41], orthorhombic [42, 43, 32], monoclinic [44, 45, 46], and pseudo-monoclinic [47]. Each investigator, however, agrees that the Se atoms form a fcc sublattice and the Cu atoms distribute over two or more various sites (e.g., tetrahedral, octahedral, and trigonal sites). For modeling the homogeneity range, the ordered nonstoichiometric α-$Cu_{2-x}Se$ phase was also described with three sublattices after formula (2.7). The Gibbs energy of such a phase ϕ (ϕ=α-$Cu_{2-x}Se$ or β-$Cu_{2-x}Se$) can also be expressed by equation (2.2) (where fcc is replaced by ϕ) with,

$$\begin{aligned} {}^{ref}G^{\phi} &= y'_{Cu}y''_{Se}\,{}^{\circ}G^{\phi}_{Cu:Se:Cu} + y'_{Cu}y''_{Va}\,{}^{\circ}G^{\phi}_{Cu:Va:Cu} \\ &\quad + y'_{Va}y''_{Se}\,{}^{\circ}G^{\phi}_{Va:Se:Cu} + y'_{Va}y''_{Va}\,{}^{\circ}G^{\phi}_{Va:Va:Cu} \end{aligned} \tag{2.12}$$

$$\begin{aligned} {}^{id}G^{\phi} &= RT[(y'_{Cu}\ln y'_{Cu} + y'_{Va}\ln y'_{Va}) \\ &\quad + (y''_{Se}\ln y''_{Se} + y''_{Va}\ln y''_{Va})] \end{aligned} \tag{2.13}$$

$$\begin{aligned} {}^{E}G^{\phi} &= y'_{Cu}y'_{Va}\left[y''_{Se}\left({}^{0}L^{\phi}_{Cu,Va:Se:Cu} + {}^{1}L^{\phi}_{Cu,Va:Se:Cu}(y'_{Cu}-y'_{Va})\right) + y''_{Va}\left({}^{0}L^{\phi}_{Cu,Va:Va:Cu} + {}^{1}L^{\phi}_{Cu,Va:Va:Cu}(y'_{Cu}-y'_{Va})\right)\right] \\ &\quad + y''_{Se}y''_{Va}\left[y'_{Cu}\left({}^{0}L^{\phi}_{Cu:Se,Va:Cu} + {}^{1}L^{\phi}_{Cu:Se,Va:Cu}(y''_{Se}-y''_{Va})\right) + y'_{Va}\left({}^{0}L^{\phi}_{Va:Se,Va:Cu} + {}^{1}L^{\phi}_{Va:Se,Va:Cu}(y''_{Se}-y''_{Va})\right)\right] \end{aligned} \tag{2.14}$$

where y_i' and y_i'' refer to the site fractions of the component i in the first and second sublattice, respectively. ${}^{\circ}G^{\phi}_{Cu:Se:Cu}$ is the standard Gibbs energy of stoichiometric α-Cu_2Se or β-Cu_2Se, which will be assessed in this work. ${}^{\circ}G^{\phi}_{Cu:Va:Cu}$ and ${}^{\circ}G^{\phi}_{Va:Va:Cu}$ can be expressed as:

$${}^{\circ}G^{\phi}_{Cu:Va:Cu} = 2\,{}^{\circ}G^{fcc}_{Cu} + a_1 + b_1T \tag{2.15}$$

$${}^{\circ}G^{\phi}_{Va:Va:Cu} = {}^{\circ}G^{fcc}_{Cu} + a_2 + b_2T \tag{2.16}$$

where, ${}^{\circ}G^{fcc}_{Cu}$ is the standard Gibbs energy of pure copper in the fcc phase, and a_i and b_i are the optimized parameters. The value of ${}^{\circ}G^{\phi}_{Va:Se:Cu}$ can be expressed by the following relation [48, 49]:

$${}^{\circ}G^{\phi}_{Va:Se:Cu} = {}^{\circ}G^{\phi}_{Cu:Se:Cu} + {}^{\circ}G^{\phi}_{Va:Va:Cu} - {}^{\circ}G^{\phi}_{Cu:Va:Cu} \tag{2.17}$$

To reduce the number of parameters, the following relations are used in the optimization [48, 49]:

$$\begin{aligned} &{}^{0}L^{\phi}_{Cu,Va:Se:Cu} = {}^{0}L^{\phi}_{Cu,Va:Va:Cu} = {}^{0}L^{\phi}_{Cu,Va:*:Cu} \\ &{}^{0}L^{\phi}_{Cu:Se,Va:Cu} = {}^{0}L^{\phi}_{Va:Se,Va:Cu} = {}^{0}L^{\phi}_{*:Se,Va:Cu} \end{aligned} \tag{2.18}$$

$${}^{1}L^{\phi}_{Cu,Va:Se:Cu} = {}^{1}L^{\phi}_{Cu,Va:Va:Cu} = {}^{1}L^{\phi}_{Cu,Va:*:Cu}$$

$${}^{1}L^{\phi}_{Cu:Se,Va:Cu} = {}^{1}L^{\phi}_{Va:Se,Va:Cu} = {}^{1}L^{\phi}_{*:Se,Va:Cu}$$

2.6 Optimization Procedure

A selected set of thermodynamic and phase diagram data (listed in Table 2.9) were used for the optimization of thermodynamic model parameters of all phases in this system. The critical review of Chakrabarti and Laughlin [2] was used as a guide for selecting the experimental phase diagram data. New experimental phase diagram data [4, 3, 5, 50] were also used in the optimization. The optimization was performed by using the PARROT module of the Thermo-Calc program package [51] and split in six steps.

First, the Gibbs energy coefficients of the stoichiometric compounds, α-Cu_2Se and β-Cu_2Se and the stoichiometric liquid Cu_2Se were estimated from enthalpy of formation, standard entropy, heat capacity, transition enthalpy, transition temperature, and melting enthalpy and temperature. Then, assuming that β-$Cu_{2-x}Se$ is a stoichiometric phase and there is no interaction between the pure elements in the liquid phase, a preliminary optimization of the liquid coefficients was performed based on the activities of selenium, miscibility gap, and three-phase equilibrium. Third, fixing the coefficients of the liquid phase, the coefficients of the ordered nonstoichiometric β-$Cu_{2-x}Se$ phase were roughly optimized based on the measurements of the activities of copper [52], two-phase equilibria between liquid and β-$Cu_{2-x}Se$, and the monotectic and eutectic equilibria data. Fourth, fixing the coefficients of the liquid and β-$Cu_{2-x}Se$ phases, the coefficients of the stoichiometric Cu_3Se_2, α-CuSe, β-CuSe (γ-CuSe), and $CuSe_2$ phases were optimized based on their enthalpies of formation, enthalpies of transition, standard entropies, and equilibria data that included these phases. As no discontinuous change in enthalpy was detected in the β-CuSe↔γ-CuSe transformation by DTA method [17], the transformation may be considered to be continuous, i.e., higher order [2]. In this work, the β-CuSe and γ-CuSe phases are assumed and modeled as one phase. Fifth, fixing the coefficients of other phases, the coefficients of the α-$Cu_{2-x}Se$ and terminal solid solution fcc(Cu) phases were optimized based on available experimental data. Finally, all parameters of the phases were optimized to fit the experimental data listed in Table 2.9.

2.7 Result and Discussion

The optimized parameters of the stable phases in the Cu-Se system were listed in Table 2.10. The parameters taken from references [24] and [25] were not reproduced in Table 2.10 to conserve space. The phase diagram and thermodynamic properties of this system have been calculated by using the optimized parameters, which were performed with the Poly-3 module of the Thermo-Calc program package.

The calculated phase diagram is shown in Figure 2.1. The dash line, which denotes the β-CuSe↔γ-CuSe - transformation is not the calculated result. It is based on the XRD measurement [17]. Figures 2.2a-c compare the calculated phase diagram and the measured data. The calculated phase diagram agrees well with the data used in the optimization. It does not agree with some of the data which was not used in the optimization, including, the Cu-rich miscibility gap data

measured [53] (Figure 2.2a), and the α-$Cu_{2-x}Se$/β-$Cu_{2-x}Se$ solvus line and related eutectoid data [54, 55] (Figure 2.2b). These data are inconsistent with the new measured results. Specifically, the Cu-rich miscibility gap data [53] are in disagreement with those reported in [23, 5]; while the α-$Cu_{2-x}Se$/β-$Cu_{2-x}Se$ equilibria and related eutectoid data report by [54, 55] are inconsistent with those measured by Abrikosov [4].

Tables 2.11a and 2.11b present the experimental and calculated temperatures and compositions of the invariant reactions in this system. The calculated values agree well with the data summarized by Chakrabarti and Laughlin [2]. The calculated critical temperature of the Cu-rich liquid miscibility gap agrees well with the experimental data of reference [5], whereas the calculated critical composition has lower Se concentration than the experimental ones [5]. The calculated compositions of the whole Cu-rich miscibility gap, however, agree well with the experimental data of reference [5] as shown in Figure 2.2a. In the calculated phase diagram, the temperatures and compositions of the Se-rich liquid miscibility gap have been predicted, which need to be verified by furture experiments.

Figure 2.3 shows the comparison between the calculated and measured chemical potential of selenium in liquid phase. The calculated values agree with the measured ones [22] when the mole fraction of selenium is larger than 0.333. When the mole fraction of selenium is less than 0.333, the calculated values lie between the measured results of Azakami and Yazawa [23] and Blachnik and Bolte [22]. The calculated and measured chemical potential of copper in the β-$Cu_{2-x}Se$ phase is shown in Figure 2.4. The calculated curves essentially agree with the experimental data. The calculated curves, however, are not as concave as the measured ones. Figure 2.5 shows the comparison between the calculated and measured Se_2 partial pressure along the liquidus and in equilibrium with the compounds in this system. To calculate the Se_2 partial pressure, an ideal gas phase containing 12 species is added to the optimized coefficient set. The parameters of the gas species Se, Se_2, Se_3, Se_4, Se_5, Se_6, Se_7, and Se_8 are given in Chapter 3 of [61], whereas the parameters of the gas species Cu, Cu_2, CuSe, and Cu_2Se are taken from reference [60]. The calculated Se_2 partial pressure values agree well with the measured data of Rau and Rabenau [8] except those at the low pressure fcc(Cu)/β-$Cu_{2-x}Se$ region. Attempts to fit would not allow other experimental data to be fitted, including the experimental Se_2 partial pressures measured by the same authors [8].

The calculated vacancy site fractions in the β-$Cu_{2-x}Se$ phase are shown in Figures 2.6 and 2.7. In the β-$Cu_{2-x}Se$ single-phase region, the Cu vacancy concentration in the first sublattice, y'_{Va}, increases with the increase of selenium concentration; whereas the Se vacancy concentration, y''_{Va}, decreases with the increase of selenium concentration. The horizontal lines from the mole fraction of selenium at 0.338 to 0.342 at 380 K in Figures 2.6 and 2.7 correspond to the α-$Cu_{2-x}Se$+β-$Cu_{2-x}Se$ two-phase region. The calculated Cu vacancy site fraction in the first sublattice is between 0.008 to 0.271 in Figure 2.6, whereas the Se vacancy site fraction is between 2.07×10^{-17} to 2.23×10^{-4} in Figure 2.7. No experimental data are available for comparison to these calculation results. However, the very limited Se vacancy and a large Cu vacancy concentration are in reasonable accord with the structural research results [32, 56, 36].

The experimental and calculated standard enthalpies of formation of the intermediate compounds at 298.15 K in the Cu-Se system are presented in Table 2.12 The corresponding standard entropies are presented in Table 2.13. The reference state for these properties is the enthalpy of the pure stable element at 298.15 K. The calculated enthalpies of formation in the

present work lie between the data measured by Gattow and Schneidener [6] and those evaluated by [12]. The calculated standard entropies agree with those evaluated by Mills [12], except that of $CuSe_2$, which lies between the value of Rau and Rabenau [8] and that evaluated by Mills [12]. Figure 2.8 shows the calculated heat capacity for Cu_2Se along with the experimental result [57]. The calculated values agree well with the measured ones. The calculated enthalpy of transition of the α-$Cu_2Se \rightarrow \beta$-Cu_2Se transition at 396 K is 6.83 kJ/mole, which is in good agreement with that measured by Kubaschewski and Nölting [57]. The calculated enthalpy of the α-CuSe$\rightarrow\beta$-CuSe transition at 324 K is 1.38 kJ/mole, which is in good agreement with that measured by Heyding [15]. As no experimental heat capacity data for CuSe are available, those data are optimized from the phase diagram data after assuming no difference between the heat capacities of α-CuSe and β-CuSe.

2.8 Conclusions

A thermodynamic description of the Cu-Se binary system was obtained by optimization of the available phase equilibrium and thermodynamic data. The Redlich-Kister polynomial, associate solution model, and sublattice model were used to represent the Gibbs energy of the fcc(Cu), liquid, and both $Cu_{2-x}Se$ phases, respectively. Other intermediate phases are modeled as line compounds. The phase diagram and thermodynamic properties of this system have been calculated by using the optimized model parameters. There is reasonable agreement between the model-calculated values and selected phase equilibrium and thermodynamic data available in the literature for all phases. Further experimental work is suggested for determining the shape and critical point of the Se-rich liquid miscibility gap.

Table 2.9 Selected data used in the optimization.

Equilibrium/Function	Reference
β-$Cu_{2-x}Se$/liquid, congruent and monotectic (Se-rich side)	[15], [16], [19], [58], [17], [50]
Liquid miscibility gap and monotectic (Cu-rich side)	[58], [23], [5]
β-$Cu_{2-x}Se$/fcc(Cu) and eutectic	[26], [27], [58], [2]
α-$Cu_{2-x}Se$+β-$Cu_{2-x}Se$, peritectoid and eutectoid	[15], [57], [17], [4], [3]
Other phase equilibrium data	[17], [2], [24], [25]
Chemical potential of Se	[8], [23], [22]
Chemical potential of Cu	[21]
Enthalpy of formation	[6], [12]
Standard Entropy	[12]
Heat capacity	[57]
Enthalpy of transition	[15], [57]
Enthalpy of fusion	[3]

Table 2.10 Optimized parameters according to the analytical description of the phases[+].

Phase or Function	Parameters
Liquid	${}^{\circ}G^{l}_{Cu_2Se} = GCu2Se\_l$ ${}^{0}L^{l}_{Cu,Cu_2Se} = 187782 - 106.9217T$ ${}^{1}L^{l}_{Cu,Cu_2Se} = -83457 + 61.4034T$ ${}^{0}L^{l}_{Cu_2Se,Se} = -19130 + 17.8305T$ ${}^{1}L^{l}_{Cu_2Se,Se} = -34873 + 15.0081T$
$\alpha Cu_{2-x}Se$	${}^{\circ}G^{\alpha}_{Cu:Se:Cu} = GCu2Se\_A$ ${}^{\circ}G^{\alpha}_{Cu:Va:Cu} = 2{}^{\circ}G^{fcc}_{Cu} + 50000$ ${}^{\circ}G^{\alpha}_{Va:Va:Cu} = {}^{\circ}G^{fcc}_{Cu} + 90000$ ${}^{\circ}G^{\alpha}_{Va:Se:Cu} = 40000 + GCu2Se\_A - {}^{\circ}G^{fcc}_{Cu}$ ${}^{0}L^{\alpha}_{*:Se,Va:Cu} = 20000$ ${}^{0}L^{\alpha}_{Cu,Va:*:Cu} = 11180 + 10T$ ${}^{1}L^{\alpha}_{Cu,Va:*:Cu} = -56789$
$\beta Cu_{2-x}Se$	${}^{\circ}G^{\beta}_{Cu:Se:Cu} = GCu2Se\_B$ ${}^{\circ}G^{\beta}_{Cu:Va:Cu} = 2{}^{\circ}G^{fcc}_{Cu} + 50000$ ${}^{\circ}G^{\beta}_{Va:Va:Cu} = {}^{\circ}G^{fcc}_{Cu} + 80000 + 36T$ ${}^{\circ}G^{\beta}_{Va:Se:Cu} = 30000 + 36T + GCu2Se\_B - {}^{\circ}G^{fcc}_{Cu}$ ${}^{0}L^{\beta}_{*:Se,Va:Cu} = 20000$ ${}^{0}L^{\beta}_{Cu,Va:*:Cu} = -32004 + 14.0367T$ ${}^{1}L^{\beta}_{Cu,Va:*:Cu} = -19864 + 11.2002T$
Cu_3Se_2	${}^{o}G^{Cu3Se2}$=-25590+62.7620T-15.66455TlnT
αCuSe	${}^{o}G^{\alpha CuSe}$=-25859+83.0760T-18.24325TlnT
βCuSe (or γCuSe)	${}^{o}G^{\beta CuSe}$=-24478+78.8145T-18.24325TlnT
$CuSe_2$	${}^{o}G^{CuSe2}$=-21989+95.3189T-19.97710TlnT
fcc(Cu)	${}^{\circ}G^{fcc}_{Se} = {}^{\circ}G^{tri}_{Se} + 5000$ ${}^{0}L^{fcc}_{Cu,Se} = -10000 - 10T$
Function	Gcu2Se_A=-80217.34+288.16728T-59.0572TlnT-0.0375096T^2 (298≤T≤395) =-98588.35+664.34671T-120.0866TlnT+0.03785T^2 -6.9635×$10^{-6}T^3$+1019900T^{-1} (395≤T≤800) Gcu2Se_B=GCu2Se_A+6830-17.29114T GCu2Se_l=GCu2Se_B+16000-11.422T

Temperature (T) is in Kelvin. The Gibbs energies of the liquid, fcc(Cu), Cu_3Se_2, α-CuSe, β-CuSe and $CuSe_2$ are in J/mole of atoms. The Gibbs energies of α-$Cu_{2-x}Se$ and β-$Cu_{2-x}Se$ are in J/mole of $(Cu,Va)_1(Se,Va)_1(Cu)_1$. The symbol * indicates Cu, Se or Va, and tri represents trigonal.

Table 2.11a. Experimental and calculated temperatures and compositions of the invariant reactions in the Cu-Se system (continued on Table 2.11b).

Phases	Composition, at. % Se	Temperature [K]	Reaction Type	Reference
L_1/L_2	18.0/18.0	1699	Critical	[5]
	15.7/15.7	1700		This work
$L_1/L_2/\beta$-$Cu_{2-x}Se$	…/32.1 /33.3	1380	Monotectic	[1]
	-	1373		[58]
	…/…/33.3	1373		[2]
	4/31.5/33.3	1380		[5]
	3.0/32.9/33.3	1373		This work
$Cu/L_1/\beta$-$Cu_{2-x}Se$	-	1336	Eutectic	[1]
	<0.02/1.8/33.3	1341		[59]
	…/1.8/33.3	1336		[2]
	0.02/2.1/33.3	1335		This work
Cu/α-$Cu_{2-x}Se/\beta$-$Cu_{2-x}Se$	0/33.3/33.3	404	Peritectoid	[15]
	0/33.3/33.3	396		[59]
	0/33.3/33.3	411		[19]
	0/33.3/33.3	435		[58]
	0/33.3/33.3	396		[17]
	0/33.3/33.3	413		[18]
	0/33.3/33.3	396		[2]
	0/33.8/33.9	396		This work
β-$Cu_{2-x}Se/L_2$	33.3/33.3	1421	Congruent	[Mas 61]
	33.3/33.3	1386		[59]
	33.3/33.3	1403		[58]
	33.3/33.3	1403		[2]
	33.5/33.5	1421		[3]
	33.6/33.6	1399		This work
L_2/L_3	68.9/68.9	1256	Critical	This work
β-$Cu_{2-x}Se/L_2/L_3$	-	796	Monotectic	[15]
	37.18/50.96/>98.78	796		[19]
	-	813		[58]
	-	796		[17]
	36.5/52.5/…	796		[2]
	36.4/50.0/97.0	796		This work

Table 2.11b. Continuation of Table 2.11 a: Experimental and calculated temperatures and compositions of the invariant reactions in the Cu-Se system.

Phases	Composition, at. % Se	Temperature [K]	Reaction Type	Reference
β-$Cu_{2-x}Se$/γ-CuSe/L_3	<38/50/…	655	Peritectic	[15]
	37.18/50/>98.78	657		[19]
	37.59/50/…	673		[58]
	–	652		[17]
	36.5/50/…	650		[2]
	36.8/50/99.4	650		This work
γ-CuSe/$CuSe_2$/L_3	50/66.7/…	615	Peritectic	[15]
	50/66.7/98.78	616		[19]
	50/66.7/…	605		[17]
	50/66.7/…	605		[2]
	50/66.7/99.8	605		This work
$CuSe_2$/Se/L_3	66.7/100/…	491	Eutectic (or peritectic)	[15]
	-	499		[19]
	-	491		[17]
	-	494		[2]
	66.7/100/100	494		This work
β-$Cu_{2-x}Se$/Cu_3Se_2/β-CuSe	<37/40/50	408	Peritectoid	[15]
	<37.18/40/50	416		[19]
	<37.6/40/50	448		[58]
	…/40/50	386		[17]
	36.5/40/50	385		[2]
	37/40/50	417		[3]
	36.5/40/50	385		This work
α-CuSe/β-CuSe	50/50	326	Polymorphic	[15]
	50/50	319-321		[43]
	50/50	333		[19]
	50/50	353		[58]
	50/50	323		[17]
	50/50	324		[2]
	50/50	324		This work
α-$Cu_{2-x}Se$/β-$Cu_{2-x}Se$/Cu_3Se_2	34.8/36.3/40	170	Eutectoid	[55]
	34.2/36.2/40	291		[4]
	34.6/36.0/40	291		This work

Table 2.12 Experimental and calculated standard enthalpies of formation ($\Delta H^{o}_{f,298.15K}$) of the intermediate compounds at 298.15 K in the Cu-Se system (kJ/mole).

Compound	$-\Delta^{\circ}H_{298}$	Method	Reference
Cu_2Se	59.3	Calorimetry	[6]
	69.9	EMF	[7]
	62.8	Vapor pressure	[8]
	65.7	EMF	[11]
	65.3	Evaluation	[12]
	59.3	Assessment	This work
Cu_3Se_2	98.9	Calorimetry	[6]
	124.5	DTA	[15]
	94.6	EMF	[11]
	104.6	Evaluation	[12]
	104.6	Assessment	This work
CuSe	39.6	Calorimetry	[6]
	46.0	EMF	[7]
	44.0	Vapor pressure	[8]
	32.6	EMF	[11]
	41.8	Evaluation	[12]
	40.8	Assessment	This work
$CuSe_2$	43.1	Calorimetry	[6]
	49.0	Vapor pressure	[8]
	39.3	EMF	[11]
	48.1	Evaluation	[12]
	48.1	Assessment	This work

Table 2.13. Experimental and calculated standard entropies ($^{\circ}S_{298}$) of the intermediate Compounds at 298.15 K in the Cu-Se system (J/K mole).

Compound	$^{\circ}S_{298}$	Method	Reference
Cu_2Se	157.4	Vapor pressure	[8]
	113.9	EMF	[11]
	129.7	Evaluation	[12]
	129.7	Assessment	This work
Cu_3Se_2	185	EMF	[11]
	207.2	Evaluation	[12]
	210.7	Assessment	This work
CuSe	86.2	Vapor pressure	[8]
	74.1	EMF	[11]
	78.2	Evaluation	[12]
	78.2	Assessment	This work
$CuSe_2$	120.6	Vapor pressure	[8]
	98.8	EMF	[11]
	107.4	Evaluation	[12]
	115.4	Assessment	This work

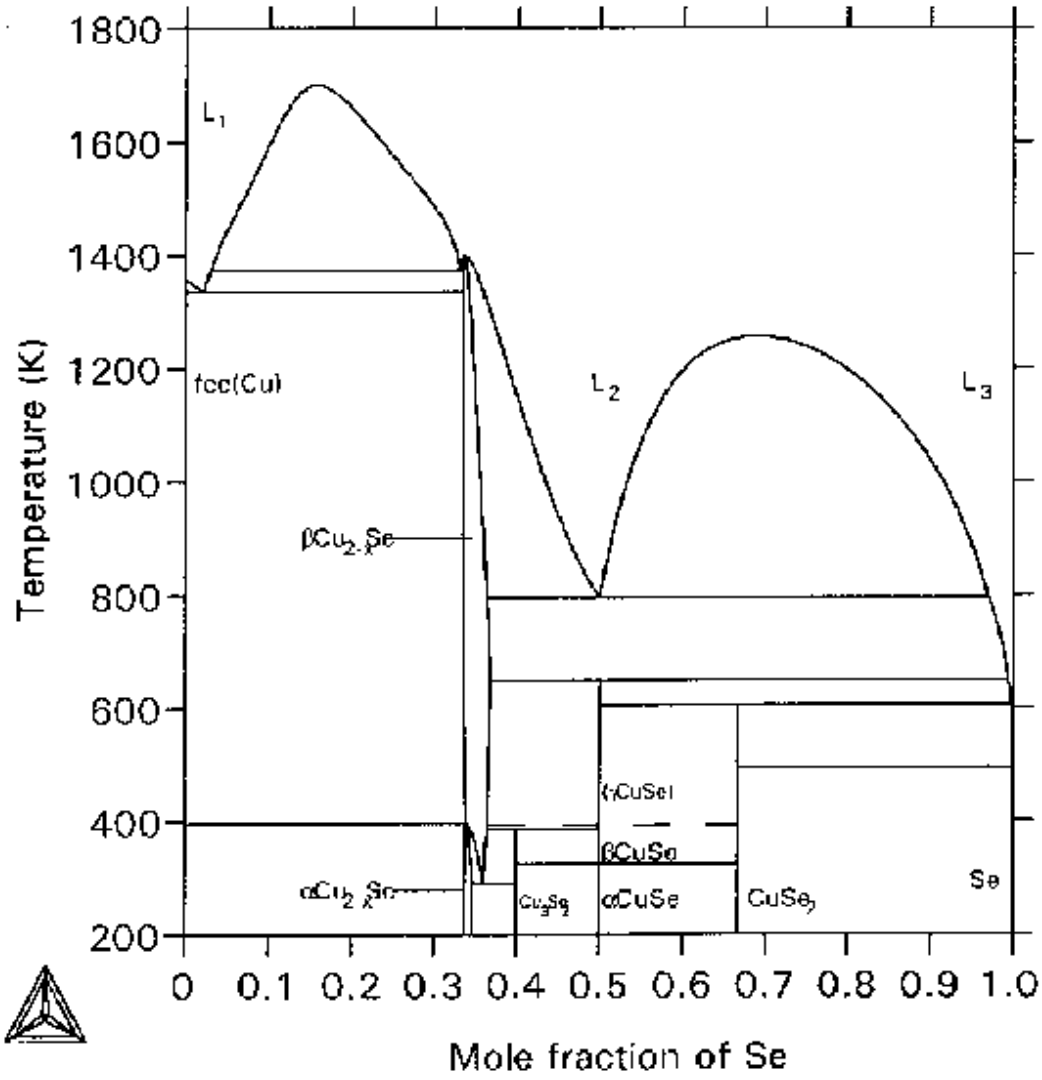

Figure 2.1. The calculated Cu-Se binary phase diagram based on the optimized parameters.

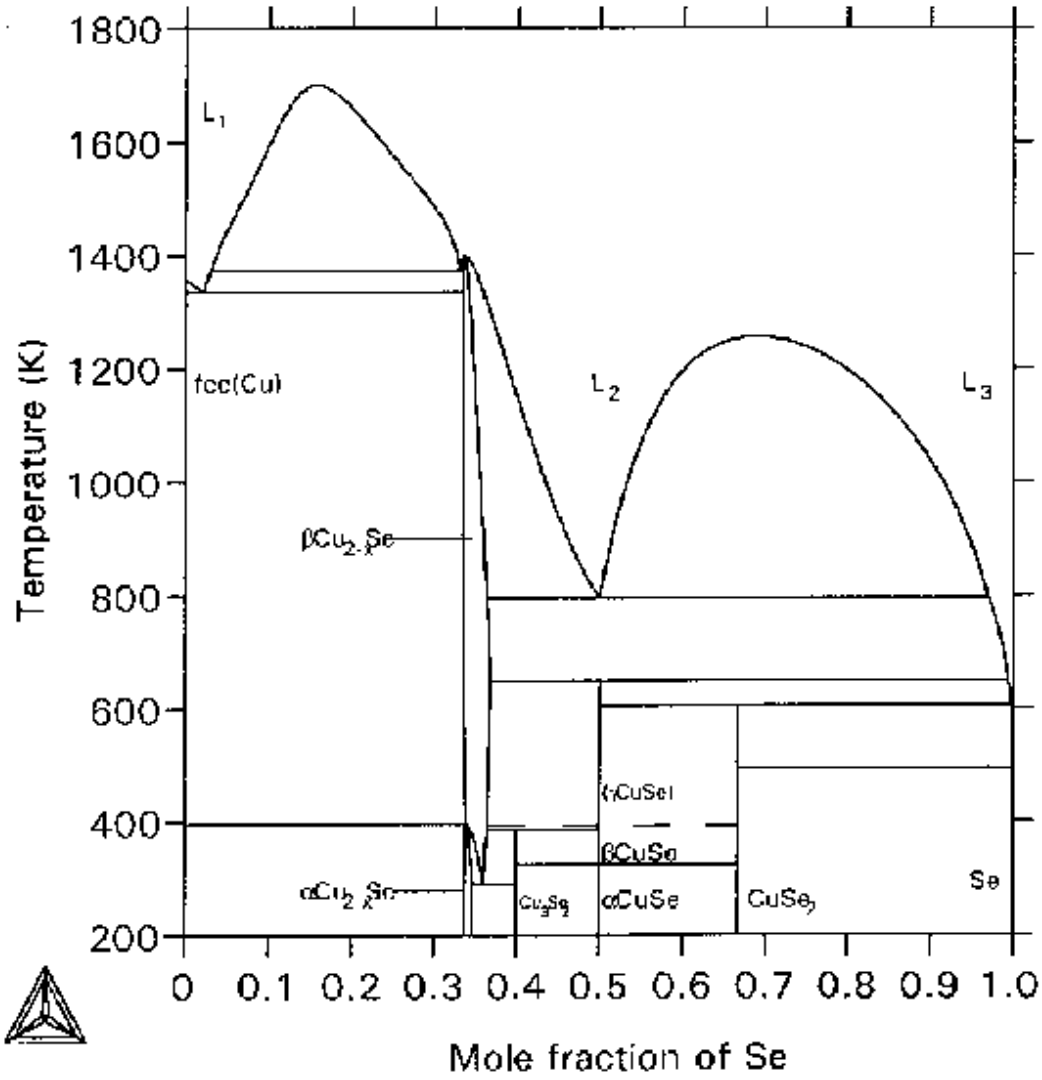

Figure 2.2a. Comparison between the calculated Cu-Se phase diagram and various experimental data.

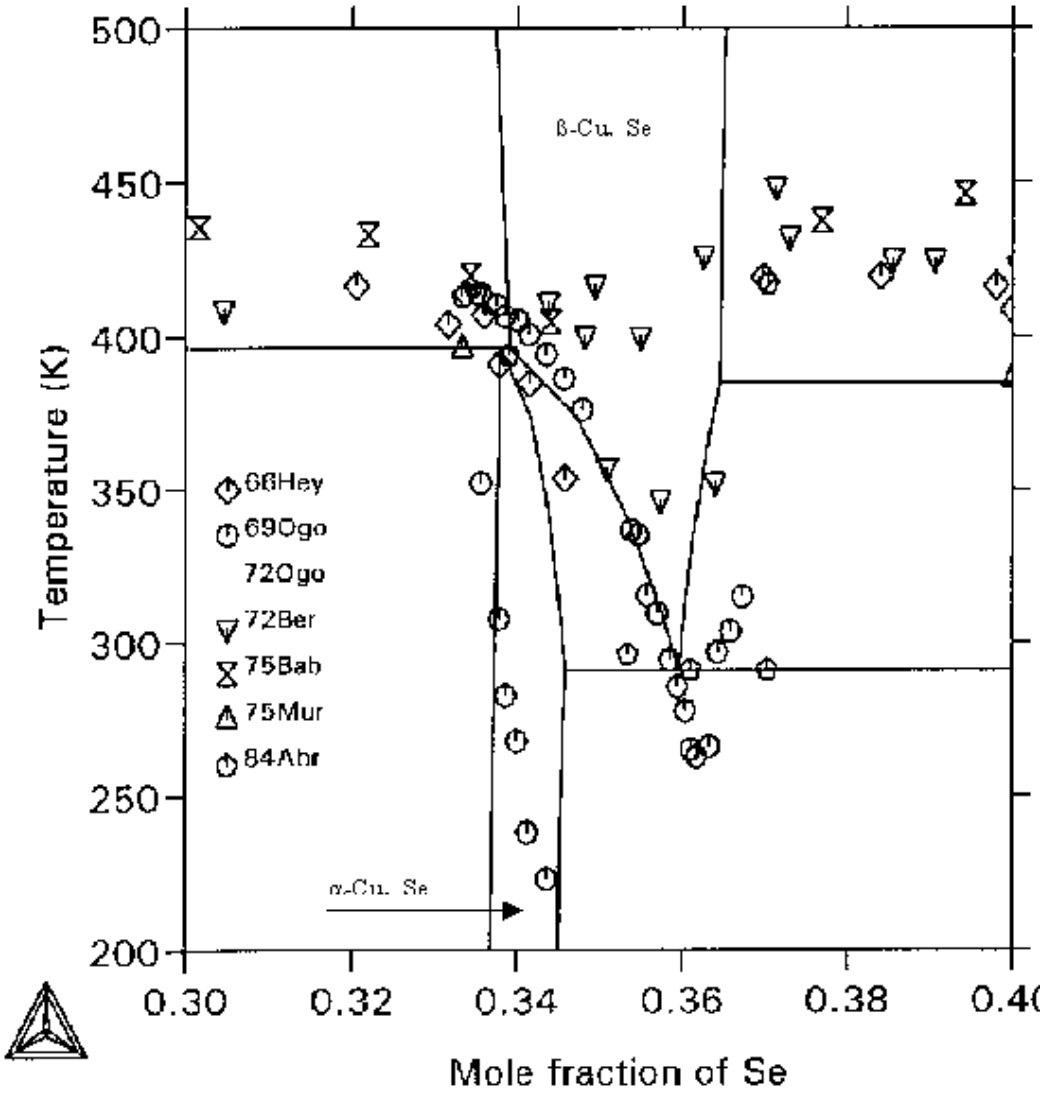

Figure 2.2b. Comparison between the calculated Cu-Se phase diagram and various experimental data available in the literature in the vicinity of α-$Cu_{2-x}Se$ and β-$Cu_{2-x}Se$ equilibria and the related eutectoid.

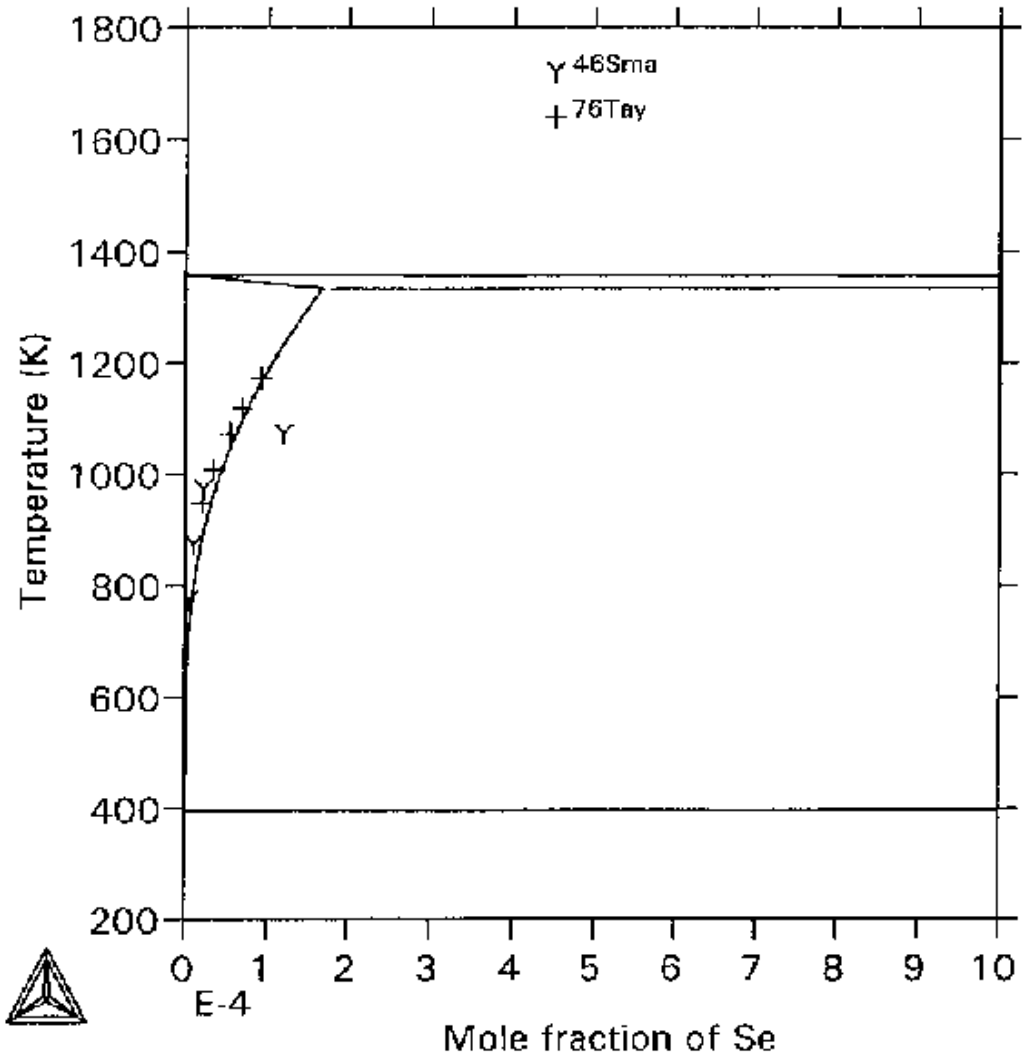

Figure 2.2c. Comparison between the calculated Cu-Se phase diagram and experimental data available in the literature for the Se solubility in Cu terminal.

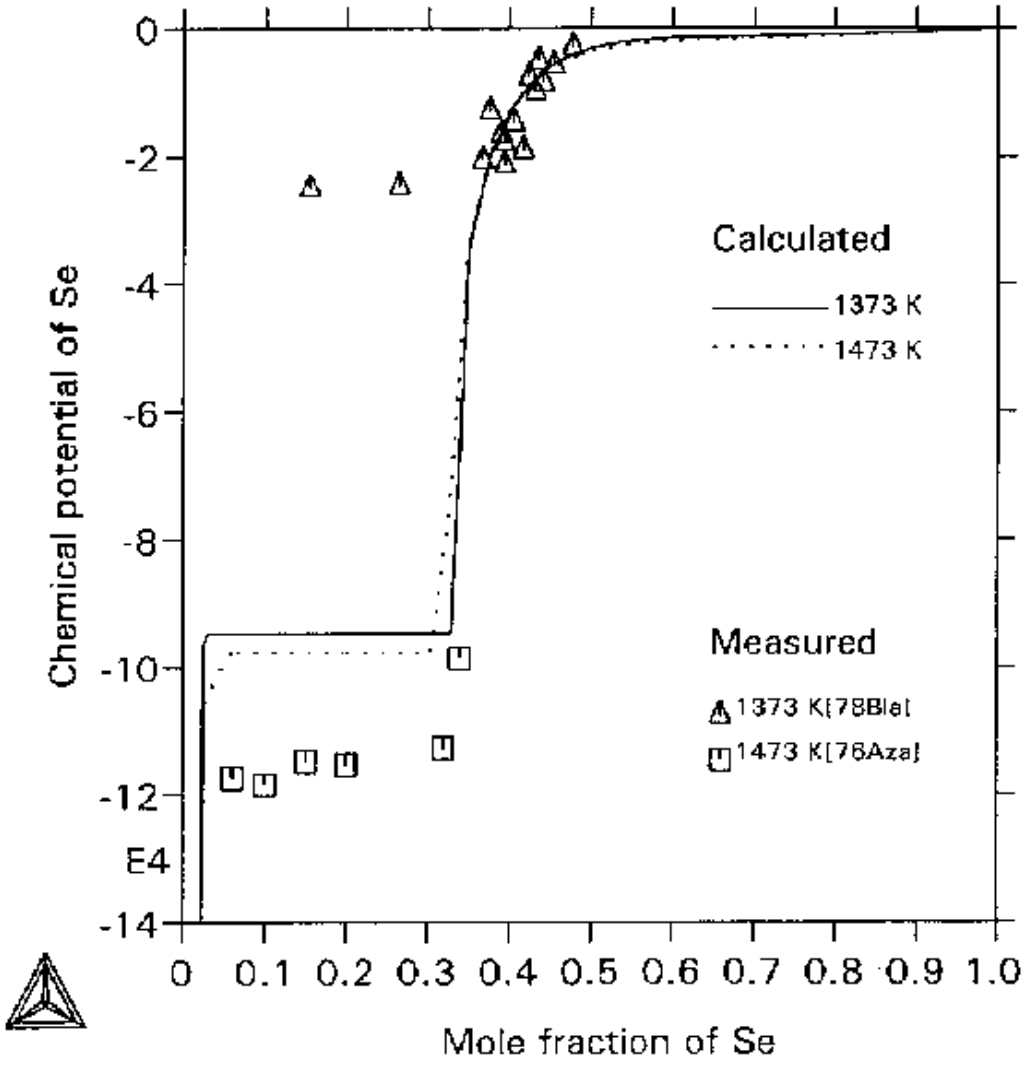

Figure 2.3. Calculated chemical potential of Se in the liquid phase along with the experimental data [76Aza, 78Bla]. The reference state is the liquid phase of pure selenium.

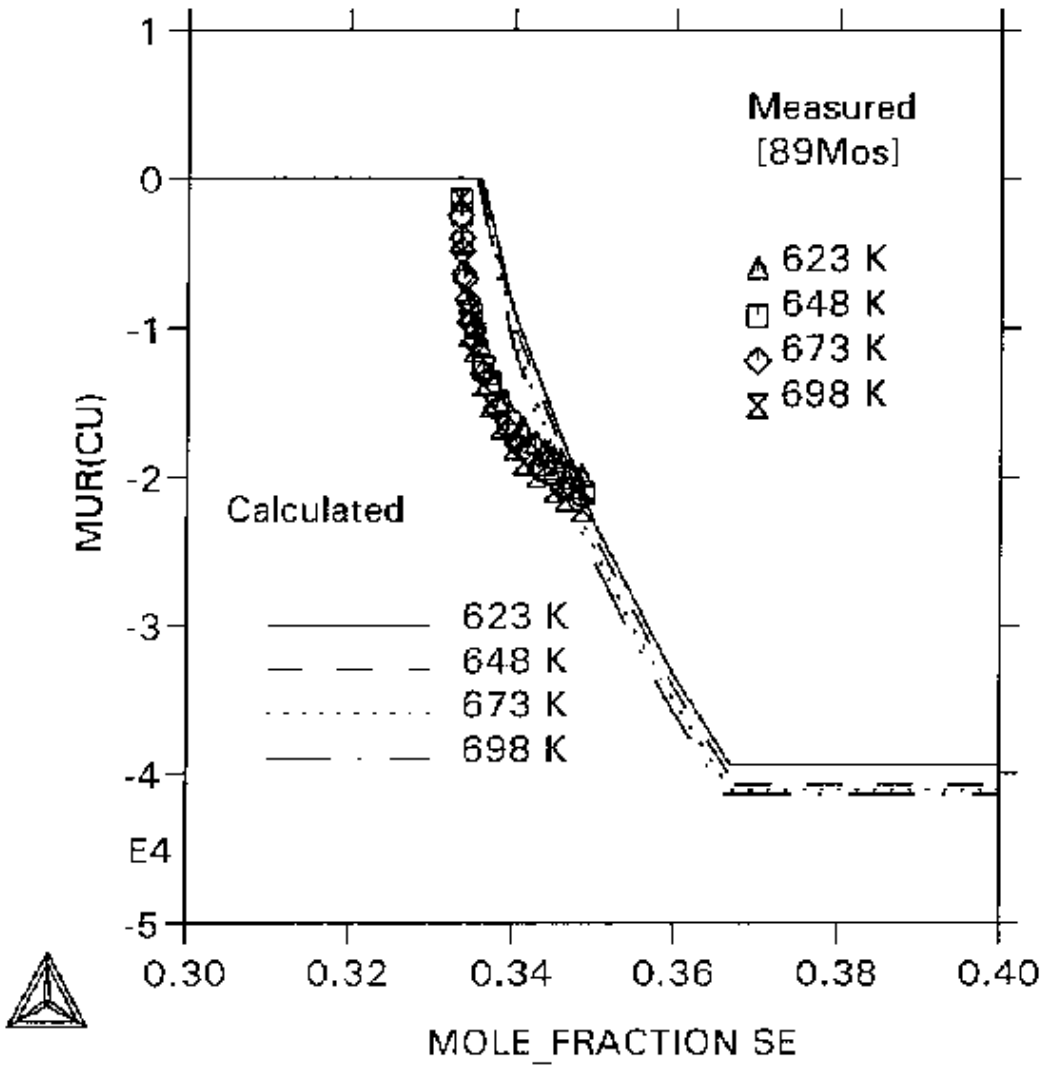

Figure 2.4. Calculated chemical potential of Cu in the β-$Cu_{2-x}Se$ phase with the experimental data [89Mos]. The reference state is the fcc phase of pure copper.

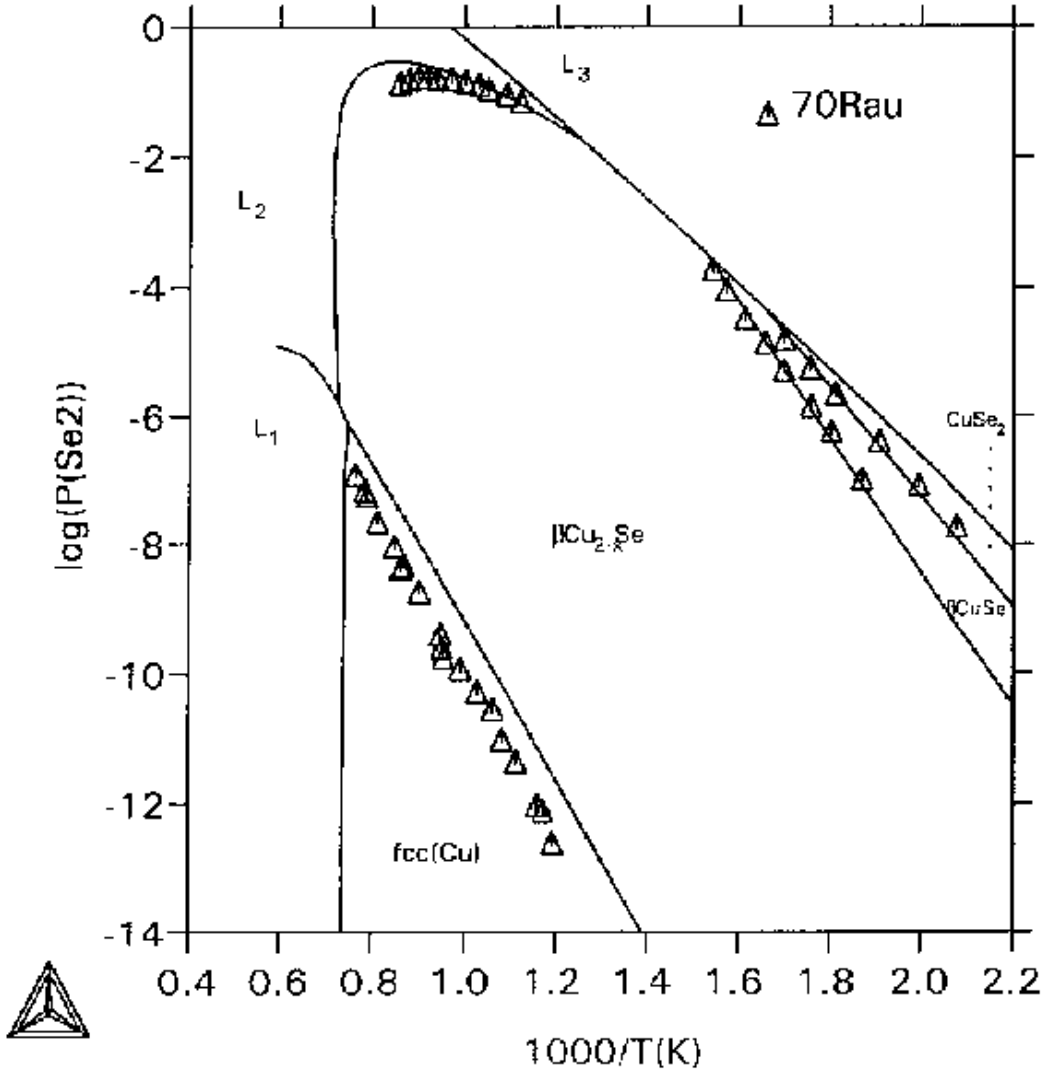

Figure 2.5. Calculated Se_2 partial pressures in the Cu-Se system (atm) along with the experimental data [8].

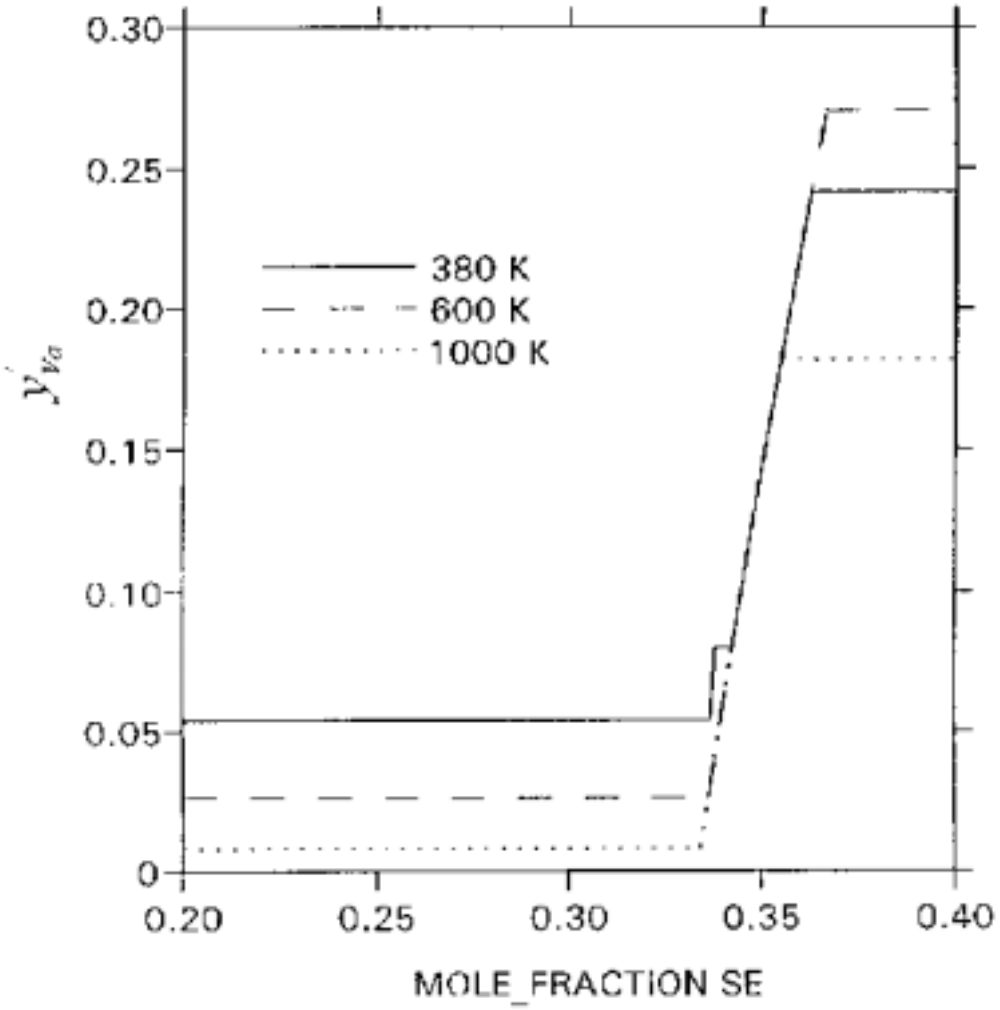

Figure 2.6. The calculated site fractions of Cu vacancy on the first sublattice for the β-$Cu_{2-x}Se$ phase.

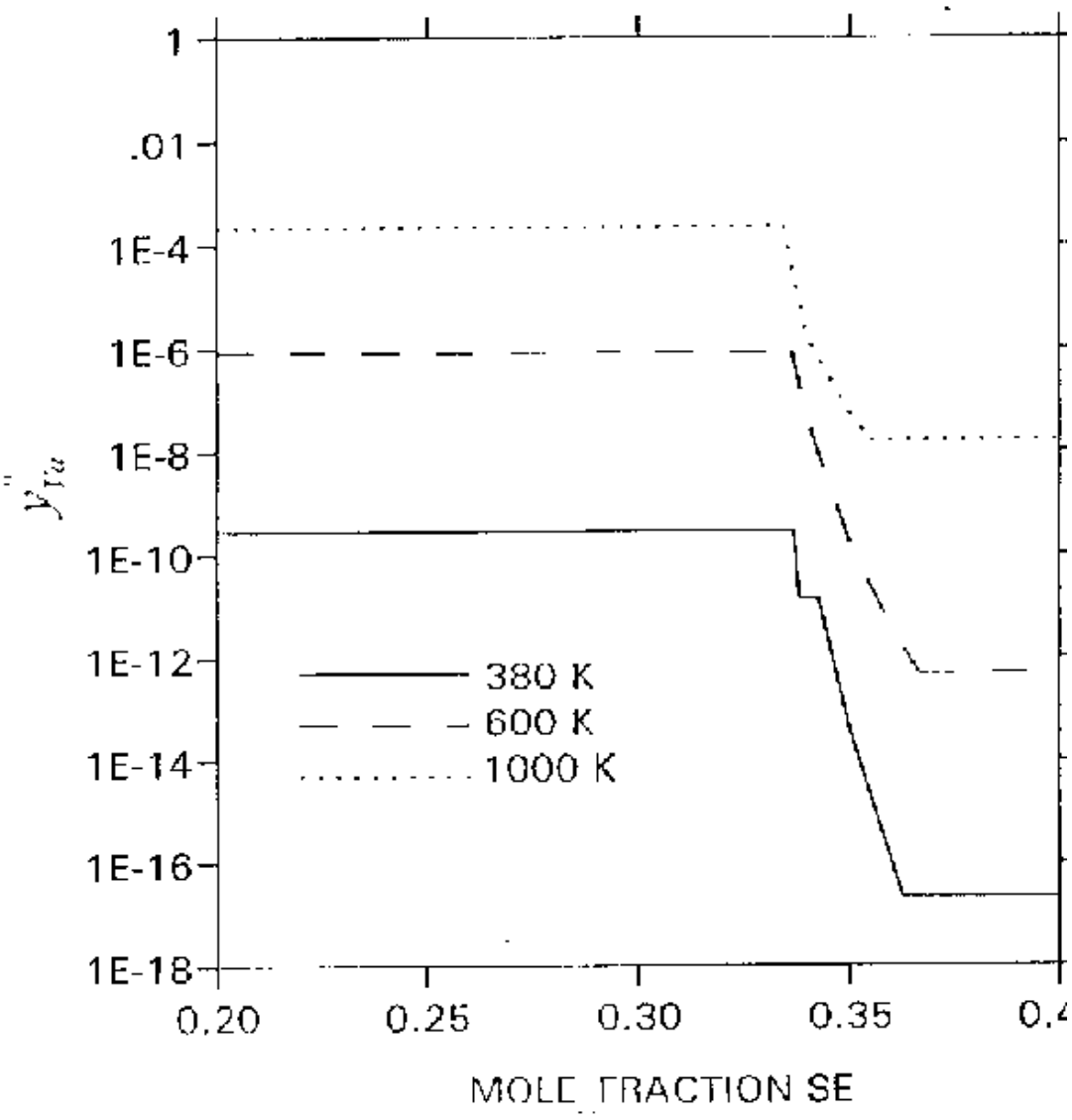

Figure 2.7. The calculated site fractions of Se vacancy on the second sublattice for the β-$Cu_{2-x}Se$ phase.

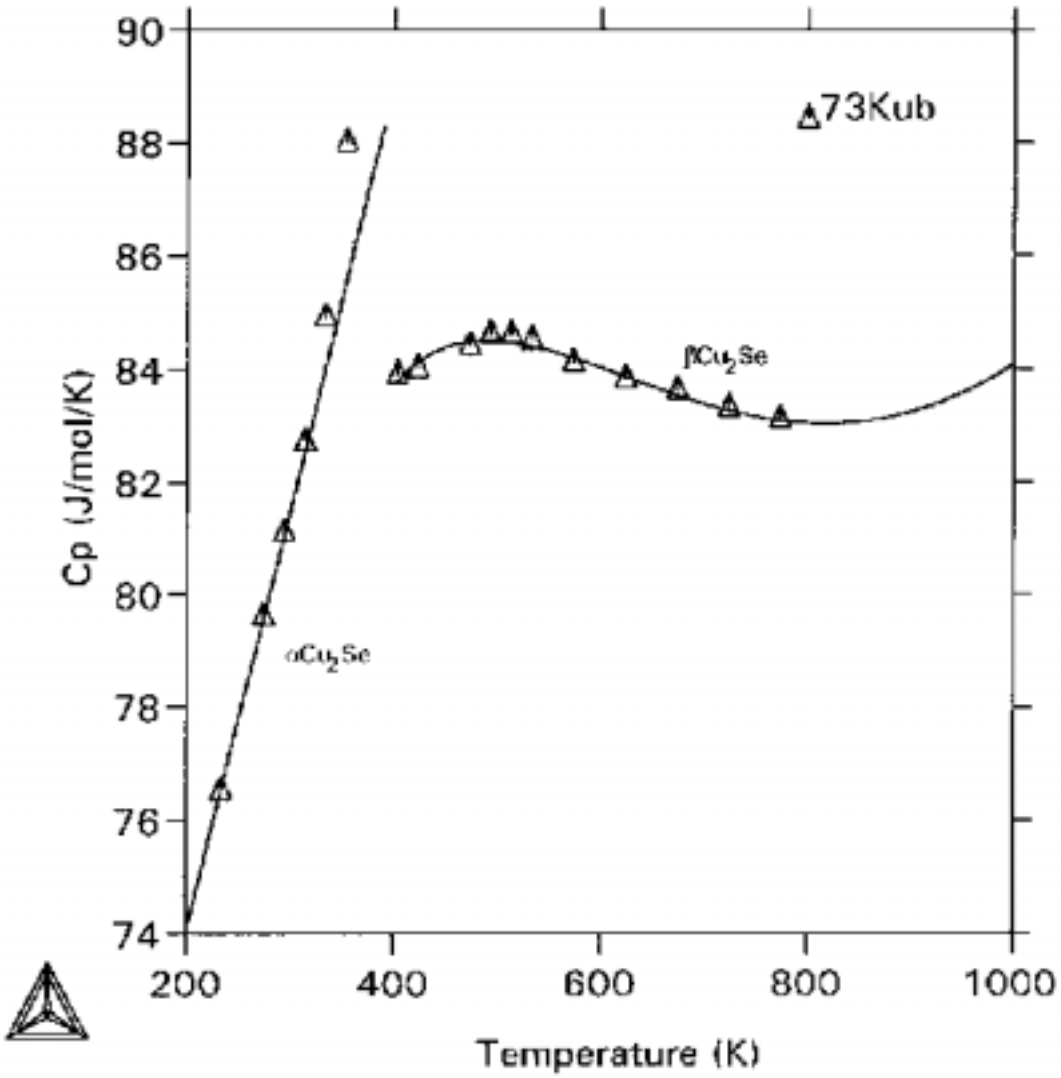

Figure 2.8. Calculated heat capacity for α-Cu_2Se and β-Cu_2Se along with the experimental values [57].

2.9 References

[1] Hansen M., & Anderko K., *Constitution of Binary Alloys*, McGraw-Hill Book Co., New York, 1958.

[2] Chakrabarti D. J. , & Laughlin D. E., *Bulletin of Alloy Phase Diagrams* 2(3): 305 , 1981.

[3] Korzhuev M. A., Baranchikov V. V., Abrikosov N. Kh., & Bankina V. F., *Sov. Phys. Solid State* 26(7): 1341, 1984.

[4] Abrikosov N. Kh., Bankina V. F., Korzhuev M. A., Demeskii G. K., & Teplov O. A., *Sov. Phys. Solid State* 25(10): 1678, 1984.

[5] Glazov, V. M.; Kim, S. G.: *Inor. Mater.*, 26: 2141, 1991.

[6] Gattow G., and Schneidener A., *Z. Anorg. Allgem. Chem*. 286: 296, 1956.

[7] Valverde N., *Zeit. Physik. Chemie Neue Folge* 61: 92, 1968.

[8] Rau H., & Rabenau A., *J. Sol. State Chem.* 1: 515, 1970.

[9] {Kub 58} missing in reference list

[10] Kubaschewski, P. and Nolting, N., *Ber. Busenges. Phys. Chem.,*77:70 (1973).

[11] Askerova K. A., Alieva N.A., Azizov T. Kh., Abbasov A. S., & Mustafayev F. M., *Izv. Akad. Nauk Azerb SSR*. 6: 137, 1976.

[12] Mills K.C., *"Thermodynamic data for inorganic sulphides, selenides and tellurides"*,London, Butterworth, 1974.

[13] Tubandt C., and Reinhold H.Z., *Z. Physik. Chem.*, A140: 291, 1929.

[14] Skeoch K. G., & Heyding R. D., *Can. J. Chem.* 51: 1235, 1973.

[15] Heyding R.D., *Can. J. Chem.*, 44: 1233, 1966.

[16] Bernardini G. P., & Catani A., *Miner. Deposita*(berl.) 3: 375, 1968.

[17] Murray R. M., & Heyding R. D., *Can. J. Chem.* 53: 878, 1975.

[18] Vucic Z., & Ogorelec Z., *Phil. Mag*. 42, 287: 1980.

[19] Bernardini G. P., Corsini F., & Trosti R., *Period. Miner*. 41: 565, 1972.

[20] [Mil 80] missing in reference list

[21] Mostafa, S.N.; Selim, S.R.; Soliman, S.A.; El-Lakwah, F.A.: *Ber. Bunsenges. Phys. Chem.*, 93: 123, 1989.

[22] Blachnik R., Bolte G., *J. Less-Common Metals* 57: 21, 1978.

[23] Azakami T., and Yazawa A., *Canadian Metallurgical Quarterly* 15: 111, 1976.

[24] Dinsdale A.T., *CALPHAD*, 15(4), 317, 1991.

[25] Chang, C.H.; Davydov, A.; Stanbery, B.J.; Anderson, T.J.: to be published, 1999.

[26] Smart, J.S.; Smith, A.A.: *Trans. AIME*, 166: 144, 1946.

[27] Tayler, P.L.; Wagner, D.L.; Pitt, C.H.: *Met. Trans.*, 7B: 103, 1976.

[28] Redlich, O.; Kister, A.: *Ind. Eng. Chem.*, 40: 345, 1948

[29] Sommer, F.: *Z.Metallkd.*, 73: 72, 1982.

[30] Rahlfs, P.: *Z.Physik. Chem.*, B31: 157, 1936.

[31] Borchert, W.: *Z. Krist.*, 106: 5, 1945.

[32] Stevels, A.L.N.; Jellinek, F.: *Rec. Trav. Chim.*, 111: 273, 1971.

[33] Tonejc, A.; Tonejc, A. M.: *J. Sol. Stat. Chem.*, 39: 259, 1981.

[34] Oliveria, M.; McMullan, R.K.; Wuensch, B.J.: *Sol. Stat. Ionic*, 28-30: 1332, 1988.

[35] Sakuma, T.; Sugiyama, K.; Matsubara, E.; Waseda, Y.: *Mater. Trans.* JIM, 30(5); 365, 1989.

[36] Yamamoto, K.; Kashida, S.: *J. Sol. Stat. Chem.*, 93: 202, 1991

[37] Hillert, M.; Staffanson, L.I.: *Acta Chim. Scand.*, 24: 3618, 1970.

[38] Sundman, B.; Agren, J.: *J. Phys. Chem. Solids*, 42: 297, 1981.

[39] Sorokin, G. P.; Idrichan, Z.; Dergach, L.V.; Kovtun, E. V.; Sorokina, Z. M.: *Izv. Akad. Nauk.* SSSR Neorg. Mater., 10(6), 969, (1974) in Russian: translated as *Inorg. Mater.*, 10(6): 834, 1974.

[40] Medicis, R.de; Thesis, Louvain, 63,1967.

[41] Asadov, J.G.; Dzabrailova, G.A.; Nasirov, Z.M.: *Neorg. Mater.*, 8: 11, 1972.

[42] Marimoto, N.; Uchimizu, M.; in: X-ray powder data file 19-401, ed. L.G.Berry, Special Technical Publications 480G ASTM, Philadelphia, 1969.

[43] Stevels, A. L. N.: *Philips Res. Rep. Suppl*., 9: 1, 1969.

[44] Vucic, Z.; Milat, O.; Horvatic, V.; Ogorelec, Z.: *Phys. Rev.* B, 24(9): 5398, 1981.

[45] Milat, O.; Vucic, Z.: *Sol. Stat. Ionics*, 23: 37, 1987.

[46] Frangis, N.; Manolikas, C.; Amelinckx, S.: *Phys. Stat. Sol.* A, 126: 9, 1991.

[47] Kashida, S.; Akai, J.: *J.Phys.* C, 21: 5329, 1988.

[48] Ansara, I.; Dupin, N.; Lukas, H.L.; Sundman, B.: in: *Applications of Thermodynamics in the Synthesis and Processing of Materials*, P.Nash and B.Sundman (eds.), The Minerals, Metals & Materials Society: 273, 1995.

[49] Zhuang, W.; Shen, J.; Liu, Y.; Ling, L.; Shang, S.; Du, Y.; Schuster, J.C.: *Z. Metallkd.*, (accepted), 1999.

[50] Pankajavalli, R.; Ider, M.; Stanbery, B.J.; Anderson, T.J.: to be published, 1999.

[51] Sundman, B.; Jansson, B.; Andersson, J.-O, *CALPHAD*, 9: 153, 1985

[52] Mostafa, S.N., Selim, S.R., Soliman, S.A. and El-Lakwah, F.A., *Ber. Bunsenges. Phys. Chem.,* 93:123, 1989.

[53] Burylev B. P., Fedorova N. N., & Tsemekhman L. Sh., *Russ. J. Inorg. Chem.* 19: 1249, 1974.

[54] Ogorelec, Z.; Celustka, B.: *J. Phys. Chem. Solids*, 30: 149, 1969.

[55] Ogorelec, Z.; Mestnik, B.; Devcic, D.: *J. Mater. Sci.*, 7: 967, 1972.

[56] Heyding R. D., & Murray R.M., *Can. J. Chem.* 54: 841, 1976.

[57] Kubaschewski P., & Nölting N., *Ber. Busenges. Physik. Chem.*, 77(2): 70, 1973

[58] Babitsyna A. A., Emelyanova T. A., Chernitsyna M. A., & Kalinnikov V. T., *Russ. J. Inorg. Chem.* 20: 1711, 1975.

[59] Dies, K.: *Kupfer und Kupferlegierungen in der Technik*, Springer, Berlin, 1967.

[60] Sundman, B.: SGTE Substance Database, SGTE, 1994

[61] C. H. Chang, Doctoral Dissertation, "Processing and Characterization of Copper, Indium Selenide for Photovoltaic Applications," Chemical Engineering Department, University of Florida, Gainesville, FL, 2000.

PART 3

A Critical Assessment of Thermodynamic Data and Phase Diagram for the In-Se Binary System

Abstract

The In-Se binary system is a member of the III-VI group and contains several semiconducting compounds (such as In_4Se_3, InSe, In_6Se_7, In_2Se_3) with possible applications to electronic devices. The understanding of the thermochemistry and phase diagram the In-Se system is motivated as a step towards predicting the behavior of the Cu-In-Se ternary system. We carried out an assessment of the In-Se system using all the relevant phase diagram and thermochemical data available in the literature, plus a published unary assessment for indium, and one for selenium. Nine intermediate solid phases (In_4Se_3, InSe, In_6Se_7, In_9Se_{11}, In_5Se_7, α-In_2Se_3, β- In_2Se_3, γ- In_2Se_3, and δ-In_2Se_3) are modeled as line compound, and an association model was used to describe the liquid phase. The key results that we obtained by coupling the thermochemical and the phase diagram data, are optimized expressions for the Gibbs free energy with respect to the stable element reference for the solid compounds and for the liquid phase, along with those for the major vapor phase species (in particular Se_n for n=1 to 8, In, InSe, In_2Se,, and In_2Se_2) . The temperature-composition and pressure-temperature projections of the phase diagram were assessed.

Section Contents

3.1 Brief Overview

3.1.1 Participants

Faculty Adviser: Prof. Timothy J. Anderson

Research Assistant: Chih-Hung "Alex" Chang

3.1.2 Objectives

The objectives of this project are to elucidate the thermochemistry and phase diagram of the In-Se system, and to make progress towards the understanding of the full Cu-In-Se system by carrying out a critical assessment of the phase diagram and thermodynamic data available in the literature for the In-Se system.

3.2 Phase Diagram Data

The phase diagram of In-Se system was studied by several investigators [3-12]. The early studies [3, 4, 5, and 6] used DTA and X-ray analysis to identify phase transformations and phases. Four intermediate compounds, In_2Se(s), InSe(s), In_5Se_6(s), and In_2Se_3(s) were reported. InSe(s) and In_2Se_3(s) were identified as congruent melting species. One miscibility gap was proposed in their diagram. Likforman and Guittard [7] investigated the In-Se system from 10 to 95 at.% Se using DTA and X-ray analysis. They reported five compounds In_4Se_3(s) (instead of In_2Se), InSe(s), In_6Se_7(s) (instead of In_5Se_6), In_5Se_7(s), and In_2Se_3(s). Only In_2Se_3(s) was identified as a congruent melting species and two miscibility gaps were proposed in their diagram. Imai et al. [8] investigated the phase diagram from 30 to 56 at.% by DTA. They also carried out the composition analysis of the compounds grown from the stoichiometric and non-stoichiometric melts using He+ ion Rutherford backscattering (RBS). Their diagram was in qualitative agreement with the diagram reported by Likforman et al. [7]. The main differences are the compositions of the peritetic reactions and the shape of the liquidus lines.

Glazov et al. [9] measured the ultrasound propagation rate at different composition and temperature of liquid In-Se alloys to study the In-rich misicibility gap. Okada and Ohno [13] investigated the electronic properties of liquid In-Se alloys, including electrical conductivity, thermopower, and magnetic susceptibility. They also determined the melting temperature of In-Se alloys at different compositions from the temperature dependence of the electronic properties. The In-Se phase diagram was reviewed by Okamoto [14] based on the work of selected authors [1,2, 3, 5, 7, 8]. Didoukh [10] measured the electroconductivity for liquid immiscible $In_{1-x}Se_x$ alloys and determined the miscibility gap on the In-rich side of the phase diagram. Daouchi et al. [11] reinvestigated the In-Se phase diagram using DTA, DSC, and XRD. Their diagram is in qualitative agreement with Okamoto [14]. Gödecke et al. [12] re-determined the stable and metastable In-Se phase diagram using DTA, XRD, optical microscopy, SEM, and TEM. They reported In_9Se_{11} and In_5Se_7 are stable phases at stoichiometric composition and β-In_2Se_3 was observed at 59.6 at. %, contrary to previous studies, which suggested β-In_2Se_3 was one of the polymorphic stoichiometric In_2Se_3 phases. They also suggested the α-In_2Se_3 phase is slightly Se-rich compared to the stoichiometric γ-In_2Se_3 phase, however, the exact composition was not reported. The formation of In_5Se_7 and In_9Se_{11} was suppressed while applying cooling rate between 2 to 10 K/min. They attributed the difference between their finding and the literature

data to the different experimental procedures. The phase diagram data from various authors are shown in Figure 3.2. The invariant equilibria are listed in Table 3.1.

Table 3.1. Invariant equilibria in the In-Se binary system

Phases	Composition, [at. % Se]	Temperature [K]	Reaction Type	Reference
$L_1/In/In_2Se$	0/0/33.33	429.15	Eutetic	[4]
$L_1/In/In_4Se_3$	–/0/42.8 0/0/42.8 0/0/42.8 0/0/42.8 $1.41x10^{-8}$/0/42.8	428.15 429.15 426 429.15 429.7	Eutetic	[7] [14] [11] [12] This study
$L_1/L_2/In_4Se_3$	4/30/42.8 –/30/42.8 –/32/42.8 4/30/42.8 3/32/42.8 -/28/42.8 4/26/42.8 4/26/42.8	793.15 793.15 793.15 793.15 793.15 793.7 794 793.15 793 793.15	Monotetic	[4] [7] [8] [9] [14] [10] [11] [12] [15] **This study**
$L_2/InSe/In_2Se$	50/28.27/33.33	823.15	Peritetic	[4]
$L_2/InSe/In_4Se_3$	50/34/42.8 50/38/42.8 50/38/42.8 50/29/42.8 50//42.8	823.15 823.15 823.15 823.15 823.15 823 818.1	Peritetic	[7] [8] [14] [11] [12] [15] **This study**
$L_2/InSe/In_6Se_7$	45/50/53.8 48.3/50/53.8 45/50/53.8 46/50/53.8 /50/53.8 /50/53.8 49.9/50/53.8	873.15 873.15 873.15 883 884.15 872 883.6	Peritetic	[7] [8] [14] [11] [12] [15] **This study**
$L_2/In_5Se_6/In_2Se_3$	52/53.8/60	933.15	Peritetic	[4]
$L_2/In_6Se_7/In_5Se_7$	51.2/53.8/58.33	933.15	Peritetic	[7]
$L_2/In_6Se_7/In_2Se_3$	50/53.8/60 52/53.8/60 52/53.8/60	918.15 918.15 903.15	Peritetic	[8] [14] [11]
$L_2/ In_6Se_7/In_9Se_{11}$	52/53.8/55 52.411/53.8/55	923.15 922.1	Peritetic	[12] **This study**

$L_2/In_9Se_{11}/In_5Se_7$	/55/58.33 53.05/55/58.33	933.15 930 934.5	Peritetic	[12] [15] **This study**
$L_2/In_5Se_7/\beta\text{-}In_2Se_3$	/58.33/59.8 53.31/58.33/59.8	943.15 938 950.4	Peritetic	[12] [15] **This study**
$L_2/\beta\text{-}In_2Se_3/\delta\text{-}In_2Se_3$	/59.6/60 57.7/59.6/60	1153.15 1145.3	Peritetic	[12] **This study**
$\beta\text{-}In_2Se_3/In_5Se_7/\gamma\text{-}In_2Se_3$	/59.6/60 59.8/59.6/60	471.15 469.5	Eutetoid	[12] **This study**
L_2/In_2Se_3	60	1173.15 1153.15 1161.15 1171.15 1159 1164.15 1157	Congruent Melting	[4] [16] [12] [14] [11] [12] **This study**
$\delta\text{-}In_2Se_3/L_2/L_3$	– 64.3/94.6 60/66/90 60/68/92 60/ - / - 60/ - / - 60/69.83/89.95	1043.15 993.15 1043.15 1017 1023.15 1033 1023.5	Monotetic	[4] [7] [14] [11] [12] [15] **This study**
$\delta\text{-}In_2Se_3/\gamma\text{-}In_2Se_3/L_3$	60/60/- 60/60/- 60/60/93.4968	1023.15 1018.15 1013.8	Peritetic	[4] [12] **This study**
$L_3/In_2Se_3/Se$	99.99/60/100 99.99/60/100 99.99/60/100 99.99/60/100 99.99/60/100 99.99/60/100	498.15 493.15 493.15 488 494.15 494	Eutetic	[4] [7] [14] [11] [12] **This study**
$\alpha\text{-}In_2Se_3/\gamma\text{-}In_2Se_3/Se$	60.04/60/100 60.04/60/100	484 487.7	Peritectoid	[12] **This study**

3.3 Enthalpy, Entropy and Heat Capacity Data

3.3.1 Unary data

Gibbs energy data of condensed phase indium was taken from the SGTE database [1]. The thermodynamic properties of pure selenium were assessed in this work as discussed by Chang [59]. The data are given in Tables 18.4 and 18.5 in the form of expressions for the Gibbs free energy with respect to the stable element ($G-H_{SER}$).

Table 3.4 Gibbs energy relative to H_{SER} of condensed indium.

Phase	Temperature Range (K)	Coefficients in the $G-H_{SER}$ expression $G-H_{SER} = A + BT + CTlnT + DT^2 + ET^3 + F/T + GT^7 + HT^{-9}$ (J/ K• mol)
Solid Hexagonal	298.15 - 429.75	A = - 6978.89 B = 92.3338115 C = - 21.8386 D = - 5.72566 x 10^{-3} E = - 2.120321 x 10^{-6} F = - 22906 G = 0 H = 0
„	429.75 - 3800 *	A = -7033.516 B = 124.476588 C = - 27.4562 D = - 0.54607 x 10^{-3} E = - 0.08367 x 10^{-6} F = -211708 G = 0 H = 3.53 x 10^{22}
Liquid	298.15 - 429.75 **	A = - 3696.798 B = 84.701255 C = - 21.8386 D = - 5.72566 x 10^{-3} E = - 2.120321 x 10^{-6} F = - 22906 G = -5.59 x 10^{-20}
„	494.4 - 3800	A = - 3749.81 B = 116.835784 C = - 27.4562 D = 0.54607 x 10^{-3} E = - 0.08367 x 10^{-6} F = -211708 G = 0 H = 0

Note: *- superheated solid, **- supercooled liquid

Table 3.5 Gibbs energy relative to H_{SER} of condensed selenium.

Phase	Temperature Range (K)	Coefficients in the $G-H_{SER}$ expression $G-H_{SER} = A + BT + CTlnT + DT^2 + ET^3 + F/T$ (J/ K mol)
Solid Hexagonal	298.15 - 494.3	A = - 6657 B = 92.53969 C = - 19.14 D = -0.012295 E = 0.2677 x 10^{-5} F = 0
„	494.3 - 760 *	A = - 6657 B = 92.53969 C = - 19.14 D = -0.012295 E = 0.2677 x 10^{-5} F = 0
„	760 - 1200 *	A = - 9059.17 B = 150.33422 C = - 28.552 D = 0 E = 0 F = 0
Liquid	298.15 - 494.3 **	A = - 9809.20 B = 288.81342 C = - 52.4 D = 0.024925 E = - 0.5455 x 10^{-5} F = 0
„	494.4 - 1000	A = - 9809.20 B = 288.81342 C = - 52.4 D = 0.024925 E = - 0.5455 x 10^{-5} F = 0
„	1000-1150	A = 8433.14 B = -78.47693 C = 5.399 D = - 0.035945 E = 0.5202 x 10^{-5} F = 0
„	1150-1500	A = - 7460.62 B = 192.64635 C = -36 D = 0 E = 0 F = 0

Note: *- superheated solid, **- supercooled liquid

3.3.2 In_2Se_3(s)

In_2Se_3(s) was reported to exist in several polymorphic phases, however, the literature contains contradictory results on the structure and phase transition temperature [3, 18, 19, 60, 16,

20, 22, 23, 11, 12]. The uncertainty about the structure of In_2Se_3 is likely related to several reasons, including: 1. Complexity and similarity of the different polymorphic structures that exist in the vicinity of this composition. 2. Different techniques used to prepare the samples. 3. The volatile nature of In_2Se_3 (s) causing the composition to drift during the heat treatment involved in phase transition experiments. 4. The difficulty in performing in-situ structural investigations without losing volatile components from the vapor phase.

Mills [24] reported the only information concerning the high temperature heat capacity and enthalpy of transition. He reported the heat capacity for In_2Se_3(s) and In_2Se_{3-x}(s) in the temperature range T=298 to700 K and the transition enthalpy at 486 K. The XRD analysis on the quenched in In_2Se_{3-x}(s) sample after the DSC measurements indicate this In-rich In_2Se_3 is β-In_2Se_3. This result is consistent with the phase diagram of Gödecke et al. [12]. Mill's C_p data were used to fit the heat capacity, $C_p(T)$, equations for α, β, and γ-In_2Se_3. The δ-In_2Se_3(s) heat capacity was estimated by Pashinkin and Zharov [25] from In_2S_3 heat capacity data. The fitted $C_p(T)$ results are given in Table 3.8.

The standard enthalpy of formation, $\Delta H^o_{f,298.15K}$, for α-In_2Se_3 has been studied by several authors using different techniques, including combustion calorimetry [26], synthesis calorimetry [27], mass-spectrometry [28], vapor pressure (absorption spectra) [17], EMF measurements [29], [15], vapor pressure measurements (Knudsen or torsion) [30, 25, 31], and analysis of the reaction: $In_2Se_3(s)+ I_2(g)=2InI(g)+1.5Se_2(g)$ [32].

Mills [24] reported the value for α-In_2Se_3 to β-In_2Se_3 transition enthalpy, ΔH_{tr}=3.85 kJ/mol, using DSC. His value was re-interpreted as α-In_2Se_3 to γ-In_2Se_3 transition based on the recent phase diagram [12]. The standard enthalpy of formation, $\Delta H^o_{f,298.15K}$= -319.9 kJ/mol, for γ-In_2Se_3 was estimated from the standard enthalpy of formation, $\Delta H^o_{f,298.15K}$= -318 kJ/mol [27], for α-In_2Se_3 using this transition enthalpy.

Vapor pressure measurements [17, 25, 30-32] were performed in the high temperature range, where δ-In_2Se_3 and γ-In_2Se_3 are the stable phases. Selected vapor pressure data [25, 30, 31] were used to derive the standard enthalpy of formation value for δ-In_2Se_3. The results are summarized in Table 3.6.

Srinivasa and Edwards [33] studied the vaporization chemistry by the simultaneous Knudsen and torsion method in the vicinity of stoichiometric In_2Se_3. If we re-interpret their data based on the new diagram by Gödecke et al. [12], the data they interpreted as the α-In_2Se_3+In_5Se_6 two-phase equilibrium vapor pressure could be re-interpreted as the T-P projection above the γ-In_2Se_3 and β-In_2Se_3 two-phase domain. Their vapor pressure data were used to estimate the value for β-In_2Se_3 according to the following vaporization reaction,

$$\gamma\text{-}In_2Se_3 \rightarrow \beta\text{-}In_2Se_{2.95} + 0.02475Se_2$$

The value, $\Delta H^o_{f,298.15K}$= - 314.8 kJ/mol, was obtained by second law method.

The value of standard entropy, $S^o_{298.15\ K,}$ for α-In_2Se_3(s) was estimated from measurements of the low temperature heat capacity [34, 41, 48], and from EMF measurements [29]. The data are summarized in Table 3.7. The standard entropy, $S^0_{298,}$ for γ-In_2Se_3(s) was estimated from $S^o_{298.15\ K}$ of α-In_2Se_3(s) using the heat capacity data for α-In_2Se_3(s) and γ-In_2Se_3(s) and $\Delta S^o_{\alpha\rightarrow\gamma}$ transition entropy data retained in this work. The value, $S^o_{298.15K}$= 210.68 J/K mol, was obtained for γ-In_2Se_3(s).

The transition enthalpy for the γ-In_2Se_3 to δ-In_2Se_3 transformation was estimated from the values of standard enthalpy of formation and the heat capacity of γ-In_2Se_3 and δ-In_2Se_3. The transition entropy was then calculated from the equation, $\Delta S_{tr}=\Delta H_{tr}/T_{tr}$. The value, $S^o_{298.15K}$=260.99 J/mol K, was obtained for δ-In_2Se_3(s) from the S^o_{298} value of γ-In_2Se_3(s) and the $\Delta S^o_{\gamma\rightarrow\delta}$ transition entropy data retained in this work.

3.3.3 In_5Se_7

No thermochemical data are available for the In_5Se_7 phase. For ionic or quasi-ionic systems, the shape of the $\Delta H^o_{f,298.15K}$ polygon vs. composition usually lies outside the basic triangle, and the summit is often the compound with the highest melting temperature [35]. Following this trend, the standard heat of formation, $\Delta H^o_{f,298.15K}$, for In_5Se_7 is estimated to be –784.4 kJ/mol from Figure 3.1. The value of standard entropy, $S^o_{298.15}$, is estimated to be 469.9 (J/K mol) by Latimer's rule [36]. The heat capacity is estimated by Unäl's rule [37]. The enthalpy, entropy and heat capacity data are listed in Tables 3.9, 3.10 and 3.11, respectively.

3.3.3.1 In_9Se_{11}

As with In_5Se_7 there are no thermochemical data available for the In_9Se_{11} phase. The standard heat of formation, $\Delta H^o_{f,298.15K}$, for In_9Se_{11} is estimated to be -1282 kJ/mole using Figure 3.1. The standard entropy, S^0_{298}, is estimated to be 796.8 (J/K mol) by Latimer's rule [36]. The heat capacity is estimated by Unäl's rule [37]. The enthalpy, entropy and heat capacity data are listed in Tables 3.9, 3.10 and 3.11, respectively.

Table 3.6 Standard heat of formation of In2Se3(s) at 298.15 K.

Author	Method	$-\Delta H^{o}_{f,298K}$ (kJ/mol)
α-In_2Se_3(s)		
[38]	Combustion calorimetry	344±13
[27]	Synthesis calorimetry	318±5
[29]	EMF	239.1±18.4
[17]	from reaction $In_2Se_3(s)+I_2=2InI(g)+1.5Se_2(g)$	209
[30]	Vapor pressure (Knudsen)	321±20
[39]	Evaluated	326.25
[31]	Vapor pressure (torsion,Knudsen)	288±20
[25]	Vapor pressure (Knudsen)	303.2±30
[40]	Assessed	275.8±25
[15]	EMF	330.9±1.6
This work (**)	Assessed	323.98
γ-In_2Se_3(s)		
This work (**)*	Calculated from [27]	319.9
This work (**)	Assessed	324.0
β-In_2Se_3(s)		
[33]*	Vapor pressure (torsion,Knudsen)	314.8
This work (**)	Assessed	320.0
δ-In_2Se_3(s)		
[30]*	Vapor pressure (Knudsen)	273.2
[25]*	Vapor pressure (Knudsen)	262.0
[31]*	Vapor pressure (torsion,Knudsen)	268.7
This work (**)	Assessed	315.8

Note: * recalculated in this work (**)

Table 3.7 Reported $S^0_{298.15\ K}$ values for In_2Se_3.

Species	$S^o_{298.15\ K}$ J /K mol	Experimental method	Reference
α-In_2Se_3	197.6	Adiabatic Calorimetry	[41]
	192.3 ± 8.8	EMF	[29]
	202.2	Adiabatic Calorimetry	[34]
	197	Estimated	[39]
	204.3	Assessed	This work (**)
γ-In_2Se_3	210.7	Estimated	This work (**)
	210.9	Assessed	This work (**)
δ-In_2Se_3	261.0	Estimated	This work (**)
	219.1	Assessed	This work (**)
β-In_2Se_3	210.4	Estimated	[33]*
	211.3	Assessed	This work (**)

Note: * calculated in this work (**)

Table 3.8 Assessed heat capacity for In_2Se_3(s).

phase	C_p= a + bT (J/Kmol)
α	107.64907+0.054328 T
β	116.78158+0.026741 T
γ	113.41683+0.035989 T
δ	151

3.3.4 In_6Se_7(s)

The standard enthalpy of formation, $\Delta H^o_{f,298.15K}$, and entropy, $S^o_{298.15K}$, for In_6Se_7(s) have been measured by Mustafaev *et al.* [29], but the values were assigned to In_5Se_6(s). Chatillon [40] has recalculated the ΔG^o_f (T) = -761578+290.849 T (J/mol). The value, $\Delta H^o_{f,298.15K}$ =-688.63 (kJ/mol), is obtained by recalculation of the EMF data of Mustafaev et al. The value, $S^o_{298.15K}$=514.14 (J/K mol), is obtained from the second law $\Delta S^o_{f,298.15K}$ value derived from the EMF data [29]. The value, 520.85 (J/K mol), is obtained if estimated by Latimer's rule [36]. The heat capacity was determined by Mills [24] from DSC measurements. The enthalpy, entropy and heat capacity data are listed in Table 3.9, 3.10 and 3.11, respectively.

3.3.5 InSe(s)

The standard enthalpy of formation, $\Delta H^{o}_{f,298.15K}$, was determined by Hahn and Burrow [42] using combustion calorimetry, and by Mustafaev *et al.* [29] from their EMF measurements. Values of the enthalpy and entropy of fusion were reported by Mills [24] using DSC. A value for the absolute entropy, $S^{o}_{298.15K}$, data were reported by Mamedov *et al.* [43] from low temperature heat capacity measurements. The value, $S^{o}_{298.15K}$ = 77.44 (J/K mol), is obtained from second law $\Delta S^{o}_{f,298.15K}$ value of the EMF data [29]. Mills [24] measured the heat capacity using DSC. The enthalpy, entropy and heat capacity data are listed in Tables 3.9, 3.10 and 3.11, respectively.

3.3.6 In_4Se_3(s)

The standard enthalpy of formation, $\Delta H^{o}_{f,298.15K}$, and entropy, $\Delta S^{o}_{f,298.15K}$, for In_2Se(s) have been measured by Mustafaev *et al.* [29], which should be assigned to In_4Se_3(s) based on the correct phase diagram. The values, $\Delta H^{o}_{f,298.15K}$ =-332.24 (kJ/mol) and $S^{o}_{298.15K}$=336.83 (J/K mol), were obtained by recalculation of the EMF data reported by Mustafaev et al. [29]. Chatillon [40] estimated the entropy value to be 292.9 (J/K mol) using Latimer's rule [36] and the heat capacity data by Unäl,s rule [37]. The enthalpy, entropy and heat capacity data are listed in Table 3.9, 3.10 and 3.11, respectively.

Table 3.9 Standard enthalpy of formation values at 298.15 K, $\Delta H^{o}_{f,298.15K}$, of In-Se compounds.

Species	$-\Delta H^{o}_{f,298.15K}$ (kJ/mol)	Experimental method	Reference
In_5Se_7	753	Estimated	This work (**)
	793.75	Assessed	This work (**)
In_9Se_{11}	1215.9	Estimated	This work (**)
	1337.6	Assessed	This work (**)
In_5Se_6	580.6± 16.3	EMF	[29]
In_6Se_7	688.63	EMF	[29]*
	808.6 ± 0.5	EMF	[15]
	855.67	Assessed	This work (**)
InSe	117.0 ± 12.5	Combustion Calorimetry	[42]
	109.1 ± 7.9	EMF	[29]
	118.0 ± 12.6	Evaluated	[39]
	98	Evaluated	[40]
	112.1± 0.4	EMF	[15]
	124.89	Assessed	This work (**)
In_2Se	147.1 ± 11.7	EMF	[29]
In_4Se_3	332.24	EMF	[29]*
	300.7	Evaluated	[40]
	382.51	Assessed	This work (**)

Note: * recalculated in this work (**), ** should be In_4Se_3

Table 3.10 Entropy values at 298.15 K for In-Se compounds.

Species	$S^{o}_{298.15\,K}$ (J/K mol)	Experimental method	Reference
In_5Se_7	469.9	Estimated	This work (**)
	479.8	Assessed	This work (**)
In_9Se_{11}	796.8	Estimated	This work (**)
	773.6	Assessed	This work (**)
In_5Se_6*	417.6 ± 7.5	EMF	[29]
In_6Se_7	514.14	EMF	[29]*
	479.7	EMF	[15]
	529.6	Assessed	This work (**)
InSe	80.9	Adiabatic Calorimetry	[43]
	77.8 ± 2.9	EMF	[29]
	84.2 ± 1.7	Assessed	[44]
	81.6	Assessed	[39]
	79.4	EMF	[15]
	85.52	Assessed	This work (**)
In_2Se**	138.4 ± 3.3	EMF	[29]
In_4Se_3	336.83	EMF*	[29]
	292.9	Estimated	[40]
	310.1	Assessed	This work (**)

Note: *Recalculated in this work (**), ** should be In_4Se_3

Table 3.11 Heat capacity data for In-Se compounds.

Phases	C_p (J / K mol)	Temperature Range (K)	Reference
In_5Se_7	$356.12 + 2.387 \times 10^{-2}\,T - 5.04 \times 10^{6}\,T^{-2}$	298-943	This work (**)*
In_9Se_{11}	$593.72 + 43.548 \times 10^{-3}\,T - 8.4 \times 10^{6}\,T^{-2}$	298-933	This work (**)*
In_6Se_7	$348.5085 - 6.7012 \times 10^{-2}\,T - 1.1198 \times 10^{6}\,T^{-2} + 9.8711 \times 10^{-5}\,T^{2}$	129-898	[24]
InSe	$52.32 - 6.28 \times 10^{-3}\,T - 1.79 \times 10^{5}\,T^{-2} + 8.40 \times 10^{-6}\,T^{2}$	129-920	[24]
In_4Se_3	$196.627 + 2.437 \times 10^{-2}\,T - 2.9288 \times 10^{6}\,T^{-2}$	298-823	[40]

Note: * Estimated by Unäl's rule [37].

3.3.7 Gas phase

The thermodynamic data for the gaseous molecules In(g), In_2Se_2(g), In_2Se(g), and InSe(g) have been studied [45, 46, 47] and assessed by Chatillon [40], including $\Delta H^{o}_{f,298.15K}$, $S^{o}_{298.15K}$, and heat capacity. The G-H_{SER} expressions are given in Tables 3.12 and 3.13.

Table 3.12 G-H_{SER} of gaseous compounds in In-Se system.

Species	Temperature Range (K)	Coefficients in (G-H_{SER}) expression G-H_{SER} = A + BT + CTlnT + DT^2 +ET^3+F/T (J/ K• mol)
In_2Se_2(g)	298.15 - 2000	A = 98948.31 B = 161.67466 C = - 83.139 D = - 0.00000179 E = 0.1585 x 10^{-7} F = 39303.5
In_2Se(g)	298.15 - 2000	A = 138075.93 B = 62.81609 C = - 58.1502 D = - 0.00029559 E = 0.3001 x 10^{-8} F = 575500
InSe(g)	298.15 - 2000	A = 222982.96 B = -4.1149 C = - 37.3103 D = -0.00008454 E = 0.6035 x 10^{-8} F = 57510

Table 3.13 G-H_{SER} of gaseous indium.

Species	Temperature Range (K)	Coefficients in (G-H_{SER}) expression G-H_{SER} = A + BT + CTlnT + DT^2 +ET^3+F/T (J/ K• mol)
In(g)	298.15 – 600	A = 236267.082 B = - 68.7705731 C = - 15.35206 D = - 0.00527185 E = - 3.98269833 x 10^{-7} F = -94519.9
	600 – 1100	A = 237868.024 B = - 110.524313 C = - 8.405227 D = - 0.0156847 E = 2.21196333 x 10^{-6} F = -110674.05
	1100 – 2900	A = 214982.499 B = 118.641773 C = - 41.36283 D = 0.00521457 E = - 2.526305 x 10^{-7} F = 2837067

3.4 Gibbs Energy Data

3.4.1 EMF measurements

Mustafaev *et al.* [29] measured the indium activity in the temperature range 510 to 710 K by electromotive force in the two phase domains, In_2Se_3-Se, (In_5Se_6)-In_2Se_3, InSe-(In_5Se_6), (In_2Se)-InSe. In_5Se_6 should be corrected to In_6Se_7 and In_2Se should be corrected to In_4Se_3. More recently Mallika *et al.* [15] measured the indium activity in solid and liquid (indium + selenium) solutions to 50 mass per cent selenium using solid-state galvanic cell.

3.4.2 Vapor pressure measurements

The following gas species were reported to exist in In-Se system, Se_n(n=1 to 8) (g), In(g), In_2Se_2(g), In_2Se(g), and InSe(g). Both total vapor pressure [30, 33, 47-50] and partial pressure [28, 45] measurements in the In-Se system are presented in Table 3.14.

Colin and Drowart [45] determined the partial pressure in equilibrium with liquid InSe by Knudsen cell mass-spectrometry. In their investigation, the condensed phase composition was not constant due to fact that the ion intensity ratio $I(Se_2^+)/I(In_2Se^+)$ varied appreciably with temperature. Grinberg *et al.* [49] studied the saturated total vapor pressure above liquid InSe by Bourdon quartz gauge and the vapor constituents by electron and IR absorption spectroscopy.

Sublimation of In_2Se_3(s) has been studied by mass-spectrometriy [28], torsion or Knudsen effusion [30, 25, 31, 33, 50], and membrane manometry [17]. In_2Se_3(s) was reported to sublime congruently according to the reaction [28, 25, 31]:

In_2Se_3 (s) = In_2Se (g) + Se_2 (g)

Congruent behavior has not always been observed and the occurrence depended on the experimental conditions. This is likely related to the effusion process changing the condensed phase composition. This efffect was shown in Srinivasa and Edwards' investigations [33, 51]. The difference between congruent sublimation and congruent effusion was discussed in [52]. In their studies, the condensed phase was not the In_2Se_3(s) one phase domain, but a liquid-In_2Se_3 two-phase mixture. Their data agreed qualitatively with the P-T phase diagram from Grinberg *et al.* [17], although the pressure measured by [50, 33] is much lower. Grinberg *et al* [49] studied the vapor phase along the three-phase boundary " In_2Se_3(s)-liquid-vapor ", by measuring the total pressure and optical absorption spectra of the vapor. They constructed the P-T projection of the phase diagram along the In_2Se_3(s) liquidus. The spectroscopic analysis indicated three major components in the saturated vapor, In_2Se (g), Se_2 (g), and In (g). A small homogeneity range (~ 0.1 at.%) was found in In_2Se_3 (s) phase by analyzing the vapor composition along the three phase boundary.

Table 3.14 Equilibrium vapor pressure measurement in the In-Se system.

Condensed Phases	Experimental method	References
InSe (liquid)	Partial pressure (Kundsen cell mass spectrometry)	[45]
InSe (liquid)	Total pressure (Bourdon gauge) and IR spectroscopy	[49]
In_2Se (solid)	Total pressure (Bourdon gauge) and IR spectroscopy	[49]
In_2Se_3 (solid)	Partial pressure (Knudsen cell mass spectrometry)	[28]
In_2Se_3 (solid)	Total pressure (Knudsen cell)	[30]
In_2Se_3 (solid) +liquid In-Se	Total pressure and IR spectroscopy	[17]
In_2Se_3 (solid)	Total pressure (Knudsen and torsion)	[31]
In_2Se_3(solid) +liquid In-Se	Total pressure (Knudsen and torsion)	[50, 53]
In_2Se_3 (solid)	Total pressure (Knudsen cell)	[25]

3.5 Thermodynamic Models

3.5.1 Pure elements and stoichiometric compound phases

The Gibbs energy of Cu is taken from Dinsdale [1], and that of Se is from Chang et al. [54]. The three-term equation given below is used to represent the temperature dependence of the

Gibbs energy of stoichiometric compound phase,

$$^{\circ}G=a+bT+cTlnT \quad (3.1)$$

Where °G is the standard Gibbs energy, T is the absolute temperature, and a, b and c are constants whose values need to be determined from experimental data.

3.5.2 Liquid Phase

The association model [2] was used to describe the Gibbs energy of the liquid phase. In_2Se_3 is the most stable compound in this system, which is stable to 1163 K and congruently melts at that temperature. The conductivity measurements of liquid $In_{1-x}Se_x$ alloys show a deep minimum around the composition of 0.6 Se mole fraction. It is reasonable then to choose In_2Se_3 as an associate species for the modeling of the liquid phase

$(In, In_2Se_3, Se)_1$

The Gibbs energy of this phase (per 1 mole of atoms) can also be expressed by equation (2), where fcc should be replaced by l (l=liquid). The term $^{ref}G^l$ is equal to

$$^{ref}G^l = y_{In}\,{}^{o}G^l_{In} + y_{In_2Se_3}\,{}^{o}G^l_{In_2Se_3} + y_{Se}\,{}^{o}G^l_{Se} \quad (3.2)$$

where y_i refers to the site fractions of the species i, with $y_{In} + y_{In_2Se_3} + y_{Se} = 1$. The terms $^{\circ}G^l_i$ represent the Gibbs energies of the liquid phases of the species i.

The ideal mixing Gibbs energy $^{id}G^l$ is equal to

$$^{id}G^l = RT(y_{In}\ln y_{In} + y_{In_2Se_3}\ln y_{In_2Se_3} + y_{Se}\ln y_{Se}) \quad (3.3)$$

The excess Gibbs energy $^{E}G^l$ is

$$\begin{aligned} {}^{E}G^l = {} & y_{In}y_{In_2Se_3}({}^{0}L^l_{In,In_2Se_3} + {}^{1}L^1_{In,In_2Se_3}(y_{In} - y_{In_2Se_3})) \\ & + y_{In_2Se}y_{Se}({}^{0}L_{In_2Se_3,Se} + {}^{1}L^l_{In_2Se_3,Se}(y_{In_2Se_3} - y_{Se})) \end{aligned} \quad (3.4)$$

where the four terms L represent the interactions between the species. They can be expressed as the function of temperature.

3.6 Optimization Procedure

A selected set of thermodynamic and phase diagram data were used for the optimization of thermodynamic model parameters of all phases in this system. The optimization was performed by using the PARROT module of the Thermo-Calc program package [55] and procedures in four steps.

First, initial estimates of the Gibbs energy coefficients of the stoichiometric compounds In_4Se_3, InSe, In_6Se_7, In_9Se_{11}, In_5Se_7, β-In_2Se_3, γ-In_2Se_3, δ-In_2Se_3, and α-In_2Se_3, were deduced from the reported enthalpy of formation, standard entropy, heat capacity. No enthalpy of melting for In_2Se_3 was reported in the literature. The Gibbs energy coefficients for liquid In_2Se_3 were deduced from the melting enthalpy of InSe reported by [24]. Second, a rough optimization of the

liquid coefficients was performed based on the activities of selenium, miscibility gap, and three-phase equilibria (those involved the liquid phase). Third, fixing the coefficients of the liquid the coefficients of the stoichiometric In_4Se_3, InSe, In_6Se_7, In_9Se_{11}, In_5Se_7, β-In_2Se_3, γ-In_2Se_3, δ-In_2Se_3, and α-In_2Se_3 phases were optimized based on the enthalpies of formation, enthalpies of transition, standard entropies, and phase diagram data. Finally, all parameters of the phases were optimized to fit the experimental data.

Table 3.15 Optimized parameters according to the analytical description of the phases.[+]

Phase or Function	Parameters
Liquid	${}^{o}G^{l}_{In_2Se_3} = GIn_2Se_3\_l$ ${}^{0}L^{l}_{In,In_2Se_3} = -90578.47$ ${}^{1}L^{l}_{In,In_2Se_3} = 45241 - 23.71235T$ ${}^{0}L^{l}_{In_2Se_3,Se} = 143000 - 143.885943T$ ${}^{1}L^{l}_{In_2Se_3,Se} = -20278$
In_4Se_3	${}^{o}G^{In4Se3} = -452040.0651 + 1030.595 - 196.627TlnT - 0.012185T^2 + 1464400T^{-1}$
InSe	${}^{o}G^{InSe} = -140889.4243 + 264.4091T - 52.32TlnT + 0.00314T^2 - 1.4x10^{-6}T^3 + 89500T^{-1}$
In_6Se_7	${}^{o}G^{In6Se7} = -961224.9318 + 1795.21T - 348.5085TlnT + 0.033551T^2 - 1.645x10^{-5}T^3 + 559900T^{-1}$
In_9Se_{11}	${}^{o}G^{In9Se11} = -1544729.723 + 3263.10972T - 593.72TlnT - 0.021774T^2 + 4.2x10^{6}T^{-1}$
In_5Se_7	${}^{o}G^{In5Se7} = -917893.3895 + 1940.7949T - 356.12TlnT - 0.011935T^2 + 2.52x10^{6}T^{-1}$
β-In_2Se_3	${}^{o}G^{\beta In2Se3} = -356008.26 + 578.83374T - 116.78158\ TlnT - 0.0133705T^2$
γ-In_2Se_3	${}^{o}G^{\gamma In2Se3} = -359437.4289 + 559.45784 - 113.41683\ TlnT - 0.0179945T^2$
δ-In_2Se_3	${}^{o}G^{\delta In2Se3} = -351165 + 551.29784T - 113.41683TlnT - 0.0179945T^2$ (298.15≤T≤1018) $= -370776.53 + 812.53003 - 151TlnT$ (1018≤T≤2000)
α-In_2Se_3	${}^{o}G^{\alpha In2Se3} = -358491.69 + 532.92563T - 107.64907TlnT - 0.027164T^2$ (298.15≤T≤474) $= -359165.45 + 565.53707T - 113.41683TlnT - 0.0179945T^2$ (474≤T≤1080) $= -378776.98 + 826.76926T - 151TlnT -$ (1080≤T≤2000)
Function	$GIn_2Se_3\_l = 14958.1541 - 5.01847226T + GIn2Se3\_D$ $GIn2Se3\_D = -304076.2 + 509.29784T - 113.41683TlnT - 0.0179945T^2$ (298.15≤T≤1018) $= -323687.73 + 770.53003T - 151TlnT$ (1018≤T≤2000)

+ Temperature (T) is in Kelvin. The Gibbs energies are in J/mole.

3.7 Results and Discussion

The optimized parameters of the stable phases in the In-Se system are listed in Table 3.15.

The phase diagram and thermodynamic properties of this system were calculated with the Poly-3 module of the Thermo-Calc program package. The calculated phase diagram is shown in Figure 3.2. Comparisons between the experimental and calculated phase diagram are shown in Figures 3.3 to 3.6. Table 3.1 presents the experimental and calculated temperatures and compositions of the invariant reactions in this system.

The calculated values are well within the uncertainty of experimental data. The calculated In-rich liquid miscibility gap agrees well with the experimental data of Glazov and Kim [56] and Gödecke [12] as shown in Figure 3.4. The calculated peritetic reactions and liquidus lines for In_4Se_3, InSe, In_6Se_7, In_9Se_{11}, In_5Se_7 and β-In_2Se_3 are shown in Figure 3.5 in detail along with the experimental data. In general, the calculated diagram is in agreement with the experimental data. The calculated phase diagram at the Se-rich side is given in Figure 3.4 in comparison with the experimental data. Figure 3.5 shows the comparison between the calculated and measured activity of indium. The calculated activity deviated more positively than the experimental data.

Figure 3.7 shows the comparison between the calculated and measured total vapor pressures in this system. To calculate the total pressure, an ideal gas phase containing 12 species is added to the optimized coefficient set. The parameters of the gas species Se, Se_2, Se_3, Se_4, Se_5, Se_6, Se_7, and Se_8 [59] were obtained from a different reference from the parameters of the gas species In, InSe, In_2Se, and In_2Se_2 [57]. The calculated total pressures agree well with the measured data. The calculated total pressure data are in good agreement with the measurements of Grinberg [17]. The calculated T-p data along the β-In_2Se_3 liquidus also agree well with the measurements [33, 58].

The experimental and calculated standard enthalpies of formation of the intermediate compounds at 298.15 K in the In-Se system are presented in Tables 3.6 and 3.9. The corresponding standard entropies are presented in Tables 3.7 and 3.10. The reference states of these data are the enthalpies of the pure stable elements at 298.15 K. The assessed enthalpy of formation for α-In_2Se_3 in the present work is close to the synthesis calorimetry value [27]. Their value was obtained by direct synthesis of α-In_2Se_3 in a bomb calorimeter. The synthesized compound was confirmed by X-ray diffraction. This technique does not rely on other thermodynamic functions, which introduces additional uncertainty. The assessed standard enthalpies for β-In_2Se_3 and γ-In_2Se_3 are close to the values derived from [33] and [27], respectively. The assessed enthalpy of formation for InSe is well within the experimental uncertainty of the value measured by Hahn and Burow [42] from combustion calorimetry. It was found that the enthalpy of formation value for In_6Se_7 is much more negative than the value derived from EMF measurements [29] and closer to the value listed in reference [15]. It was also found that the enthalpy of formation value for In_4Se_3 is much more negative than the evaluated value [40] and the recalculated value [29]. A more positive value of the enthalpy of formation resulted in the disappearance of In_4Se_3 phase in the calculated T-x phase diagram.

The assessed entropy values are well within the available experimental values. The calculated heat capacity data for α-In_2Se_3, γ-In_2Se_3, β-In_2Se_3, In_6Se_7 and InSe along with the measured data by Mills [24] are given in Figure 3.8, 3.9, and 3.10, respectively. The calculation values agree well with the measured ones.

3.8 Conclusions

A thermodynamic description of the In-Se binary system was obtained by optimization of the available phase equilibrium and thermodynamic data. The associate solution model was used to represent the Gibbs energy of the liquid phase, while the intermediate phases were modeled as line compounds. The phase diagram and thermodynamic properties of this system have been calculated by using the optimized model parameters. There is reasonable agreement between the model-calculated values and the phase equilibrium and thermodynamic data available in the literature for all phases.

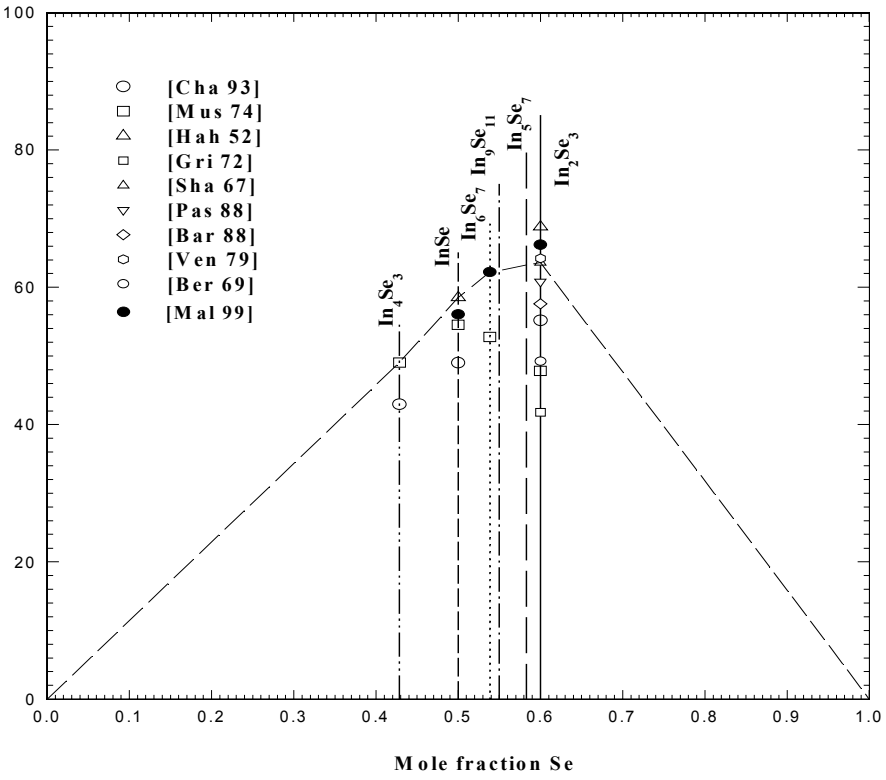

Figure 3.1 Enthalpies of formation of the compounds in the In-Se system as a function of composition.

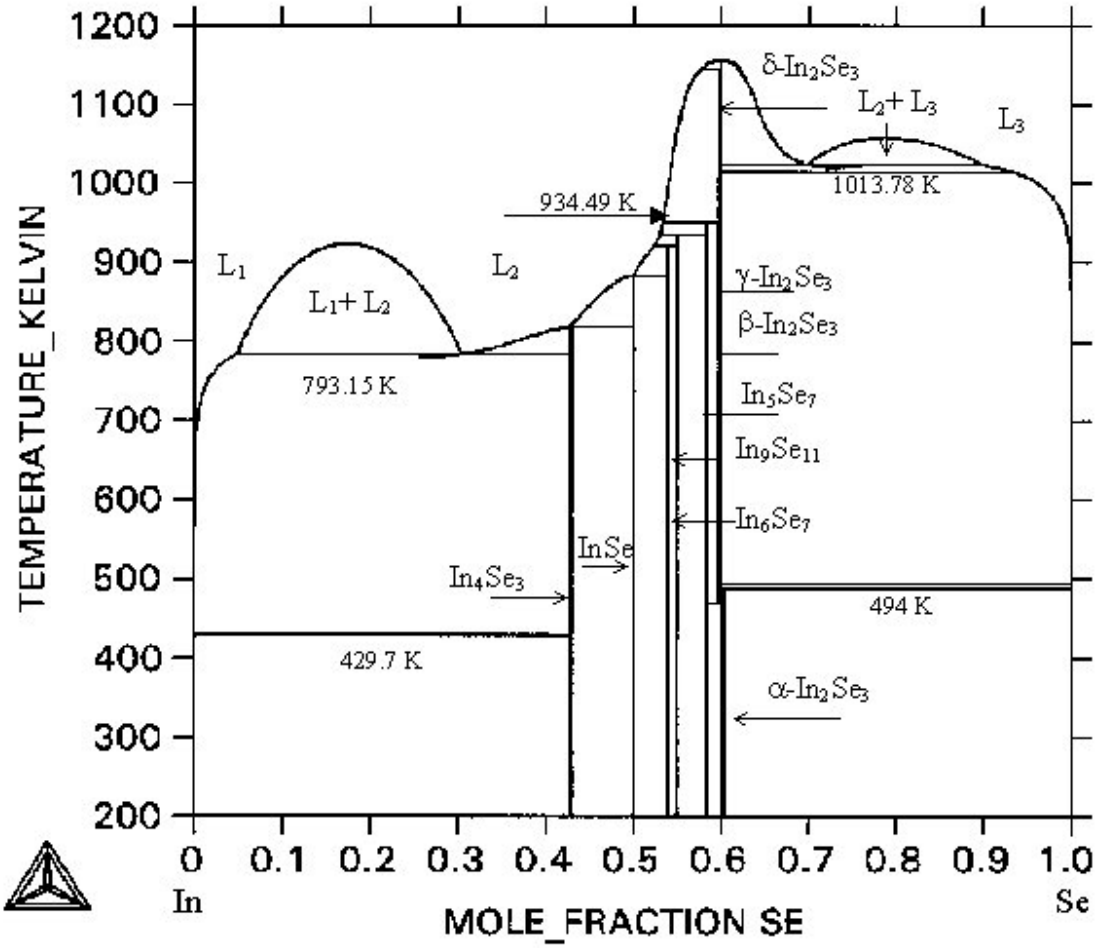

Figure 3.2 Calculated In-Se phase diagram based on the optimized parameters.

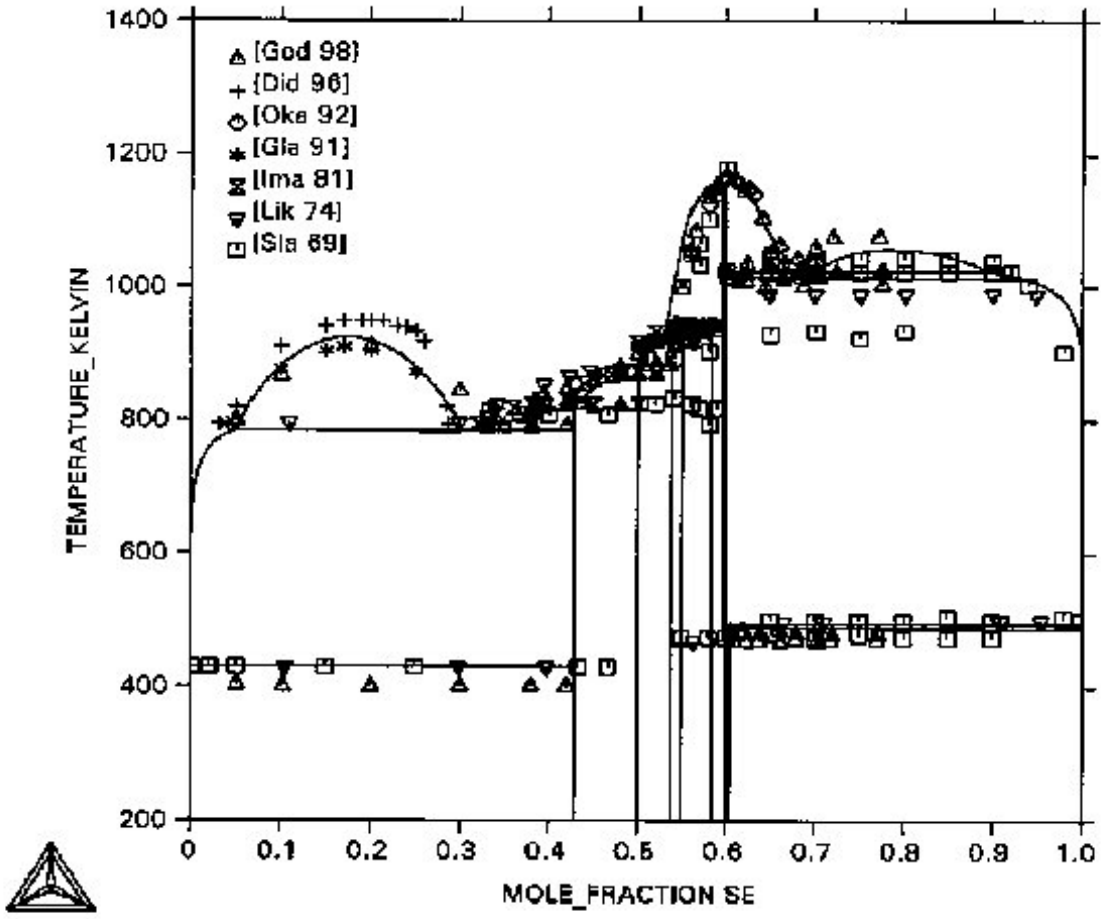

Figure 3.3 Calculated In-Se phase diagram along with the experimental data.

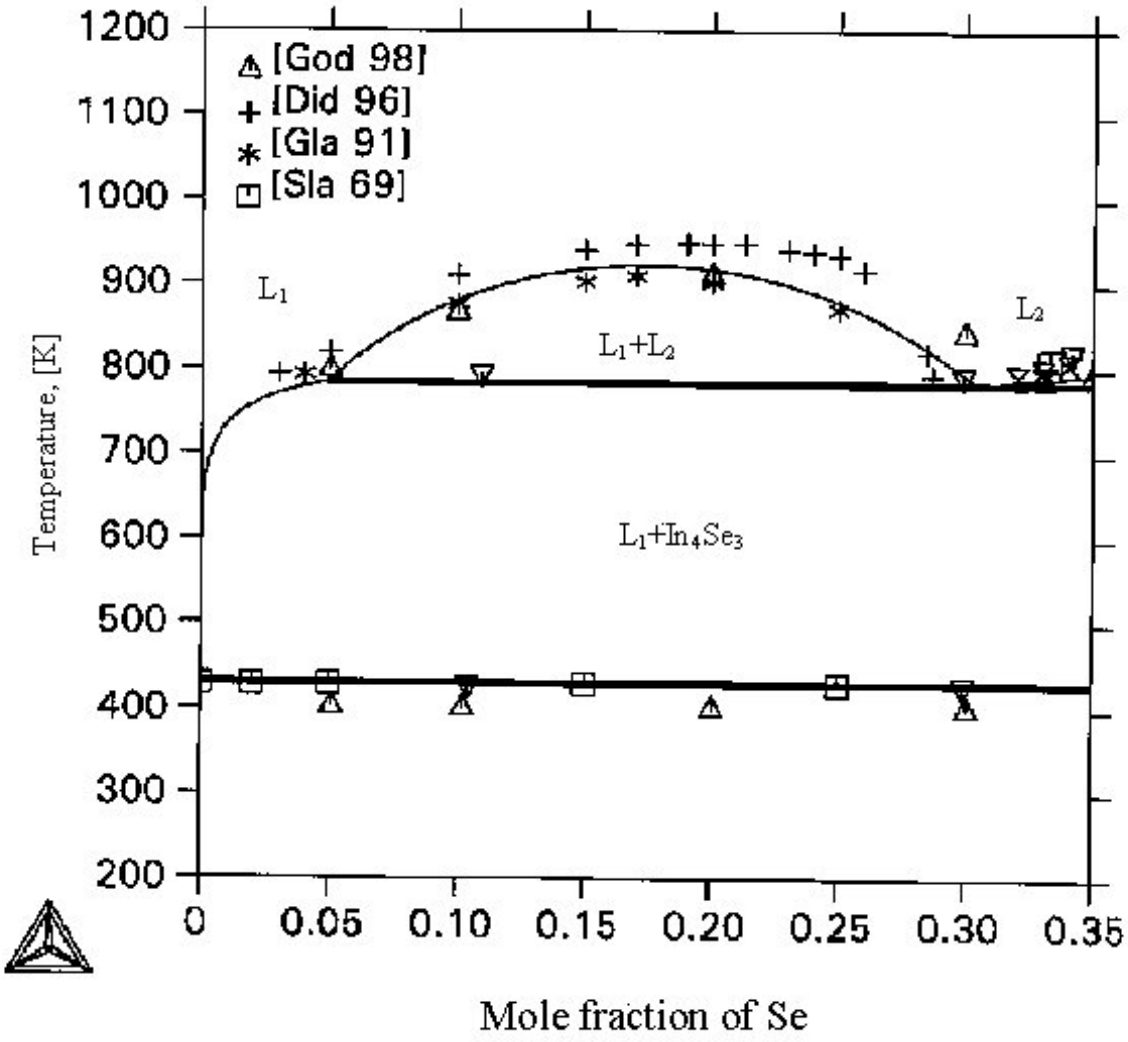

Figure 3.4 Comparison between the calculated In-Se phase diagram and experimental data in the vicinity of the In-rich miscibility gap.

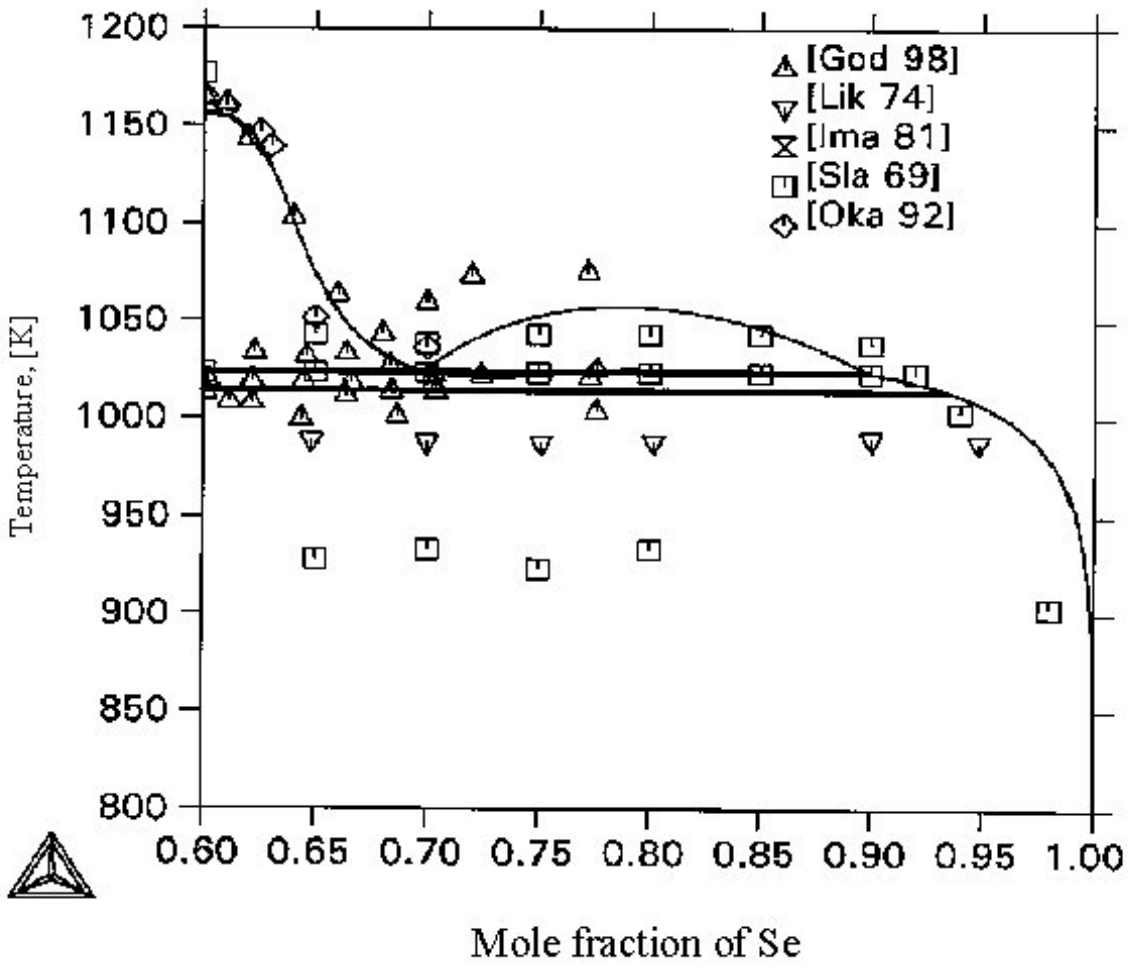

Figure 3.5 Comparison between the calculated In-Se phase diagram and various experimental data in the vicinity of Se-rich miscibility gap.

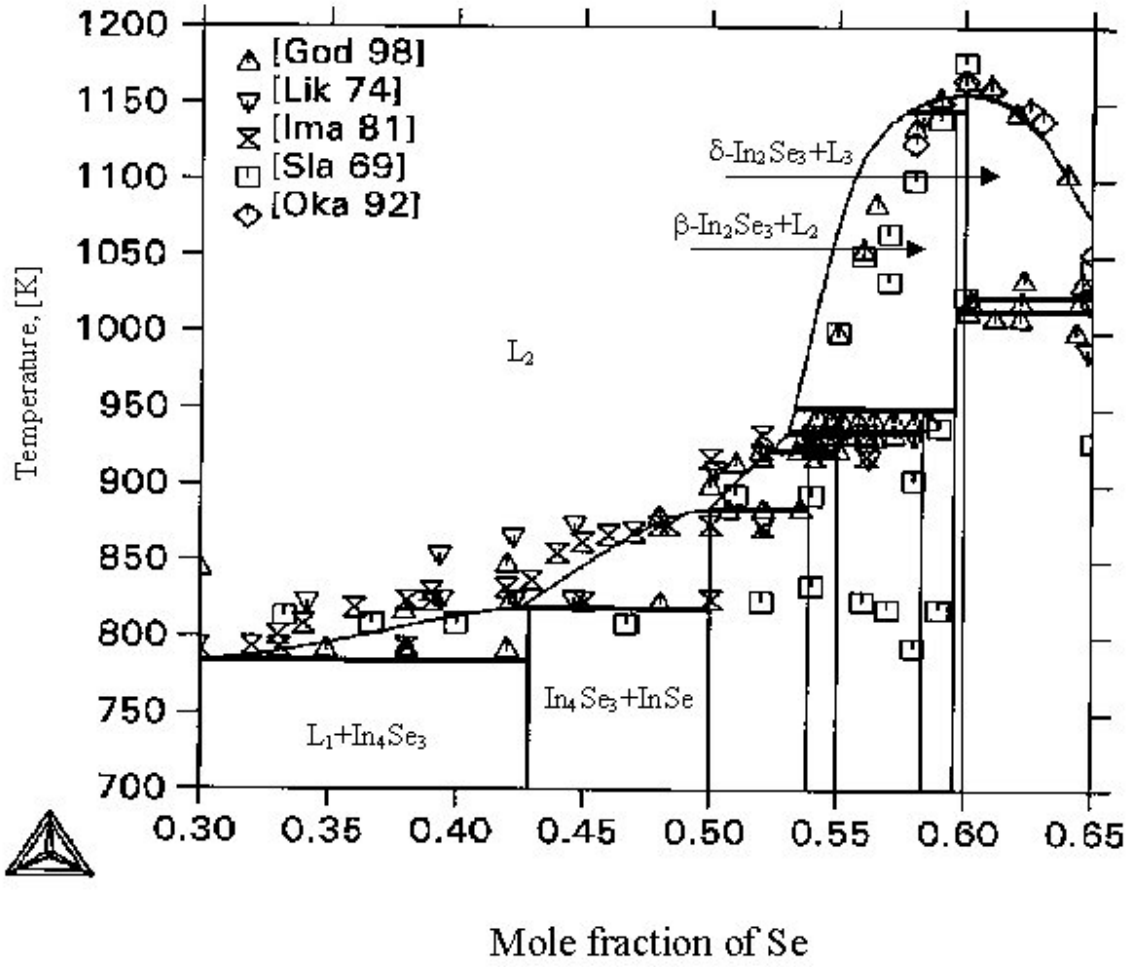

Figure 3.6 Comparison between the calculated In-Se phase diagram and various experimental data from 0.3 to 0.65 mole fraction of Se.

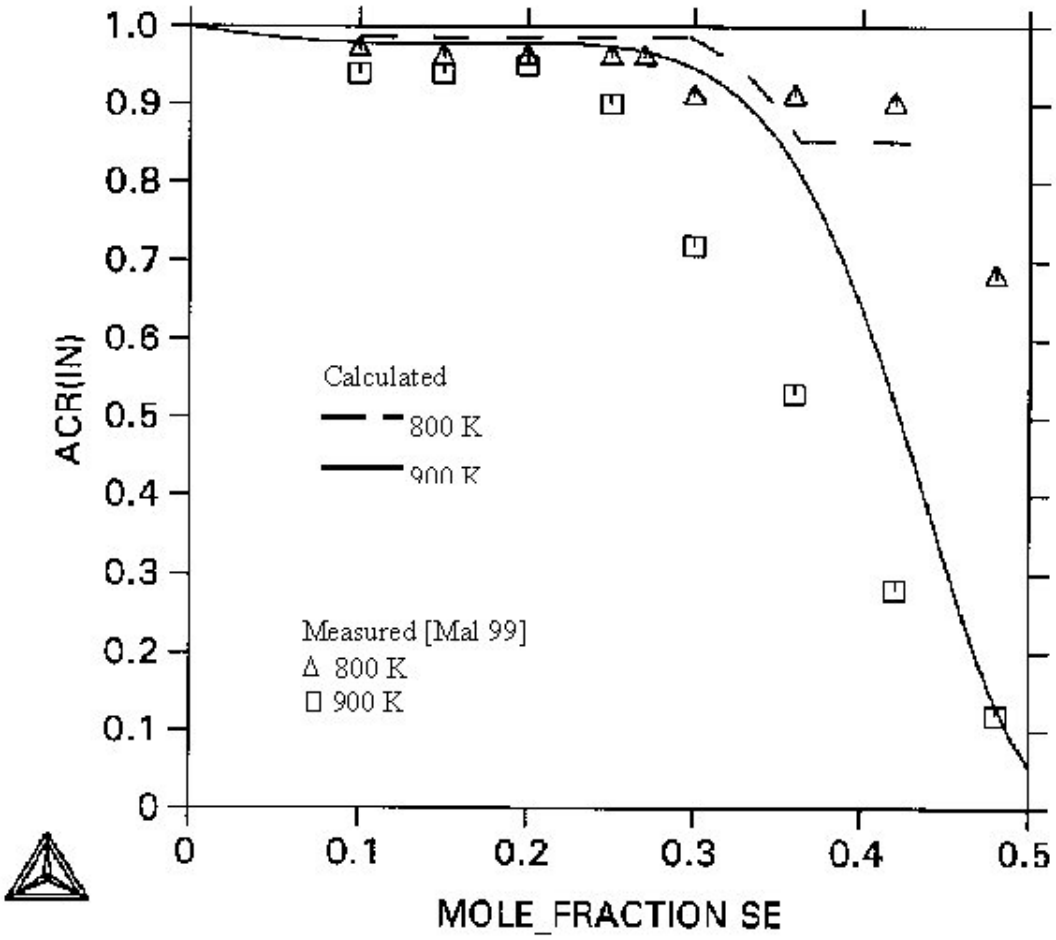

Figure 3.7 Calculated activity of In with the experimental data [15] with the pure liquid In phase as the reference state.

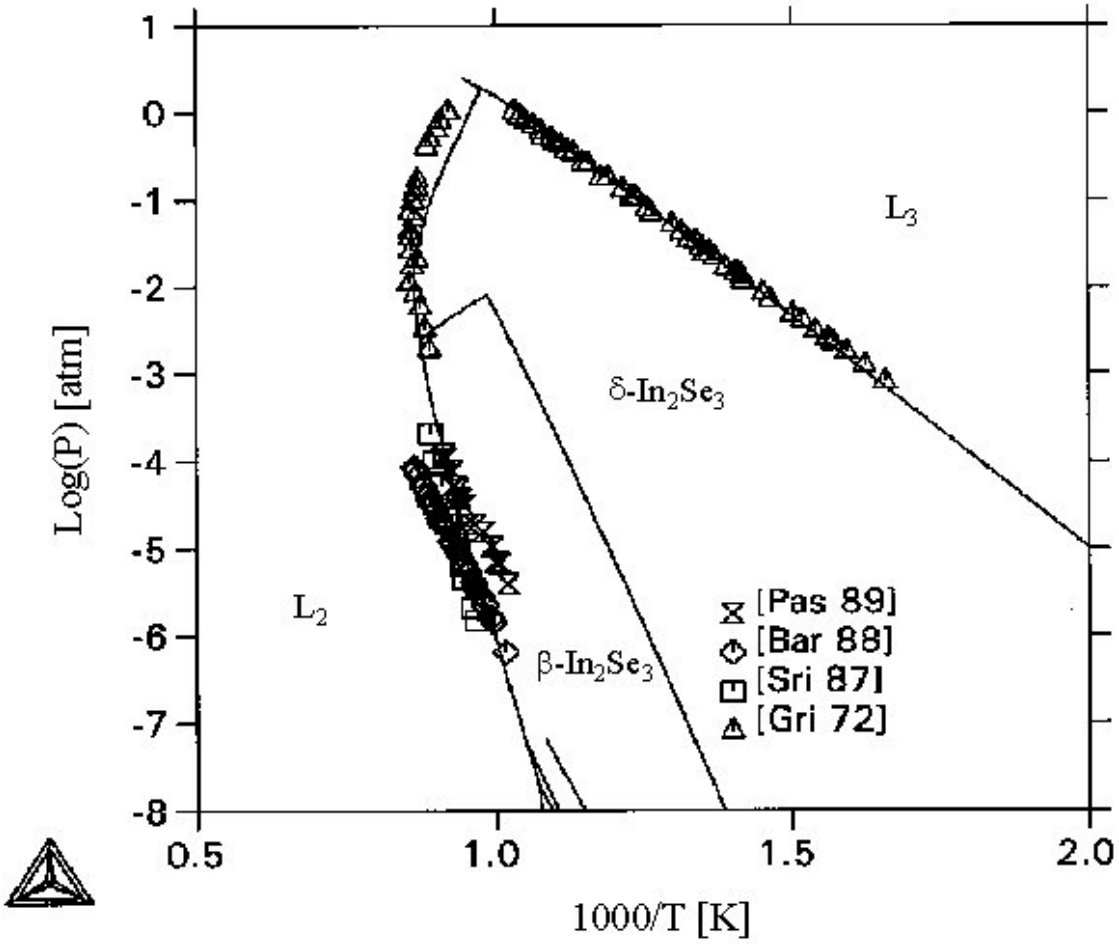

Figure 3.8 Comparison of the total vapor pressure in the In-Se system with the experimental data.

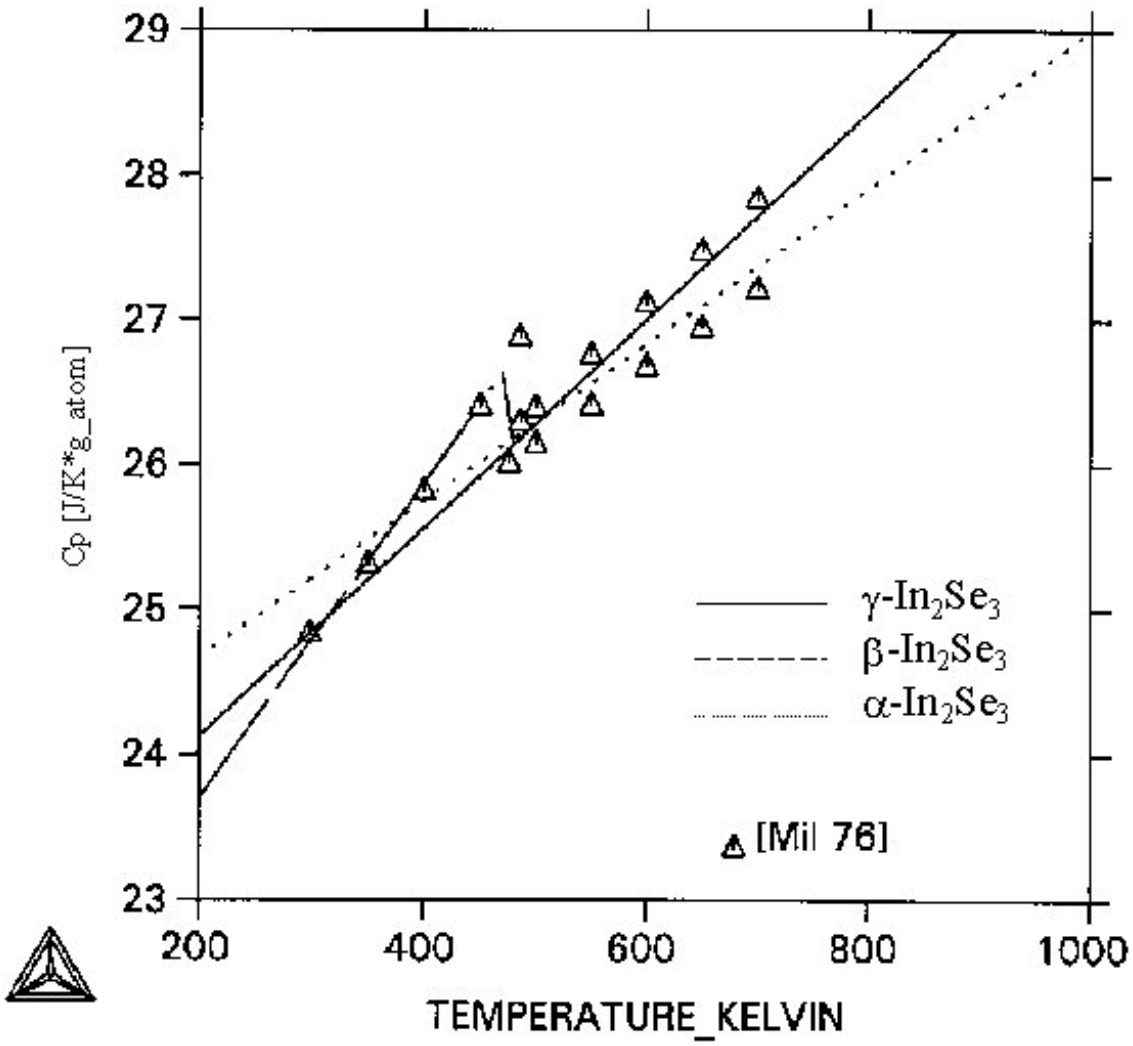

Figure 3.9 Assessed and measured heat capacity data for α-In_2Se_3, β-In_2Se_3, and γ-In_2Se_3.

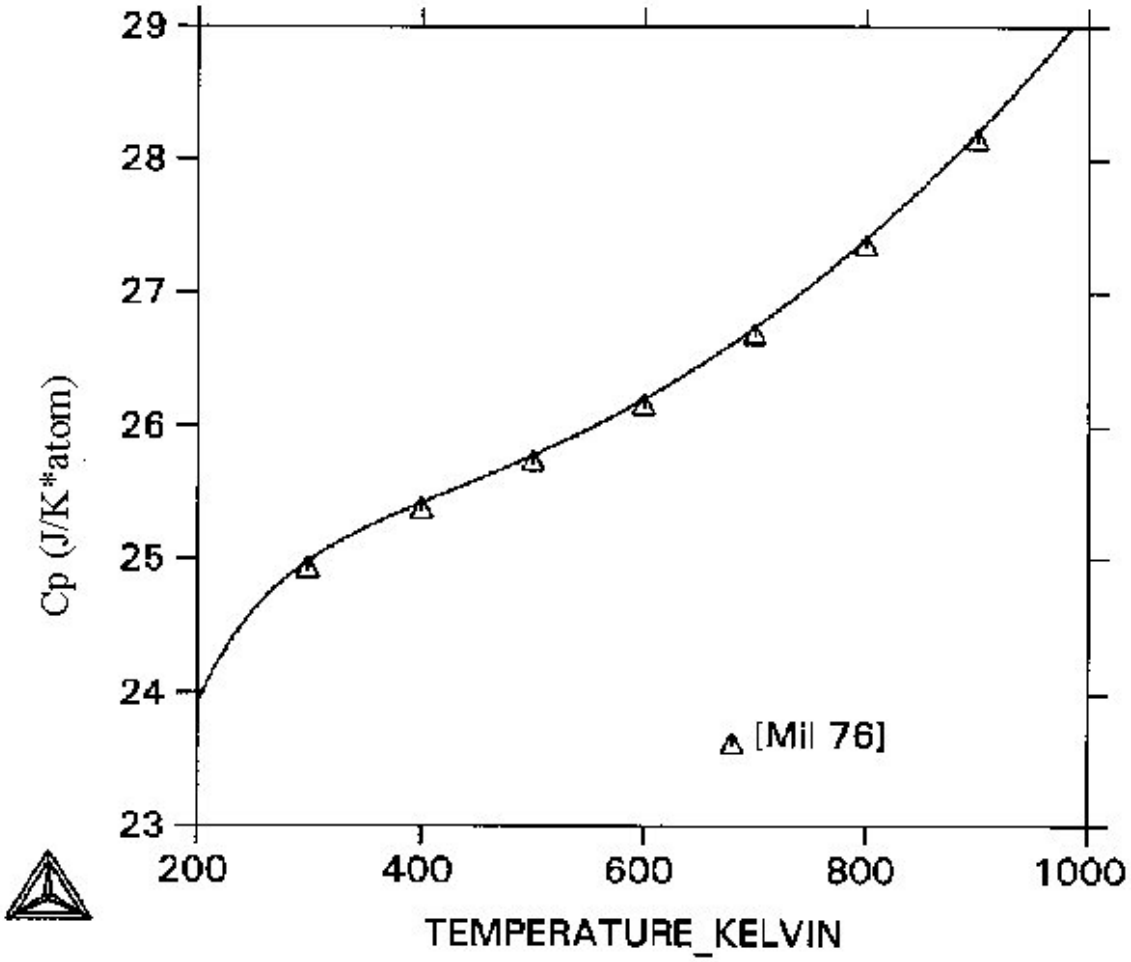

Figure 3.10 Assessed and measured heat capacity data for In_6Se_7.

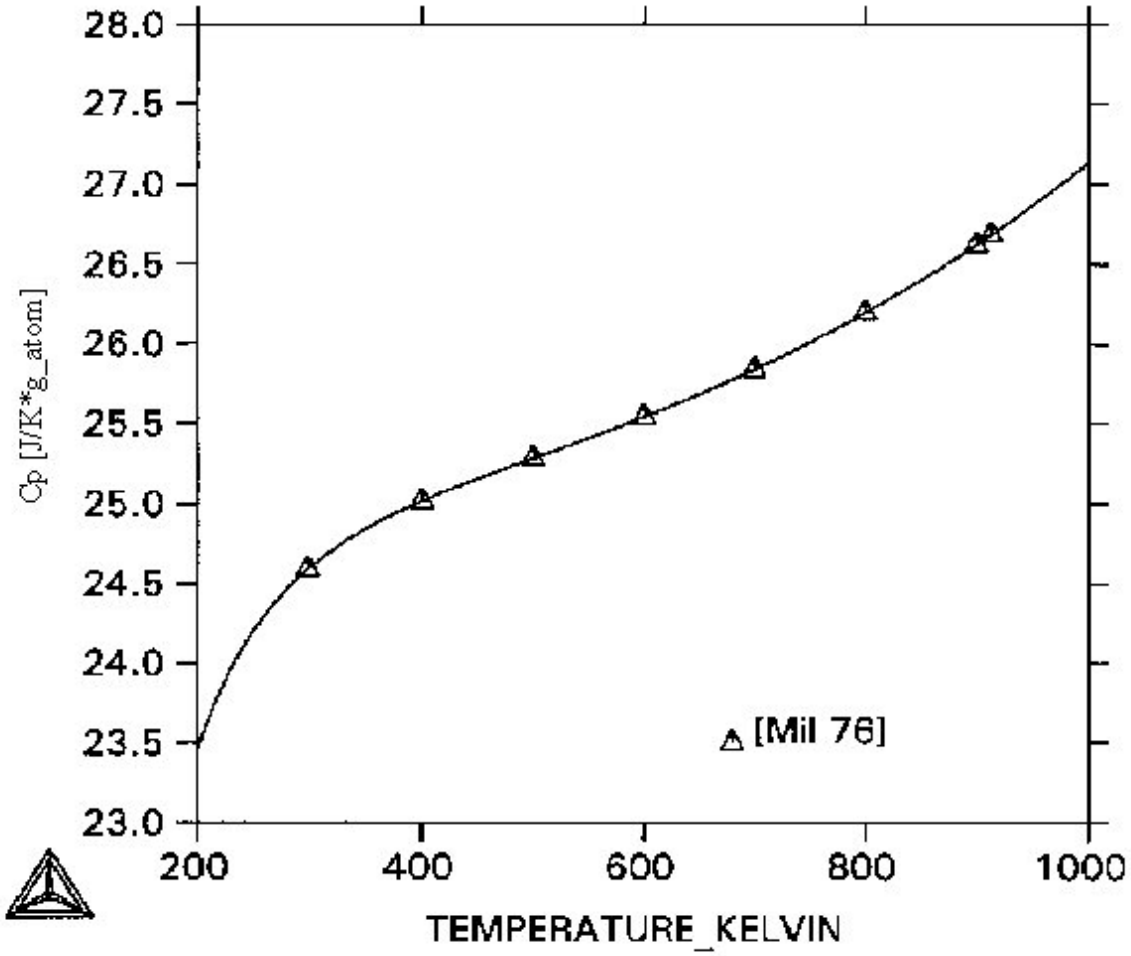

Figure 3.11 Assessed and measured heat capacity data for InSe.

3.9 References

[1] Dinsdale A.T., CALPHAD, 15(4), 317, 1991.

[2] Sommer, F.: Z.Metallkd., 73: 72, 1982.

[3] Slavnova G.K., Luzhnaya N.P., Medvedeva Z.S., Russ. J. Inorg. Chem., 8(5): 78, 1963.

[4] Slavnova G.K., Luzhnaya N.P., Medvedeva Z.S., Russ. J. Inorg. Chem., 8(5): 622, 1963.

[5] Slavnova G.K., Eliseev A. A., Russ. J. Inorg. Chem., 8(7): 861, 1963.

[6] Guliev T.N., Medvedeva Z.S., Russ. J. Inorg. Chem., 10(7): 1520, 1965.

[7] Likforman A., Guittard M., Compt. Rend. C, 279(4): 33, 1974.

[8] Imai K.,Suzuki K., Haga T., Hasegawa Y., Abe Y., J. Cryst. Growth, 54(3): 501, 1981.

[9] Glazov V. M., Kim S. G., Nurov K. B., Inorg. Mater. , 25(5): 727, 1989.

[10] Didoukh V., Plevachuk Yu., Sokolovskii B., J. Phase Equilibria, 17: 414, 1996.

[11] Daouchi B., Record M.-C., Tedenac J. C., Vassilev G., Z. Metallkd., 89(9): 612, 1998.

[12] Gödecke T., Haalboom T., Sommer F., J. Phase Equilibria, 19(6): 576, 1998.

[13] Okada T., Ohon S., J. Phys. Soc. Jpn., 62(5): 1669, 1993.

[14] Okamoto H., Binary Alloys Phase Diagrams, ASM.

[15] Marimoto, N.; Uchimizu, M.; in: X-ray powder data file 19-401, ed. L.G.Berry, Special Technical Publications 480G ASTM, Philadelphia, 1969.

[16] Popovic S., Celustka B., Bidjin D., Phys. Status Solidi A, 6: 301, 1971.

[17] Grinberg Ya. Kh., Boryakova V.A., Shevelkov V. F., Medvedeva Z. S., Inorg. Mater., 8: 2099, 1972.

[18] Medicis, R.de; Thesis, Louvain, 63(1967) cited by [Mil 87].

[19] Van Landuyt J., Van Tendeloo G., and Amelinckx S., Phys. Status Solodi A, 26: K103, 1974.

[20] Popovic S., Tonjec A., Plenkovic B. G., Celustka B., Trojko R., J. Appl. Crystallogr., 12: 416, 1979.

[21] Likforman A., Fourcroy P., Guittard M., Flahaut J., Poinier R., Srydlo N., J. Solid State Chem., 33: 91, 1980.

[22] Manolikas C., J. Solid State Chem., 33: 91, 1980.

[23] Okada T., Ohon S., J. Phys. Soc. Jpn., 62(5): 1669, 1993.

[24] Mills K. C., High Temp. High Pressure, 8: 225, 1976.

[25] Pashinkin A. S., Zharov Vl V., Inorg. Mater., 24(9): 1458, 1988.

[26] Hansen M., & Anderko K., Constitution of Binary Alloys, McGraw-Hill Book Co., New York, 1958.

[27] Sharifov K. A., Azizov T. Kh., Russ. J. Inorg. Chem., 41(5): 645, 1967.

[28] Berger L. I., Strel'chenko S.S., Bondar S. A., Molodyk A. D., Balanevskaya A. E., Lebedev V.V., Izv. Akad. Nauk SSSR, Neorg. Mater., 5: 872, 1969.

[29] Mustafaev F. M., Azizov T. KH., Aliev I. Ya., Abbasov A. S., Azerb. Khim. Zh., 2: 93, 1974.

[30] Vendrikh. N. F., Pashinkin A. S., Lebedev V.V., Izv. Akad. Nauk SSSR, Neorg. Mater., 15: 766, 1979.

[31] Bardi G., Piacente V., Scardala P., High Temp. Sci., 25: 175, 1988.

[32] Grinberg Y.K., Illel R., Boriakova V. A., Chevelkkov V. F., J. Neorg. Mater., 11: 1945, 1975.

[33] Srinivasa R. S., Edwards J. G., J. Electrochem. Soc., 134: 1811, 1987.

[34] Koshenko V. I., Grinberg Ya. Kh., Karpuchok A. M., Koshchenko R.V., Izv. Akad. Nauk SSSR, Neorg. Mater., 20(10): 1765, 1984.

[35] Kubaschewski O., Alcock C. B., “ Metallurgical Thermochemistry ”, 5th ed. (pergamon, Oxford, 1979).

[36] Latimer W. M., J. Am. Chem. Soc., 73: 1480, 1975.

[37] Kubaschewski O., Unäl H., High Temp. High Pressure, 9: 361, 1977.

[38] Hahn H., Burow F., Agnew. Chem., 68: 382, 1952.

[39] Van Landuyt J., Van Tendeloo G., and Amelinckx S., Phys. Status Solodi A, 26: K103, 1974.

[40] Chatillon C., J. Crystal Growth, 129: 297, 1993.

[41] Demidenko A. F., Koshenko V. I., Grinberg Ya. Kh., Boryakova V. A., Gastev S. V., Izv. Akad. Nauk SSSR, Neorg. Mater., 11: 2141, 1975.

[42] Hahn H., Burow F., Agnew. Chem., 68: 382, 1952.

[43] Mamedov K. K., Kerimov I. G., Kostryukov V. N., Guseinov G. D., Russ. J. Phys. Chem., 41: 645, 1967.

[44] Rymkevich P.P., Maslov P. G., Zaitesev N.M., Pao Hoang Van, Ban Vu Xuan, Zh. Prikl. Khim., 48: 209, 1975.

[45] Colin R., Drowrat J., Trans. Faraday Soc., 64: 2611, 1968.

[46] Grinberg Ya. Kh., Boryakova V. A., Shevelkov V. F., Izv. Akad. Nauk SSSR, Neorg. Mater.,7(5): 769, 1971.

[47] Greenberg J. H., Borjakova V. A., Shevelkov V. F., J. Chem. Thermodynamics, 5: 233, 1973.

[48] Grinberg Ya. Kh., Boryakova V.A., Shevelkov V. F., Medvedeva Z. S., Inorg. Mater., 8: 2099, 1972.

[49] Grinberg Ya. Kh., Boryakova V. A., Shevelkov V. F., Izv. Akad. Nauk SSSR, Neorg. Mater.,7(5): 769, 1971.

[50] Srinivasa R. S., Ph. D. Dissertation, The University of Toledo, Toledo, OH, 1985.

[51] Srinivasa R. S., Edwards J. G., J. Electrochem. Soc., 134: 1811, 1987.

[52] Edwards J. G., High. Temp. Sci., 32: 37, 1991.

[53] Srinivasa R. S., Edwards J. G., J. Electrochem. Soc., 134: 1811, 1987.

[54] Chang, C.H.; Davydov, A.; Stanbery, B.J.; Anderson, T.J.: to be published, 1999.

[55] Sundman, B.; Jansson, B.; Andersson, J.-O, CALPHAD, 9: 153, 1985.

[56] Glazov, V. M.; Kim, S. G.: Inor. Mater., 26: 2141, 1991.

[57] Sundman, B.: SGTE Substance Database, SGTE, 1994.

[58] Pashinkin A. S., Zharov Vl V., Inorg. Mater., 24(9): 1458, 1988.

[59] C. H. Chang, Doctoral Dissertation, "Processing and Characterization of Copper, Indium Selenide for Photovoltaic Applications," Chemical Engineering Department, University of Florida, Gainesville, FL, 2000.

PART 4

$CuInSe_2$ Thin Film Formation by Rapid Thermal Processing

Abstract

We investigated the use of two novel precursor structures that used stacked In-Se and Cu-Se binary layers instead of conventional elemental layers, followed by rapid thermal processing (RTP) to produce CIS films. The first test structure was composed of 3 layers, namely an $In_4Se_3/CuInSe_2/CuSe$ stack, while the second structure considered consisted of 2 layers, namely an InSe/CuSe stack. The ramp rate, anneal temperature, and anneal time were varied and the resulting films analyzed for formation of CIS using XRD, AES, ICP, and Raman measurements. The results show that relatively larger grain $CuInSe_2$ could be formed.

Section Contents

4.1 Brief Overview

4.1.1 Participants

Faculty Adviser: Prof. Timothy J. Anderson

Research Assistant: Chih-Hung "Alex" Chang

4.1.2 Objective

Test the use of rapid thermal processing (RTP) and a novel stacked binary layer precursor structure for formation of $CuInSe_2$.

4.2 Previous Work on RTP-CIS

The requirement for a large-area, high-throughput, and low-cost absorber film formation process has motivated the use of physical deposition techniques using elemental sources that first deposit a precursor film of an appropriate overall composition, and subsequent annealing via RTP leads to the synthesis of large grained CIS. RTP is particularly attractive due to inherent advantages such as its low thermal budget and the potential for better control of the process kinetics. Several precursor structures have been utilized in the RTP-annealed synthesis of $CuInSe_2$ thin films, but only three types of precursor structures have been reported in the literature.

One type of precursor structure stacked the elemental components to form a sandwich-like structure. A variety of precursors could be fabricated by alternating the layer sequence and changing the number of layers. Compositions of the films were controlled by the relative thickness of the individual layers. It often incorporated excess Se due to the high volatility of Se gas species. A number of groups have reported successful $CuInSe_2$ thin film formation using this approach [1-3] and formation of $Cu(In_{1-x}Ga_x)Se_2$ [4, 5]. The important processing parameters in this approach included stacking arrangement of the layers, Cu/In ratio, RTP ramping rate, and annealing temperature.

The first device quality CIS produced by RTP was synthesized by Karg et al. [2]. It consisted of Mo, Cu, In, and Se sequentially deposited by DC-magnetron sputtering (Mo, Cu, In) and/or evaporation (Cu, In, Se). The Cu/In ratio varied from 0.85 to 0.95, while Se was typically 40% in excess of the stoichiometric amount. A furnace type (low ramp rate, 1°C/s) processing was also performed in their investigation. Two critical process steps were found from this type of process. The first one is the severe dewetting of the amorphous Se layer starting at about 100°C which caused a laterally inhomogeneous nucleation and grain growth of the CIS layer. This laterally inhomogeneous growth process resulted in voids between the CIS and Mo back contact, which produced poor adhesion and low cell performance. The second critical process period is when the sample in the temperature range of 100 to 250°C where the formation of Cu_2Se is favored as compared to $CuInSe_2$, a detrimental secondary phase. Their results indicated the Cu/In ratio is the most significant parameter. At a Cu/In precursor of 0.89 small grained material is obtained in contrast to the coarse grained film at Cu/In of 0.92 with a grain size in the range of 1~3 μm. TEM results revealed that copper-rich and indium-rich films were distinct in their defect structure. Copper-rich films had a significant number of dislocations and stacking faults. In contrast to copper-rich films, there were a significant number of twins in

In-rich films. These features revealed different reaction mechanisms during synthesis for these two Cu/In ratios.

Using the same process strategy, [4] fabricated Cu(In,Ga)Se_2 thin film cells by RTP. They also developed two ways to incorporate sodium into CIS to quantify its impact on grain morphology and cell performance. They varied the outdiffusion of sodium from the soda lime glass by employing a partially permeable Mo-backelectrode in the first process. Sodium selenide was added to the precursor in the second process. The optimization of the sodium amount in RTP-CIGS films on soda lime glass resulted in cells with average efficiency of 12% and a peak efficiency of 13.2%.

More recently Probst et al. [5] developed a new stacked elemental layer process to produce Cu(In,Ga)Se_2 and Cu(In, Ga)(Se, S)$_2$ cell. The key process steps are 1)deposit a barrier coating on the soda lime glass substrate and add a sodium compound to the elemental Cu/In/Ga/Se precursor stack 2)rapid thermal processing this structure to form CIGS thin films. The first step better controls the sodium distribution. A thin layer of SiO_x, Al_2O_3 or Si_xN_y was used as the barrier material. They suggested a liquid assisted growth mechanism for the stacked elemental layer process has two main prerequisites: 1) the processing conditions must favor the formation of the CuSe phase, 2) a dynamic heating process to exceed the melting temperature of CuSe before it is consumed in the reaction. Cell peak efficiencies of 13.3% for Cu(In,Ga)Se_2 and of 14.6% for Cu(In,Ga)$(SeS)_2$ devices were obtained with this technique.

The second precursor structure used co-evaporated elemental Cu, In and Se [6, 7]. This processing approach had bubbling and adhesion problems, especially with Mo-coated glass substrates. The bubbling was worse with higher Cu contents and faster ramp rates. The device made from this approach had an efficiency < 1%, after 2 hrs 200^{o}C air annealing an efficiency 3.5% was obtained.

The third approach used RTP to re-crystallized $CuInSe_2$. Albin et al. [8] rapid thermal annealed small-grained (≤1 μm) $CuInSe_2$ to produce large-grained $CuInSe_2$ (~100 μm). This approach suffered from severe oxygen incorporation and $CuInSe_2$ decomposition at high temperature, and other defects such as excessive voids and pinholes in the films.

It is obvious from this review that the precursor film structure and the subsequent reaction pathway during annealing can dramatically affect the eventual device performance. For example, studies by [9] showed a different chemical reaction pathway when the precursor was formed by mixing powders of pure Cu, In and Se in the 1:1:2 stoichiometry as compared to mixing powders of the intermetallic compound CuIn with Se in the same stoichiometry. The latter approach led to CIS formation at a much lower temperature.

This is consistent with the observation that a co-deposited Cu+In+Se amorphous mixture [7, 6] precursor structure does not lead to device quality CIS films, in contrast to the successful SEL process. In the SEL process the elements are sequentially deposited on a substrate, usually in the sequence substrate/Cu/In/Se [5]. This precursor structure usually leads to the formation of a Cu_xIn_y intermetallic phase during an intermediate reaction step [2]. Based on these results, it is anticipated that alternative precursor structures might yield improved CIS thin film growth.

4.3 Reaction Pathway Engineering

Phase diagram information is essential in designing new precursor structures. Figure 4.1 shows the Cu-In-Se ternary composition diagram along with the accepted compounds and several tie-lines connecting pairs of them. Inspection of this diagram suggests several reaction pathways to synthesize $CuInSe_2$ from binary compounds using RTP. Although previous approaches have started with the pure elements to form a physical mixture or a stacked layer structure, certain advantages exist when starting with binary compounds or alloys. Among these compounds, those within the Cu-Se and In-Se couples are attractive due to existence of low melting temperature phases [10]. There are several combinations of these two couples that could lead to CIS formation.

Examining the evaluated Cu_2Se-In_2Se_3 pseudobinary T-x phase diagram (Figure 4.2) reveals that the liquid phase that exists at the lowest temperature in this section is the ~870°C eutetic alloy lying in the In_2Se_3-rich composition field. This temperature is much too high for the glass substrate.

The following guidelines were used to suggest suitable Cu-Se and In-Se compounds to serve as precursors for ex-situ RTP synthesis of CIS.

- Avoid high melting temperature phases such as In_2Se_3 and Cu_2Se, especially the conducting Cu_2Se secondary phase.
- Utilize an intermediate liquid phase to assist grain growth.
- Minimize evaporation losses during RTP.
- Select highly reactive pairs.

At first glance, one choice would be to deposit a bilayer structure of Cu_2Se and In_2Se_3 and react them to form CIS according to:

$$Cu_2Se + In_2Se_3 \rightarrow 2CuInSe_2$$

An examination of the Cu-Se (Figure 4.3) and In-Se (Figure 4.4) binary T-x diagrams from Parts 2 and 3 of this report suggests that a suitable combination would be selenium-rich copper compounds (CuSe, $CuSe_2$) and selenium-rich indium compounds (InSe,In_6Se_7). When these binary compounds are heated the copper compounds will form a liquid phase and the indium compounds will form a solid-liquid mixture in the temperature range 523 to 620^{o}C. To reach the liquid phase, rapid thermal processing might be required to avoid solid-solid phase transformations. The binary diagrams alone, however, do not indicate if a liquid phase exists after the reacting precursor film enters the ternary domain.

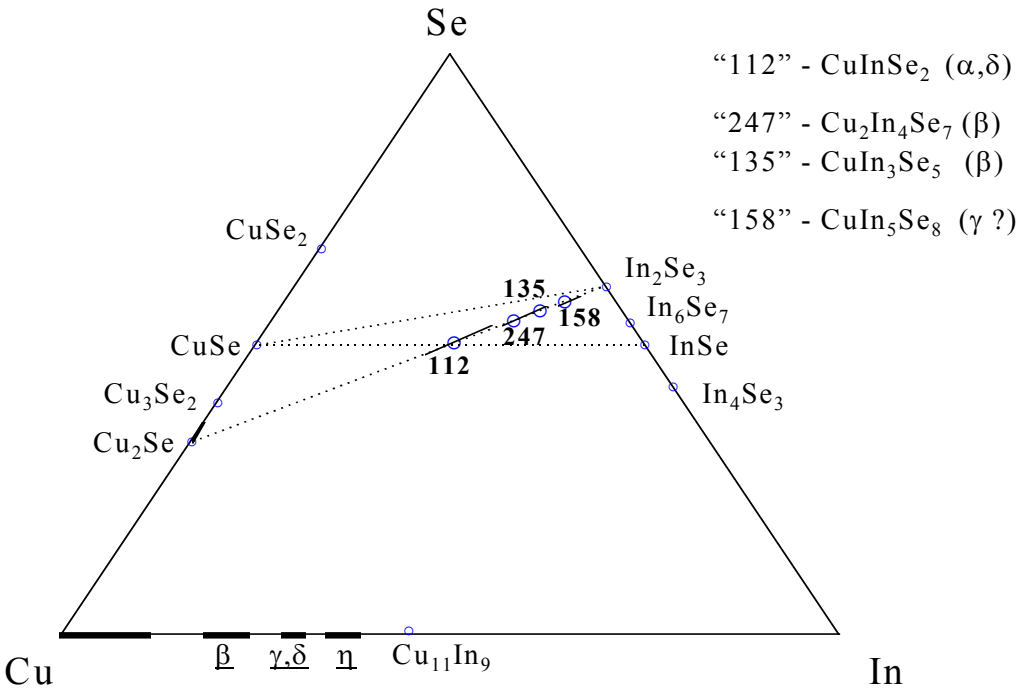

Figure 4.1 Cu-In-Se ternary composition diagram.

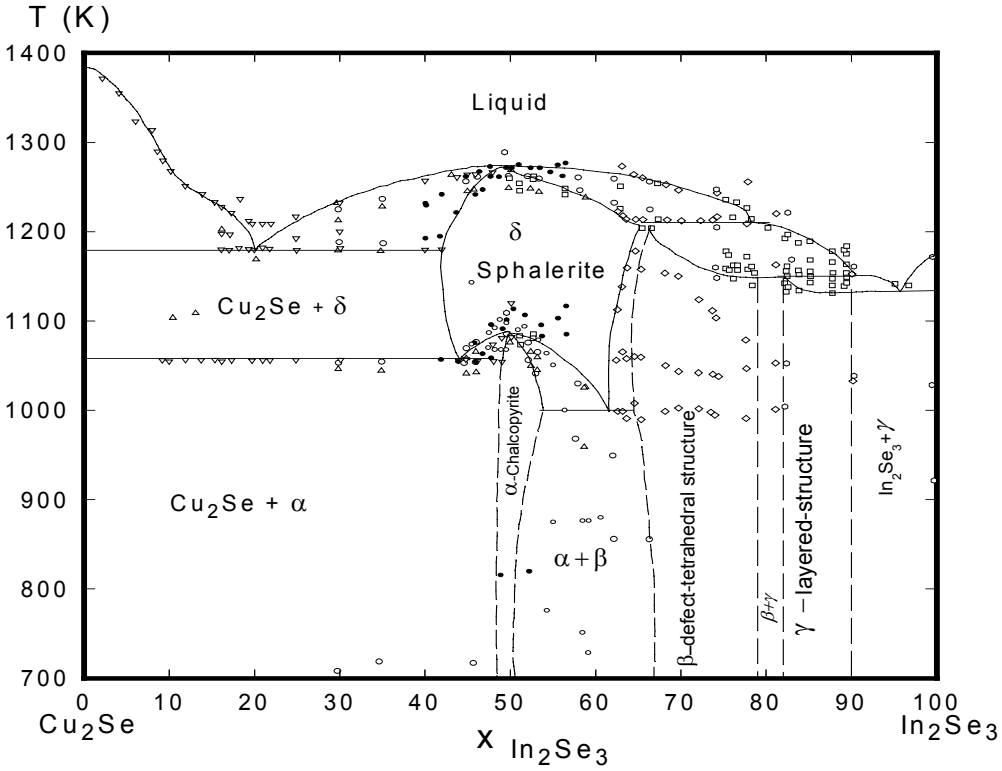

Figure 4.2 Cu_2Se-In_2Se_3 pseudobinary phase diagram

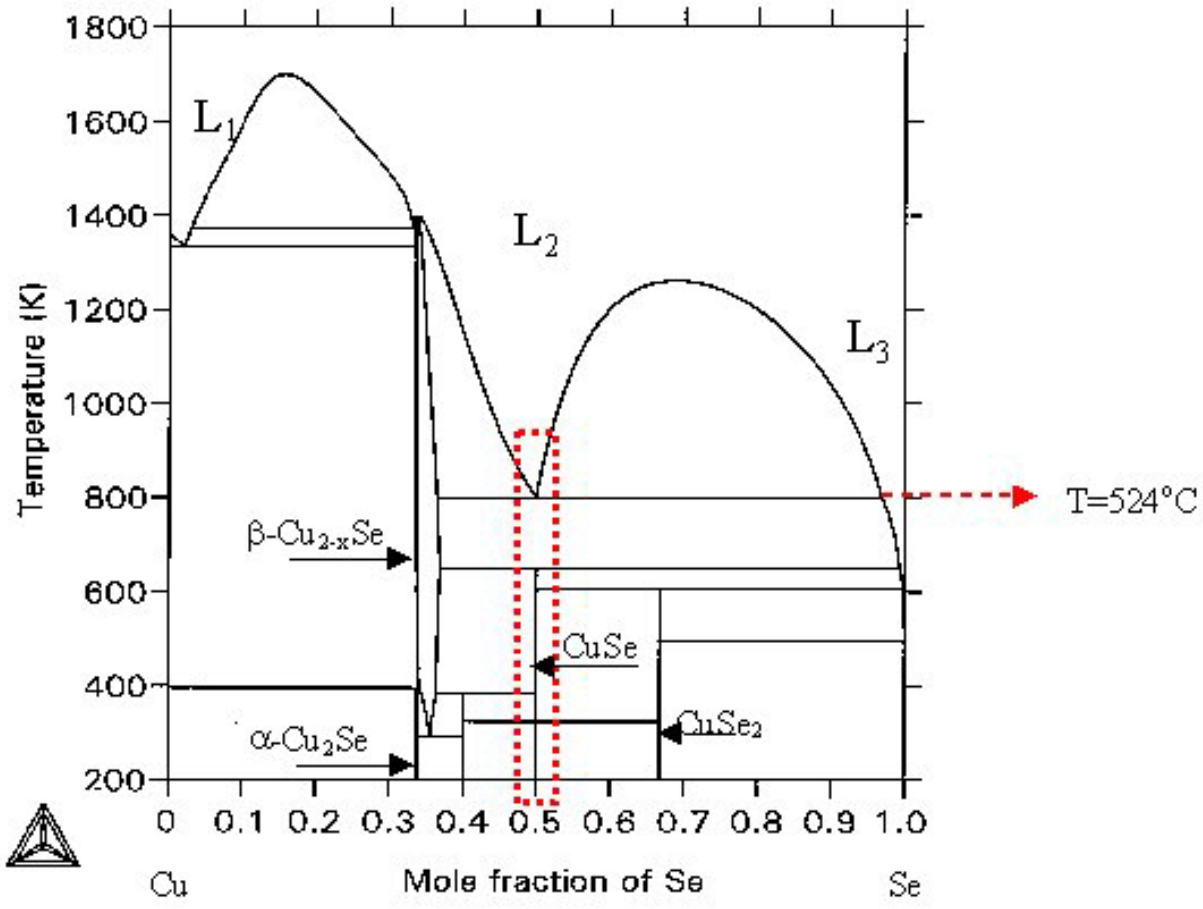

Figure 4.3 Cu-Se binary T-x phase diagram.

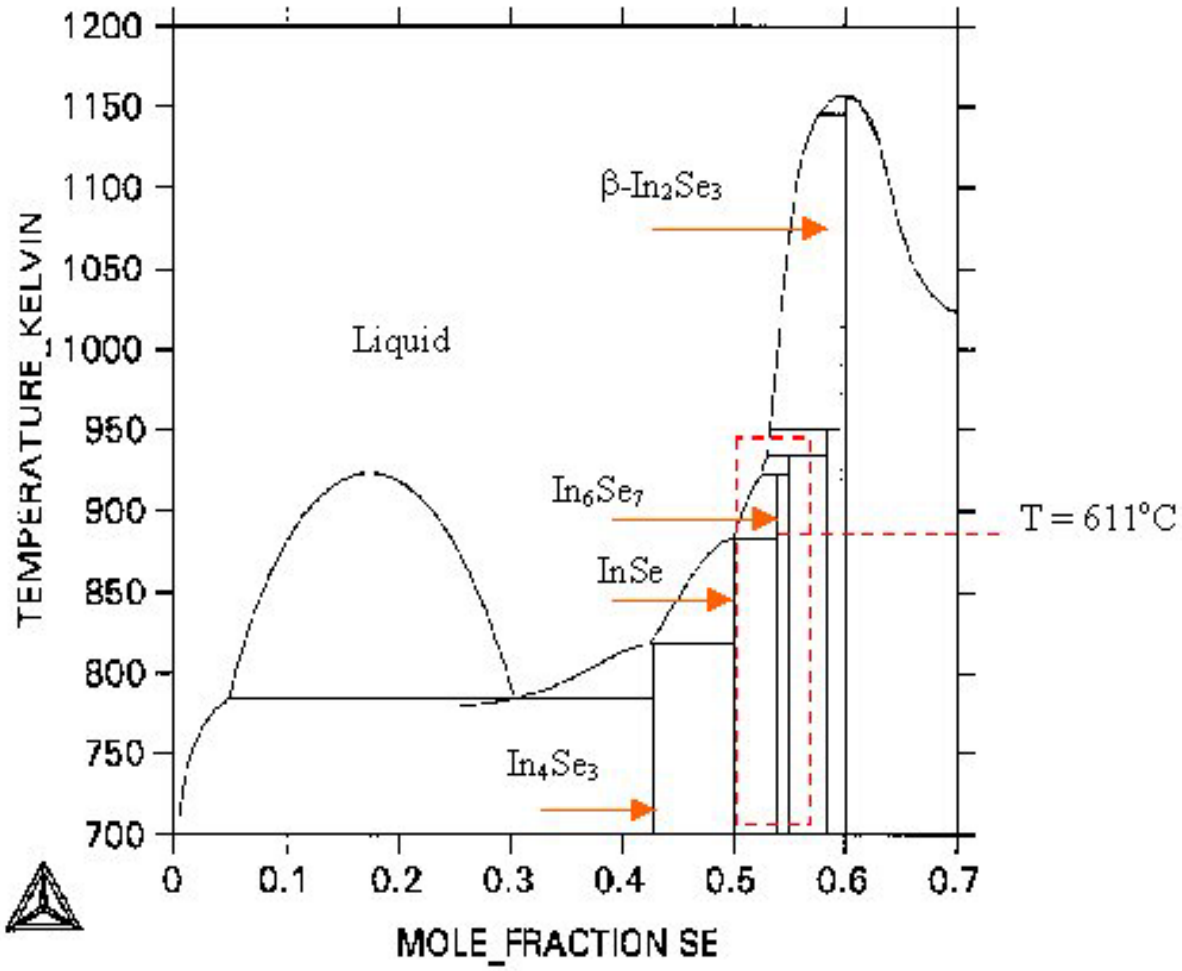

Figure 4.4 In-Se binary T-x phase diagram.

Although Se is in excess of the 112 stoichiometry in the above scheme, Se should easily volatilize to leave single phase CIS. An estimation of the ternary Cu-In-Se phase diagram has been developed and a projection of the liquidus surface is shown in Figure 4.6. With this diagram possible compound combinations can be further evaluated. In particular, the eutetic valley between the binary eutetic compositions E_1 and E_2 should be nearly degenerate and thus exist at slightly below 220^{o}C. Overall compositions along a line in Figure 4.6 connecting the pure Se corner to the $CuInSe_2$ compound indicates it should be possible to form CIS in the presence of an intermediate, low-temperature, Se-rich liquid phase by the reaction:

$$\text{Liquid} \rightarrow CuInSe_2 + Se$$

The relative amounts of the binary compounds should be adjusted to lie on this line.The above approach suggested a precursor structure that consists of an In-Se layer (50 to 55 Se at.%) (see dashed box in In-Se phase diagram in Figure 4.4) deposited on a Cu-Se (50 to 55 Se at.%) (see dashed box in Cu-Se phase diagram in Figure 4.3) layer, which is deposited on a Mo coated soda-lime glass substrate. A schematic diagram of this structure is given in Figure 4.5. The composition ranges for the binary pairs and the overall precursor films are indicated in Figure 4.6 as heavy lines along the In-Se and Cu-Se limits near the CuSe and InSe compounds. With this composition a Cu-Se liquid phase should form to assist growth and the small amount of remaining excess Se should be volatile. The presence of solid In-Se layer on top will minimize the evaporation loss during the RTP process. It is also likely that an even lower temperature Se-rich liquid could participate in the growth mechanism.

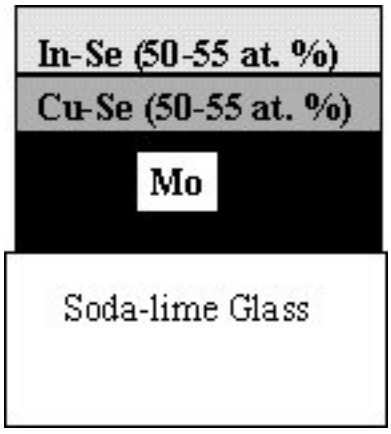

Figure 4.5 Proposed precursor structure.

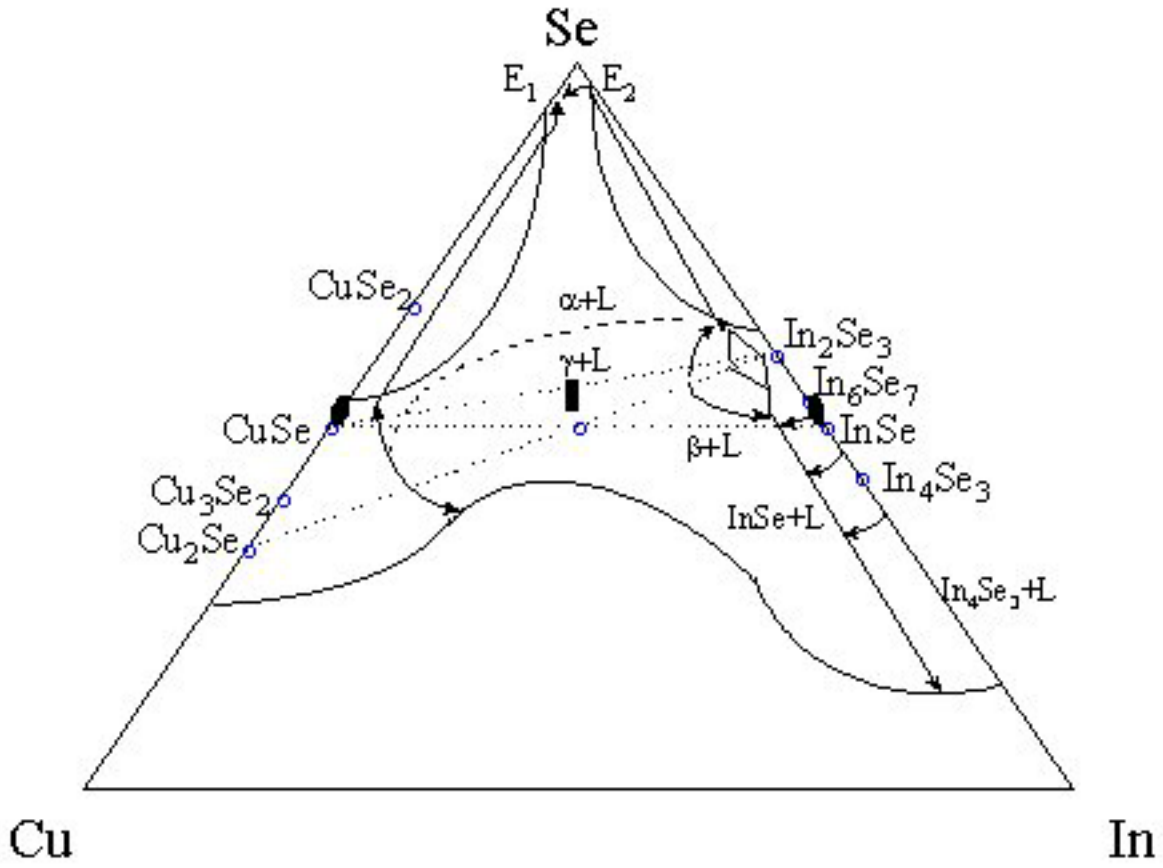

Figure 4.6 Liquidus projection for Cu-In-Se ternary system.

4.4 Precursor Growth

A low temperature precursor growth is desirable for higher throughput manufacturing equipment, lower equipment cost, lower thermal budget, and thus a lower capital cost for modules. A rotating-disc migration-enhanced deposition system was used for precursor deposition, which included two Langmuir evaporation sources for copper and indium and a double-oven thermal cracking source for selenium. A schematic drawing of the reactor is shown in Figure 4.7. The growth conditions (substrate temperature and flux ratio) of In-Se binary system have been thoroughly studied [11]. In their investigations they utilized a Langmuir evaporation source and suggested the low selenium sticking coefficient is most likely due to the formation of larger polymer molecules (e.g., Se_8). The use of a cracking source allowed the Se decomposition temperature to be adjusted independent of source temperature (flux control) and thus control the selenium flux species distribution.

The precursor films used in this study were deposited at a 200^{o}C substrate temperature. To fabricate the desired precursor structure, the In-Se and Cu-Se growth conditions were studied separately by fixing the selenium flux and adjusting the selenium to copper and selenium to indium molar flux ratios. The molar fluxes were cross-calibrated by EIES and quartz-crystal monitors.

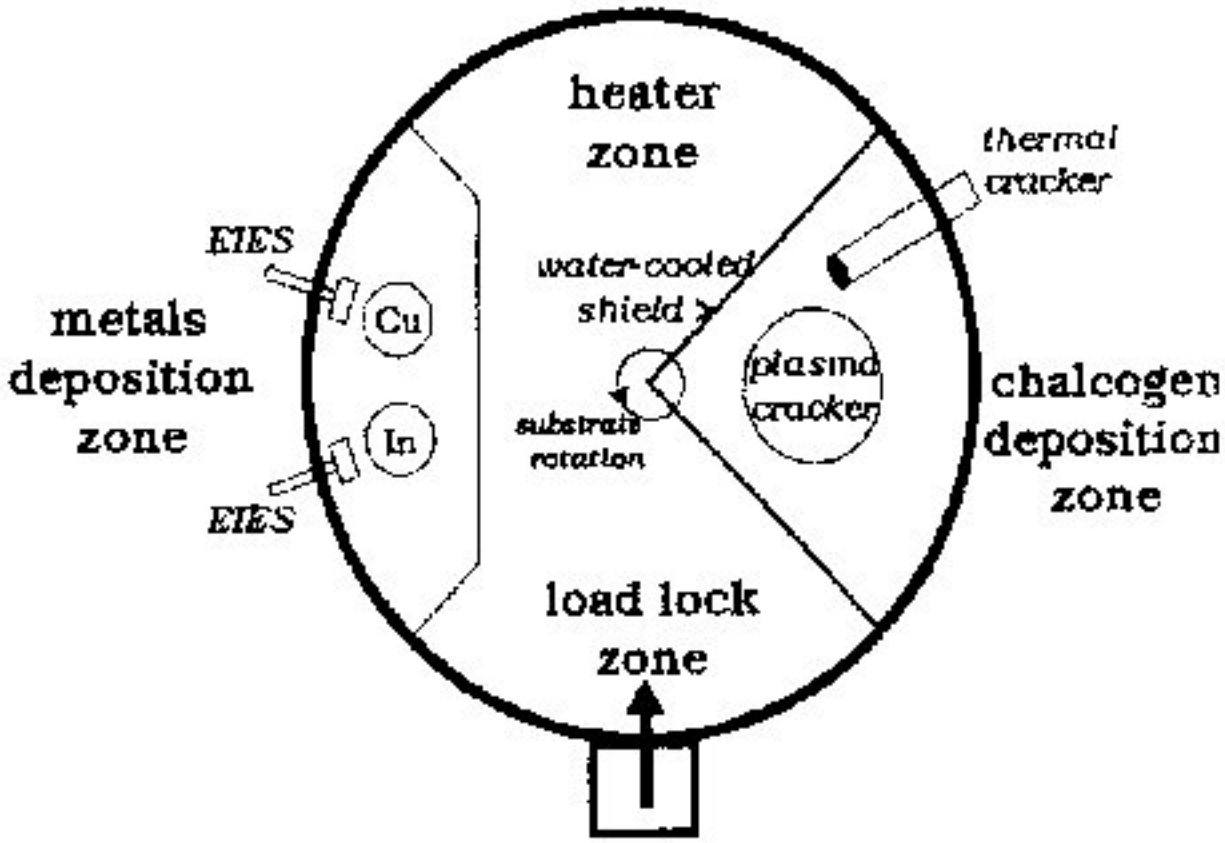

Figure 4.7 Schematic diagram of the migration-enhanced epitaxy reactor.

4.5 Rapid Thermal Processing

Ex-situ RTP was performed on samples placed in a closed rectangular quartz susceptor. A flat sheet of SiC coated graphite was placed at the bottom of the susceptor to improve the temperature uniformity. The susceptor and sample were loaded into a customized RTP furnace heated by a bank of 12 tungsten-halogen quartz lamps from both sides under flowing N_2. The schematic diagram of the RTP reactor is given in Figure 4.9. The processing temperature was controlled by a thermocouple in direct contact with the glass substrate. The RTP annealing recipe was input and controlled by a PID controller. Due to the significant difference in the absorption characteristics between the precursor films and the soda-lime glass substrate, it is anticipated a non-negligible temperature gradient exists between the thermocouple reading and surface film temperature. This temperature difference was estimated by visualizing the eutetic reaction at 575^{o}C of a Mg/Au layer deposited prior to the In-Se compound (see Figure 4.8). The In-Se layer is about 1000 Å. The temperature difference is estimated to be around 200^{o}C.

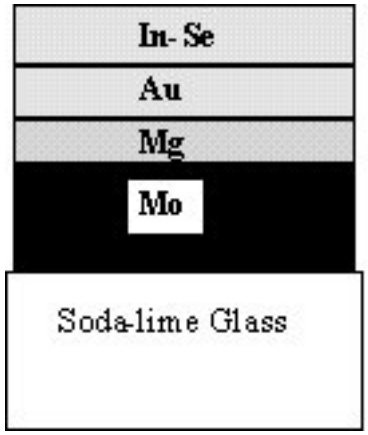

Figure 4. 8 Temperature calibration sample.

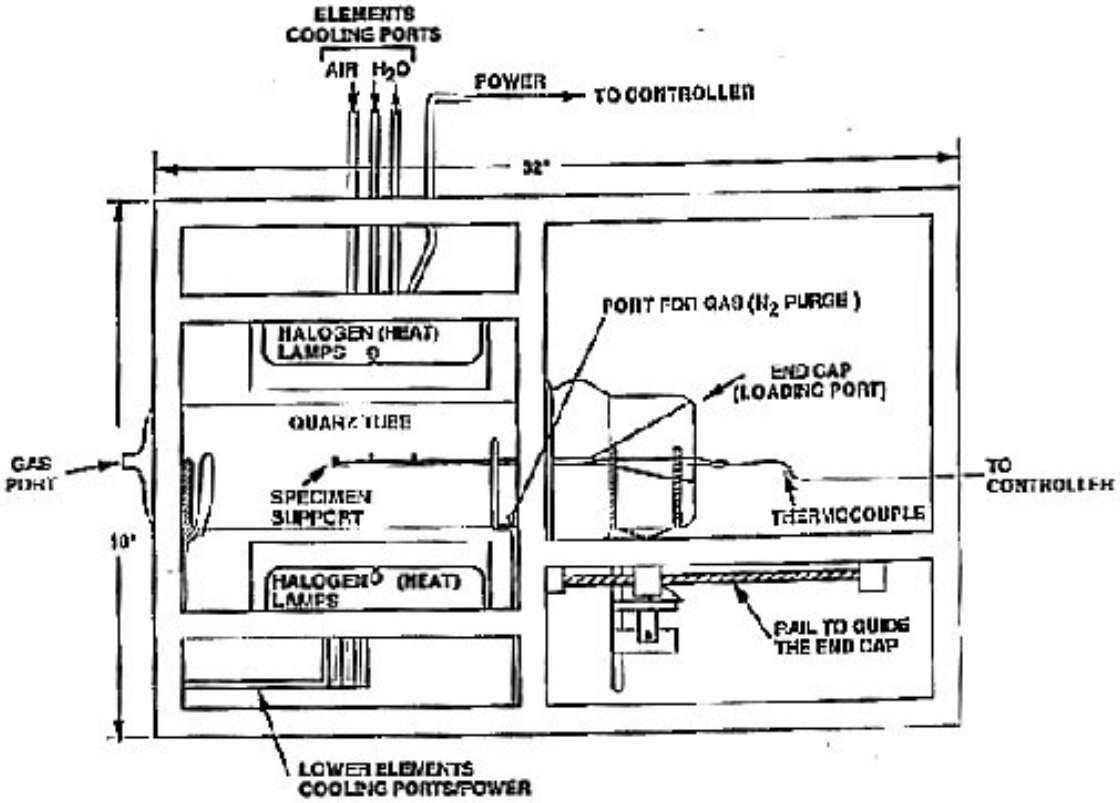

Figure 4.9 Schematic of the rapid thermal processing system

4.6 Film Characterization

The film morphology was studied by plan-view and cross-section Scanning Electron Microscope (SEM). Compositional analysis was performed by Inductively Coupled Plasma (ICP) emission spectrometry for the atomic ratios of CIS. The samples were dissolved in 5 % (by volume) nitric acid. The standard solution is also based on 5% nitric acid. Composition depth profiles were measured by sputter Auger Electron Spectroscopy (AES) using a Perkin-Elmer PHI660 AES/SAM microscope, equipped with a CMA spectrometer and an Ar-ion gun. All spectra were obtained at 5KeV.

The structural properties of the films, such as phase constitution, crystallinity, and texture were determined by Powder X-ray Diffraction (PXRD) and Grazing Incidence X-ray Diffraction (GIXRD) at various angles. The GIXRD measurements were carried out using a Siemens

diffractometer equipped with an area detector using Cu Kα radiation. This non-destructive technique allows determining the depth distribution of the phases in the films. The utilization of an area detector provided the opportunity to assess the texturing of the films at the same time. This feature is essential when diffraction peak intensities are needed to identify the phase constitution.

The unpolarized Raman scattering signals were measured using a double monochromator, an Ar+ laser excitation at two wavelength (λ=514.5nm and 477 nm), and standard backscattering sample geometry. The longer wavelength excitation laser will provide information with deeper penetration in the film.

4.7 Result and Discussion

Two precursor structures were fabricated. The first one possesses a three layered structure, $In_4Se_3/CuInSe_2/Cu_2Se$. The second one possesses a two layered structure, InSe/CuSe

4.7.1 Precursor structure

It is a challenge to distinguish $CuInSe_2$ from Cu_2Se using XRD spectra since most of the peaks overlap. A major difference in the powder spectra between these two phases is the peak intensity ratio of the (111)/(022) ≅ 0.5 for Cu_2Se and (112)/(024) ≅ 2 for $CuInSe_2$ phase. Simulated powder XRD patterns for $CuInSe_2$ and Cu_2Se are given in Figure 4.10(a) and (b), respectively. Unfortunately, the possibility of preferred orientation renders this difference useless in a conventional diffractometer equipped with a point detector. With the aid of an area detector, the difference can be exploited. An area detector allows assessment of the effects of preferred orientation. It is clearly seen in Figure 4.11 that only those diffraction rings belonging to the Mo substrate indicate signs of texturing. The XRD spectra of the precursor film taken at various X-ray incidence angles (0.5 to 6^o) clearly shows a change of the relative intensity of the peak around $2\theta = 26.5^o$ [$(111)_{Cu2Se}$, $(112)_{CuInSe2}$] and the peak around $2\theta = 44.5^o$ [$(022)_{Cu2Se}$, $(024)_{CuInSe2}$]. The relative intensity for peak at 44.5^o is increasing with the X-ray incident angle, as shown in Figure 4.12 (a) and (b). All the spectra show the presence of In_4Se_3 phase in addition to Cu_2Se and $CuInSe_2$. These data suggested a three layered structure, $Mo/Cu_2Se/CuInSe_2/In_4Se_3$, was formed in the deposition process.

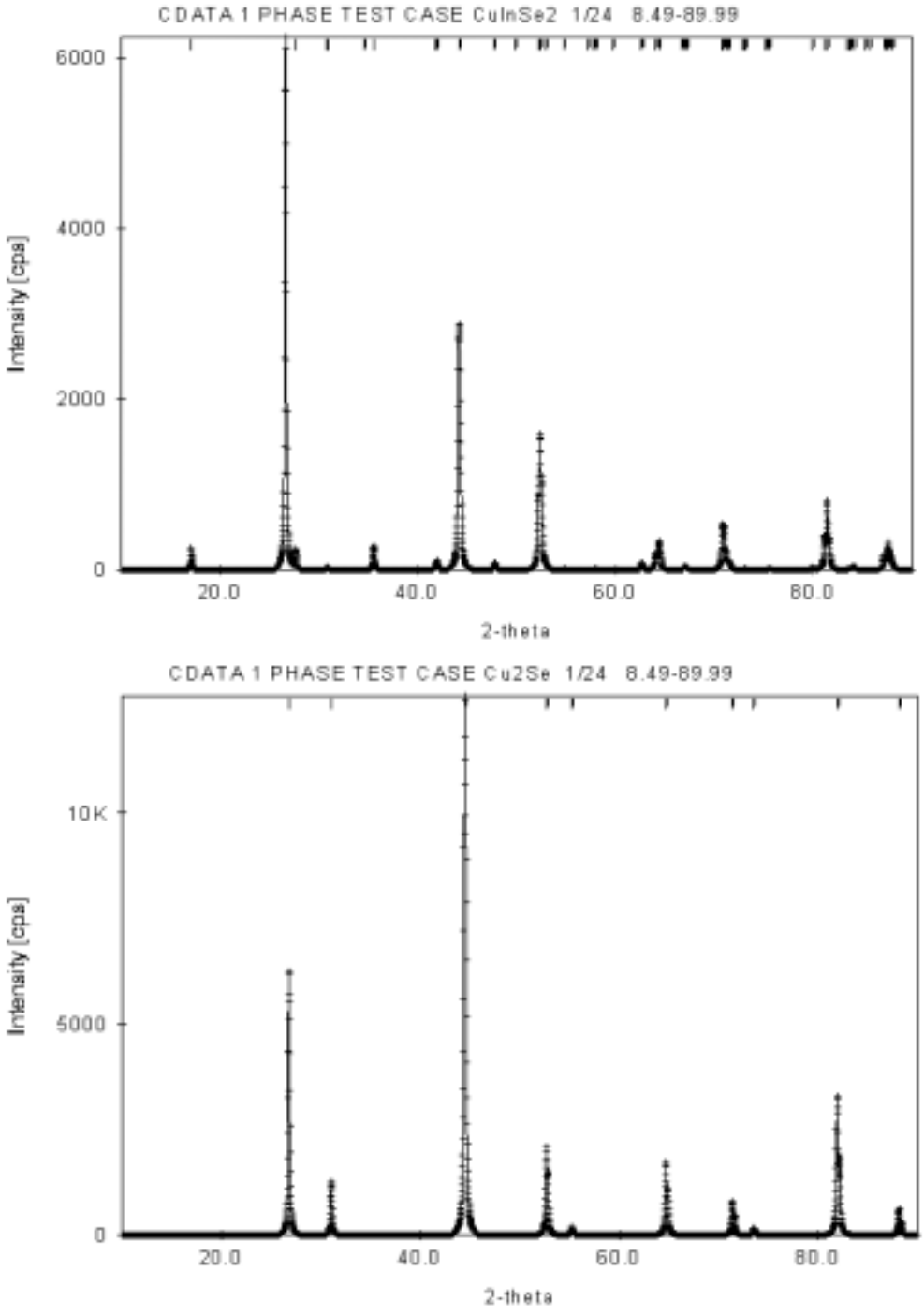

Figure 4.10 Simulated powder Cu-Kα XRD patterns for (a) $CuInSe_2$, and (b) Cu_2Se.

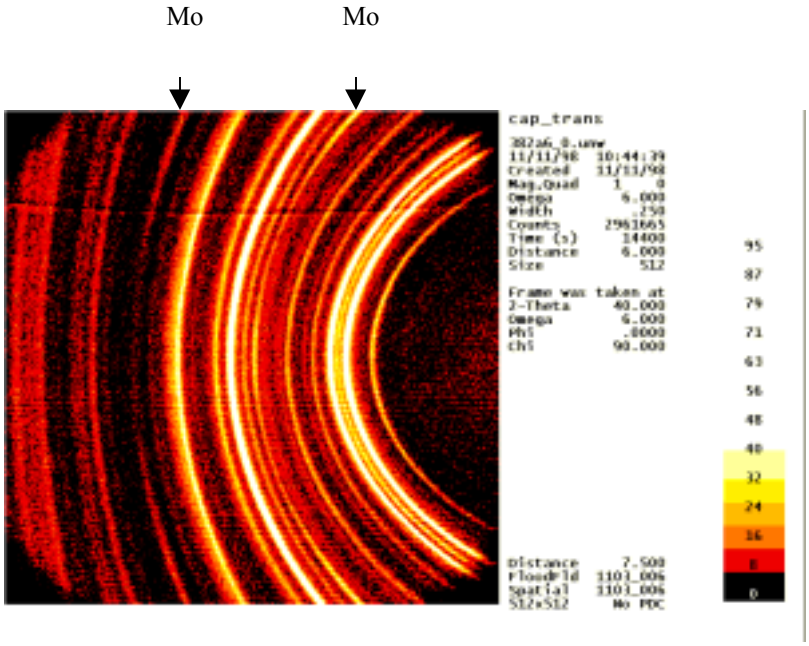

Figure 4.11. X-ray diffraction pattern at 6^{o} incident angle of the precursor film.

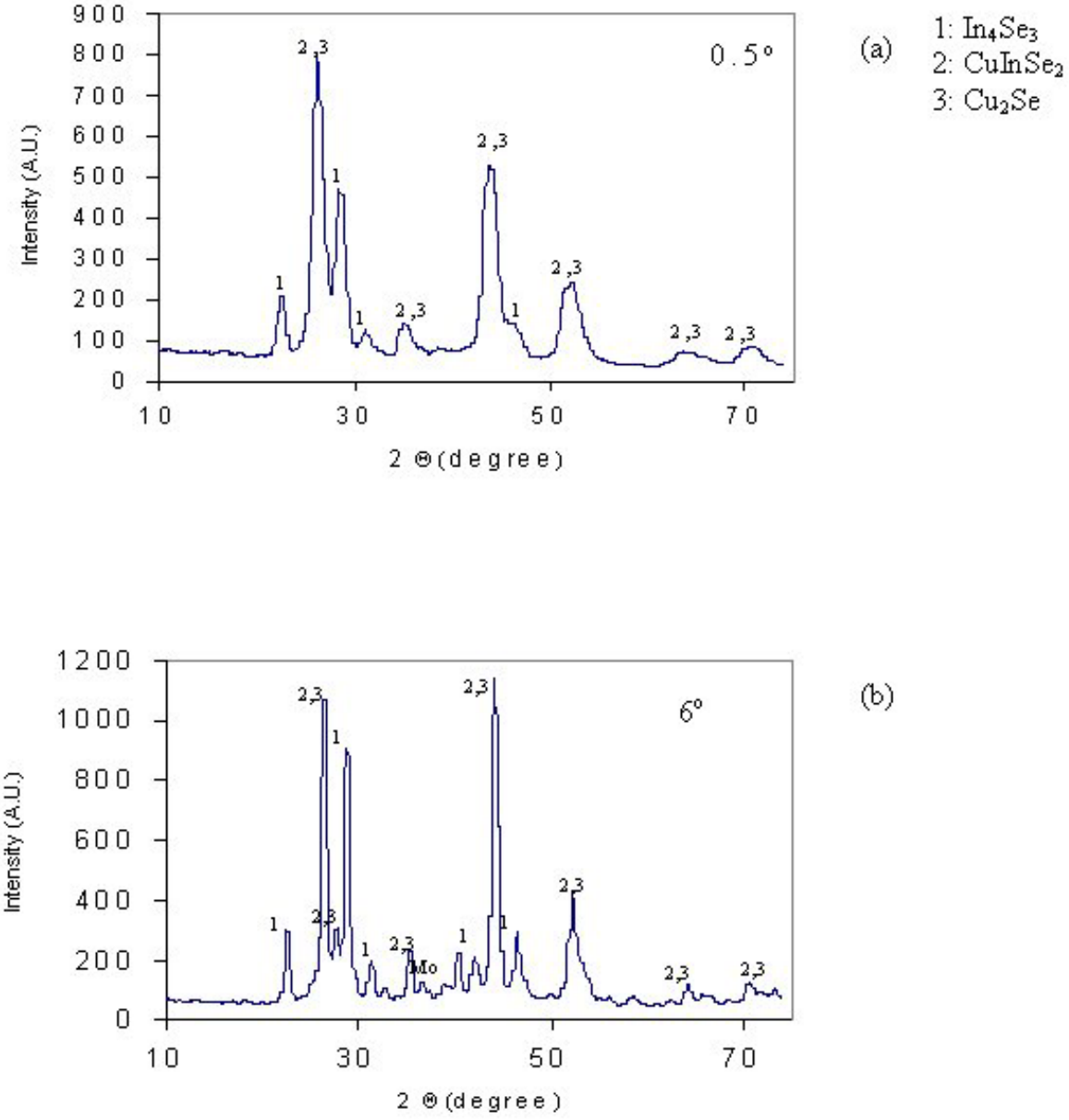

Figure 4.12 XRD spectra of precursor film measured at (a) 0.5^{o} incident angle and (b) 6^{o} incident angle.

The Raman spectra shown Figure 4.13(a) and (b) provide further evidence for this structure. A much more intense $CuInSe_2$ phonon peak is evident in the spectrum measured at 514 nm as compared to the one measured at 477 nm.

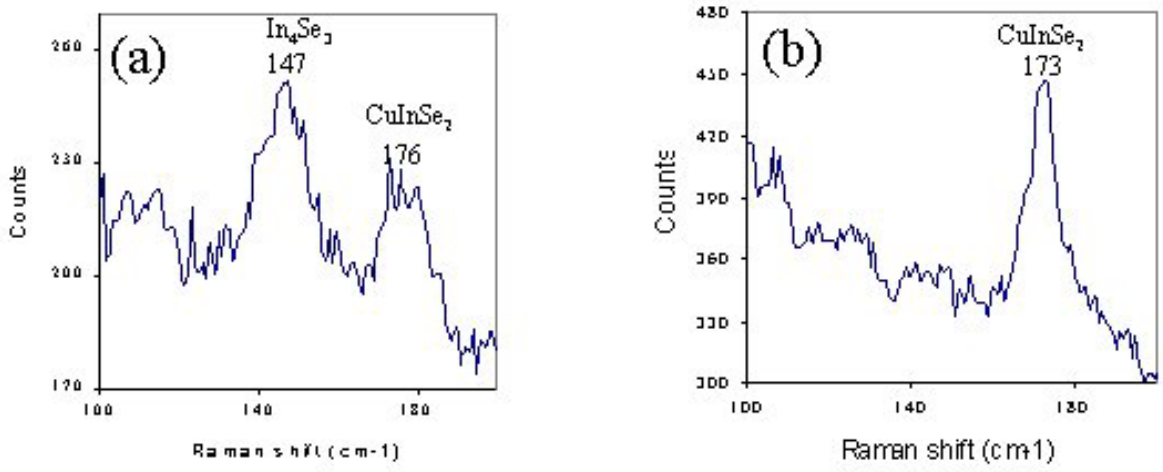

Figure 4.13 Raman spectra at two excitation wavelengths (a) λ = 477 nm and (b) λ = 514 nm measured on the precursor film.

RTP 290°C

Upon performing RTP on this sample to a set point of 290°C (thermocouple temperature) for 70s, the majority of the In_4Se_3 phase disappeared and reacted to form $CuInSe_2$ after 290°C (TC temperature) RTP annealing for 70 s as indicated by the PXRD spectrum shown in Figure 4.14. The appearance of the (101) peak and the increasing (112) peak intensity of $CuInSe_2$ are good indications of productions of additional CIS. The GIXRD patterns vary only slightly with various X-ray incident angles. This indicated the binary precursor layers were reacting and formed more $CuInSe_2$ during RTP. GIXRD spectra, however, still shows the presence of In_4Se_3. This indicated the reaction is not complete at this processing condition. The XRD spectra at 6° incident angle are given in Figure 4.15.

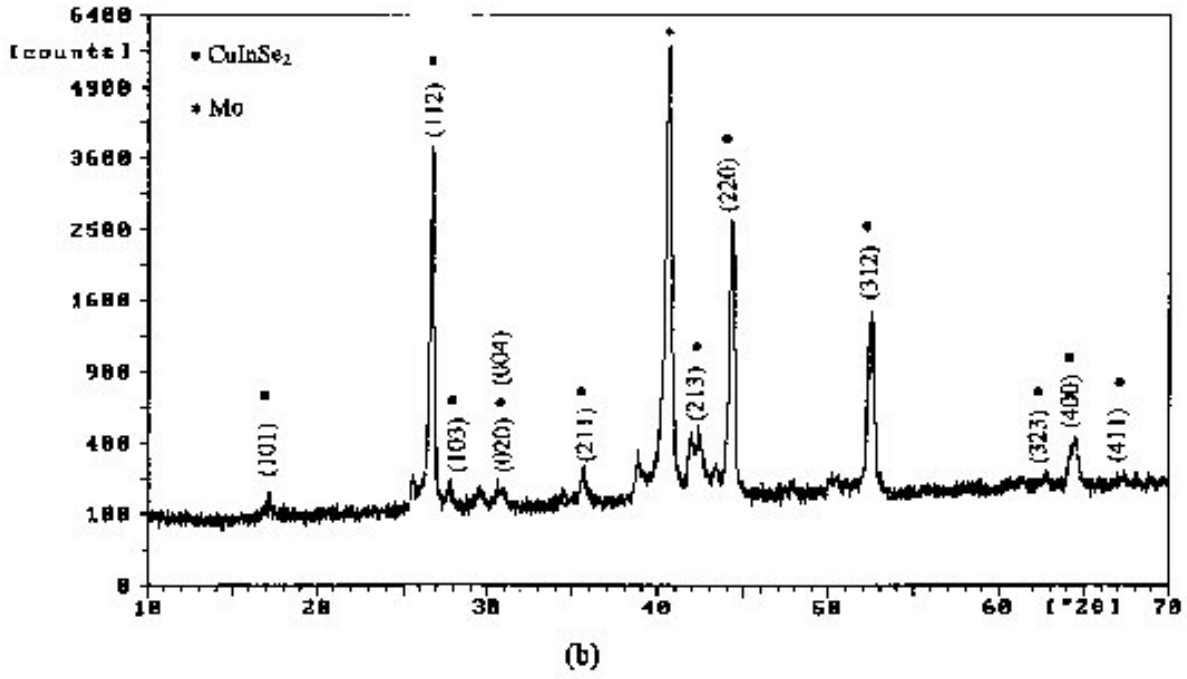

Figure 4.14 PXRD spectrum of the film after RTP at 290^{o}C (thermocouple temperature) for 70 s.

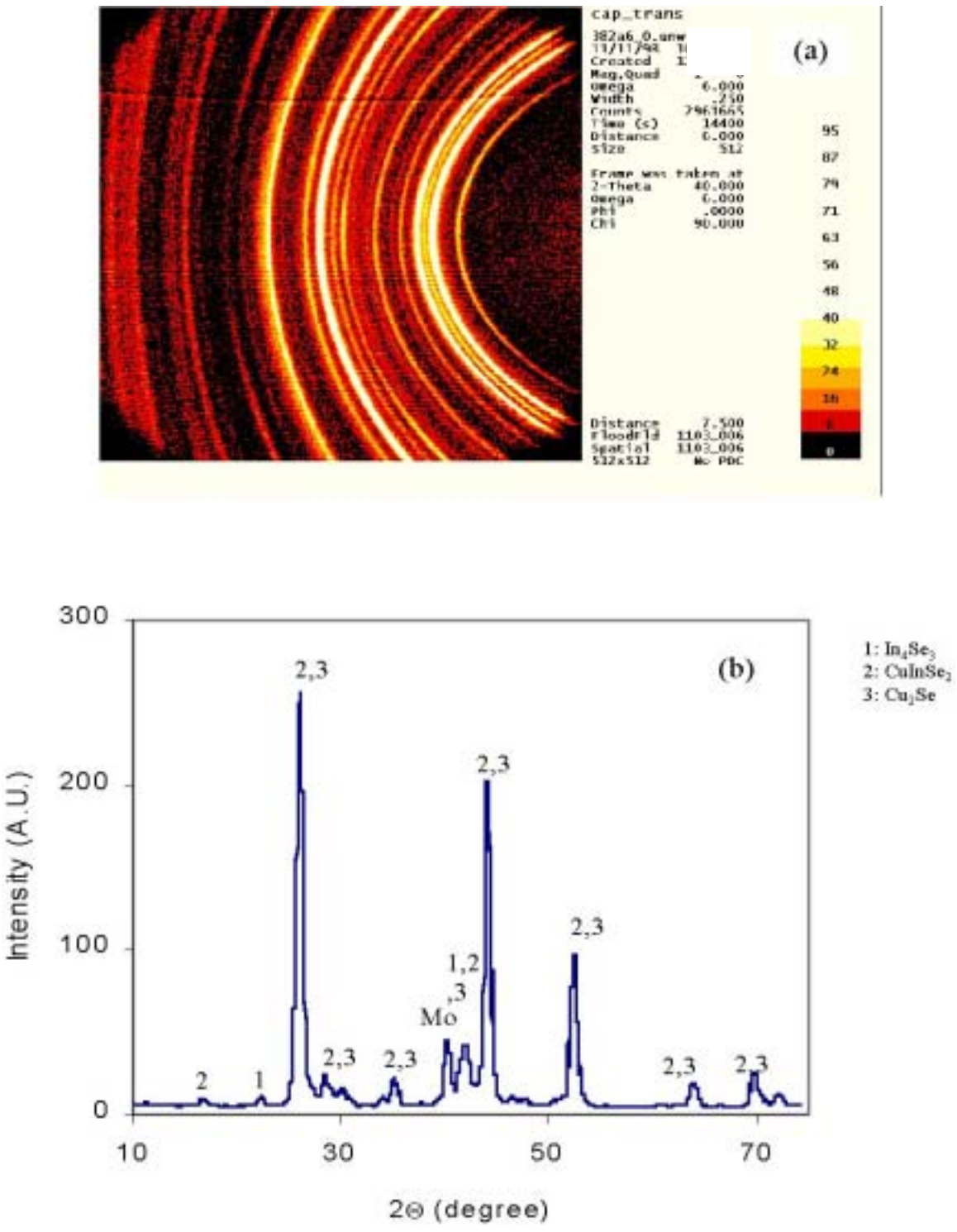

Figure 4.15 (a) X-ray diffraction pattern (b) integrated spectra at 6^{o} incident angle of the film after RTP at 290^{o}C (thermocouple temperature) for 70 s.

RTP at 500°C

Figure 4.16 shows the XRD pattern of the film after annealing at 500^{o}C for 70 s. The spotty pattern instead of the ring pattern for the precursor film indicated a dramatic grain growth process at this annealing temperature. The reason for this enhanced grain growth is the formation of an In-Se liquid by In_4Se_3 undergoing a monotetic reaction (see Figure 5.1). Figure 4.17 shows the XRD diffractogram measured at 0.5^{o} incident angle indicated formation of Cu or $Cu_{11}In_9$ intermetallic and high temperature $Cu_{2-x}Se$ phases at the near surface region. Figure 4.18 shows an integrated XRD spectrum measured at 6^{o} incident angle.

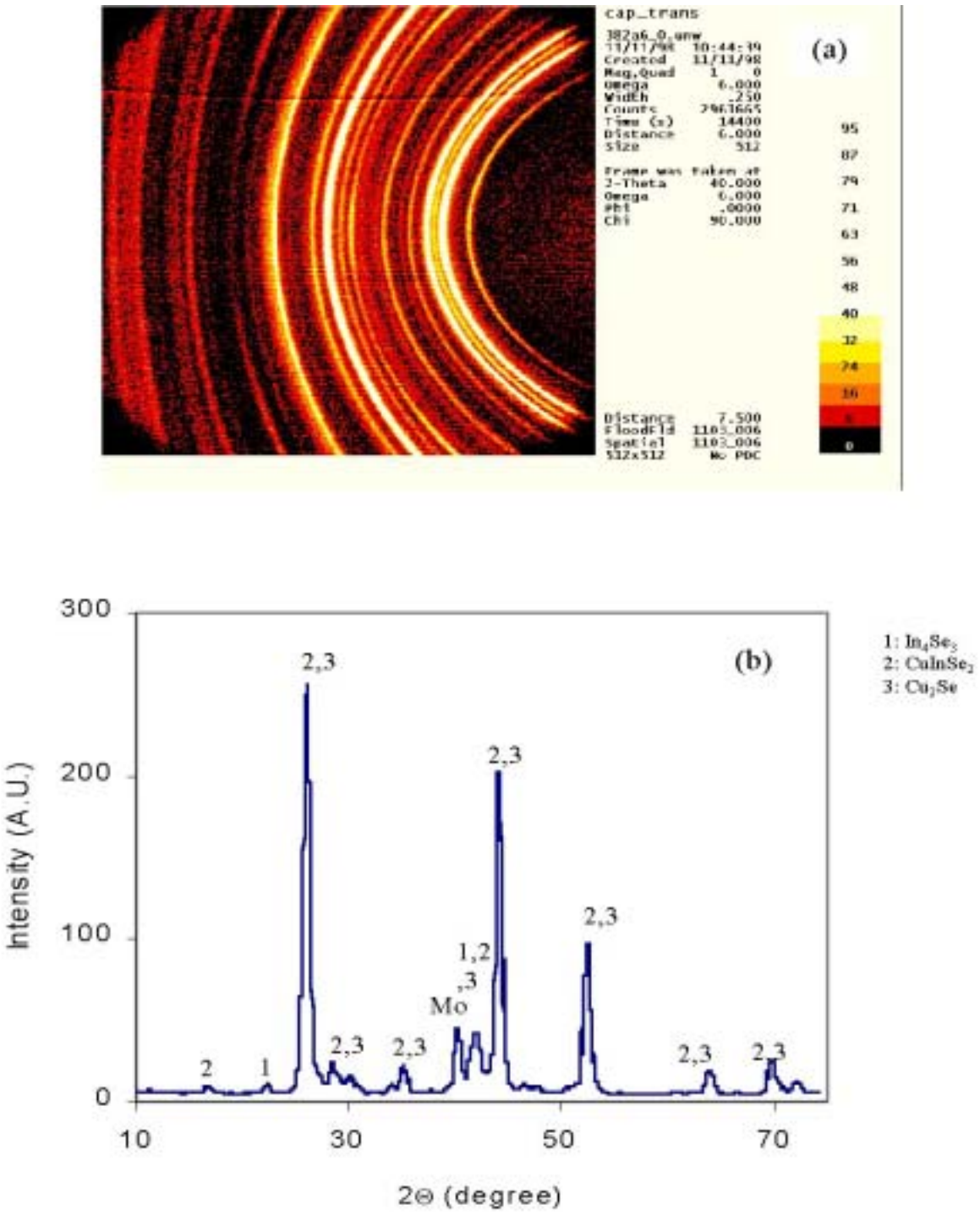

Figure 4.16 X-ray diffraction pattern at 6^{o} incident angle of the film after RTP at 500^{o}C (TC temperature) for 70 s.

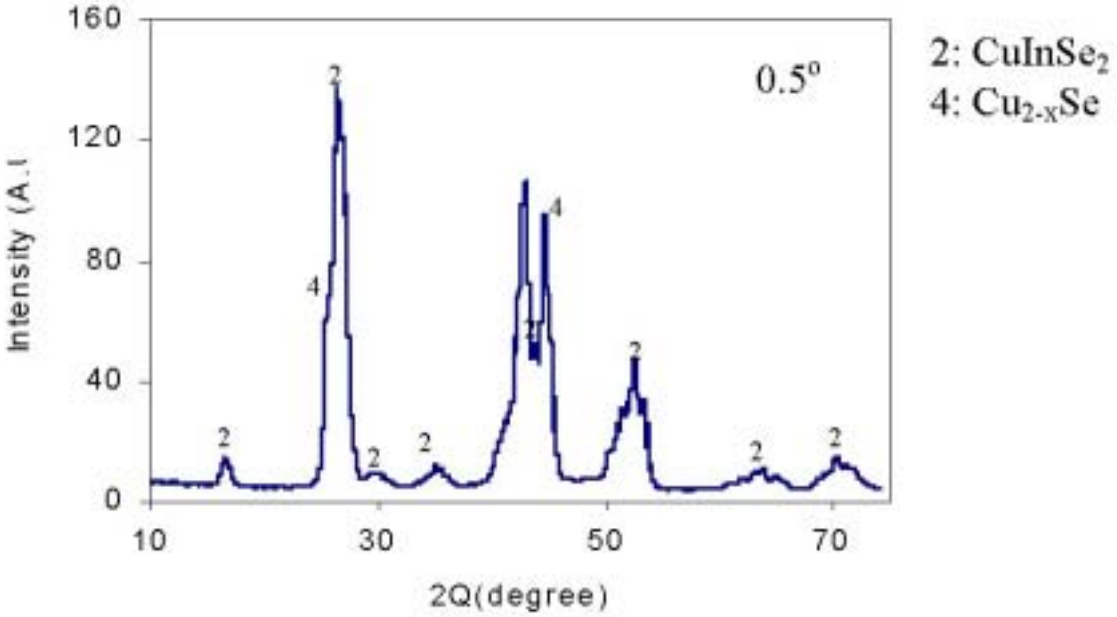

Figure 4.17 XRD spectra at 0.5° incident angle of thin film after RTP for 70 s at 500°C (TC).

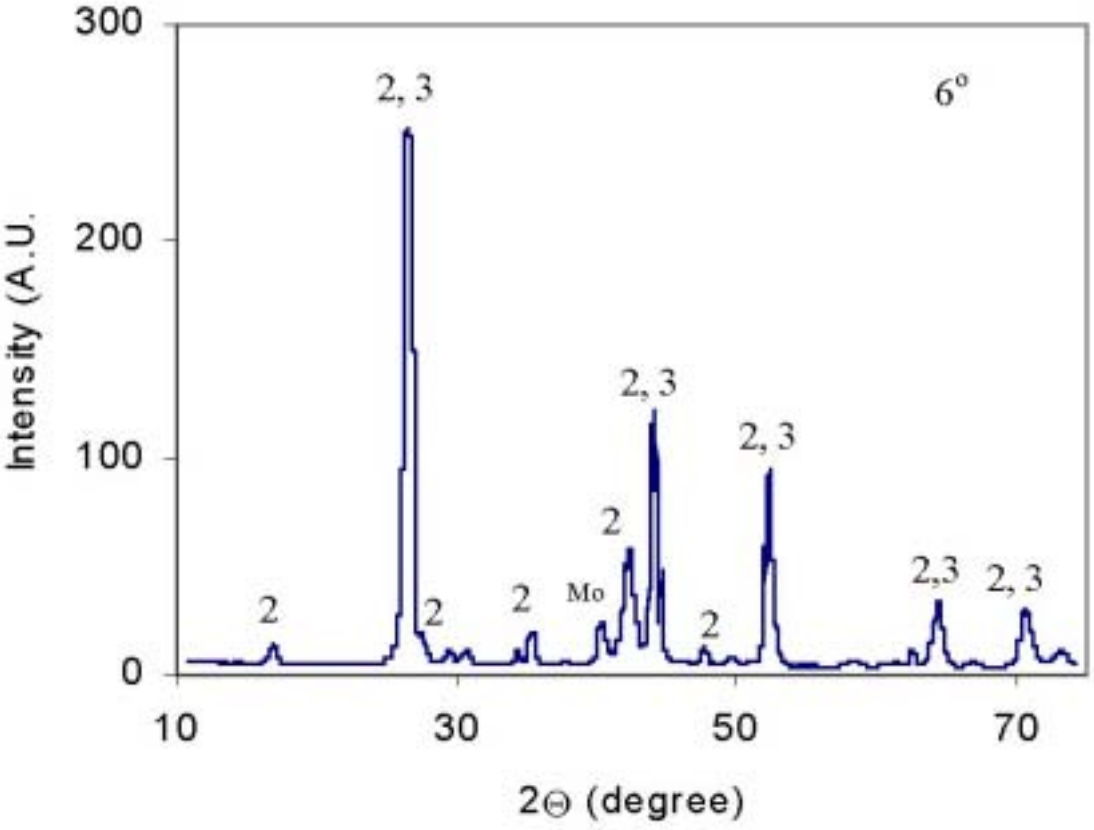

Figure 4.18 X-ray diffraction spectra at 6^{o} incident angle of the film after RTP at 500^{o}C (TC temperature) for 70 s.

Surface Morphology

Plan-view (a, c, e) and cross-sectional (b, d, and f) SEM photographs of the precursor and RTP films are given in Figure 4.19. The plane-view SEM photograph shows no change in the surface morphology after the 290°C (TC temperature), 70 s heat treatment (Figure 4.19(c)). A significant change was observed in the cross-sectional photograph in Figure 4.19(d). These results suggested an interface reaction between the precursor layers, and the reaction did not extend to the top surface region. Dramatic changes were observed after the 500°C (TC temperature), 70 seconds heat treatment in both plan-view and cross-section photographs as shown in Figures 4.19(e) and (f). The surface morphology suggests a liquid phase formed during the rapid thermal process. This could be attributed to the melting of In_4Se_3 phase, which undergoes a binary monotetic reaction at 524°C [12]. This is an expected result since we already know the temperature on the surface is about 200°C higher than that of the TC temperature at this ramp rate, as indicated by our temperature calibration studies.

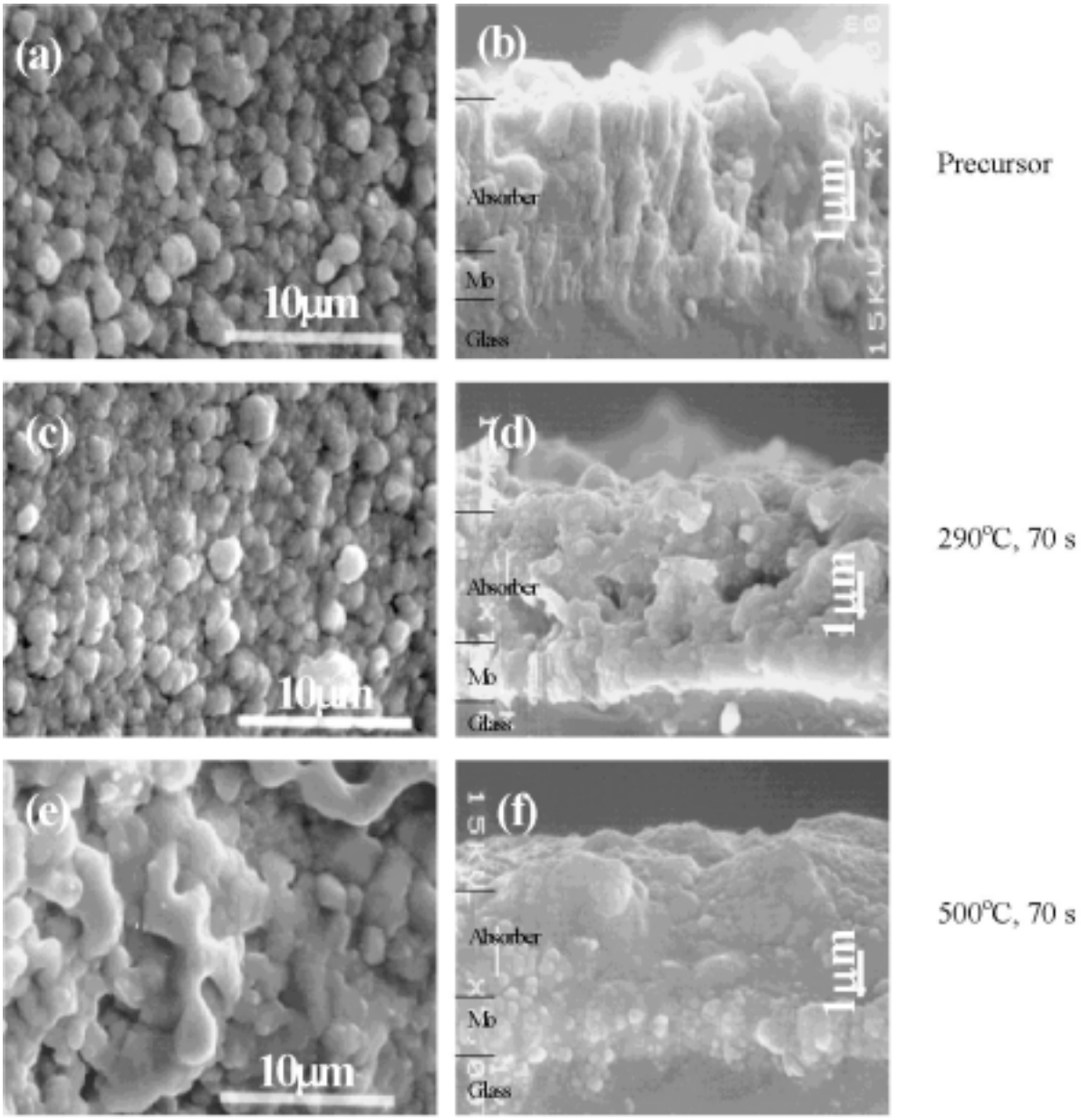

Figure 4.19 Plan-view and cross-section SEM photographs of the precursor and RTP films.

Compositional Analysis

The overall composition of the samples was analyzed by (ICP) spectrometry. The estimated uncertainty for ICP analysis is ±0.5% relative. Major sources for uncertainty are variabilities in the plasma, pump rate, and nebulizer efficiency. The precursor has an overall composition of Cu: In: Se = 35.6: 25.2: 39.1. The AES survey spectrum for the as received precursor is given in Figure 4.20. The intense oxygen signal indicated the precursor surface is mainly covered by native oxide. The surface composition estimated by AES is given in Table 4.2. The peak intensity depth profile data are shown in Figure 4.21. The oxygen signal decreased drastically after sputtering for a short time. The bottom layer composition as estimated by AES is given in Table 4.3. The depth profile is consistent with the XRD data, which suggested the formation of a three layer, $In_4Se_3/CuInSe_2/Cu_{2-x}Se$, structure.

Table 4.1. ICP chemical analysis of the investigated samples

Sample	Cu at.%	In at.%	Se at.%
Precursor	35.6	25.2	39.2
290°C (TC) , 70 s	36.3	25.3	38.4
500°C(TC), 70 s	36.1	25.4	38.5

RTP at 290°C

The overall composition of the films changed only a small amount after RTP at 290°C (TC) for 70 s as shown by the ICP data in Table 4.1. However, the AES data shown in Figure 4.23 did show a dramatic change after RTP. The depth profile clearly showed a deep Cu diffusion from the backside of the film into the top In_4Se_3 layer. This indicated the reaction front between Cu_2Se and In_4Se_3 layer was moving forward and forming $CuInSe_2$ during the RTP. This is consistent with the XRD data, which showed the disappearance of XRD In_4Se_3 peaks and increasing $CuInSe_2$ peak intensity. However, the reaction mechanism is mainly through solid state diffusion.

RTP at 500°C

Again the overall composition of the film showed little change after RTP at 500°C (thermocouple) for 70 s as shown by the ICP data in Table 4.1. This clearly demonstrates an advantage of using binary layers as precursors as compared to stacked elemental layer structures. The AES survey spectrum on the as received sample is given in Figure 4.24. The strong Cu signal indicated the reaction had reached the surface of the film during the RTP. The AES depth profile given in Figure 4.25 showed a uniform distribution of Cu, In and Se atomic species. Such fast mass transport is believe to be a result of liquid phase formation as In_4Se_3 underwent a monotetic reaction, as supported by the XRD and SEM data.

Table 4.2. Precursor film surface composition measured by AES.

Element	Atomic %
O	48.7
Cu	11.4
In	26.2
Se	13.8

Table 4.3 Precursor film composition measured by AES after 100 min sputtering

Element	Atomic %
O	3.3
Cu	43.6
In	0.9
Se	35.6
Mo	16.7

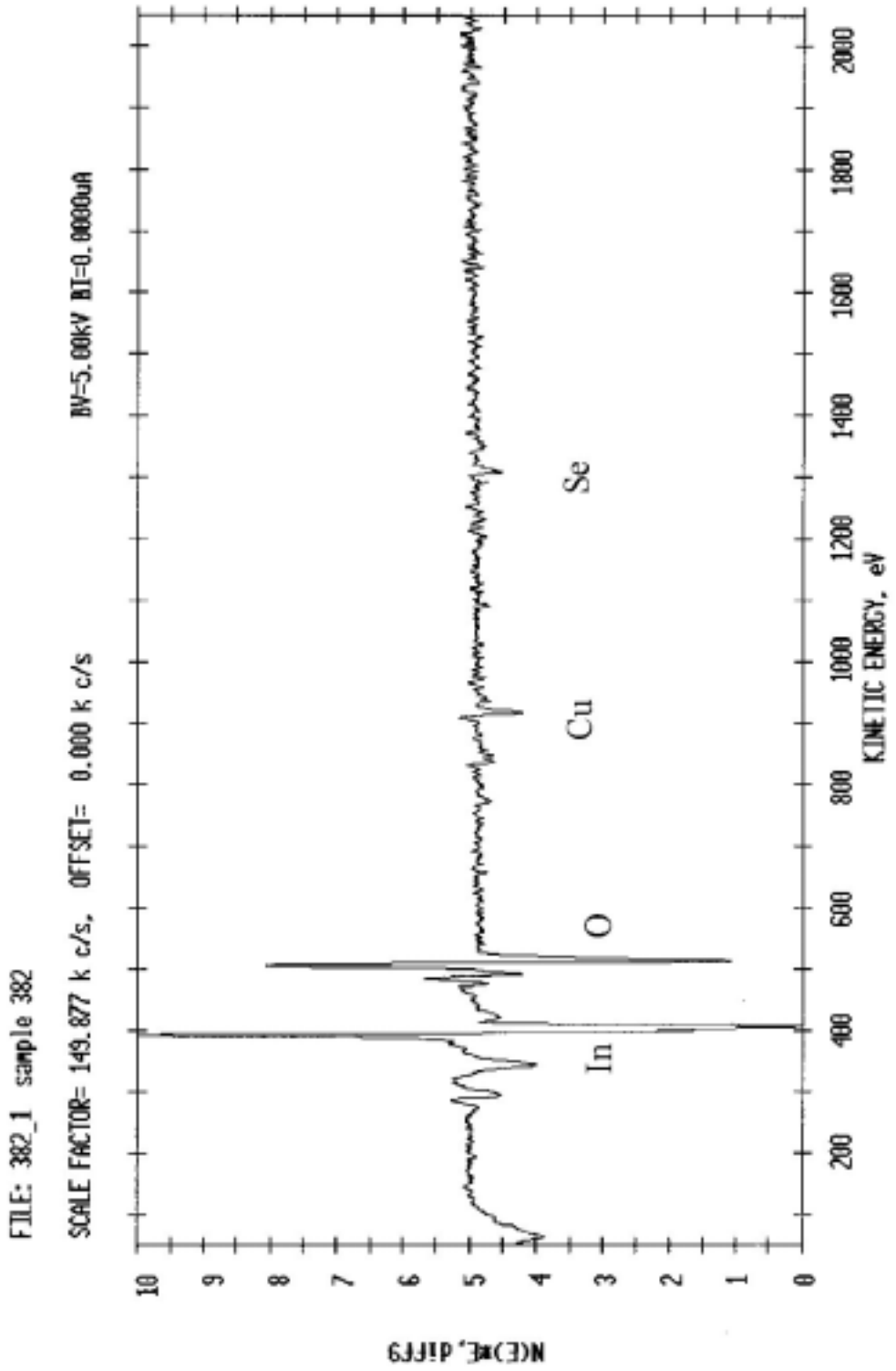

Figure 4.20 AES survey scan on as received precursor film.

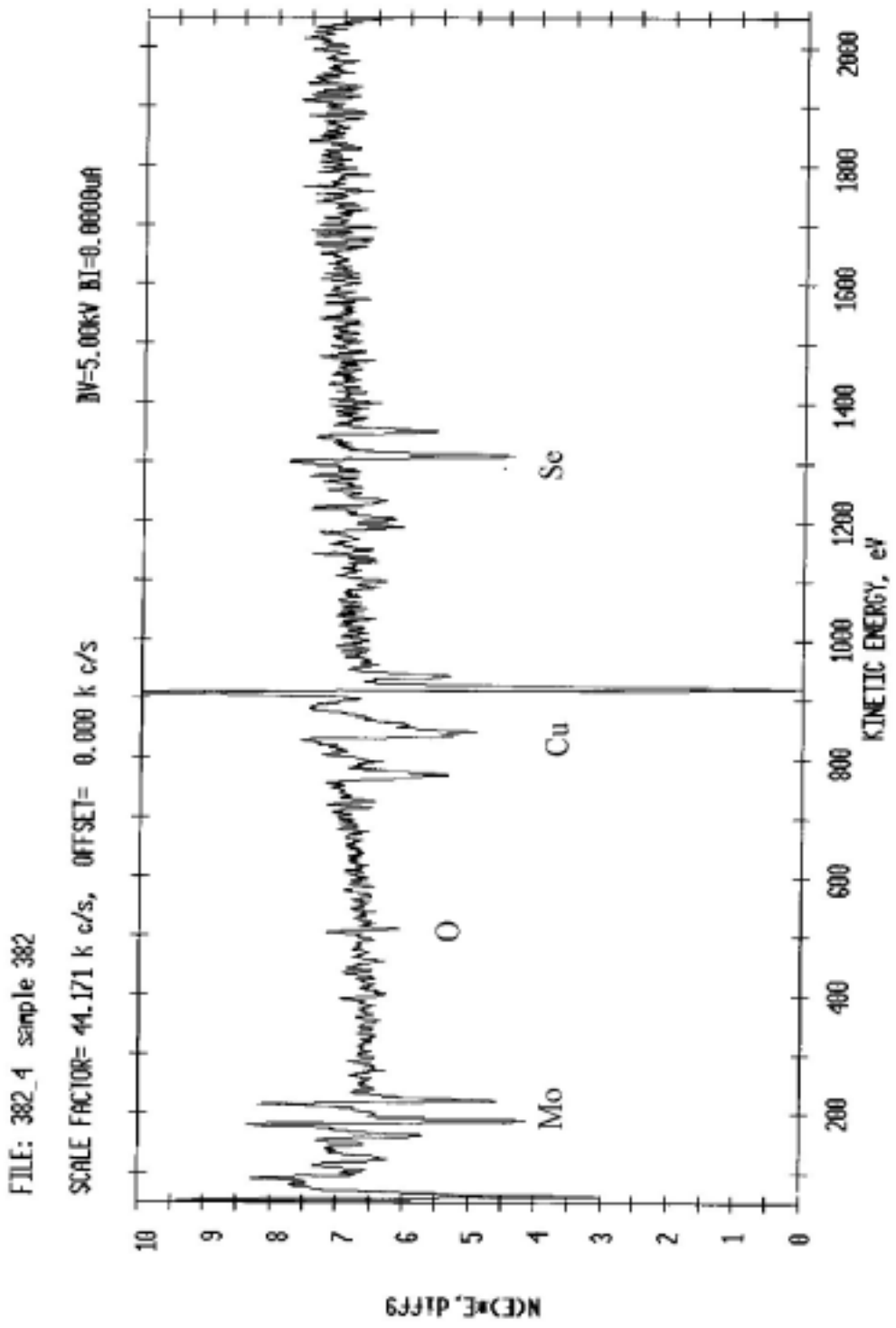

Figure 4.21 AES survey scan on precursor film after 100 min sputtering etching.

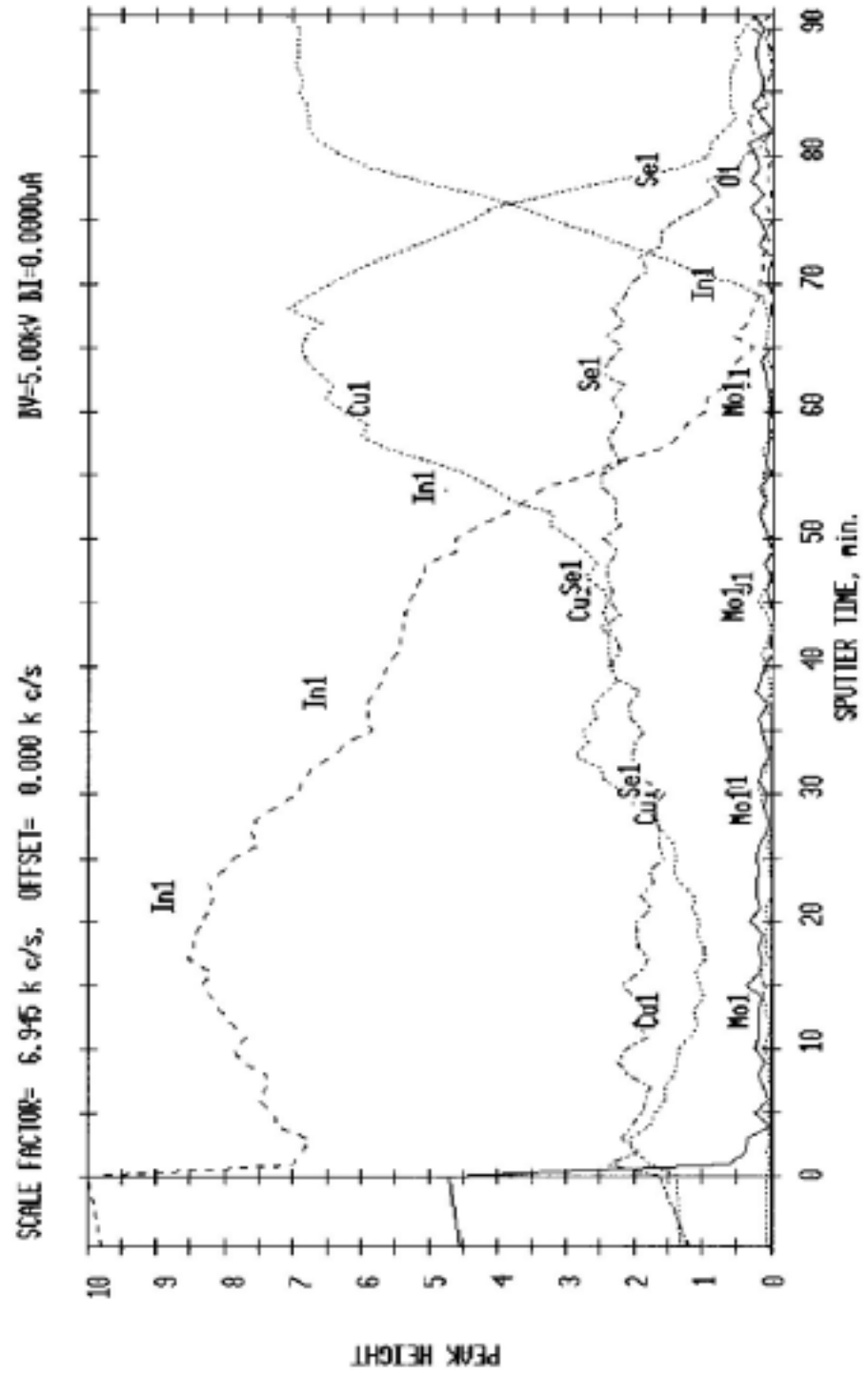

Figure 4.22 AES depth profile of the precursor film.

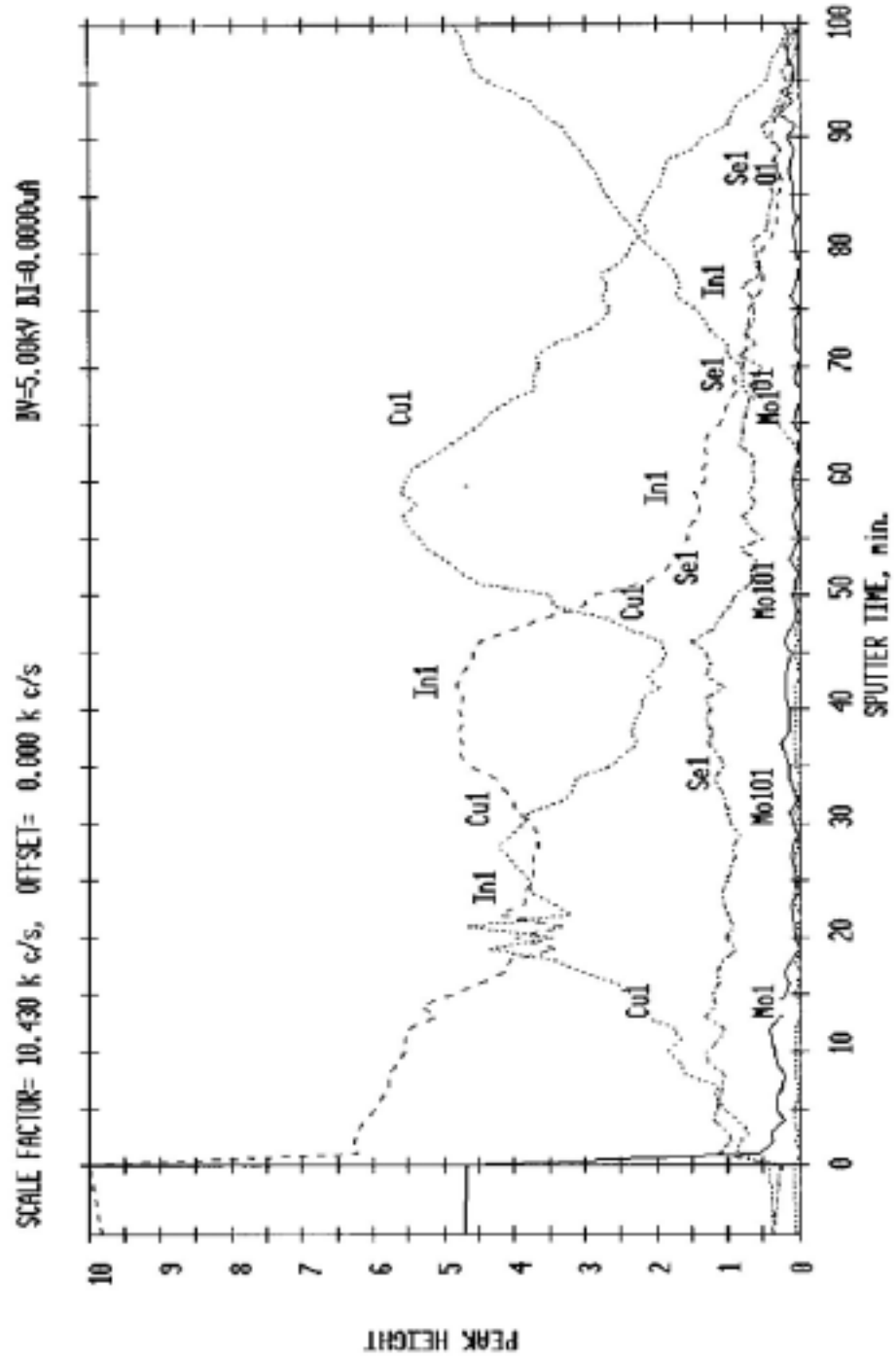

Figure 4.23 AES depth profile of the film after RTP at 290^0C.

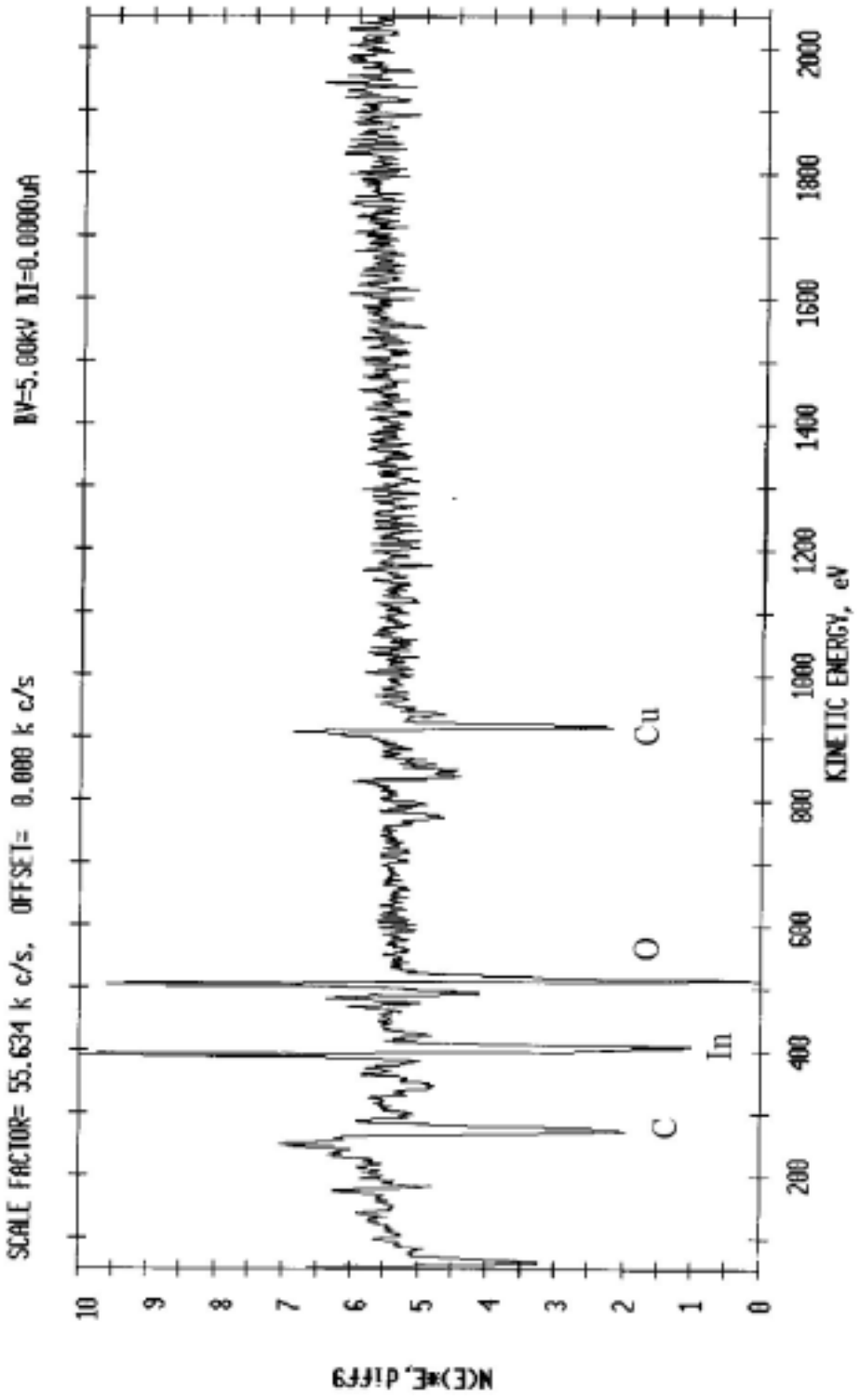

Figure 4.24 AES survey scan of the film surface after RTP at 500^0C.

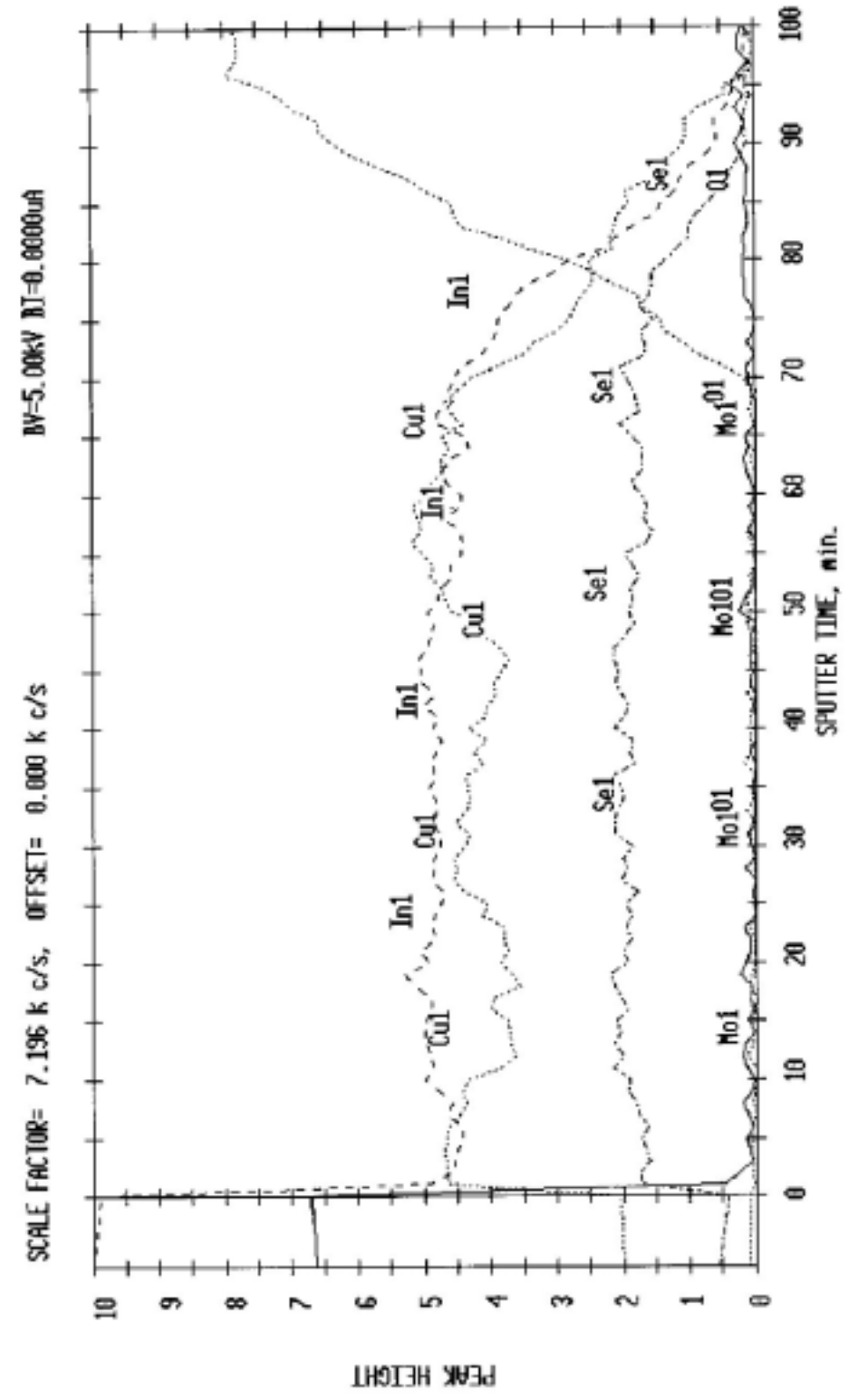

Figure 4.25 AES depth profile of the film after RTP at 500^0C.

4.8 Results and Discussion-Precursor Structure-II

4.8.1 Precursor

A second precursor structure was deposited using the same MEE system. Unlike the first structure, this one contained only 2 binary layers, CuSe/InSe. The composition analysis for the precursor and the reference binary layers is shown in Table 4.4. The WDS analysis is in agreement with the ICP data for the binary samples. For the bi-layer precursor structure, WDS is not able to provide the correct overall composition. The ICP data show the overall precursor structure is slightly Cu-rich. The overall composition should be adjusted by increasing the In-Se binary layer thickness.

The XRD spectra are shown in Figures 4.26 and 4.27 for the In-Se and Cu-Se reference samples respectively. The In-Se layer primarily consists of small crystallites, which showed a broad peak in the XRD spectrum. The Cu-Se layer mainly consists of the α-CuSe phase. The XRD spectrum for the bilayer precursor is given in Figure 4.28. The increased peak height at $2\theta=26.7$ value and the small extra peak $2\theta=44.2$ indicates a small amount of pre-reaction to form $CuInSe_2$ during the deposition process. A schematic drawing for the precursor structure is shown in Figure 4.29. The AES depth profile of the precursor film given in Figure 4.30 is consistent with this structure.

Table 4.4. Composition analysis.

Samples	ICP		
141-1 (Cu-Se reference)	Cu: 51.99	Se: 48.01	
144-1 (In-Se reference)	In: 50.35	Se: 49.65	
InSe/NaF/CuSe bilayer	Cu:26.78	In:23.84	Se:49.37

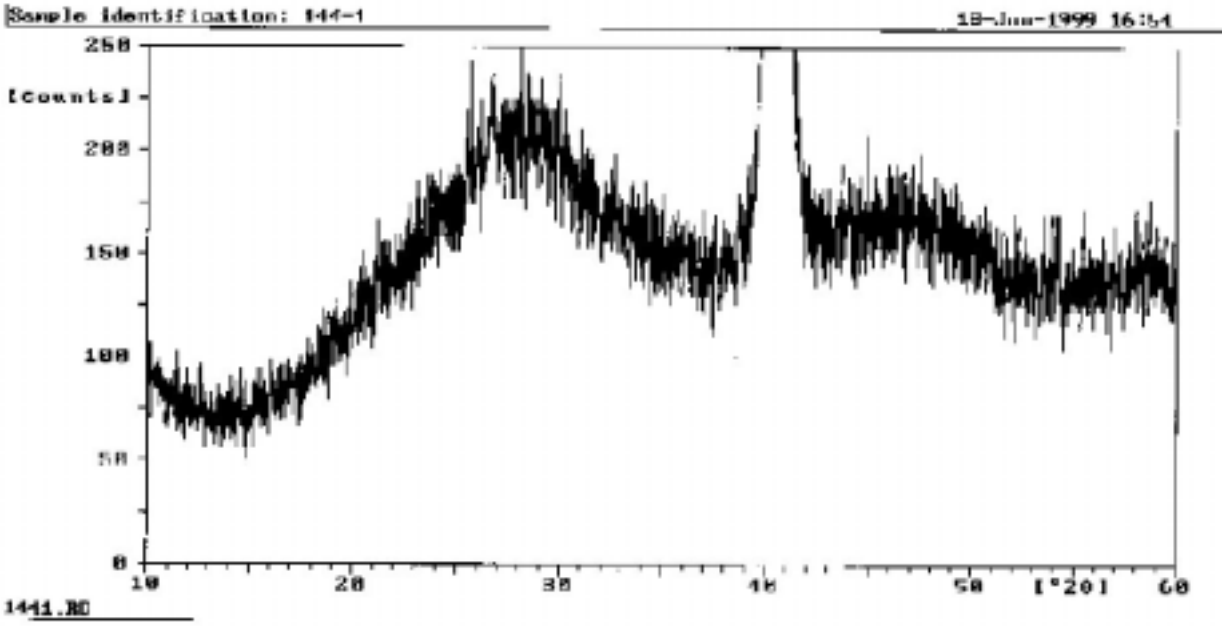

Figure 4.26 XRD spectrum for In-Se binary reference sample.

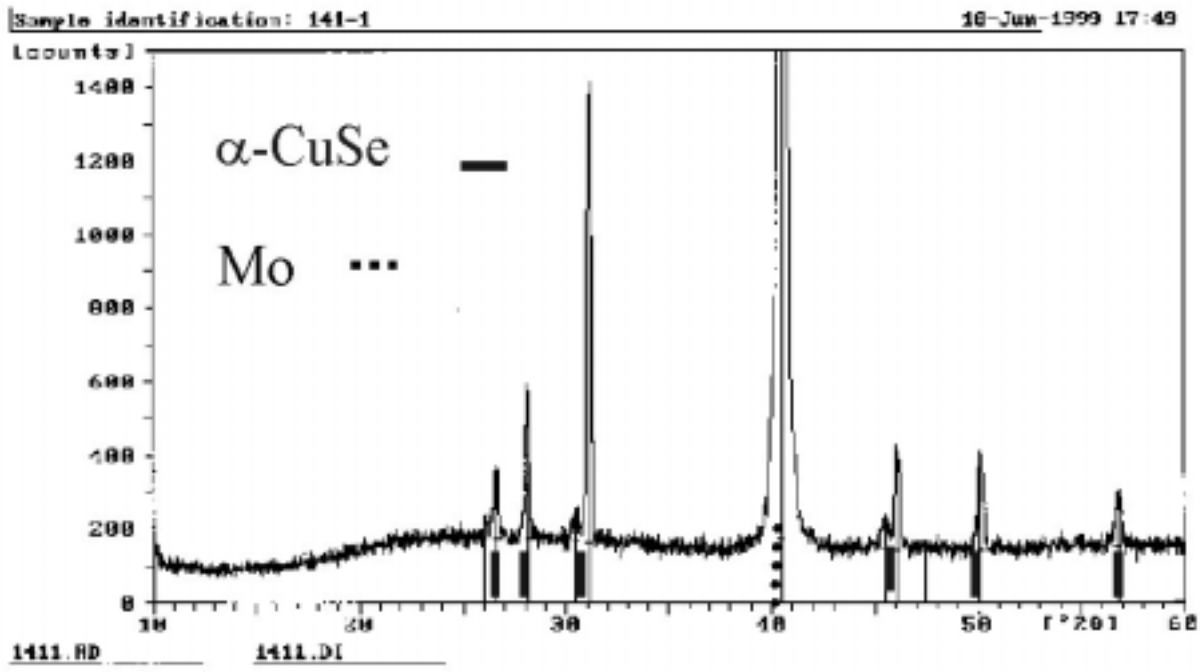

Figure 4.27 XRD spectrum for Cu-Se binary reference sample.

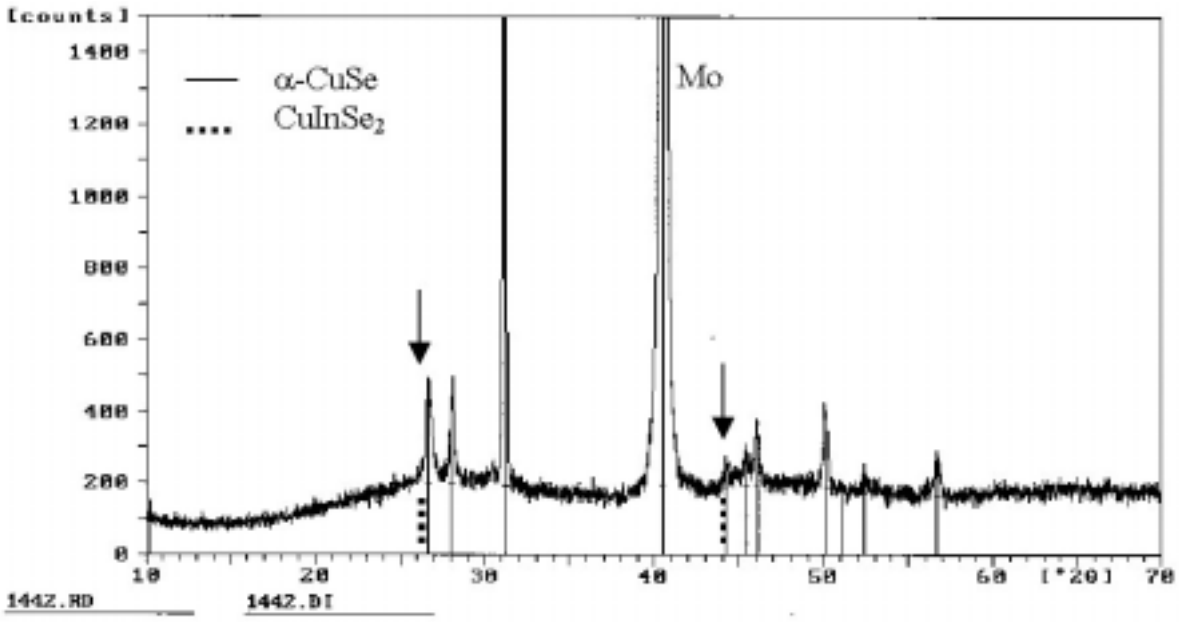

Figure 4.28 XRD spectrum for the bilayer precursor.

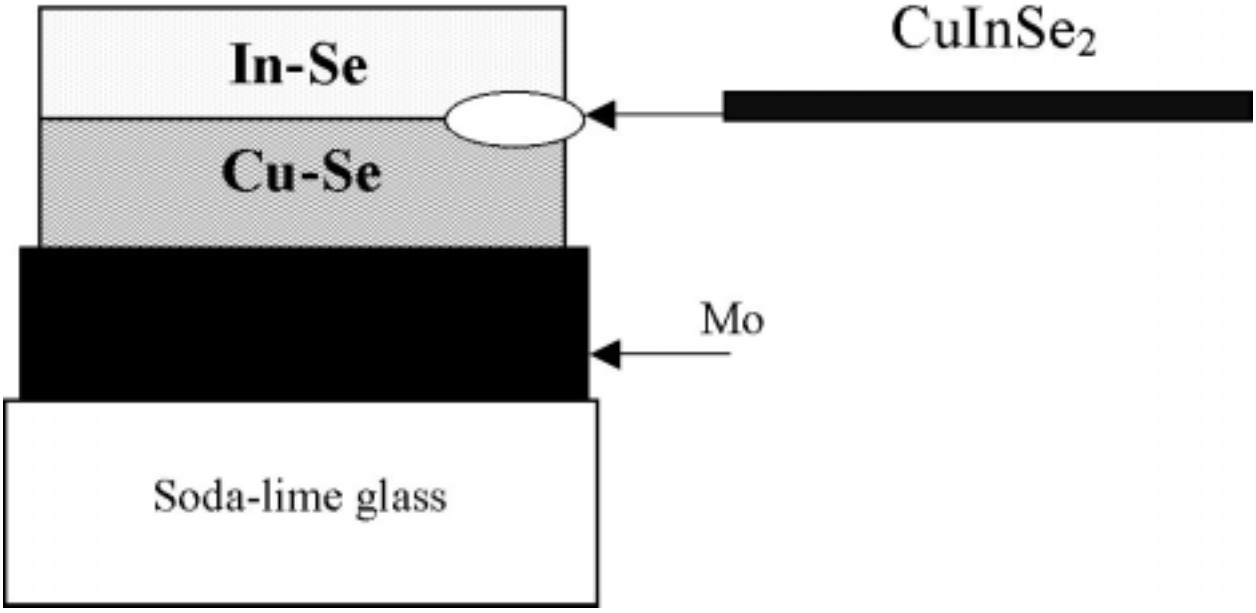

Figure 4.29 Schematic drawing of the bilayer precursor.

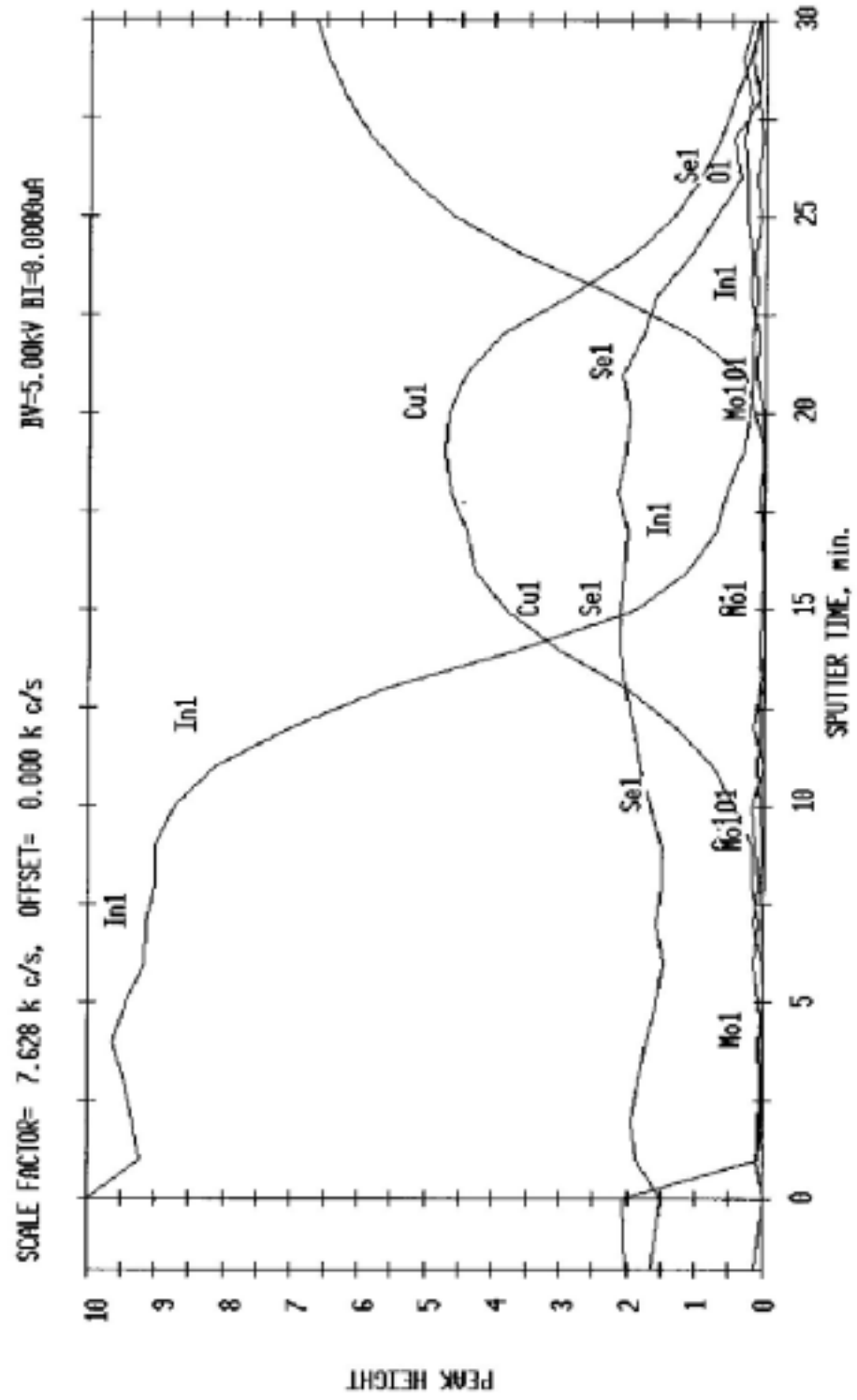

Figure 4.30. AES depth profile of the precursor structure-II.

A set of experiments was performed to understand the influence of ramp rate. Three ramp rates 1, 2, and 10 ^{o}C/s were used in the study. The slow ramp rate resulted in bubble formation and de-lamination of the films as evidenced in the plan-view optical micro-graph shown in Figure 4.31. The mechanism can be easily understood by examining the Cu-Se binary phase diagram given in Figure 4.3. The CuSe phase decomposes to from $Cu_{2-x}Se$ phase and Se_2 vapor during the heating process before forming the CuSe liquid phase. The production of Se_2 vapor causes bubble formation and thus de-lamination of the film.

At higher ramp rate, it is expected that the single liquid phase domain will appear more quickly. Although the Se vapor pressure is high (Figure 4.5) in this domain, the mass transport and reactivity are also higher. On the other hand, at the slower ramp rate most of the α-CuSe phase has time to transform to $Cu_{2-x}Se$ before the temperature reaches the single-phase domain. Thus, the higher ramp rate produced more $CuInSe_2$ with better crystallinity and reduced de-laminating. This is clearly shown in the optical plan-view image of the RTP film processed at a ramp rate of 10 ^{o}C/s (Figure 4.32). The XRD spectra for the 10 ^{o}C/s, and 1 ^{o}C/s cases are shown in Figure 4.33 and 4.34, respectively. The XRD spectra indicate the peaks for the 10 ^{o}C/s ramp rate RTP sample have higher intensity than the corresponding XRD peaks processed at a ramp rate of 1^{o}C/s.

A reference α-CuSe binary film was subjected to RTP treatment at a ramp rate 1 ^{o}C/s for 70 s to further confirm the conclusion of Se loss and $Cu_{2-x}Se$ formation at the lower ramp rate. WDS analysis indicated the film composition changed from Cu:50.33, Se:49.46 to Cu:60.78, Se: 39.22. XRD analysis indicated the film has changed to the $Cu_{2-x}Se$ phase (Figure 4.35). These results clearly show the Se_x vapor evaporated from α-CuSe during the RTP process to produce $Cu_{2-x}Se$. The ICP analysis of the bi-layer samples after RTP treatment is given in Table 4.5. In contrast to the result for the RTP experiment of reference α-CuSe sample, the ICP data indicated the overall film composition did not change much after the bi-layer precursor was subjected to RTP treatment.

These results are encouraging that our precursor structure design is feasible. Putting the InSe layer on top of the CuSe layer to minimize the Se_x evaporation loss appears to be effective. Figure 4.36 shows the AES depth profiles of the film after RTP treatment with a ramp rate of 10^{o}C/s and annealed at 470^{o}C (TC temperature) for 10 s. A uniform composition profile was achieved throughout the film. The high mass-transport and reaction rate is believed to be a result of liquid phase formation in the CuSe layer. Plan-view SEM photographs of the precursor film and the film after RTP annealing (10^{o}C/s) are shown in Figures 4.37a and b, respectively. The SEM images show the formation of crystals with grain size on the order of several microns.

Table 4.5. Composition analysis after RTP treatment

141-1 (Cn-Se reference)	WDS 25kV	Cu: 60.78		Se: 39.22
CuSe/InSe bi-layer after RTP (1^{o} / s)	ICP	Cu:27.60	In:23.54	Se:48.86
CuSe/InSe bi-layer after RTP (10^{o}C / s)	ICP	Cu:25.63	In:24.80	Se:49.57

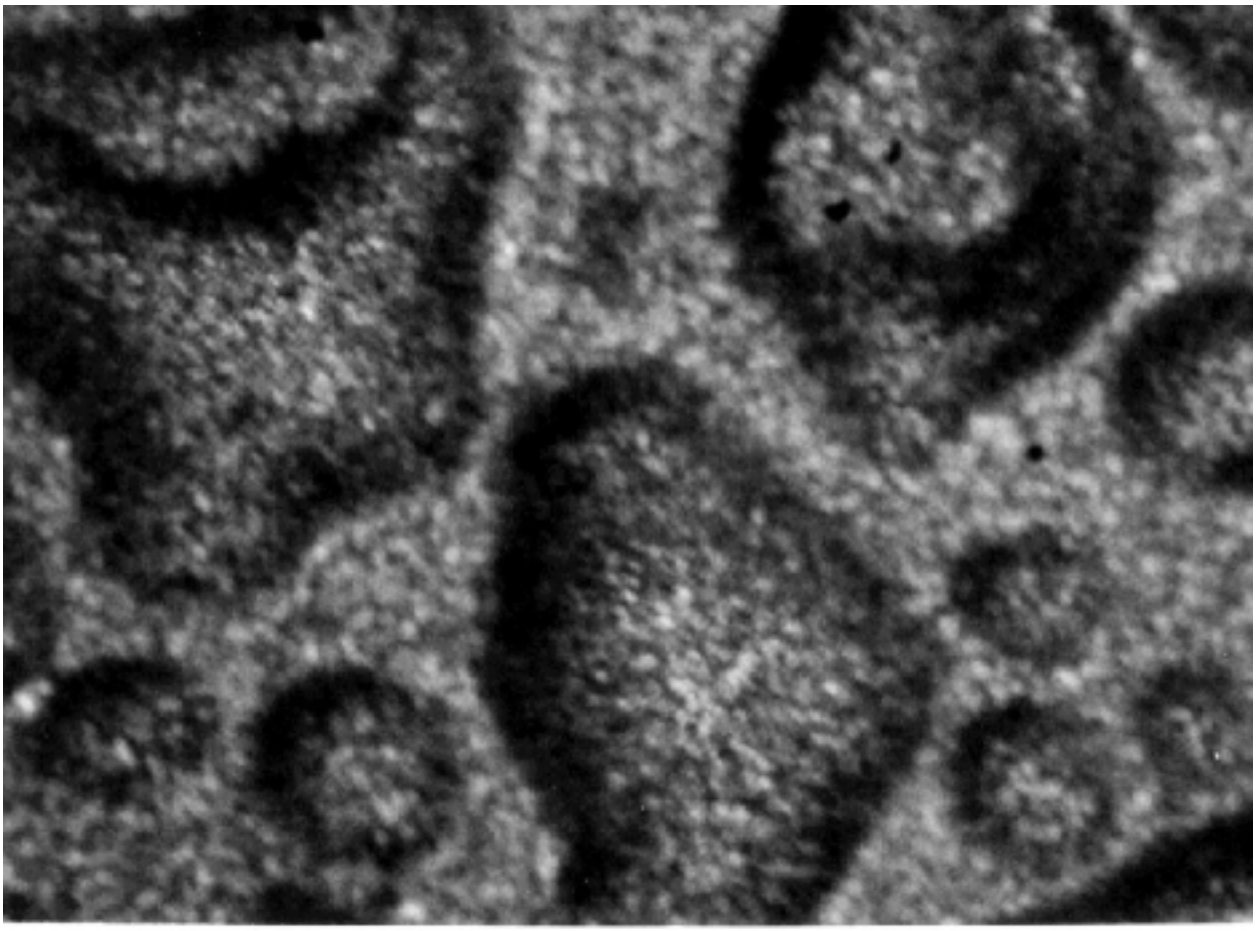

Figure 4.31 Plan-view optical micro-graph at the slow ramp rate (1 ^{o}C/s).

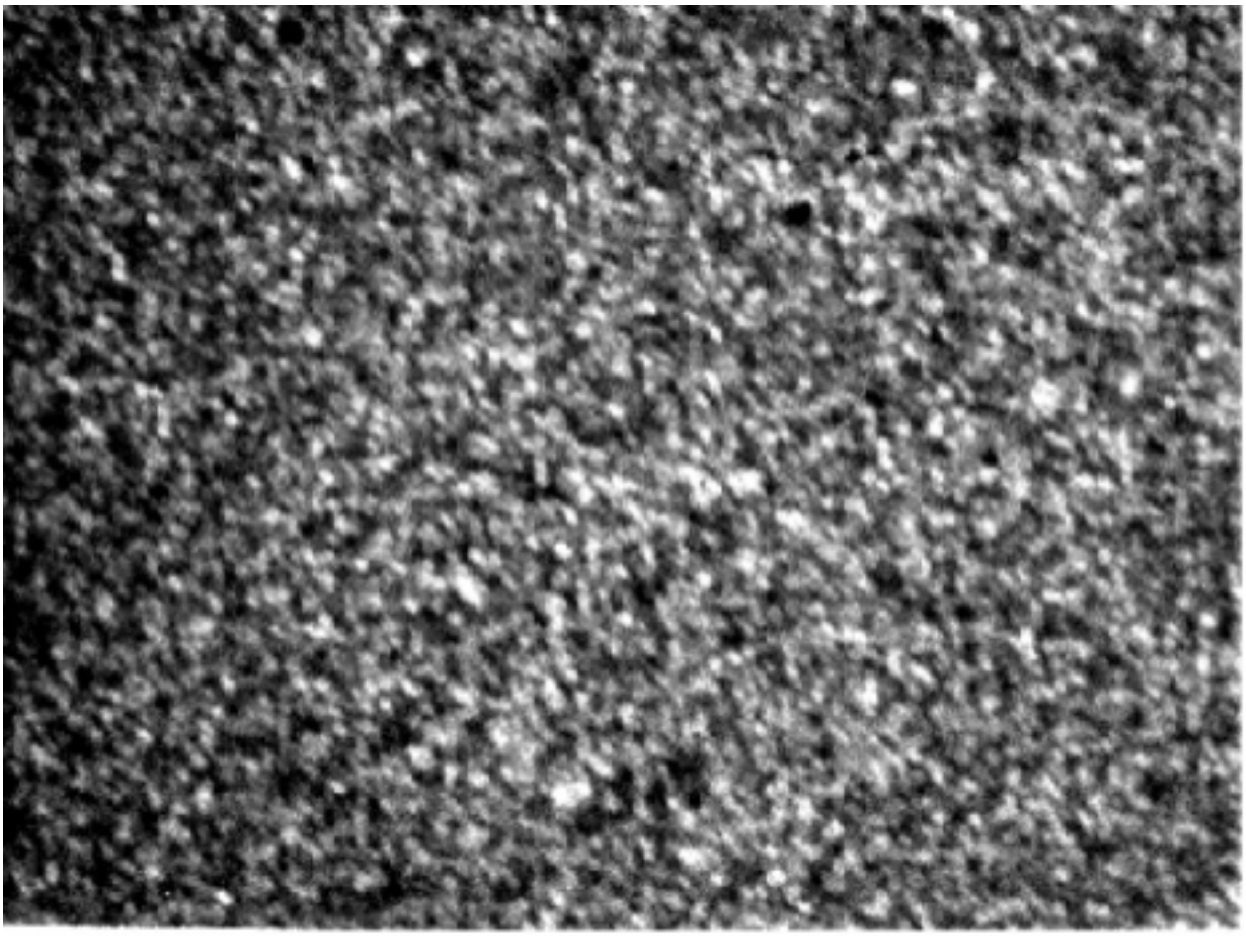

Figure 4.32 Plan-view optical micro-graph at ramp rate (10 ^{o}C/s)

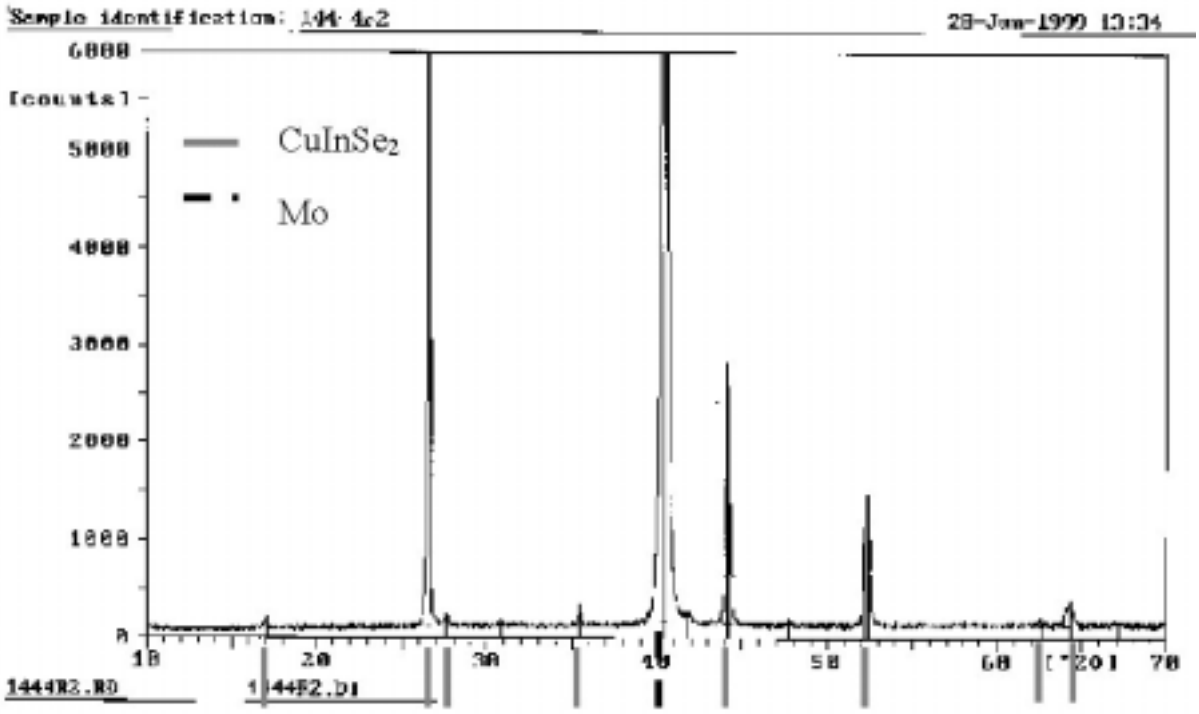

Figure 4.33 XRD spectrum for RTP $CuInSe_2$ film with ramp rate 10 ^{o}C/s.

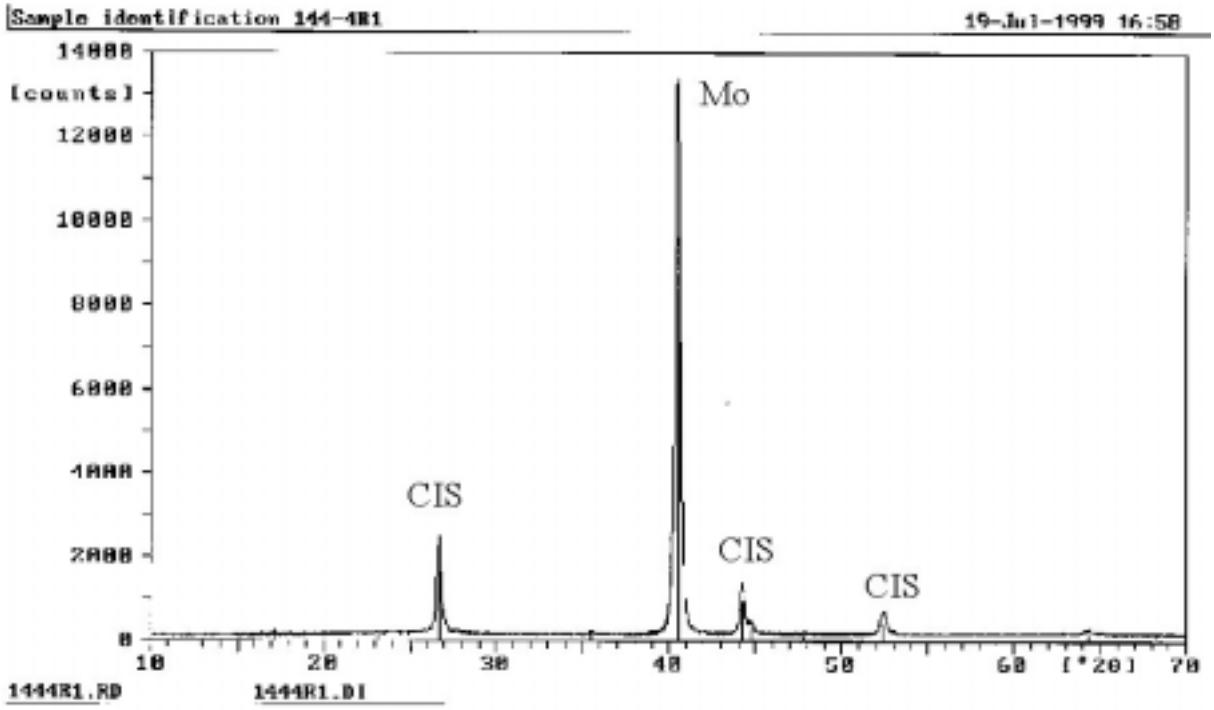

Figure 4.34 XRD spectrum for CuSe/InSe bi-layer film after RTP with ramp rate 1 ^{o}C/s.

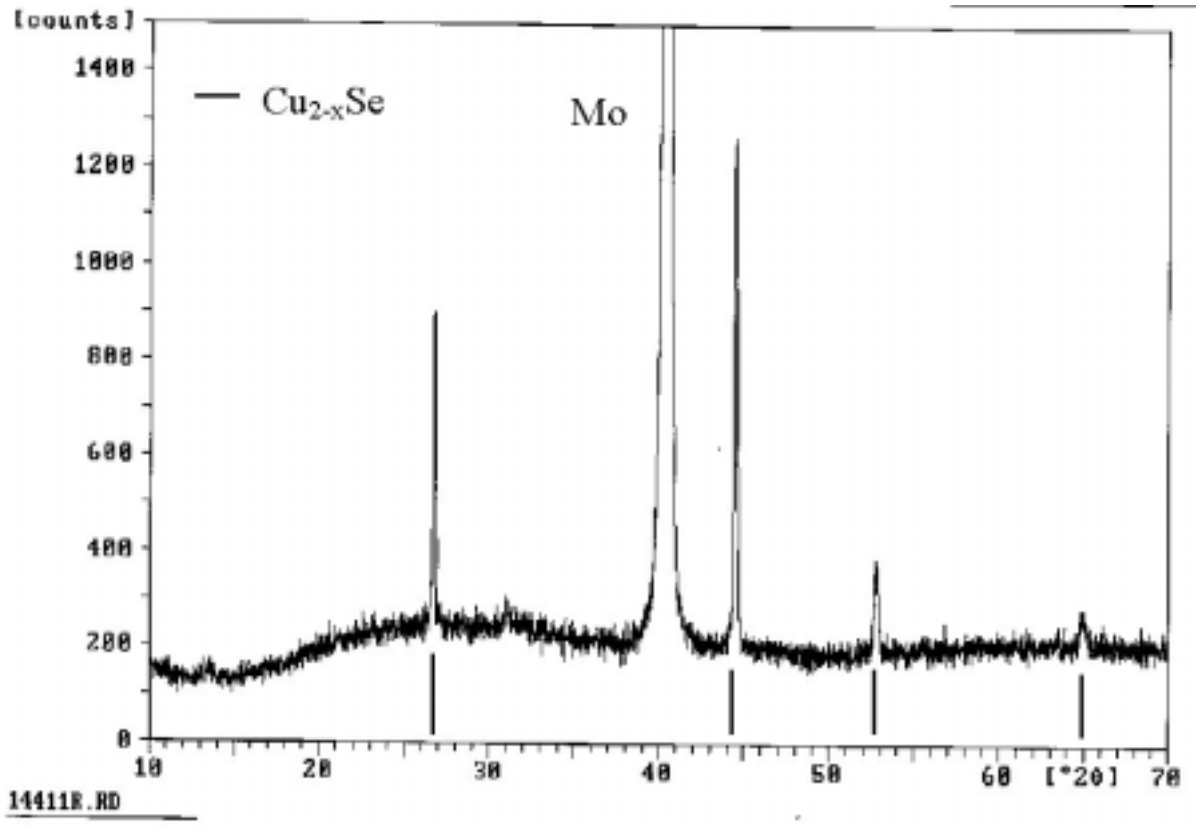

Figure 4.35 XRD spectrum for α-CuSe film after RTP with ramp rate 1 ^{o}C/s.

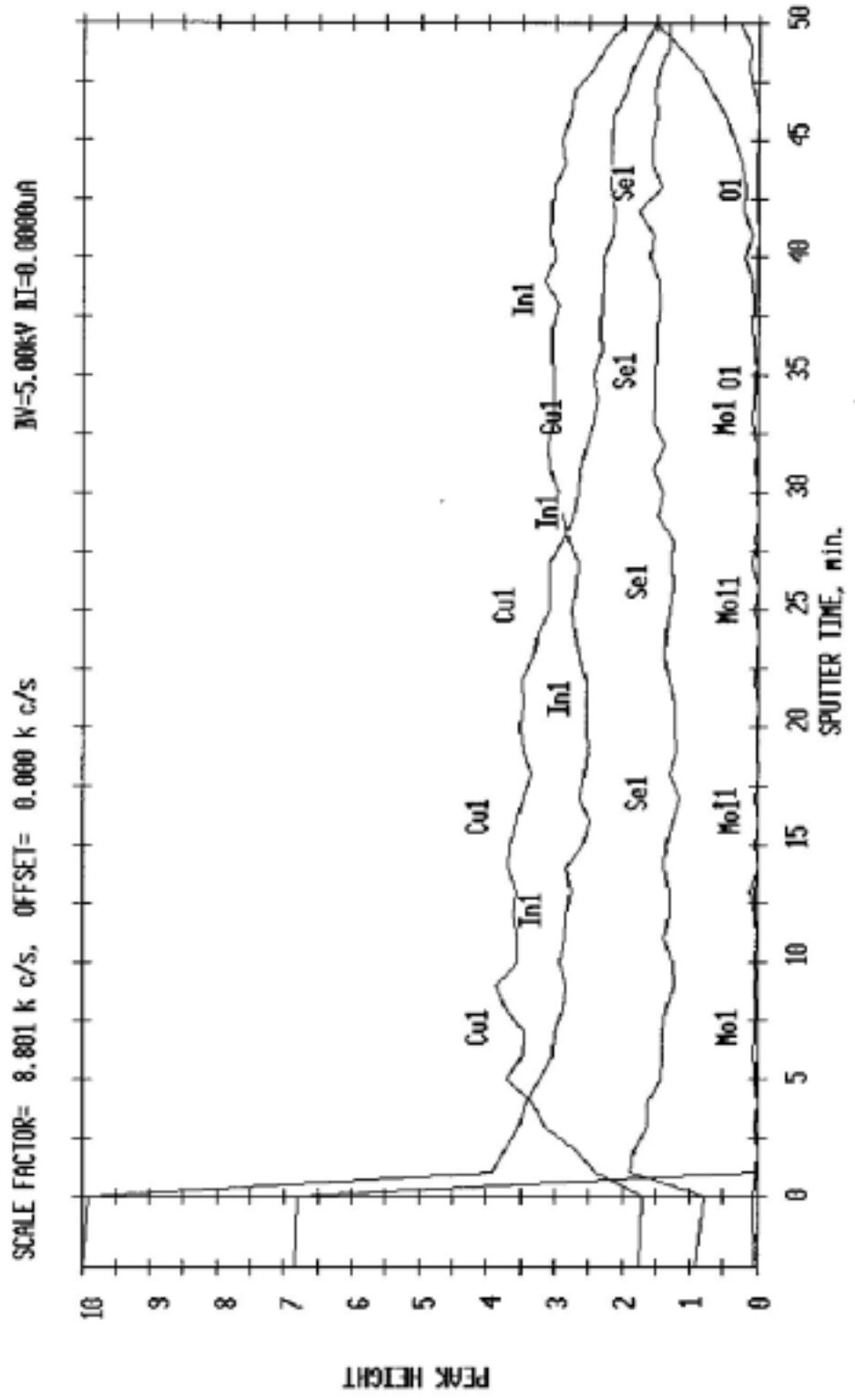

Figure 4.36 AES depth profile of the precursor structure (II)

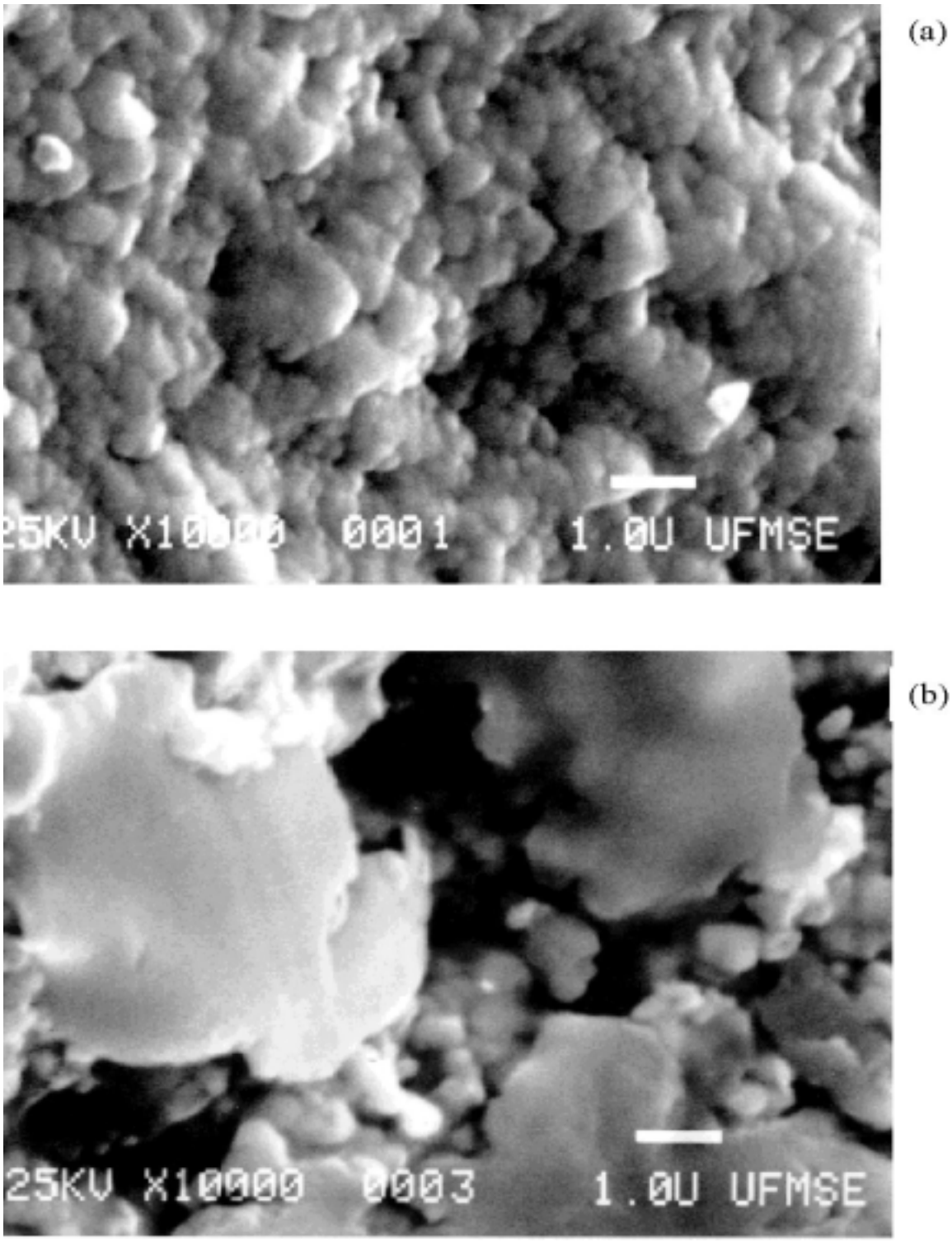

Figure 4.37 The plan-view SEM photographs of the precursor (a) and RTP (b) films.

4.9 Conclusions

Three proposed $CuInSe_2$ layer growth mechanisms are illustrated in Figure 4.38, 4.39, and 4.40. The first growth mechanism involves solid state inter-diffusion between In_4Se_3 and Cu_2Se binary layers (Figure 4.38). The second growth mechanism is a liquid-solid reaction due to the melting of In_4Se_3. Coarse-grained $CuInSe_2$ crystals grow from the liquid-solid mixture. Uniform mass-transport was achieved in a short time (70 s) as shown in the AES depth profile (Figure 4.25). The main phases to appear in the film after 500°C RTP are $CuInSe_2$, Cu_2Se and a small amount of a Cu-In inter-metallic phase. The third mechanism is a liquid-solid reaction due to the melting of α-CuSe in the bottom layer. Coarse-grained single phase $CuInSe_2$ crystals were synthesized from the liquid-solid mixture as suggested in the reaction pathway analysis (section 4.3). Uniform mass-transport was achieved in short time (70 s) as shown in the AES depth profile (Figure 4.36).

In this study an alternative strategy for low temperature precursor fabrication of CIS films has been proposed and tested using ex-situ rapid thermal processing. The experiments showed that large grain CIS could be synthesized through this approach.

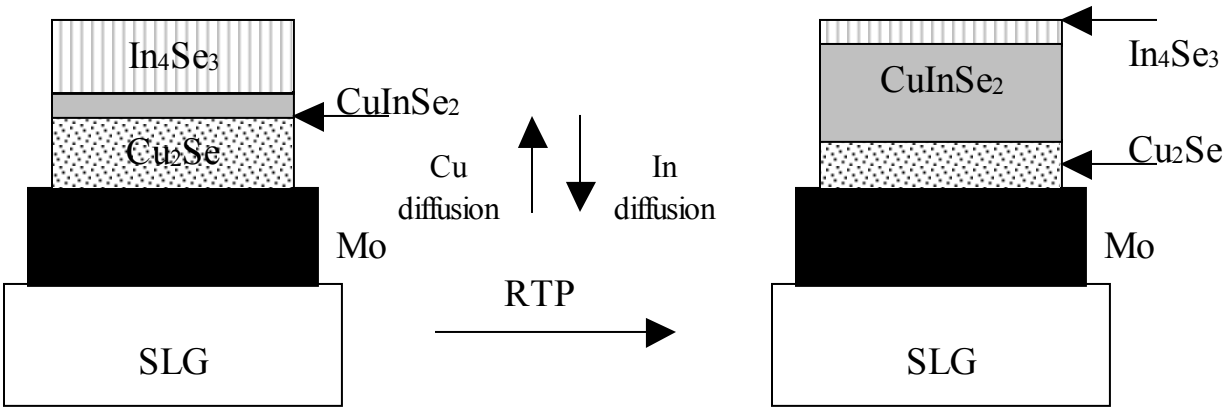

Figure 4.38 Illustration of the solid-state diffusion growth model.

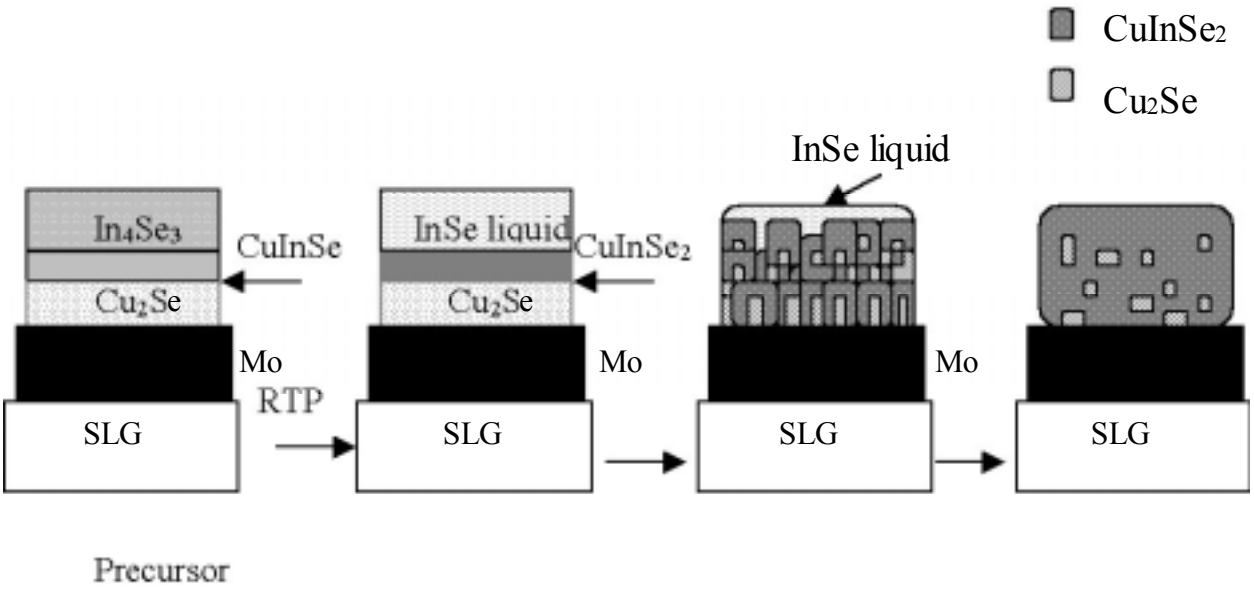

Figure 4.39 Illustration of the liquid assisted growth mechanism for precursor structure-I.

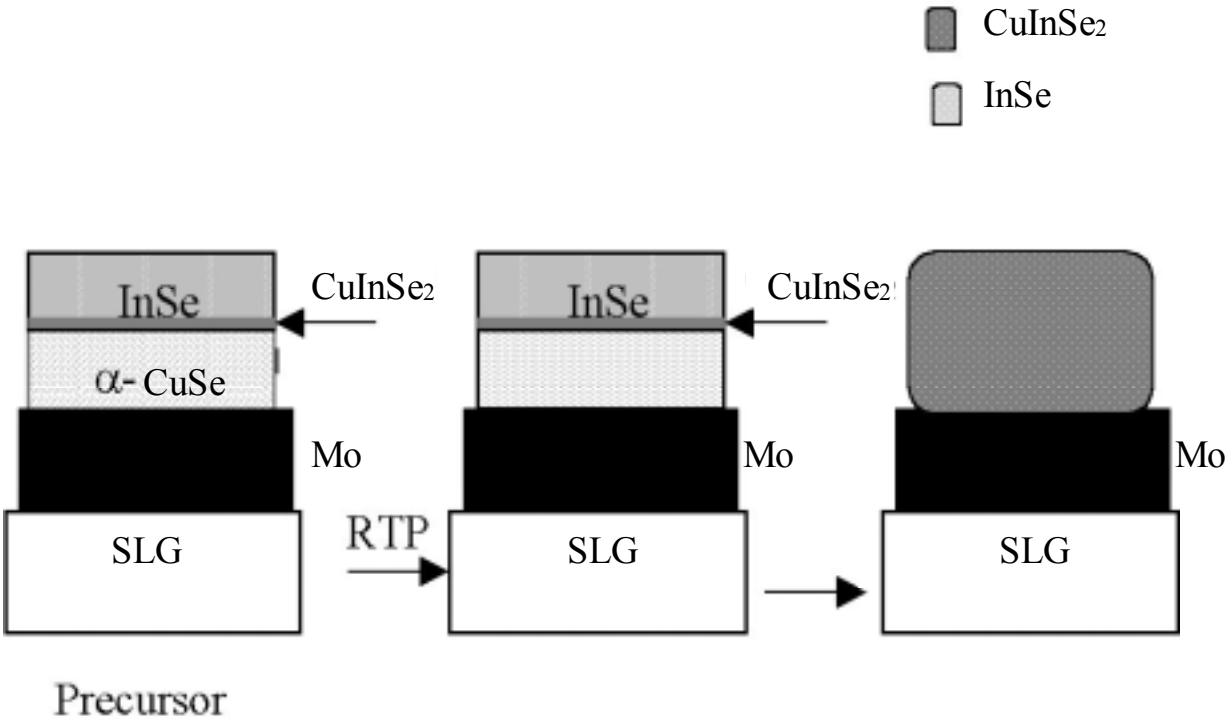

Figure 4.40 Illustration of the liquid assisted growth mechanism for precursor structure-II

4.10 References

[1] H. Oumous, A. Knowles, M.H. Badawi, M.J. Carter and R. Hill, Proc. of the 9th EC Photovoltaic Solar Energy Conference Freiburg: 153, 1989.

[2] Karg F., Probst V., Harms H., Rimmasch J., Riedl W., Kotschy J., Holz J., Treichler R., Eibl O., Kiendl A., 23th IEEE PVSC: 441, 1993.

[3] Baumgartner F.P., Regula M., and Bucher E., Proc. of the 12th EC Photovoltaic Solar Energy Conference, Amsterdam: 637, 1994.

[4] Probst V., Rimmasch J., Riedl W., Stetter W., Holz J., Harms H., Karg F., Schock H.W., Proc. 24th IEEE PV Spec. Conf., Hawaii: 144, 1994.

[5] Probst V., Karg F., Rimmasch J., Riedl W., Stetter W., Harms H., Eibl O., Mat. Res. Soc. Symp. Proc. Vol. 426: 165, 1996.

[6] Mooney G.D., Hermann A.M., Tuttle J.R., Albin D.S., and Noufi R., Appl. Phys. Lett. 58 (23): 2678, 1991.

[7] Gabor A.M., Hermann A.M., Tuttle J.R., Albin D.S., Swartzlander A., and Noufi R., AIP Conference Proceedings 268: 236, 1992.

[8] Albin D.S., Mooney G.D., Duda A., Tuttle J., Matson R. and Noufi R., Solar Cells, 30: 47, 1991.

[9] Matson R.J., Noufi R., Bachman K.J., Cahen D., Appl. Phys. Lett.: 50(3), 158, 1987.

[10] Stanbery B.J., Davydov A., Chang C.-H., Anderson T.J., AIP Conference Proceedings 394: 579, 1997.

[11] Emery J.-Y., Brahim-Ostmane L., Herlemann C. and Chevy A., J. Appl. Phys., 71: 3256, 1992.

[12] C. H. Chang, Doctoral Dissertation, "Processing and Characterization of Copper, Indium Selenide for Photovoltaic Applications," Chemical Engineering Department, University of Florida, Gainesville, FL, 2000.

PART 5

Evolution of Electrical and Microstructural Properties of Sputter-Deposited ZnO:Al Thin Films

Abstract

Degenerately doped thin films of zinc oxide are useful in a variety of applications, including front transparent contacts to Cu(In,Ga)Se_2 thin film solar cells and flat panel displays. To gauge the influence of the interface on the performance of sputter-deposited ZnO:Al transparent electrodes, the structure and electrical properties of the interfacial region has been investigated during nucleation and growth of the thin films. RF magnetron sputter deposited films with thicknesses ranging from ~20 to 1580Å were characterized using Atomic Force Microscopy (AFM), Auger Electron Spectroscopy (AES), Hall measurements, and four point probe. AES spectra of the films with thickness between ~20 and 60Å exhibited clear Si (1619eV) peaks suggesting the thin films were discontinuous islands on the substrate. AFM micrographs indicated a distribution of hillocks on the surface which agrees with AES results, and suggest a Volmer-Webber nucleation and growth mechanism. Hall measurements indicated that the films had electron carrier concentrations on the order of 10^{19} to 10^{20} cm^{-3}, mobilities lower than $10 cm^2/V{\cdot}s$, and resistivities on the order of 10^{-2} to 10^{-3} $\Omega{\cdot}cm$ depending on the film thickness. The possible impact of these results on solar cell performance is discussed.

Section Contents

5.1 Brief Overview

5.1.1 Participants

Faculty Adviser: Professor Paul Holloway

Research Assistants: Loren W. Rieth

5.1.2 Objectives

The objective of this research program is to develop Transparent Conductive Electrode (TCE) and molybdenum underlayer sputter deposition processes for the use in fabrication of CIS photovoltaic cells.

5.2 Introduction

Zinc oxide thin films are used in applications including Transparent Conducting Electrodes (TCEs)[1], Surface Acoustic Wave (SAW) devices[2], and chemical sensors[3]. Their application as the front TCE for thin film copper indium diselenide (CIS) solar cells is the focus of this research. Figure 1 presents a schematic of a typical CIS solar cell. ZnO is suitable for use as a large area TCE because of its large bandgap (Eg=3.2eV)[4], ease of heavy n-type doping by a variety of dopants, high transparency in the visible spectrum, low cost, high availability, and compatibility with large area deposition technology.

Figure 5.1. Crossectional schematic of a CIS solar cell structure.

The objective of this research is to improve the performance of CIS thin film solar cells by investigation and improvement of the TCE. Optimization is typically pursued by improvement of electrical and optical properties with goals of high transparency (>90%) and low resistivity (10^{-4} Ω·cm). Drude's theory for free electrons indicates that carrier concentration influences optical absorption through the plasma resonance frequency (ω_p) defined in Equation 5.1 [5], where n is the number of electrons, e is the electrons charge, m^* is electron effective mass, and ε_0 and ε_∞ are the dc and high frequency dielectric constants, respectively.

$$\omega_p = \left(\frac{ne^2}{\varepsilon_0 \varepsilon_\infty m^*} \right)^{\frac{1}{2}} \tag{5.1}$$

Light with a frequency lower than the plasma resonance frequency is strongly absorbed. This fundamentally restricts the maximum carrier concentration to less than ~10^{21}/cm^3 due to free carrier absorption of light used in photovoltaic process. Based on the Equation 5.2[5], where σ is the conductivity, n is the carrier concentration, μ is the mobility, and e is the electrons charge,

$$\sigma = ne\mu \tag{5.2}$$

the electrical properties can be improved by increasing the carrier mobility and/or carrier concentration. Mobility can also be increased without significant losses in optical transparency. It is influenced by carrier scattering events, of which scattering events involving microstructural defects are the primary avenue available for improvement. The carrier concentration is related to both optical absorption and mobility, and therefore it must be optimized in regards to these values. Resistivity of the TCE film influences the solar cell's Fill Factor (FF) by its control of the series resistance (R_s) as can be seen in Equation 3[6], where the variable are C (constant), I_{sc} (short circuit current), V_{oc} (open circuit voltage), R_{sh} (shunt resistance), V_m (maximum power voltage), and F_2 (field strength).

$$FF = FF_0 - CI_{sc}\frac{R_s}{V_{oc}} - \frac{V_m}{V_{oc}}\frac{V_m}{I_{sc}R_{sh}} - \frac{V_m}{V_{oc}} S_I \frac{\left[1 - F_2(V_m)/F_2(0)\right]}{S_I + \mu_2 F_2(V_m)} \tag{5.3}$$

Increasing R_s has a strong negative influence on FF. The term S_1 is the interfacial recombination velocity at the interface between the solar cell and the TCE. A lower interfacial recombination velocity will improve the fill factor, therefore a high quality interface is desired. Literature and experimentation indicates that typical sputtering processes yield a highly defective Near Substrate Interfacial Region (NSIR), therefore improvement of this region potentially improves the solar cells fill factor.

Our hypothesis is that the NSIR is a significant negative influence on the TCE performance for CIS solar cells. Films of different thickness can be used to evaluate the influence of the NSIR region. These data will be used to gauge the current state of this region, and to develop strategies for improvement.

5.3 Experimental Procedure

The films used in this investigation were deposited by RF magnetron from a 2" diameter $ZnO:Al_2O_3$ (98wt%:2wt%) sputtering target onto 1"x1" soda-lime glass substrates cleaned with Alkonox. The vacuum system utilizes a cryotrapped oil diffusion pump backed by an oil sealed rotary vane pump to achieve a base pressure of $8x10^{-7}$ Torr measured on an ionization gauge. The sputtering gas was ultrahigh purity Ar supplied to the system through a mass flow controller. The diffusion pump was throttled using a variable orifice yielding controlled pressures in the mTorr range as read by a capacitance manometer. The sputtering process parameters were a pressure of 5 mTorr, RF power of 100 W, a target to substrate distance of 5 cm, an Ar flow rate of 7 sccm, and a substrate temperature of 150°C. The system is a "sputter up" geometry with the substrate suspended off the target normal to reduce negative ion bombardment by oxygen ions[7,8]. Deposition time was used to control the film thickness. The sputtering rate was determined by masking the substrate, sputter depositing for 30 minutes, and measuring the step height with a stylus profilometer. The sputtering process included a 5 minute presputter with a closed shutter, allowing the assumption of constant rate for very brief processes.

The deposited films were characterized by Atomic Force Microscopy (AFM), Auger Electron Spectroscopy (AES), Hall measurements, and four point probe. A Digital Instruments Nanoscope III AFM in the tapping mode was used to investigate the surface morphology. AES was used to measure surface composition, especially the concentration of silicon (1619eV) which is an indication the film continuity. A sputter depth profile was then recorded to check the film thickness and composition through the thickness. AES spectra taken after the depth profile were used to check the composition of the glass, and to calibrate the Si peak heights for estimation of the surface coverage. Microstructural information such as surface morphology, surface coverage, and grain size were related to film thickness to investigate their evolution. Hall measurements where taken using the van der Pauw method with thermally evaporated Al dot contacts forming a 4mm square. A 6700 gauss normal incidence magnetic field was used. A computer system controls the apparatus and reduces the data for values of mobility, carrier concentration, and resistivity. Four point probe (FPP) data taken at a constant current of 1mA were used to measure resistivity to corroborate Hall data. The electrical measurements were correlated with thickness. Sample ZIP14 was used only for rate calibration and electrical measurements.

5.4 Results

Table 5.1 contains the sample IDs, estimated thicknesses, length of the sputter deposition, grain size estimated from AFM micrographs, RMS roughness, and surface coverage estimated by the Si Auger peak height. More detailed AES and AFM data will be presented for the samples highlighted in gray. An AFM micrograph of the glass substrate appears in Figure 5.2. The height scale for this image is 4nm (40Å), smaller than the 10nm (100Å) scale used for the remaining AFM images. In all cases a 0.5µm by 0.5µm area was scanned. For the micrograph of the substrate shown in Figure 5.2, the individual line scans indicate an extremely flat surface, which is consistent with expectations for float glass. For the micrograph of ZIP16 presented in Figure 5.3, the larger structures are approximately an order of magnitude taller than the average film thickness, with smaller features in between the larger features that are approximate the

height as the average film thickness. AFM and AES results from ZIP16 are typical for noncontinuous films and are presented in Figures 5.3(a-d). The films ZIP16 through ZIP19 were electrically discontinuous, therefore their resistivity was too high to measure.

An AFM micrograph and an as-deposited AES spectrum from ZIP 18 are presented in Figures 5.4 (a-b). The AES spectrum in Figure 5.4b does not contain a Si peak, indicating that the film is physically continuous. The very high resistance for this film indicates that it is not electrically continuous. AFM and AES results from ZIP21 are representative of continuous films, and are presented in Figures 5.5 (a-b). Significant evolution of the grain size can be seen in comparison with thinner films. Both AES and electrical measurements indicate the film is continuous.

Table 5.1. Sample identification, deposition time, calculated thickness, estimated grain size, RMS roughness, and percentage surface covered by the deposited ZnO:Al film

Sample ID	Dep. Time (seconds)	Thickness (Å)	Grain Size (Å)	RMS Roughness (Å)	Surface Coverage (%)
ZIP14	900	1580			
ZIP16	10	18	~100	08.2	60%
ZIP17	20	36	~100	07.19	70%
ZIP18	60	105	~200	03.33	100%
ZIP19	30	58	~150	02.16	80%
ZIP20	180	315	~250	04.99	100%
ZIP21	300	525	~500	08.86	100%
ZIP22	420	735	~500	09.96	100%

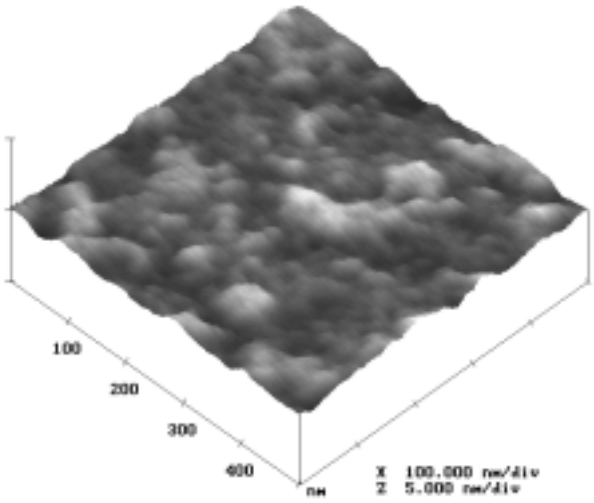

Figure 5.2. AFM micrograph of the bare glass substrate.

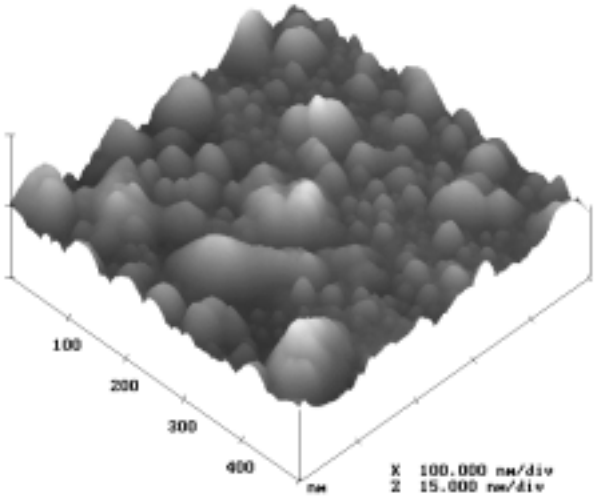

(a)

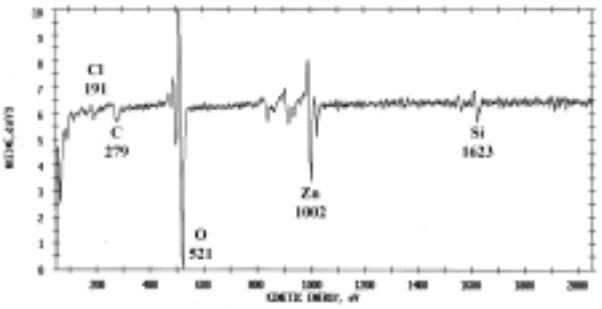

(b)

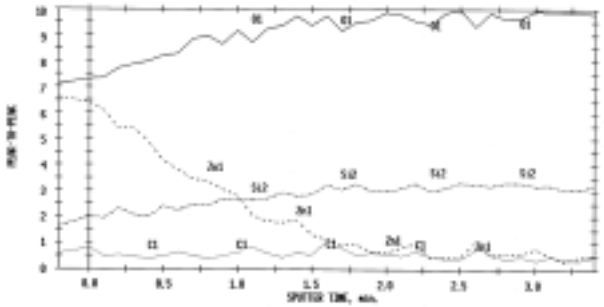

(c)

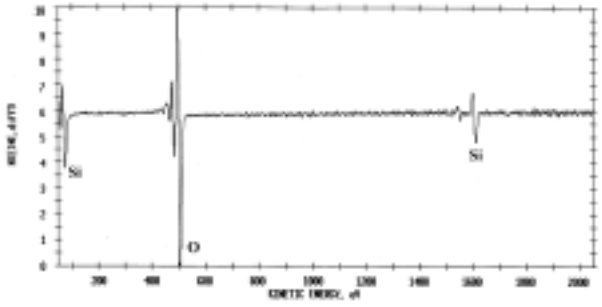

(d)

Figures 5.3 (a-d). AFM micrograph (a), AES spectrum from as deposited sample (b), AES depth profile (c), and AES spectrum from depth profiled sample (d) for sample ZIP 16 at 18Å in thickness.

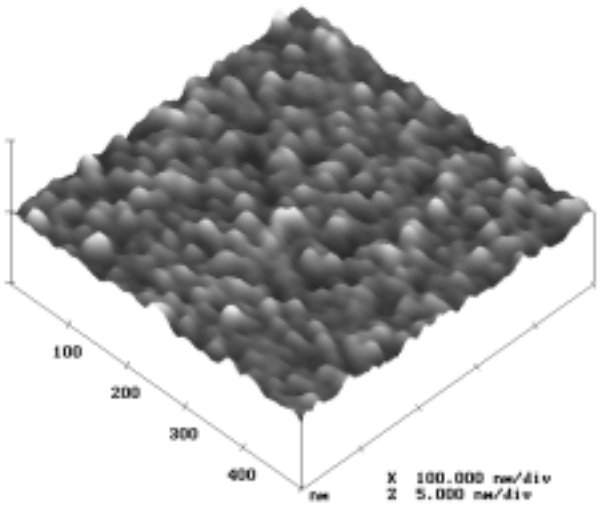

(a)

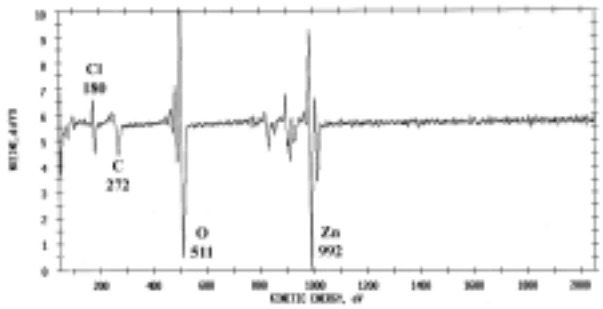

(b)

Figures 5.4 (a-b). AFM micrograph (a) and AES survey spectra (b) from as deposited sample ZIP 18 at 105Å in thickness

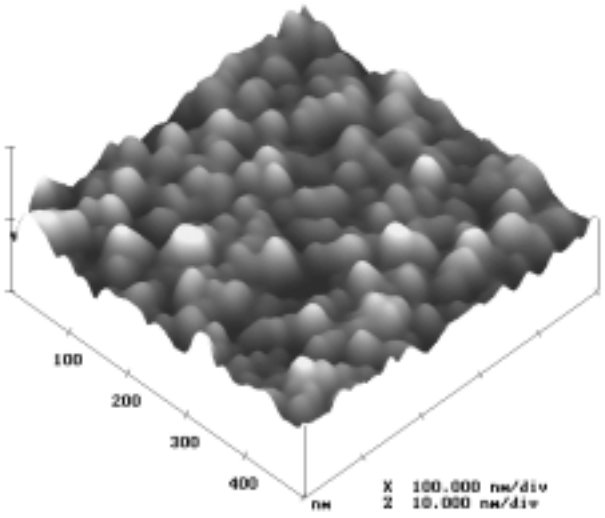

(a)

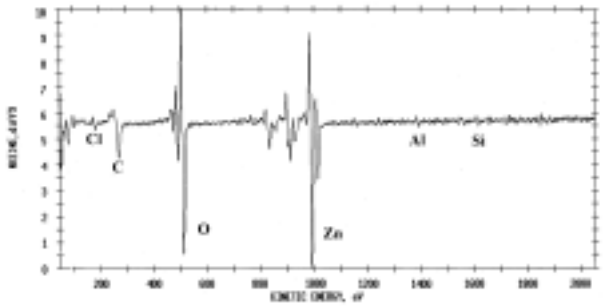

(b)

Figures 5.5 (a-b). AFM micrograph (a) and AES survey spectrum (b) from as deposited sample 21 at 735Å

Results from Hall measurements are presented in Figures 5.6 (a-c). Film resistivities measured by FPP are consistent with Hall measurements. A factor of five variation in the resistivity measured by the FPP occurred for different spots on the surface. This variation may be due to nonuniform fluxes of ZnO, negative oxygen ions, and reflected Ar atoms during sputter deposition. Previous work has indicated that negative ion bombardment significantly degrades

the electrical properties of these films, and therefore is believed to be the source of the variation.

5.5 Discussion

Based on AFM and Auger data, sputter deposited ZnO:Al films on glass substrates follow Volmer-Webber nucleation and growth. The detection of Si, Zn, and O in ZIP16, 17, and 19 indicate that a ZnO film is being deposited, but the glass surface is not completely covered. Changes in surface morphology after deposition to a roughly hemispherical cap nucleus morphology also indicates island growth. The off scale electrical resistivity of ZIP16-19 also indicates noncontinuous films. For ZIP18, at 100Å, no Si AES signal was detected indicating the film is continuous, whereas the high resistivity indicates the film is electrically discontinuous. This indicates ZIP18 is near the transition to a completely continuous film. Island growth with initial nuclei sizes on the order of 100Å yields a highly defective interfacial region. Improvement of the microstructure at the interface would be beneficial to current transport, as can be seen by the improved electrical properties with thicker films. The improved electrical properties could, as seen in Equation 5.3, improve the cell fill factor. As the film thickness increased, the grain size increased to approximately 500Å. In general the films RMS roughness was near 10Å, indicating all films were very smooth.

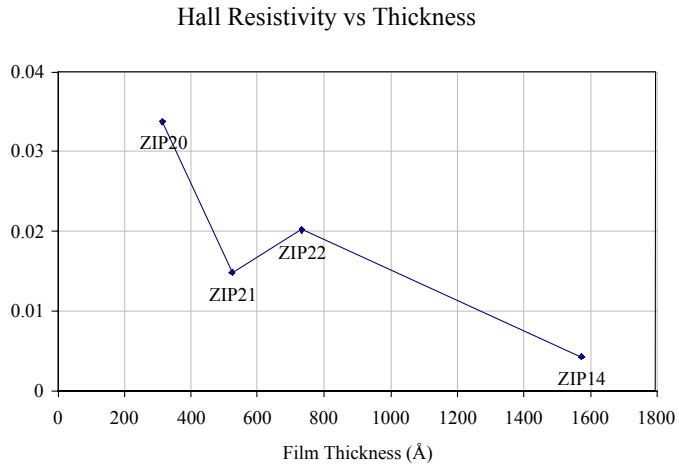

(a)

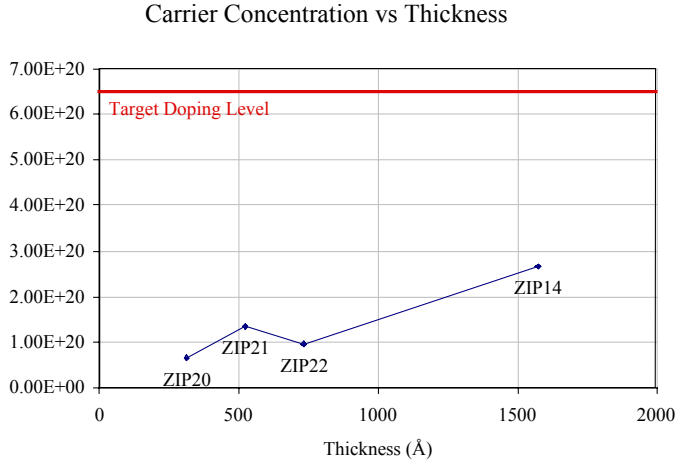

(b)

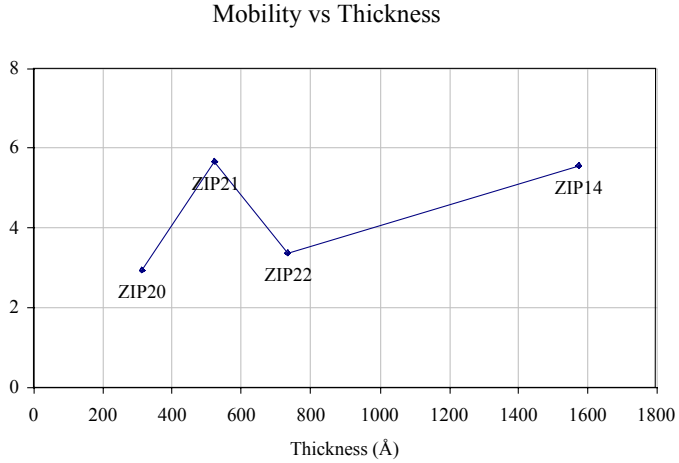

(c)

Figures 5.6 (a-c). Film resistivity (a), carrier concentration (b), and Hall mobility (c) derived by Hall measurements and plotted as a function of thickness (Å).

The microstructural properties of ZnO films evolve as a function of thickness. The grain size ranges from less than 100Å for the thinnest film (20Å) to approximately 500Å for the 735Å thick film. The increase in grain size is consistent with the competitive grain growth model, which specifies that certain crystal planes grow faster, and grains with this facet normal to the

growth surface grow more quickly effectively blocking out smaller grains as the film thickness increases[9]. Previous powder X-ray diffraction results from similar films indicate ZnO films have the Wurtzite crystal structure with a strong (002) basal texture. This suggests nuclei with (002) planes parallel to the surface grow faster and dominate the film. In general substrate heating could help improve microstructure by suppressing nucleation, and enhancing growth of the basal oriented nuclei. This should improve the microstructure in the NSIR. Unfortunately substrate temperatures above 200°C for the ZnO deposition degrade performance of the solar cell device. Sputter deposition parameters can also have a large effect on nucleation and growth, therefore optimization of these parameters could yield microstructural improvements in the NSIR.

The electrical properties also change with film thickness. The resistivity of the films decreases due to increased carrier concentration with increasing thickness. Changes in carrier concentration can result from changes in dopant compensation, carrier trapping, poor dopant activation, changes in intrinsic doping, and interfacial depletion effects. Intrinsic n-type doping is popularly attributed to zinc interstitials and oxygen vacancies. Determination of whether intrinsic doping is significant and which defect is responsible for the lower carrier concentrations in the thinner films requires additional experimentation. The mobility showed no clear changes with film thickness. The factor of two difference in the mobility values could depend on the section of substrate from which the samples were taken, error from the Hall measurement system, or changes in the microstructure. This effect could be related to the factor of five variation in measured resistivity across the sample. Hall data as a function of position on the substrate where not collected, so it is unknown whether the carrier concentration, mobility, or film thickness gradient caused the effect. The best electrical properties occurred on the region of the substrate farthest away from the sputtering axis.

5.6 Conclusions

Consistently prepared thin films of ZnO:Al with varying thickness were prepared by RF magnetron sputter deposition. Microstructural characterization by AFM and AES indicate the films form by island (Volmer-Webber) nucleation and growth, and become a physically continuous film at approximately 100Å. AFM micrographs show an increase in grain size from approximately 100 to 500Å in diameter with increasing film thickness. Hall and four point probe measurements indicate the films become electrically continuous at a thickness between 100 and 300Å. The resistivity decreased from initial values of 3.4×10^{-2} Ω-cm to 4.3×10^{-3} Ω-cm with increasing film thickness. The mobility showed no clear trend of change with film thickness, and had an average value of 4.4 $cm^2/V \cdot s$. The carrier concentration was found to increase from 6.5×10^{19} cm^{-3} to 2.7×10^{20} cm^{-3} for increasing film thickness, indicating it is the source of the changes in resistivity. Resistivities measured by four point probe were consistent with values measured by Hall measurements. FPP also indicates that the electrical properties have a gradient across the substrate, with the better values occurring at the edge farthest from the sputtering source. It is proposed that the changes in the carrier concentration result from the evolution of the microstructure. As the film thickness increases, the density of grain boundaries, and possible point and line defects, are decreasing. These defects are most likely either acting as carrier traps or preventing the ionization of the dopant atoms.

5.7 References

[1] K. Chopra, S. Major, and D. Pandya, "Transparent Conductors-A Status Review", *Thin Solid Films* vol. 102, pp. 1-46 (1983)

[2] S. J. Chang, Chang, Y. K. Su, and Y. P. Shei, "High Quality ZnO thin films on InP substrates prepared by radio frequency magnetron sputtering. II. Surface acoustic wave device fabrication", *Journal of Vacuum Science and Technology A*, Vol. 13, No. 2, pp. 385-8 (1995)

[3] P. Mitra, A. P. Chatterjee, and H. S. Maiti, "ZnO thin film sensor", *Materials Letters*, Vol. 35, pp. 33-38 (1998)

[4] S. Sze, *Physics of Semiconductor Devices*, John Wiley & Sons, NY 1981

[5] R. Hummel, *Electronic Properties of Materials*, Springer-Verlag, NY, 1993

[6] A. Rothwarf and A. M. Barnett, "Design Analysis of the Thin Film CdS-Cu_2S Solar Cell", *IEEE Transactions on Electron Devices*, Vol. 24, No. 4, pp. 381-387 (1977)

[7] S. Zafar, C. Ferekides, D. Morel, "Optimization and Characterization of Reactively Sputtered ZnO", *Journal of Vacuum Science and Technology A*, Vol. 13, No. 4, pp. 2177-2182 (1995)

[8] K. Tominaga, K. Kuroda, and O. Tada, "Radiation Effect Due to Energetic Oxygen Atoms on Conductive Al-doped ZnO Films", *Japanese Journal of Applied Physics*, Vol. 27, No. 7, pp. 1176-1180 (1988)

[9] K. Chopra, *Thin Film Phenomena*, Robert E. Krieger Publishing Co., NY 1979

PART 6

Assessment of the Cu_2Se-Ga_2Se_3 Pseudobinary System

Abstract

An assessment of the thermodynamics of the pseudobinary Cu_2Se-Ga_2Se_3 was done making use of available experimental data, as well as use of an empirical method for estimating interactions in semiconductor solid solutions. Four phases were considered in this work, namely a liquid, a Cu_2Se-rich solid solution (ss1), a non-stoichometric chalcopyrite compound $CuGaSe_2$ (ch(ss)), and a Ga_2Se_3-rich solid solution (ss2) which melts congruently at 1112°C with a composition of 28.5% Ga. The thermodynamic description began with the Cu_2Se-rich solid solution, where the interaction between Cu_2Se and Ga_2Se_3 is estimated using the delta lattice parameter model. This estimation is modified to a sub-regular solution model considering the asymmetric deviation from regular solution of the Cu_2Se-rich solid solution phase. A sublattice model is used or the non-stoichometric chalcopyrite compound $CuGaSe_2$ and the Ga_2Se_3-rich solid solution, where the Gibbs energy of the pure compounds are obtained from the reported values. The liquid phase is modeled as an associated solution using the Redlich-Kister expression for the Gibbs energy. The final results obtained show that the calculated phase boundaries and the calculated points for all the invariant equilibria are in good agreement with the available experimental data.

Section Contents

6.1. Brief Overview

6.1.1. Participants

Faculty Advisor: Prof. Tim Anderson

Research Assistant: Lei L. Kerr

6.1.2. Objectives

Characterize the thermodynamics of the pseudobinary Cu_2Se-Ga_2Se_3 system to develop the theoretical foundations necessary for eventually gaining an understanding of the CIS reaction pathways.

6.2. Introduction

Thermodynamic modeling of the Cu-Ga-In-Se system provides a foundation to understand the reaction pathways that lead to forming the absorber layer for a CGIS precursor. A full description of phase diagram of this system, however, is lacking. In this work, a critical assessment of the pseudobinary Cu_2Se-Ga_2Se_3 system is performed based on measured and estimated phase-diagram and thermodynamic data. The Redlich-Kister polynomial model [6], the associate solution model [7], and the sublattice model [8,9], are used to describe the different solutions appearing in this system.

6.3. Phases and Structures

The phase diagram in the composition range 40 to 100% Ga_2Se_3 in the pseudobinary Cu_2Se-Ga_2Se_3 was first studied by Palatnik and Belova [2]. They determined that $A^{I}GaC_2^{VI}$-type phases with a chalcopyrite structure form in the presence of 50 mole% $B_2^{III}C_3^{VI}$, and that binary $B_2^{III}C_3^{VI}$-type defect compounds exhibit a zinc blend type crystal lattice. They also indicated that the chacopyrite phase extended from 50 to 65 mole %; a solid solution (based on $CuGa_5Se_8$ with 83.3 mole% Ga_2Se_3) from 71 to 89% Ga_2Se_3; and a solid solution (based on Ga_2Se_3) from 91 to 100 mole% Ga_2Se_3. However, they did not study phase relations near Cu_2Se. Later, Mikkelsen

[1] investigated the ternary Cu-Ga-Se phase diagram by DTA and x-ray analysis and revised the solid solution range on Ga_2Se_3-rich side to extend from 70 to 100 mole % Ga_2Se_3. Therefore, according to Mikkelsen, there are four condensed phases:

(i) Cu_2Se-rich solid solution

(ii) Non-stoichiometric chalcopyrite compound $CuGaSe_2$

(iii) Liquid phase

(iv) Ga_2Se_3-rich solid solution.

Specific solution models used to describe the Gibbs energy of each of these phases are described in the next section.

6.4. Thermodynamic Models

In this work, the mixing compounds Cu_2Se and Ga_2Se_3 are considered to be represented respectively by the symbols A and B. The sublattice model for Ga_2Se-rich solid solution and Chalcopyrite phase are considered to be based on anti-site defects.

6.4.1. Cu_2Se and Ga_2Se_3 Stoichiometric Compound Phases

The Gibbs energy of Cu_2Se and Ga_2Se_3 are taken from a previous assessment performed by Zhuang et al. [4]:

$$
\begin{aligned}
{}^{o}G_{Cu2Se\_\alpha} &= -80217.34+288.16728T-59.0572TlnT-0.0375096T^2 \quad (298\le T\le 395)\\
&= -98588.35+664.34671T-120.0866TlnT+0.03785T^2\\
&\quad -6.9635\times10^{-6}T^3+1019900T^{-1} \quad (395\le T\le 800)\\
{}^{o}G_{Cu2Se\_\beta} &= {}^{o}G_{Cu2Se\_\alpha}+6830-17.29114T\\
{}^{o}G_{Cu2Se\_liq} &= {}^{o}G_{Cu2Se\_\beta}+16000-11.422T\\
{}^{o}G_{Ga2Se3\_\beta} &= -438940.855+538.75145T-105.7297TLn(T)-.01765648T^2;\ (298\le T\le 1293K)\\
{}^{o}G_{Ga2Se3\_\alpha} &= -{}^{o}G_{Ga2Se3\_\beta}+17190-17.758264T;\ (298K\le T\le 2000K)
\end{aligned}
$$

6.4.2. Cu_2Se-rich Solid Solution

The Cu_2Se-rich solid solution is considered to be a sub-regular solution. The Gibbs energy of this solution has not been measured, and thus the Delta Lattice Parameter Model was used to estimate the interaction energy between Cu_2Se and Ga_2Se_3 in a regular solution of these 2 components. The DLP model was developed by Stringfellow [3] to predict the interaction on III-V solid solutions and estimates the enthalpy of mixing based on strain energy contributions. This estimate will be included in a sub-regular model by taking asymmetric deviation from a regular solution.

6.4.2.1. Delta Lattice Parameter Model

This regular solution model relies on the following assumptions:

a) The distribution of the constituents on a lattice is random ($\Delta S^{ex} = 0$).

b) The enthalpy of mixing in a binary solution is given by $\Delta H^M = x(1-x)\Omega$, where x is the mole fraction of Cu_2Se.

A relationship for the interaction parameter is determined as a function of the lattice constants by setting the interaction parameter equal to the enthalpy of mixing at x=0.5 and using Vegard's law to estimate the lattice constant of the alloy at the equimolar composition. When x=0.5, $\Delta H^M = \Omega^s$ and 4 Ω^s is determined by the lattice parameter mismatch between the two end components of the solid solution. This model assumes the bonding energy in semiconductors is linearly related to the average band gap energy. The average band gap was found to vary approximately $a_0^{-2.5}$ in III-V semiconductors. Thus, the enthalpy of atomization, ΔH^{at}, which is a measure of bonding energy might be written as

$$\Delta H^{at} = k\, a_0^{-2.5},$$

$$\Delta H^M = (1-x)\,\Delta H_A^{at} + x\Delta H_B^{at} - \Delta H_{alloy}^{at}$$

where at x=0.5

$$\Delta H^M = 0.25\,\Omega^s$$

$$\Delta H^M = 0.5k\, a_A^{-2.5} + 0.5k a_B^{-2.5} - k a_{alloy}^{-2.5}$$

and

$$a_{alloy} = (a_A + a_B)/2$$

Therefore,

$$\Omega^s = 2k\{a_A^{-2.5} + a_B^{-2.5} - 2[(a_A + a_B)/2]^{-2.5}\}$$

In this work we adopt the value of $k=1.15\times10^7$cal/mol $Å^{-2.5}$ for III-V compound alloys suggested in the literature [3]. The calculation results are compared with the results based on the k value for II-VI from Cho's dissertation [4]. According to Cho, the bandgap energy was described to vary approximately as $a_0^{-5.0}$ for II-VI semiconductors and $k=1.87\times10^8$cal/mol $Å^{-5.0}$. The lattice parameters for the compounds are Cu_2Se=5.84Å Ga_2Se_3=5.38Å In_2Se_3= 4.05Å. The results based on both k values and corresponding reports are close to each other and are listed in the Table 5.1.

Table 6.1 Regular Solution Interaction Parameters.

	$k=1.15\times10^7$cal/mol $Å^{-2.5}$ [1]	$k=1.87\times10^8$cal/mol $Å^{-5.0}$ [2]
$CuGaSe_2$	Ω^s = 19,034 J	Ω^s = 14,299 J
$CuInSe_2$	Ω^s = 544,707 J	Ω^s = 608,525 J

6.4.2.2. Sub-regular Solution Model

The Gibbs energy for a disordered solution phase solution is given by

$$G = {}^{ref}G + {}^{id}G + {}^{E}G \quad (1)$$

where for a binary system the idea-solution Gibbs free energy is given by

$${}^{id}G^{\theta} = RT[y \ln y + (1-y)\ln(1-y)] \quad (2)$$

and the reference gibbs energy

$${}^{ref}G^{\theta} = y^{\circ}G_{Cu2Se} + (1 - y)^{\circ}G_{Ga2Se3} \quad (3)$$

is simply the mole fraction averaged Gibbs energy of the 2 end compounds.. In the two previous equations θ stands for the Cu_2Se-rich solid solution phase in question, and y is the mole fraction of Cu_2Se in this phase. Finally, the Redlich-Kister expression

$$ {}^{E}G^{\theta} = y(1-y)\{{}^{0}L_{Cu2Se,Ga2Se3} + {}^{1}L_{Cu2Se,Ga2Se3}\,(\mathrm{y_{Cu2Se}} - y_{Ga2Se3})\} \qquad (4) $$

is used to describe the solid solution with 2 adjustable parameters.

6.4.3. Ordered Non-Stoichiometric Chalcopyrite Compound $CuGaSe_2$ Phase

The non-stoichiometric chalcopyrite compound $CuGaSe_2$ is described by the sublattice model. The sublattice model for Ga_2Se-rich solid solution and Chalcopyrite phase include only anti-site defects. The defect occurs when the position of Cu_2Se compound in the crystal lattice is occupied by Ga_2Se_3, and Cu_2Se is the defect when it dislocated (solved in) the position of one Ga_2Se_3 compound.

6.4.3.1. Formation Energies

This section considers the formation energy of $CuGaSe_2$ for the assessment of Chalcopyrite phase region of pseudobinary Cu_2Se-Ga_2Se_3. The reaction considered for the standard Gibbs energy for pure compound is:

$$ 1/2Cu_2Se + 1/2Ga_2Se_3 \rightarrow CuGaSe_2 \qquad (5) $$

and

$$ \Delta G^0(5) = G_T(CuGaSe_2) - 1/2G_T(Cu_2Se) - 1/2G_T(Ga_2Se_3) \qquad (6) $$

where $G_T(CuGaSe_2)$, $G_T(Cu_2Se)$ and $G_T(Ga_2Se_3)$ are the Gibbs energies of formation of the compounds calculated based on the thermodynamic data from Cahen [10] using the expression:

$$ G_T = H_{298.15} + \Delta CpdT - T[S_{298.15} - \Delta Cp/T\,dT] $$

For $G_T(Cu_2Se)$ this involves the formation reaction

$$ 2Cu + Se \rightarrow Cu_2Se \qquad (7) $$

The enthalpy of the element in its stable phase at 298.15 K is chosen as this reference state resulting in

$H(T, Cu) = H(298.15, Cu) + \Delta CpdT = 0$ and $H(T, Se) = H(298.15, Se) + \Delta CpdT = 0$ (8)

$H(T, Cu_2Se) = H(298.15, Cu_2Se) = \Delta H_f(298.15, Cu_2Se) = -59\ kJ\ mol^{-1}$ (9)

$S(T, Cu_2Se) = S(298.15, Cu_2Se) + \Delta Cp/TdT = S(298.15, Cu_2Se) = 157\ J\ mol^{-1}\ k^{-1}$ (10)

which finally leads to

$$G(T, Cu_2Se) = H(T, Cu_2Se) - TS(T, Cu_2Se) = -59000-157T \quad (11)$$

We can calculate the remaining terms in a similar fashion, yielding

$$G(T, Ga_2Se_3) = -439000-179T \quad (12)$$

$$G(T, CuGaSe_2) = -316000-147T \quad (13)$$

so that we have

$$\Delta G^0(1) = -316000-147T-1/2(-59000-157T)-1/2(-439000-179T) = -67000+21T \quad J/mol \quad (14)$$

Based on the earlier discussion, we can write the sublattice as

$$(Cu_2Se, Ga_2Se_3)_I(Ga_2Se_3, Cu_2Se)_{II}$$

For modeling the solid solution range, the ordered non-stoichiometric $CuGaSe_2$ phase is also described via two sublattices. The Gibbs energy of phase ϕ can be given by the expressions

$$\begin{aligned} {}^{ref}G^{\phi} = {} & y'_{Cu2Se}y''_{Cu2Se}\,{}^{\circ}G^{\phi}_{Cu2Se:Cu2Se} + y'_{Ga2Se3}y''_{Ga2Se3}\,{}^{\circ}G^{\phi}_{Ga2Se3:Ga2Se3} \\ & + y'_{Cu2Se}y''_{Ga2Se3}\,{}^{\circ}G^{\phi}_{Cu2Se:Ga2Se3} + y'_{Ga2Se3}y''_{Cu2Se}\,{}^{\circ}G^{\phi}_{Ga2Se3:Cu2Se} \end{aligned} \quad (15)$$

$$ {}^{id}G^{\phi} = RT[y'_{Cu2Se}\ln y'_{Cu2Se} + y'_{Ga2Se3}\ln y'_{Ga2Se3}] + RT[y''_{Cu2Se}\ln y''_{Cu2Se} + y''_{Ga2Se3}\ln y''_{Ga2Se3}] \quad (16)$$

$$\begin{aligned} {}^{E}G^{\phi} = {} & y'_{Cu2Se}y'_{Ga2Se3}\left[y''_{Cu2Se}\left({}^{0}L^{\phi}_{Cu2Se,Ga2Se3:Cu2Se}\right) + y''_{Ga2Se3}\left({}^{0}L^{\phi}_{Cu2Se,Ga2Se3:Ga2Se3}\right)\right] \\ & + y''_{Cu2Se}y''_{Ga2Se3}\left[y'_{Cu2Se}\left({}^{0}L^{\phi}_{Cu2Se:Ga2Se3,Cu2Se}\right) + y'_{Ga2Se3}\left({}^{0}L^{\phi}_{Ga2Se3:Ga2Se3,Cu2Se}\right)\right] \end{aligned} \quad (17)$$

where ϕ stands for non-stoichiometric chalcopyrite $CuGaSe_2$ phase, and where y_i' and y_i'' refer to the site fractions of the component i in the first and second sublattice, respectively. Furthermore, ${}^{\circ}G^{\phi}_{Cu2Se:Ga2Se3}$ is the standard Gibbs energy for the stoichiometric compound $CuGaSe_2$ Combining these equations now yields

$$ {}^{\circ}G^{\phi}_{Cu2Se:Ga2Se3} = 0.5\ {}^{0}\mathrm{G}_{\mathrm{Cu2Se}\_\beta} + 0.5\ {}^{\mathrm{o}}\mathrm{G}_{\mathrm{Ga2Se3}\_\beta} - 67000 + 21T \tag{18} $$

Finally, ${}^{\circ}G^{\phi}_{Cu2Se:Cu2Se}$ and ${}^{\circ}G^{\phi}_{Ga2Se3:Ga2Se3}$ can be expressed as

$$ {}^{\circ}G^{\phi}_{Cu2Se:Cu2Se} = {}^{\circ}G_{Cu2Se\_\beta} + a_1 + b_1 T \tag{19} $$

$$ {}^{\circ}G^{\phi}_{Ga2Se3:Ga2Se3} = {}^{\circ}G_{Ga2Se3\_\beta} + a_2 + b_2 T \tag{20} $$

where a_i and b_i are adjustable parameters. The values of ${}^{\circ}G^{\phi}_{Ga2Se3:Cu2Se}$ can be obtained by the following relation [11,12]:

$$ {}^{\circ}G^{\phi}_{Ga2Se3:Cu2Se} = {}^{\circ}G^{\phi}_{Cu2Se:Cu2Se} + {}^{\circ}G^{\phi}_{Ga2Se3:Ga2Se3} - {}^{\circ}G^{\phi}_{Cu2Se:Ga2Se3} \tag{21} $$

To reduce the number of adjustable parameters, the following relations are used in the optimization problem [11,12]:

$$ {}^{0}L^{\phi}_{Cu2Se,Ga2Se3:Ga2Se3} = {}^{0}L^{\phi}_{Cu2Se,Ga2Se3:Cu2Se} = {}^{0}L^{\phi}_{Cu2Se,Ga2Se3:*} \tag{22} $$

$$ {}^{0}L^{\phi}_{Cu2Se:Ga2Se3,Cu2Se} = {}^{0}L^{\phi}_{Ga2Se3:Ga2Se3,Cu2Se} = {}^{0}L^{\phi}_{*:Ga2Se3,Cu2Se} \tag{23} $$

6.4.4. Ga_2Se_3-rich Solid Solution

Mikkelsen [1] and Palatnik and Belova [2] considered the Ga_2Se_3-rich Solid Solution solid solution a non-stoichiometric zinc blende type compound. Therefore, similar to the modeling of the ordered non-stoichiometric $CuGaSe_2$ phase, we can also use two sublattices to describe this phase, as follows:

$$ (Cu_2Se,\ Ga_2Se_3)_{\mathrm{I}}(Ga_2Se_3,\ Cu_2Se)_{\mathrm{II}} $$

Given that the solid solution melts congruently at 1112°C with a composition of 28.5% Ga. The hypothetical stoichiometric compound $(Cu_2Se)_{0.4}(Ga_2Se_3)_{0.6}$ has the composition of 28.5%, the Gibbs energy can be expressed by the equations (where ϕ = Ga_2Se_3-rich solid solution):

$$^{ref}G^{\phi} = y'_{Cu2Se}y''_{Cu2Se}\,{}^{\circ}G^{\phi}_{Cu2Se:Cu2Se} + y'_{Ga2Se3}y''_{Ga2Se3}\,{}^{\circ}G^{\phi}_{Ga2Se3:Ga2Se3} + y'_{Cu2Se}y''_{Ga2Se3}\,{}^{\circ}G^{\phi}_{Cu2Se:Ga2Se3} + y'_{Ga2Se3}y''_{Cu2Se}\,{}^{\circ}G^{\phi}_{Ga2Se3:Cu2Se} \quad (24)$$

$$^{id}G^{\phi} = RT[(y'_{Cu2Se}\ \ln y'_{Cu2Se} + y'_{Ga2Se3}\ \ln y'_{Ga2Se3}\ ] + RT[y''_{Cu2Se}\ln y''_{Cu2Se} + y''_{Ga2Se3}\ln y''_{Ga2Se3}] \quad (25)$$

$$^{E}G^{\phi} = y'_{Cu2Se}y'_{Ga2Se3}\left[y''_{Cu2Se}\left({}^{0}L^{\phi}_{Cu2Se,Ga2Se3:Cu2Se}\right) + y''_{Ga2Se3}\left({}^{0}L^{\phi}_{Cu2Se,Ga2Se3:Ga2Se3}\right)\right] + y''_{Cu2Se}y''_{Ga2Se3}\left[\begin{array}{l} y'_{Cu2Se}\left({}^{0}L^{\phi}_{Cu2Se:Ga2Se3,Cu2Se} + {}^{1}L^{\phi}_{Cu2Se:Ga2Se3,Cu2Se}(y''_{Cu2Se} - y''_{Ga2Se3})\right) + \\ y'_{Ga2Se3}\left({}^{0}L^{\phi}_{Ga2Se3:Ga2Se3,Cu2Se} + {}^{1}L^{\phi}_{Ga2Se3:Ga2Se3,Cu2Se}(y''_{Cu2Se} - y''_{Ga2Se3})\right) \end{array}\right] \quad (26)$$

where y_i' and y_i'' refer to the site fractions of the component i in the first and second sublattice, respectively. No thermodynamic data is available in the literature for $^{\circ}G^{\phi}_{Cu2Se:Ga2Se3}$, which is the standard Gibbs energy of the stoichiometric compound $(Cu2Se)_{0.4}(Ga2Se3)_{0.6}$. Writing $^{\circ}G^{\phi}_{Cu2Se:Ga2Se3}$ as:

$$^{\circ}G^{\phi}_{Cu2Se:Ga2Se3} = 0.4\ {}^{0}G_{Cu2Se\_\beta} + 0.6\ {}^{o}G_{Ga2Se3\_\beta} + a_3 + b_3T \quad (27)$$

$^{\circ}G^{\phi}_{Cu2Se:Cu2Se}$ and $^{\circ}G^{\phi}_{Ga2Se3:Ga2Se3}$ can be expressed as:

$$^{\circ}G^{\phi}_{Cu2Se:Cu2Se} = {}^{\circ}G_{Cu2Se\_\beta} + a_4 + b_4T \quad (28)$$

$$^{\circ}G^{\phi}_{Ga2Se3:Ga2Se3} = {}^{\circ}G_{Ga2Se3\_\beta} + a_5 + b_5T \quad (29)$$

where a_i and b_i are adjustable parameters to be optimized. The value of $^{\circ}G^{\phi}_{Ga2Se3:Cu2Se}$ can be obtained by the following relation [11,12]:

$$^{\circ}G^{\phi}_{Ga2Se3:Cu2Se} = {}^{\circ}G^{\phi}_{Cu2Se:Cu2Se} + {}^{\circ}G^{\phi}_{Ga2Se3:Ga2Se3} - {}^{\circ}G^{\phi}_{Cu2Se:Ga2Se3} \quad (30)$$

To reduce the number of parameters, the following relations are used in the optimization [11,12]:

$$ {}^{0}L^{\phi}_{Cu2Se,Ga2Se3:Ga2Se3} = {}^{0}L^{\phi}_{Cu2Se,Ga2Se3:Cu2Se} = {}^{0}L^{\phi}_{Cu2Se,Ga2Se3:*} \quad (31) $$

$$ {}^{0}L^{\phi}_{Cu2Se:Ga2Se3,Cu2Se} = {}^{0}L^{\phi}_{Ga2Se3:Ga2Se3,Cu2Se} = {}^{0}L^{\phi}_{*:Ga2Se3,Cu2Se} \quad (32) $$

$$ {}^{1}L^{\phi}_{Cu2Se:Ga2Se3,Cu2Se} = {}^{1}L^{\phi}_{Ga2Se3:Ga2Se3,Cu2Se} = {}^{1}L^{\phi}_{*:Ga2Se3,Cu2Se} \quad (33) $$

6.4.5 Liquid Phase

The associated model developed by Sommer [7] is used to describe the Gibbs energy of the liquid phase

$$ (Cu_2Se, Ga_2Se_3)_l $$

The Gibbs energy of this phase (given for 1 mole of atoms) can also be expressed as,

$$ G^{Liq} = {}^{ref}G^{Liq} + {}^{id}G^{Liq} + {}^{E}G^{Liq} \quad (34) $$

The term ${}^{ref}G^{l}$ is equal to

$$ {}^{ref}G^{liq} = y_{Cu2Se}\,{}^{\circ}G^{liq}_{Cu2Se} + y_{Ga2Se3}\,{}^{\circ}G^{liq}_{Ga2Se3} \quad (35) $$

where y_i refers to the site fractions of the species i, ${}^{y}Cu_2Se + {}^{y}Ga2Se3 = 1$. The term ${}^{\circ}G^{l}_{i}$ represent the Gibbs energy of pure liquid i. The ideal mixing Gibbs energy ${}^{id}G^{l}$ is equal to

$$ {}^{id}G^{l} = RT(y_{Cu_2Se}\ln y_{Cu_2Se} + y_{Ga2Se3}\ln y_{Ga2Se3}) \quad (36) $$

The excess Gibbs energy ${}^{E}G^{l}$ is

$$ {}^{E}G^{l} = y_{Cu_2Se}y_{Ga2Se3}({}^{0}L^{l}_{Cu_2Se,Ga2Se3} + {}^{1}L^{l}_{Cu_2Se,Ga2Se3}(y_{Cu_2Se} - y_{Ga2Se3}) + {}^{2}L^{2}_{Cu_2Se,Ga2Se3}(y_{Cu_2Se} - y_{Ga2Se3})^{2}) \quad (37) $$

where the four terms with the superscript "L" represent the interactions between the species and are expressed as a function of temperature.

6.5. Optimization Procedure

Mikkelson's critical review [1] is used as a guide for the experimental phase diagram data for the optimization of thermodynamic model parameters of all phases in this system. The

summary of the data is listed in Table 6.2. The optimization procedure is performed by using the PARROT module of the Thermo-Calc program package. First, we fixed all the Gibbs energy coefficients for other phases and optimized the coefficients for the liquid. Second, we set all the coefficients for liquid to the optimized coefficients and fix them while optimizing the coefficients for Cu_2Se-rich solid solution phase and non-stoichiometric chalcopyrite $CuGaSe_2$ phase. The coefficients for the liquid phase as well as the parameter for Cu_2Se-rich solid solution phase and chalcopyrite $CuGaSe_2$ phase parameters are fixed, the optimization on Ga_2Se-rich solid solution phase is performed.

Table 6.2 Data sources used during the optimization

Equilibrium/Function	Reference
Ga_2Se_3-rich solid solution /liquid, congruently melting at 1378 K	[1], [2]
Eutectic Temperature 1250K Liquid→Cu_2Se-rich solid solution +Chalcopyrite $CuGaSe_2$	[1]
Peritectic temperature at 1360 K Liquid+Ga_2Se_3-rich solid solution→ Chalcopyrite $CuGaSe_2$	[1], [2]

Table 6.3 Optimized parameters according to the analytical description of the phases[+].

Phase or Function	Parameters
Liquid	${}^{\circ}G^{liq}_{Cu2Se} = {}^{\circ}G_{Cu2Se\_\beta} + 16000 - 11.422T$ ${}^{\circ}G^{liq}_{Ga2Se3} = {}^{\circ}G_{Ga2Se3Cu2Se\_\beta} + 101190 - 79.595204T$ ${}^{0}L^{\phi}_{Cu2Se,Ga2Se3} = -108800$ ${}^{1}L^{\phi}_{Cu2Se,Ga2Se3} = 38900$ ${}^{2}L^{\phi}_{Cu2Se,Ga2Se3} = -2000$
Cu_2Se-rich Solid Solution	${}^{\circ}G_{Cu2Se} = {}^{\circ}G_{Cu2Se\_\beta}$ ${}^{\circ}G_{Ga2Se3} = {}^{\circ}G_{Ga2Se3\_\beta}$ ${}^{0}L_{Cu2Se,Ga2Se3} = 19034$ ${}^{1}L_{Cu2Se,Ga2Se3} = -98500$

+ Temperature (T) is in Kelvin. The Gibbs energies are in J/mole of atoms. The symbol * indicates Cu_2Se or Ga_2Se_3.

Table 6.3 Continued

Ga_2Se_3-rich solid solution	${}^{\circ}G^{\phi}_{Cu2Se:Ga2Se3} = 0.4\ {}^{0}G_{Cu2Se\_\beta} + 0.6\ {}^{o}G_{Ga2Se3\_\beta} - 49700$ ${}^{\circ}G^{\phi}_{Ga2Se3:Cu2Se} = 0.6\,{}^{0}G_{Cu2Se\_\beta} + 0.4\ {}^{o}G_{Ga2Se3\_\beta} + 49800$ ${}^{\circ}G^{\phi}_{Cu2Se:Cu2Se} = {}^{\circ}G_{Cu2Se\_\beta} + 100$ ${}^{\circ}G^{\phi}_{Ga2Se3:Ga2Se3} = {}^{\circ}G_{Ga2Se3\_\beta}$ ${}^{0}L^{\phi}_{Cu2Se,Ga2Se3:*} = -40040 + T$ ${}^{0}L^{\phi}_{*:Ga2Se3,Cu2Se} = 13000$ ${}^{1}L^{\phi}_{*:Ga2Se3,Cu2Se} = -11500 + 10.60T$
Non-stoichicmetric Chalcopyrite $CuGaSe_2$ Compound	${}^{\circ}G^{\phi}_{Cu2Se:Ga2Se3} = 0.5\ {}^{0}G_{Cu2Se\_\beta} + 0.5\ {}^{o}G_{Ga2Se3\_\beta} - 67000 + 21T$ ${}^{\circ}G^{\phi}_{Ga2Se3:Cu2Se} = 0.5\ {}^{0}G_{Cu2Se\_\beta} + 0.5\ {}^{o}G_{Ga2Se3\_\beta} + 69200 + 21T$ ${}^{\circ}G^{\phi}_{Cu2Se:Cu2Se} = {}^{\circ}G_{Cu2Se\_\beta} + 1000$ ${}^{\circ}G^{\phi}_{Ga2Se3:Ga2Se3} = {}^{\circ}G_{Ga2Se3\_\beta} + 1200$ ${}^{0}L^{\phi}_{Cu2Se,Ga2Se3:*} = -9656 - 10T$ ${}^{0}L^{\phi}_{*:Ga2Se3,Cu2Se} = 19000$
Function	${}^{o}G_{Cu2Se\_\alpha}$=-80217.34+288.16728T-59.0572TlnT-0.0375096T^2 (298≤T≤395) =-98588.35+664.34671T-120.0866TlnT+0.03785T^2 -6.9635×$10^{-6}T^3$+1019900T^{-1} (395≤T≤800) ${}^{o}G_{Cu2Se\_\beta}$=GCu2Se_α+6830-17.29114T ${}^{o}G_{Cu2Se\_liq}$=GCu2Se_β+16000-11.422T ${}^{o}G_{Ga2Se3\_\beta}$=-438940.855+538.75145T-105.7297TLn(T)-.01765648T^2 (298≤T≤1293K) ${}^{o}G_{Ga2Se3\ \alpha}$ =-${}^{o}G_{Ga2Se3\ \beta}$ +17190-17.758264T; (298K≤T≤2000K)

+ Temperature (T) is in Kelvin. The Gibbs energies are in J/mole of atoms. The symbol * indicates Cu_2Se or Ga_2Se_3.

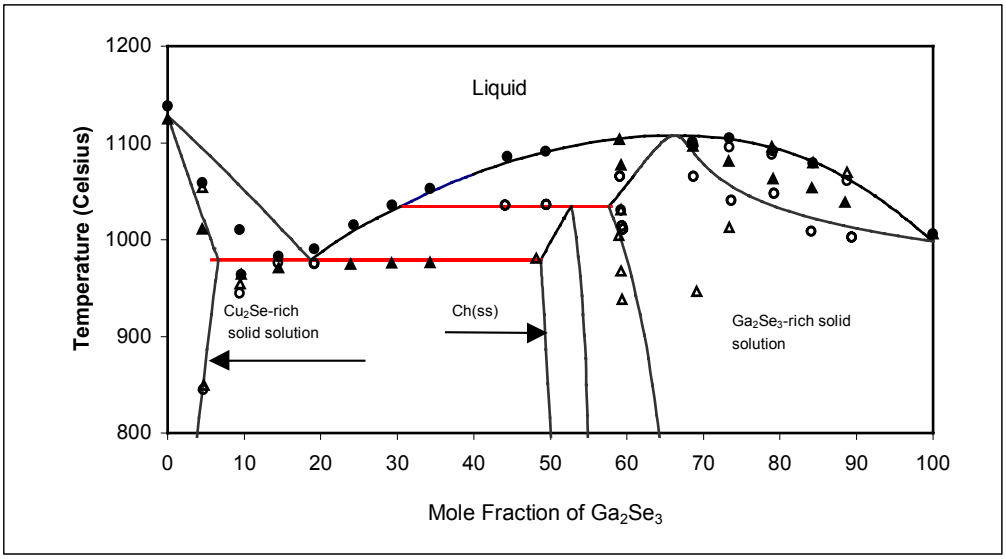

Figure 6.1 Comparison of calculated and experimental pseudobinary phase diagram of Cu_2Se-Ga_2Se_3 (Δ▲Heating[1]) (○●Cooling[1]).

6.6. References

[1] J.C. Mikkelsen, *J. Elec. Mat.,* Vol. 10, No.3 pp. 541-558 (1981).

[2] L.S. Palatnik and E.K. Belova, Izvestiya Academii Nauk SSSR, Neorganicheskie Materialy, Vol. 3, No.12 pp. 2194-2202 (1967).

[3] G.B. Stringfellow, J. Phys. Chem. Solids, Vol. 34, pp. 1749-1751 (1973).

[4] W.D. Zhuang, C.H. Zhang. M. Ider, J.Y. Shen and T.J. Anderson, CALPHAD XXIX, Cambridge, 2000

[5] M.W. Chase, C.A. Davies, J.R. Downey, D.J. Frurip, R.A. McDonald and A.N. Syverud, J. Phys. Chem. Ref. Data Vol. 14, Suppl. 1(1985).

[6] Redlich, O.; Kister, A.: Ind. Eng. Chem., Vol. 40, 345(1948).

[7] Sommer, F.: Z. Metallkd., Vol. 73, 72(1982).

[8] Hillert, M.; Staffanson, L.I.: Acta Chim. Scand., Vol. 24, 3618 (1970).

[9] Sundman, B.; Agren, J.: J. Phys. Chem. Solids, Vol. 42, 297(1981).

[10] D. Cahen (1992)

[11] Ansara, I.; Dupin, N.; Lukas, H.L.; Sundman, B.: in: Applications of Thermodynamics in the Synthesis and Processing of Materials, P. Nash and B. Sundman (eds.), The Minerals, Metals & Materials Society, 273(1995).

[12] Zhuang, W.; Shen, J.; Liu, Y.; Ling, L.; Shang, S.; Du, Y.; Schuster, J.C.: Z Metallkd., (1999).

PART 7

Progress on the Optimization of RTP Processing of Binary Bilayer Precursors

Abstract

Optimization studies were conducted to characterize *the rapid thermal processing (RTP) of binary bilayer precursors for CIS synthesis using a custom-made RTP furnace and a newly acquired AG Associates Heatpulse furnace. In addition, two susceptor designs were conceived and tested, along with a variety of target temperatures, soak times, and temperature-ramp rates, delay times, sample size, and preheat intensity leading to improved understanding of the RTP processing operation.*

Section Contents

7.1 Brief Overview

7.1.1 Participants

Faculty Adviser: Prof. Tim Anderson

Research Assistants: Lei L. Kerr

7.1.2 Objectives

Optimize the parameters of the rapid thermal processing operation used for growing CIS films from precursor layers.

7.2 Introduction

The development of photovoltaic devices based on $CuIn_xGa_{1-x}Se_2$(CIGS) thin films has advanced rapidly during the last several years. It is considered a most promising material for thin film photovoltaic devices because of its demonstrated efficiency, desirable bandgap and high absorption coefficient for solar radiation. Laboratory-scale device efficiencies of 18.8% have been reported. In our research group these films are generally deposited by rapid deposition of a stacked binary compound bilayer precursor at low substrate temperature using a Migration Enhanced Epitaxy (MEE) reaction system. The absorber layer is subsequently synthesized via a liquid phase assisted process using rapid thermal processing (RTP).

7.3 RTP Experiments Conducted in a custom-made RTP Furnace

Three samples with precursor structure InSe/CuSe/Mo/sodium-lime glass were processed in a custom-made RTP furnace available at the University of Florida. Samples were placed on a thin piece of 4-inch diameter graphite with a N_2 purge flow originating from the back of the oven. The RTP annealing recipes used for the 3 samples are described in Table 7.1.

Table 7.1 RTP Conditions

Sample	Soak time	Temperature	Ramp rate
1-1	70s	550°C	20°C/s
1-2	70s	750°C	20°C/s
1-3	140s	550°C	20°C/s

The processed films were characterized by XRD, Auger, and optical microscopy. From the XRD data shown in Figure 7.1, we can see that after RTP the α-CuSe phase disappeared and the $CuInSe_2$ and $Cu_{2-x}Se$ phases formed. The relative intensity of the peak around $2\theta = 26.560$ degrees decreased when the soak time increased from 70s (sample 1-1) to 140s (sample 1-3). This is attributed to the longer soak time increasing the In and Se losses and thus increasing the extent of formation of the $Cu_{2-x}Se$ phase. It is likely that the In_2Se species is responsible since it

has a high vapor pressure. There is no significant difference in the XRD spectra when the temperature is increased from 550°C (sample 1-1) to 750°C (sample 1-2) for the same soak time.

From the plane-view optical micrographs, Figures 7.2, 7.3, and 7.4, we can see that when the temperature is 750°C (sample 1-2) the surface morphology of the processed film is much rougher than the one processed at 550°C.

Figures 7.5, 7.6 and 7.7 show the Auger composition depth profiles of samples 1-0, 1-1, and 1-3, respectively. These results indicate that the In is depleted in the samples after RTP. Sample 1-3 (soak time 140s) has a more uniform composition distribution than sample 1-1 (soak time 70s), although there is more In and Se loss.

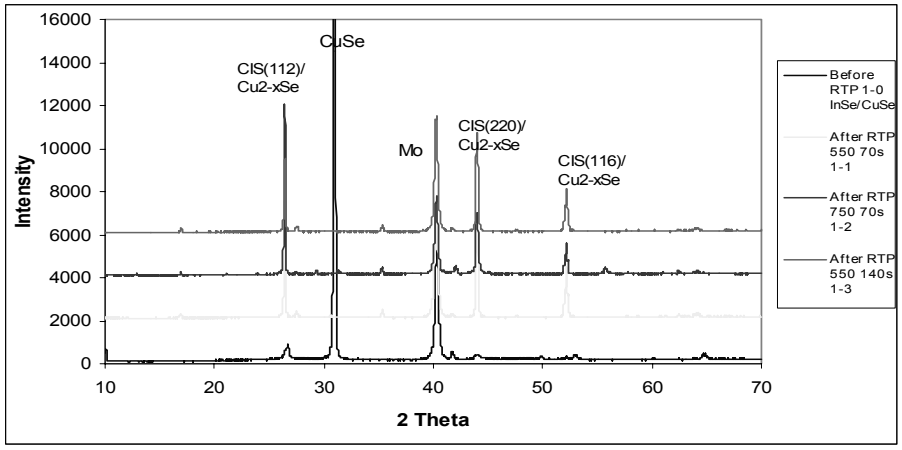

Figure 7.1 XRD pattern comparison of each sample

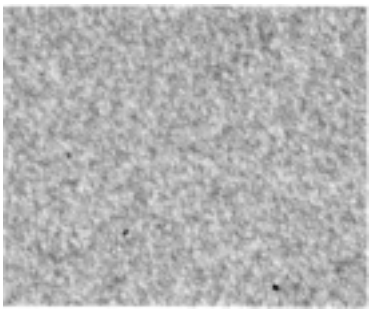

Figure 7.2 Plane-view optical micrograph of sample 1-0 before RTP.

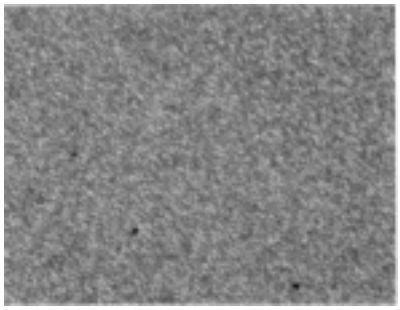

Figure 7.3 Plane-view optical micrograph of sample 1-1 after RTP at 550°C.

Figure 7.4 Plane-view optical micrograph of sample 1-2 after RTP at 750°C.

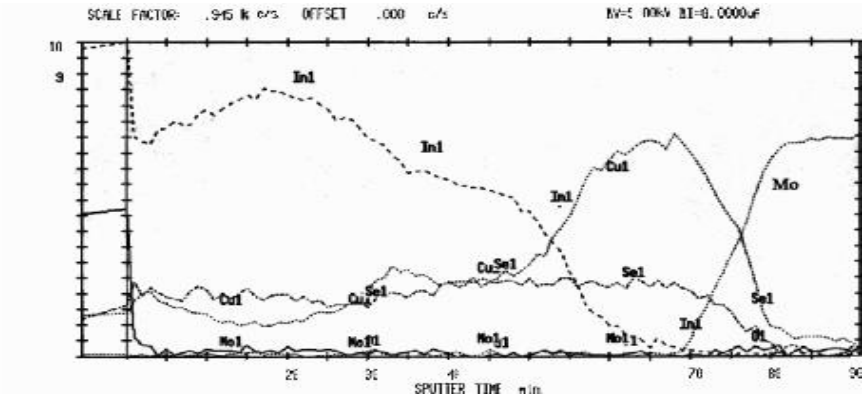

Figure 7.5. Auger depth profile of sample before RTP.

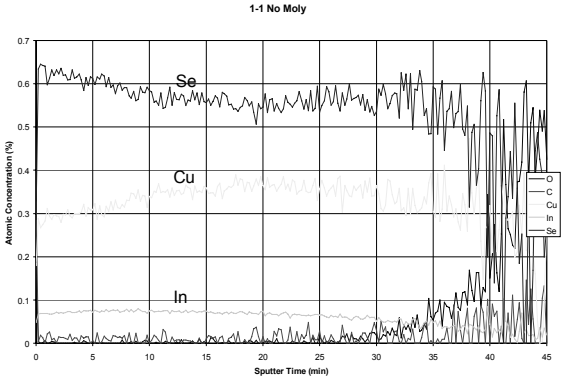

Figure 7.6. Auger depth profile after RTP (sample 1-1) at 550°C for 70 s.

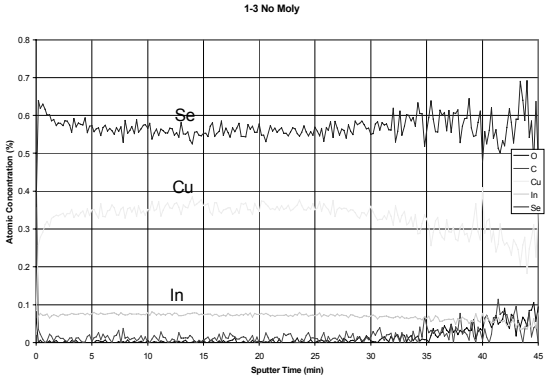

Figure 7.7. Auger depth profile after RTP (sample 1-3) at 550°C for 140 s.

The experimental results reported in this section indicated that a high RTP temperature should be avoided and that the observed the losses of In and Se needs to be reduced. Therefore, two new susceptors (sample holders) were designed that incorporates flat quartz cover to reduce volatilization losses. Further studies were conducted in a newly acquired RTP furnace, as explained in the next section.

7.4 RTP Experiments Conducted in Heatpulse RTP Furnace

A commercial RTP furnace, namely an AG ASSOCIATES model HEATPULSE 4100RTP system was acquired. The equipment incorporates a N_2-purge feature and it can realize a maximum temperature ramp rate of 120 °C/s. This furnace uses an optical pyrometer instead of a thermocouple to measure the temperature. Two susceptor designs were considered:

a) Susceptor design I Described in Figure 7.15 and in section 7.4.1

b) Susceptor design II Described in Figure 7.19 and in section 7.4.2

The results of our experimental studies with the two susceptor designs are reported in the following subsections.

7.4.1 RTP experiments on sample series 157 using susceptor design I

Several RTP runs were performed on test samples with the bilayer precursor structure CuSe/InSe/Mo/glass using susceptor design I (shown in Figure 7.15). In this design, the sample is placed on top of a piece of a silicon wafer, and a quartz lid is used to cover the sample to minimize volatilization losses. After RTP processing films, the bottom of the soda-lime glass (SLG) was observed to have exceeded its glass transition temperature. The test samples were cracked and adhered to the silicon wafer. Optical micrographs of the samples were taken before and after RTP and are shown in Figures 7.8 and 7.9. Therefore, a 4-inch diameter graphite plate was substituted for the silicon wafer to increase the heat conductivity of the sample tray. Several RTP experiments were conducted using graphite wafer. The plane view optical micrograph shown in Figure 7.10, shows that cracking and sticking were avoided by using a graphite tray.

Figure 7.8. Test sample before RTP.

Figure 7.9. Test sample after RTP using a silicon wafer as the susceptor.

Figure 7.10. Test sample after RTP using a graphite plate as the susceptor.

A set of RTP experiments was performed on precursor samples with the CuSe/InSe/Mo/SLG structure to determine the effects of the RTP processing variables (temperature, soak time, delay times, sample size, and preheat intensity) on the composition change and phase transition of the film. Figure 7.11 shows a comparison of the XRD patterns measured for the films before and after RTP. It can be seen that all the $CuInSe_2$ films synthesized by RTP from the binary bilayer precursors exhibited a chalcopyrite structure as indicated by the presence of the 101, 103, 211 and 105 reflections [1, 2]. The α-CuSe phase, which is the dominant phase in precursor film, disappeared and reacted to form $CuInSe_2$ upon RTP. The narrow peaks indicate large crystal sizes. Figures 7.12 and 7.13 and Table 7.2 show the overall composition of the films used in this study as determined by Inductively Coupled Plasma (ICP) emission spectroscopy. We can see that the overall composition of the film changes slightly after the bi-layer precursor was subjected to RTP treatment.

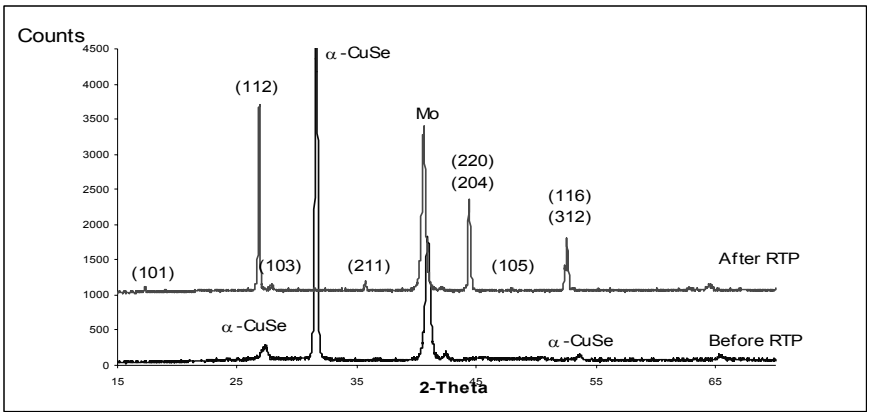

Figure 7.11. XRD pattern for precursor film (before RTP) and $CuInSe_2$ thin film (after RTP).

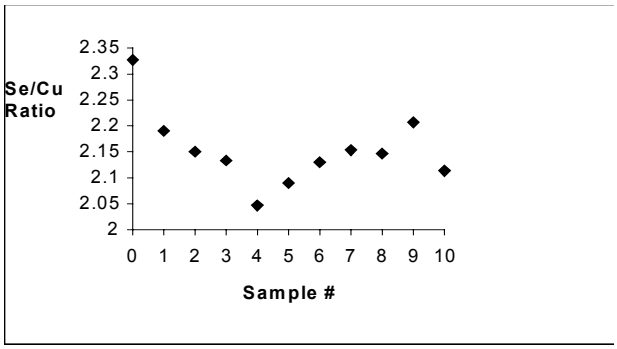

Figure 7.12. Se/Cu ratio comparison of samples before (sample 0) and after RTP (samples to 10).

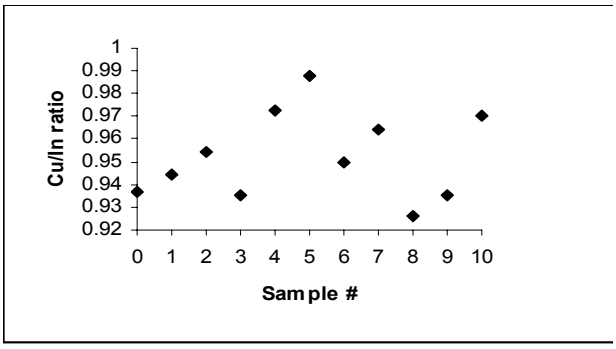

Figure 7.13. Cu/In ratio comparison of samples before (sample 0) and after RTP (samples 1 to 10).

Table 7.2. ICP chemical analysis of the investigated samples.

Sample	Cu (at%)	In (at%)	Se (at%)	RTP Conditions		
				Temperature (°C)	Soak time (s)	Ramp Rate (°C/s)
Precursor	22.6	24.3	52.9	---	---	---
Sample #2	23.8	24.9	51.1	480	60	60
Sample #3	23.8	25.4	50.8	480	120	60
Sample #5	24.4	24.7	50.9	600	60	60
Sample #6	23.9	25.2	50.9	600	120	60
Sample #7	23.9	24.7	51.4	600	60	20

From the XRD and ICP results it can be concluded that the more significant RTP conditions for processing the precursor structure CuSe/InSe/Mo/SLG are: higher ramp rate, shorter soak time, higher preheat intensity, and lower soak temperature.

A preliminary study of samples with an In-Se binary layer on top of the Cu-Se layer (precursor structure InSe/CuSe/Mo/SLG) was undertaken. When processed in the temperature range 450 to 600°C, the samples showed a rough surface morphology after RTP, as shown in Figure 7.14. This is believed to be a result of the melting of the bottom CuSe layer while the top InSe layer remained solid within the temperature range 450 to 600°C. The rough surface disappeared when decreasing the soak temperature to 300°C or increasing it to 800°C. This is because at 300°C or 800°C, both layers are solid or both liquid. The EDX results showed that the area with rough morphology (average Cu:In:Se =1:1.016:1.835) was richer in In than alternate area (average Cu:In:Se = 1:0.883:1.841).

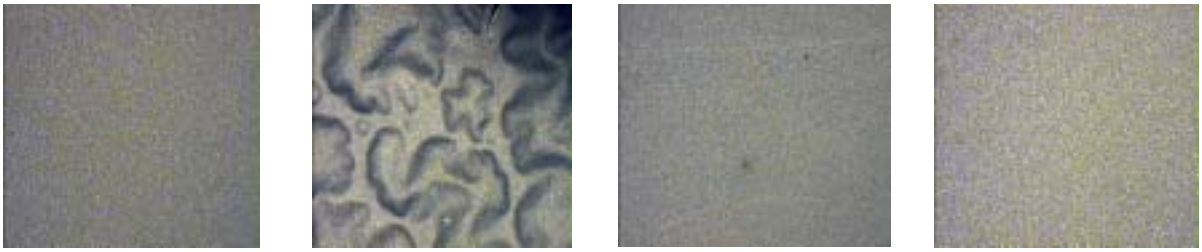

Before RTP | 450 to 600°C | 800°C | 300°C

Figure 7.14. Plane-view optical micrographs.

In conclusion, difficulties with cracking and volatilization losses were largely resolved by using a graphite sample tray and quartz cover as shown in Figure 7.15. Using the precursor structure CuSe/InSe/Mo/SLG, the a-CIS phase was successfully formed (XRD). Further optimization of RTP on structure InSe/CuSe/Mo/SLG is under study.

7.4.2 RTP experiments on sample series 230 using susceptor design I

RTP experiments were performed on a new precursor series (growth run 230) with the structure CuSe/InSe/Mo/SLG. For this sample set, the sample size was increased to 1" by 1" to allow cells to be fabricated. Experiments performed in the susceptor design I (Figure 7.15) produced large lateral temperature gradients during RTP because of the relatively small size of the quartz cover. XRD spectra at three different locations (see Figure 7-16) were taken and the comparison of the three regions is shown in Figure 7.17. It is seen that the Cu-Se secondary phase peak (2θ=21.3°) in the center region decreased as compared to the edge, consistent with a higher center temperature. The reaction in the center is thus more complete than at the edge. To improve heating uniformity, a new sample holder referred to as susceptor design II was conceived (Figure 7.19). In this design, a recess was milled in a piece of graphite stock that holds the sample. A second recess was milled at a larger diameter to accommodate a flat quartz cover.

7.4.3 RTP experiments on sample series 230 using susceptor design II

7.4.3.1 Experiments with optimized process conditions from previous experiments. (Set-point temperature 480°C, Soak time 70 s, Ramp rate 60°C/s)

As a starting point, the RTP conditions used with the previous sample series (set-point temperature 480°C, soak time 70s, ramp rate 60°C/s) were first tested. XRD results, however, indicated that complete formation of α-CIS did not occur, but rather that an intermediate phase remained as shown in Figure 7.19. The thickness of the new set of precursor films was twice as large as the original set as determined from the ICP data reported in Table 7.3. Therefore, we suspect that a longer soak time and possibly higher temperature may be required.

Table 7.3. ICP and film thickness comparison of original precursor and 230 series.

	Precursor Series 157	Precursor Series 230
ICP	Cu 22.88%, In 24.66%, Se 52.46%	Cu 24.28%, In 26.43%, Se 49.28%
Film Thickness	1 μm	2 μm

7.4.3.2 Longer soak time and higher process temperature (Set-point temperature 600°C, Soak time 120 s, Ramp rate 60°C/s)

Increasing the set point temperature from 480 to 600°C and lengthening the soak time from 70 to 120 sec did not produce good results. The XRD data shown in Figure 7.21 does not show a significant change. The ICP measured composition of the sample is Cu 29.43%, In 23.6%, Se 47.01%. This composition is located in the three-phase region (Liquid + $Cu_{2-x}Se$ + α-CIS) according to the ternary CIS phase diagram.

7.4.3.3 Lower process temperature and shorter soak time (Set-point temperature 550°C, Soak time 70 s, Ramp rate 60°C/s)

Lowering the soak temperature to 550°C to prevent Se loss improved the RTP results. Comparing XRD data from a sample processed at 480°C, soak time 70 s, ramp rate 60°C/s with that for once processed at 600°C, soak time 120 s, ramp rate 60°C/s (Figures 7.21 and 7.22), it is seen that the extent of Cu-Se and In-Se secondary phase formation decreased. However, the secondary phases still exists, since the precursor is Se deficient.

7.4.3.4 Proposed solutions and plans

In light of the results reported in the preceding subsections it was proposed to increase the Se concentration in the precursor in a controllable manner. A reproducible way of achieving this

is to establish a Se over pressure by depositing a thin layer InSe or Se on the bottom of the quartz lid of the RTP susceptor. This approach will be explored in subsequent studies to be conducted at the University of Florida.

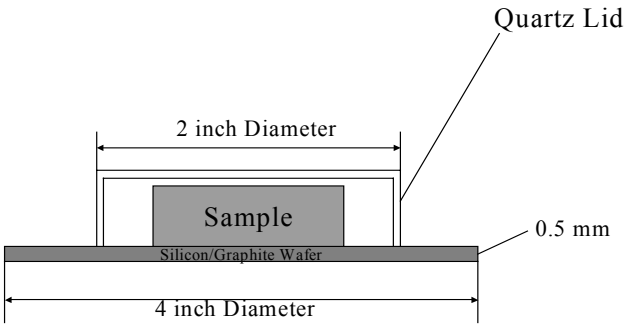

Figure 7.15. Susceptor design I.

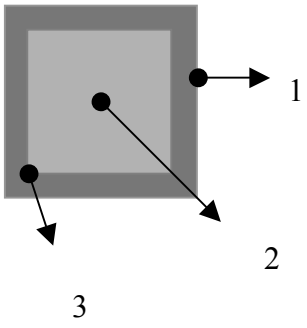

Figure 7.16. Non-uniformly heated surface.

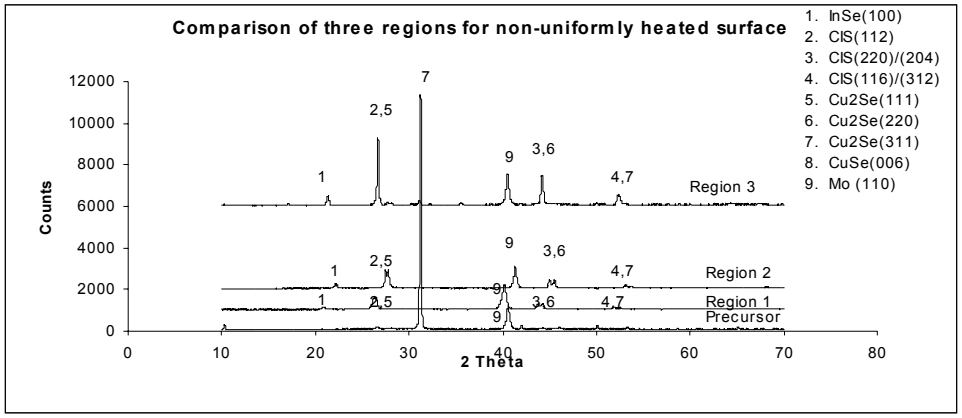

Figure 7.17. XRD pattern of different regions of the non-uniform heated surface (see Figure 7-16).

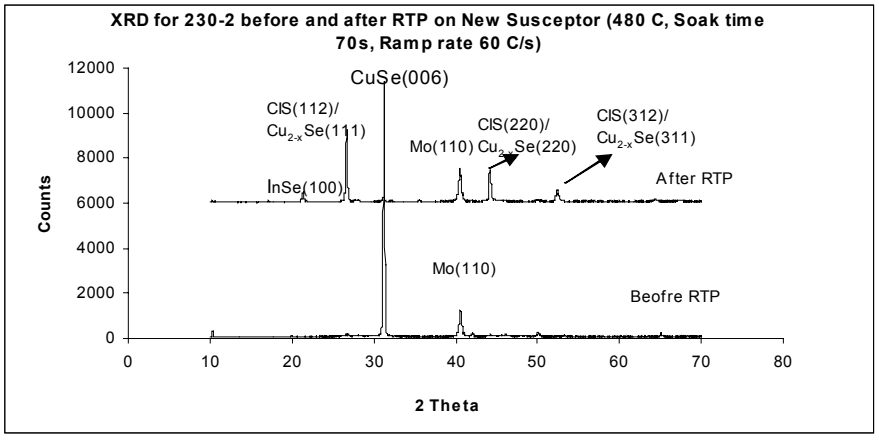

Figure 7.18. XRD spectra for sample 230-2 on new susceptor design with set-point temperature 600°C, soak time 120 s, and ramp rate 60°C/s.

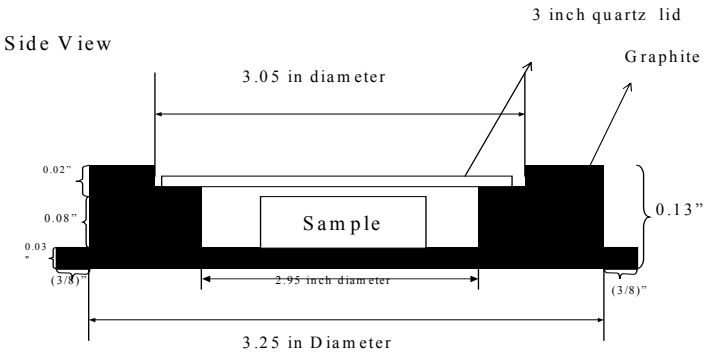

Figure 7.19. New susceptor design II.

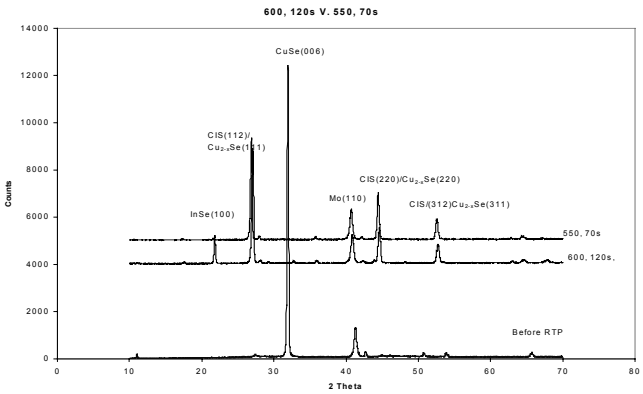

Figure 7.21. XRD spectra for two samples from the 230 series processed at set-point temperature 600°C, soak time 120s, and ramp rate 60°C/s, and another sample at 550°C, soak time 70 s, and ramp rate 60°C/s

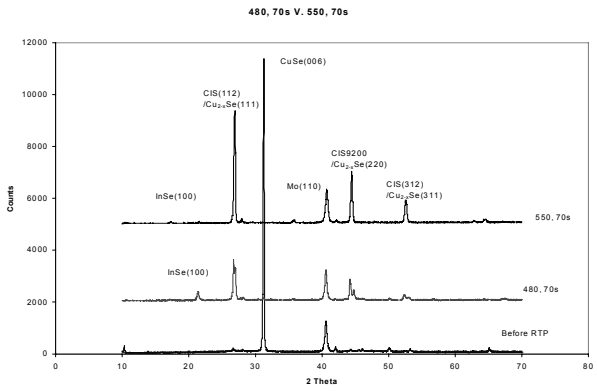

Figure 7.22. XRD patterns for two samples from the 230 series processed at set-point temperature 480°C, soak time 70s, and ramp rate 60°C/s, and another sample at 550°C, soak time 70s, and ramp rate 60°C/s

7.5 References

[1] R. Friedfeld, R.P. Raffaelle, and J.G. Mantovani, "Electrodeposition of $CuIn_xGa_{1-x}Se_2$ Thin Films", *Solar Energy Materials and Solar Cells*, Vol. 58, pp. 375-385 (1999).

[2] I. Forbes, F.O. Adurodija and M.J. Carter, "Novel Sputtered Ultra-Thin CuIn Multilayers for High Quality $CuInSe_2$ Thin Films", *Proc. 6th Internat. PVSEC, New Delhi*, pp. 1965-1968 (1996).

[3] S.R. Kumar, R.B. Gore and R.K. Pandey, "Rapid Thermal Annealing of Cu-In/Se Stacked Layers", *Semicond. Sci. Technol*, Vol. 6, pp. 940-941 (1991).

PART 8

Progress on the Calculation of the 500°C Isothermal Section of Cu-In-Se System

Abstract

Progress was made on the calculation of the 500°C isothermal section of the phase diagram of the ternary Cu-In-Se system. A preliminary though comprehensive thermodynamic model was developed to describe each phase in the Cu-In-Se system. The calculated phase diagram is in reasonable agreement with experimental results reported in the literature

Section Contents

8.1 Brief Overview

8.1.1 Participants

Faculty Adviser: Prof. Tim Anderson

Research Assistant: Lei L. Kerr

8.1.2 Objective

The objective of this project is to provide a thermodynamic foundation to understand reaction processes for the manufacture of CIS and CIGS solar cells.

8.2 Introduction

The phase equilibria of Cu-In-Se alloys are of interest for basic research as well as for technical applications: the α phase of the system, a semiconductor with the chalcopyrite structure and the stoichiometric composition $CuInSe_2$, represents one of the most promising materials for high-efficiency thin-film photovaltaic devices. A thorough investigation of the entire Cu-In-Se phase diagram was carried out by Gödecke et al. [1]. In our work, a preliminary though comprehensive thermodynamic model was developed to describe each phase in the Cu-In-Se system. The calculated phase diagram is compared with the experimental phase diagram by Gödecke et al. [1].

8.3 Phase Equilibria

The most complete and recent study of phase equilibria in the Cu-In-Se system was conducted by Gödecke et al. [1] using DTA, XRD, LM, TEM and SEM measurements. Figure 8.2 shows the experimental isothermal section of the Cu-In-Se phase diagram at 500ºC over the entire composition triangle. The isothermal section at 500ºC is of major technical importance for the fabrication of thin films for photovoltaic devices because precursor films are often processed at a temperature near 500ºC. A summary of the phase equilibria is listed in the Table 8.1. There are sixteen phases participating in the equilibria, of which nine are solutions: α-CIS ($CuInSe_2$), β_R-CIS ($Cu_1In_3Se_5$), γ-CIS($Cu_1In_5Se_8$), β_H-CIS($Cu_2In_4Se_7$), α_{Cu}, η (Cu_2In_1), δ (Cu_7Se_3), β-Cu_2Se,

and finally, the liquid CIS solution. The other phases are line compounds: In_5Se_7, In_9Se_{11}, In_6Se_7, γ-In_2Se_3, β-In_2Se_3, InSe, and In_4Se_3. According to [1], in the Se-rich and In-rich corners the isothermal section at 500ºC features small regions of liquid phase (L_4 and L_2, repectively). The α-CIS establishes equilibria with eight solid phases and one liquid phase(L_4). Among the solid phases, α_{Cu}, η (Cu_2In_1), and δ (Cu_7Se_3) originate from the In-Cu boundary, β-Cu_2Se from the Cu-Se boundary, and InSe and In_4Se_3 from In-Se boundary. The remaining two phases in equilbrium with α-CIS ($CuInSe_2$) are β_R-CIS ($Cu_1In_3Se_5$) and β_H-CIS($Cu_2In_4Se_7$).

8.4 Thermodynamic Modeling

8.4.1 α-CIS ($CuInSe_2$)

To model the homogeneity range, the non-stoichiometric chalcopyrite compound α-CIS($CuInSe_2$) is described by a three sublattice model (Compound Energy Model). Four main defects are incorprated into this sublattice model: Va_{Cu}, Va_{Se}, In_{Cu}, Cu_{In}. (e.g., Va_{Cu} denotes a vacancy on a Cu site). This model is represented by:

$$(\mathbf{Cu}, Va, In)^{I}_{1}(\mathbf{In}, Cu)^{II}_{1}(\mathbf{Se}, Va)^{III}_{2}$$

where the superscripts, I, II and III identify the sublattices. The major constituents on the normal sublattices are highlighted in boldface font. The Gibbs energy of the α phase can also be expressed by the equation $G^{\alpha} = {}^{ref}G^{\alpha} + {}^{ID}G^{\alpha} + {}^{EX}G^{\alpha}$ (where "ref" denotes a reference composition, "ID" is the ideal mixing, and "EX" is the excess mixing term resulting from non-ideality), where

$$\begin{aligned}
{}^{ref}G^{\alpha} = {} & + y^{I}_{Cu} y^{II}_{In} y^{III} \circ G^{\alpha}_{Cu:In:Se} + y^{I}_{Cu} y^{II}_{Cu} y^{III} \circ G^{\alpha}_{Cu:Cu:Se} \\
& + y^{I}_{Cu} y^{II}_{In} y^{III}_{Va} \circ G^{\alpha}_{Cu:In:Va} + y^{I}_{Cu} y^{II}_{Cu} y^{III}_{Va} \circ G^{\alpha}_{Cu:In:Va} \\
& + y^{I}_{In} y^{II}_{In} y^{III} \circ G^{\alpha}_{In:In:Se} + y^{I}_{In} y^{II}_{Cu} y^{III} \circ G^{\alpha}_{In:Cu:Se} \\
& + y^{I}_{In} y^{II}_{In} y^{III}_{Va} \circ G^{\alpha}_{In:In:Va} + y^{I}_{In} y^{II}_{Cu} y^{III}_{Va} \circ G^{\alpha}_{In:In:Va} \\
& + y^{I}_{Va} y^{II}_{In} y^{III} \circ G^{\alpha}_{Va:In:Se} + y^{I}_{Va} y^{II}_{Cu} y^{III} \circ G^{\alpha}_{Va:Cu:Se} \\
& + y^{I}_{Va} y^{II}_{In} y^{III}_{Va} \circ G^{\alpha}_{Va:In:Va} + y^{I}_{Va} y^{II}_{Cu} y^{III}_{Va} \circ G^{\alpha}_{Va:In:Va}
\end{aligned}$$

$$
\begin{aligned}
{}^{ID}G^{\alpha} = &+ RT(y^{I}_{Cu}\, ln\, y^{I}_{Cu} + y^{I}_{In}\, ln\, y^{I}_{In} + y^{I}_{Va}\, ln\, y^{I}_{Va}) \\
&+ RT(y^{II}_{Cu}\, ln\, y^{II}_{Cu} + y^{II}_{In}\, ln\, y^{II}_{In}) \\
&+ RT(y^{III}_{Se}\, ln\, y^{III}_{Se} + y^{III}_{Va}\, ln\, y^{III}_{Va}) \\
{}^{EX}G^{\alpha} = &\; y^{I}_{Cu} y^{I}_{In} \left[\begin{array}{l} y^{II}_{Cu} y^{III}_{Se} \left({}^{0}L^{\alpha}_{Cu,In:Cu:Se} \right) + y^{II}_{In} y^{III}_{Se} \left({}^{0}L^{\alpha}_{Cu,In:In:Se} \right) \\ + y^{II}_{Cu} y^{III}_{Va} \left({}^{0}L^{\alpha}_{Cu,In:Cu:Va} \right) + y^{II}_{In} y^{III}_{Va} \left({}^{0}L^{\alpha}_{Cu,In:In:Va} \right) \end{array} \right] \\
&+ y^{I}_{Cu} y^{I}_{Va} \left[\begin{array}{l} y^{II}_{Cu} y^{III}_{Se} \left({}^{0}L^{\alpha}_{Cu,Va:Cu:Se} \right) + y^{II}_{In} y^{III}_{Se} \left({}^{0}L^{\alpha}_{Cu,Va:In:Se} \right) \\ + y^{II}_{Cu} y^{III}_{Va} \left({}^{0}L^{\alpha}_{Cu,Va:Cu:Va} \right) + y^{II}_{In} y^{III}_{Va} \left({}^{0}L^{\alpha}_{Cu,Va:In:Va} \right) \end{array} \right] \\
&+ y^{II}_{Cu} y^{II}_{In} \left[\begin{array}{l} y^{I}_{Cu} y^{III}_{Se} \left({}^{0}L^{\alpha}_{Cu:Cu,In:Se} \right) + y^{I}_{In} y^{III}_{Se} \left({}^{0}L^{\alpha}_{In:Cu,In:Se} \right) \\ + y^{I}_{Cu} y^{III}_{Va} \left({}^{0}L^{\alpha}_{Cu:Cu,In:Va} \right) + y^{II}_{In} y^{III}_{Va} \left({}^{0}L^{\alpha}_{In:Cu,In:Va} \right) \\ + y^{I}_{Va} y^{III}_{Se} \left({}^{0}L^{\alpha}_{Va:Cu,In:Se} \right) + y^{I}_{Va} y^{III}_{Va} \left({}^{0}L^{\alpha}_{Va:Cu,In:Va} \right) \end{array} \right] \\
&+ y^{III}_{Va} y^{III}_{Se} \left[\begin{array}{l} y^{I}_{Cu} y^{II}_{Cu} \left({}^{0}L^{\alpha}_{Cu:Cu:Se,Va} \right) + y^{I}_{In} y^{II}_{Cu} \left({}^{0}L^{\alpha}_{In:Cu:Se,Va} \right) \\ + y^{I}_{Cu} y^{II}_{In} \left({}^{0}L^{\alpha}_{Cu:In:Se,Va} \right) + y^{I}_{In} y^{II}_{In} \left({}^{0}L^{\alpha}_{In:In:Se,Va} \right) \\ + y^{I}_{Va} y^{II}_{Cu} \left({}^{0}L^{\alpha}_{Va:Cu:Se,Va} \right) + y^{I}_{Va} y^{II}_{In} \left({}^{0}L^{\alpha}_{Va:In:Se,Va} \right) \end{array} \right]
\end{aligned}
$$

and where y^{I}_{i}, y^{II}_{i} and y^{III}_{i} are site fractions on the three sublattices. In these expressions ºG is the Gibbs energy of an end member (12 in this system), and it can represent a real or a fictitious compound. The tems showing the "^{0}L" symbol are interaction parameters that describe the interaction between species on each sublattice.

The Gibbs energies of a defect-free $CuInSe_2$, , ${}^{\circ}G^{\alpha}_{Cu:In:Se}$ has been calculated by Lamoreaux et al. [6]. They determined that the enthalpy of formation for $CuInSe_2$ is $\Delta H^{0}_{f,298} = -48.9$ kcal mol^{-1} and $\Delta S^{0}_{f,298} = 2.4$ cal mol^{-1} K^{-1}. Then, the Gibbs energy of formation is calculated using the approximate relation (assuming $\Delta C_p = 0$):

$$\Delta G^{0}_{f,T} = \Delta H^{0}_{f,298} - T\Delta S^{0}_{f,298} = -205.38 - 7.79184\ \text{kJ mol}^{-1}$$

The Gibbs energies of the end-members that have one defect ($^{\circ}G^{\alpha}_{Cu:Cu:Se}$, $^{\circ}G^{\alpha}_{Va:In:Se}$, $^{\circ}G^{\alpha}_{In:In:Se}$, $^{\circ}G^{\alpha}_{Cu:In:Va}$) and retrieved from the calculations of Stanbery [2] and Zhang et al. [3, 4]. The latter authors calculated cation defect and defect complex formation enthalpies in $CuInSe_2$. According to their study, the formation energy ΔH_f (j,q =0) of a neutral (q = 0) defect of type *j* in $CuInSe_2$ depends on the chemical potentials μ as follows:

$$\Delta H_f\,(j,q=0) = E(j,q=0) - E(CuInSe_2) + n_{Cu}\mu^{j}_{Cu} + n_{In}\mu^{j}_{In} + n_{Se}\mu^{j}_{Se}$$

where E(j, q=0) is the total energy of a supercell containing a neutral defect of type *j*, E($CuInSe_2$) is the total energy for the same supercell in the absence of the defect. The symbol "n" is used along with a corresponding subscript to denote the numbers of Cu, In and Se atoms that are transferred from the defect-free supercell to the reservoirs in forming the defect cell. Stanbery [2] also summarized their calculation results of formation enthalpies. Stanbery calculated the lattice entropy for the α and β-CIS phases by employing a cluster-based approach based on a 16-site cluster of four normally occupied tetrahedra. The species in his calculation are clusters of primitive chalcopyrite unit cells within which lattice point defects or their associates are embedded. He calculated the configurational excess entropies using a mixing model incorporating Hagemark's nearest-neighbor site exclusion correction. Stanbery's calculation is also on the basis of a deviation from that of the same quantity of non-defective CIS. The summary of both calculation results is listed in the Table 8.2. The Gibbs energy deviation from defect-free CIS is then calculated in a straightforward fashion.

Based on the above ideas, we have the following relations:

$$^{\circ}G^{\alpha}_{Va:In:Se} = {}^{\circ}G^{\alpha}_{Cu:In:Se} + \Delta\,{}^{\circ}G^{\alpha}_{Va_{Cu}} - GCUFCC\#$$

$$^{\circ}G^{\alpha}_{In:In:Se} = {}^{\circ}G^{\alpha}_{Cu:In:Se} + \Delta\,{}^{\circ}G^{\alpha}_{In_{Cu}} - GCUFCC\#+GIN\_S\#$$

$$^{\circ}G^{\alpha}_{Cu:Cu:Se} = {}^{\circ}G^{\alpha}_{Cu:In:Se} + \Delta\,{}^{\circ}G^{\alpha}_{Cu_{In}} + GCUFCC\#-GIN\_S\#$$

$$^{\circ}G^{\alpha}_{Cu:In:Va} = {}^{\circ}G^{\alpha}_{Cu:In:Se} + \Delta\,{}^{\circ}G^{\alpha}_{Va_{Se}} - GSE\_S\#$$

For the end-members that have two defects, we can use a simple reciprocal relation [5] to obtain the corresponding Gibbs energy expressions

$$^{\circ}G^{\alpha}_{Va:Cu:Se} = {}^{\circ}G^{\alpha}_{Cu:Cu:Se} + {}^{\circ}G^{\alpha}_{Va:In:Se} - {}^{\circ}G^{\alpha}_{Cu:In:Se}$$

$$^{\circ}G^{\alpha}_{In:Cu:Se} = {}^{\circ}G^{\alpha}_{Cu:Cu:Se} + {}^{\circ}G^{\alpha}_{In:In:Se} - {}^{\circ}G^{\alpha}_{Cu:In:Se}$$

$$^{\circ}G^{\alpha}_{Cu:Cu:Va} = {}^{\circ}G^{\alpha}_{Cu:Cu:Se} + {}^{\circ}G^{\alpha}_{Cu:In:Va} - {}^{\circ}G^{\alpha}_{Cu:In:Se}$$

$$^{\circ}G^{\alpha}_{Va:In:Va} = {}^{\circ}G^{\alpha}_{Cu:In:Va} + {}^{\circ}G^{\alpha}_{Va:In:Se} - {}^{\circ}G^{\alpha}_{Cu:In:Se}$$

$$^{\circ}G^{\alpha}_{In:In:Va} = {}^{\circ}G^{\alpha}_{Cu:In:Va} + {}^{\circ}G^{\alpha}_{In:In:Se} - {}^{\circ}G^{\alpha}_{Cu:In:Se}$$

The Gibbs energy of the end-members that have three or more than three defects are simply set to an arbitrarily large value, for example 0 [5].

The interaction Parameter L obeys the following relations that are invoked in the optimization study in order to reduce the parameters:

$$^{\alpha}L^{0}_{Cu,In:*:*} = {}^{\alpha}L^{0}_{Cu,In:In:Se} = {}^{\alpha}L^{0}_{Cu,In:Cu:Se} = {}^{\alpha}L^{0}_{Cu,In:In:Va} = {}^{\alpha}L^{0}_{Cu,In:Cu:Va}$$

$$^{\alpha}L^{0}_{Cu,Va*:*} = {}^{\alpha}L^{0}_{Cu,Va:In:Se} = {}^{\alpha}L^{0}_{Cu,Va:Cu:Se} = {}^{\alpha}L^{0}_{Cu,Va:In:Va} = {}^{\alpha}L^{0}_{Cu,Va:Cu:Va}$$

$$^{\alpha}L^{0}_{*:Cu,In:*} = {}^{\alpha}L^{0}_{Cu:Cu,In:Se} = {}^{\alpha}L^{0}_{In:Cu,In:Se} = {}^{\alpha}L^{0}_{In:Cu,In:Va} = {}^{\alpha}L^{0}_{Cu:Cu,In:Va} = {}^{\alpha}L^{0}_{Va:Cu,In:Se} = {}^{\alpha}L^{0}_{Va:Cu,In:Se} = {}^{\alpha}L^{0}_{Va:Cu,In:Va} = {}^{\alpha}L^{0}_{Va:Cu,In:Va}$$

$$^{\alpha}L^{0}_{*:*:Se,Va} = {}^{\alpha}L^{0}_{Cu:Cu:Se,Va} = {}^{\alpha}L^{0}_{In:Cu:Se,Va} = {}^{\alpha}L^{0}_{Va:Cu:Se,Va} = {}^{\alpha}L^{0}_{Cu:In:Se,Va} = {}^{\alpha}L^{0}_{In:In:Se,Va} = {}^{\alpha}L^{0}_{Va:In:Se,Va}$$

8.4.2 Phases β_R-CIS ($Cu_1In_3Se_5$), γ-CIS($Cu_1In_5Se_8$), and β_H -CIS($Cu_2In_4Se_7$)

The phases β_R-CIS ($Cu_1In_3Se_5$), γ-CIS($Cu_1In_5Se_8$), and β_H -CIS($Cu_2In_4Se_7$) compounds are Ordered Defect Compounds (ODC) formed by repeating periodically m units of ($2Va_{Cu} + In_{Cu}$) for every n unit of α-CIS ($CuInSe_2$) [3, 4], as given by the transformation

$$n(CuInSe2) + m(In) \rightarrow Cu_{(n-3m)}In_{(n+m)}Se_{2n} + 3m(Cu) + \Delta H_f(n,m)$$

where the subscript notation (In) and (Cu) denotes In and Cu in their respective equilibrium chemical reservoirs. The energy factor $\Delta H_f(n,m)$ is close to zero [3].

For β_R-CIS ($Cu_1In_3Se_5$), n=5 m=1, for γ-CIS($Cu_1In_5Se_8$), n=4 n=1 and for β_H -CIS($Cu_2In_4Se_7$), n=7 m=1, hence it follows that

$$°G(\beta_R\text{-CIS } (Cu_1In_3Se_5)) = 0.5\times°G\ (2Va_{Cu} + In_{Cu}) + 2.5\times°G(\alpha\text{-CIS } (CuInSe_2))$$

$$°G(\gamma\text{-CIS}(Cu_1In_5Se_8)) = °G\ (2Va_{Cu} + In_{Cu}) + 4°G(\alpha\text{-CIS } (CuInSe_2))$$

$$°G(\beta_H\text{-CIS}(Cu_2In_4Se_7)) = 0.5\times°G\ (2Va_{Cu} + In_{Cu}) + 3.5\times°G(\alpha\text{-CIS } (CuInSe_2))$$

Similar to the approach followed for modeling a non-stoichiometric α-CIS ($CuInSe_2$) phase, we also use three sublattice model to describe these compounds:

For β_R -CIS ($Cu_1In_3Se_5$) phase : $(\mathbf{Cu}, Va, In)^{I}_{1}(\mathbf{In}, Cu)^{II}_{3}(\mathbf{Se}, Va)^{III}_{5}$

For γ - CIS($Cu_1In_5Se_8$) phase : $(\mathbf{Cu}, Va, In)^{I}_{1}(\mathbf{In}, Cu)^{II}_{5}(\mathbf{Se}, Va)^{III}_{8}$

For β_H-CIS($Cu_2In_4Se_7$) phase : $(\mathbf{Cu}, Va, In)^{I}_{2}(\mathbf{In}, Cu)^{II}_{4}(\mathbf{Se}, Va)^{III}_{7}$

The Gibbs energy for these compounds can also be expressed in the similar fashion as α-CIS ($CuInSe_2$). We can describe the Gibbs energy of the end-members of these compounds in relation to the Gibbs energy of the end-members of α-CIS ($CuInSe_2$) by the following:

$$^{\circ}G^{\beta_R}_{i:j:k} = 2.5\times{}^{\circ}G^{\alpha}_{i:j:k},\ {}^{\circ}G^{\beta_H}_{i:j:k} = 3.5\times{}^{\circ}G^{\alpha}_{i:j:k},\ {}^{\circ}G^{\gamma}_{i:j:k} = 4\times{}^{\circ}G^{\alpha}_{i:j:k}$$

where i, j, and k represent the various sublattice constituents. For example, $^{\circ}G^{\beta_R}_{Cu:In:Se} = 2.5\times{}^{\circ}G^{\alpha}_{Cu:In:Se}$.

Finally, the interaction parameters are as follows:

$$^{\beta_R}L^{0}_{Cu,In:*:*} = 2.5\times{}^{\alpha}L^{0}_{Cu,In:*:*} + V_{11},\ {}^{\beta_H}L^{0}_{Cu,In:*:*} = 3.5\times{}^{\alpha}L^{0}_{Cu,In:*:*} + V_{21},\ {}^{\gamma}L^{0}_{Cu,In:*:*} = 4\times{}^{\alpha}L^{0}_{Cu,In:*:*} + V_{31}$$
$$^{\beta_R}L^{0}_{Cu,Va:*:*} = 2.5\times{}^{\alpha}L^{0}_{Cu,Va*:*} + V_{12},\ {}^{\beta_H}L^{0}_{Cu,Va:*:*} = 3.5\times{}^{\alpha}L^{0}_{Cu,Va*:*} + V_{22},\ {}^{\gamma}L^{0}_{Cu,Va:*:*} = 4\times{}^{\alpha}L^{0}_{Cu,Va:*:*} + V_{32}$$
$$^{\beta_R}L^{0}_{*:Cu,In:*} = 2.5\times{}^{\alpha}L^{0}_{*:Cu,In:*} + V_{13},\ {}^{\beta_H}L^{0}_{*:Cu,In:*} = 3.5\times{}^{\alpha}L^{0}_{*:Cu,In:*} + V_{23},\ {}^{\gamma}L^{0}_{*:Cu,In:*} = 4\times{}^{\alpha}L^{0}_{*:Cu,In:*} + V_{33}$$
$$^{\beta_R}L^{0}_{*:*:Se,Va} = 2.5\times{}^{\alpha}L^{0}_{*:*:Se,Va} + V_{14},\ {}^{\beta_H}L^{0}_{*:*:Se,Va} = 3.5\times{}^{\alpha}L^{0}_{*:*:Se,Va} + V_{24},\ {}^{\gamma}L^{0}_{*:*:Se,Va} = 4\times{}^{\alpha}L^{0}_{*:*:Se,Va} + V_{34}$$

where V_{11}, V_{12}, V_{13}, V_{14},V_{21}, V_{22}, V_{23}, V_{24}, V_{31}, V_{32}, V_{33}, and V_{34} are the parameters that need to be optimized.

8.4.3 FCC(Cu) phase

A regular solution model is used to describe the Gibbs energy of fcc(Cu) phase.

(**Cu**, Se, In)

Combining the previous Cu-Se and Cu-In binary assessment work, we add the ternary interaction parameter ${}^{CuFcc}L^{0}_{Cu,In,Se}$. This parameter needs to be optimized.

8.4.4 Phase β-Cu_2Se phase

The β-Cu_2Se are described by the sublattice model with two Cu sublattices and one Se sublattice represented by the formula:

$$(\mathbf{Cu},In,Va)_1(\mathbf{Se},Va)_1(\mathbf{Cu})_1$$

We add a ternary interaction parameter, ${}^{\beta-Cu_2Se}L^{0}_{Cu,In,Va:Se:Cu}$ to the binary Cu-Se system to model the In solubility.

8.4.5 η(Cu_2In_1) and δ(Cu_7In_3) phases

In the binary assessment work, both phases are described by a two-sublattice model. In order to model the solubility, we modified the two sublattice model so that all the three elements will be involved:

$(Cu, In, Se)_2(Cu, In, Se)_1$ for η(Cu_2In_1) phase

$(Cu, In, Se)_7(Cu, In, Se)_3$ for δ(Cu_7In_3) phase

In a fashion analogous to the previous section we add the ternary interaction parameter ${}^{\phi}L^{0}_{Cu,In,Se:*}$, ${}^{\phi}L^{0}_{*:Cu,In,Se}$, where ϕ stands η($Cu_2In_1$), δ($Cu_7In_3$) phases.

8.4.6 Liquid phase

The liquid phase is described by an ionic sublattice model with two sublattices . Based on the work on the modeling of liquid phase in Cu-Se, In-Se and Cu-In three binary systems, we schematically describe the liquid phase in this ternary system as

$$(Cu^{+1},Cu^{+2}, In^{+3})p(Se^{-2},Va^{-1},Se)q$$

Therefore three ternary interaction parameters were added to the ionic liquid to describe the Gibbs energy: ${}^{Ionic\_Liq}L^{0}_{Cu^{+1},Cu^{+2},In^{+3}:Se^{-2}}$, ${}^{Ionic\_Liq}L^{1}_{Cu^{+1},Cu^{+2},In^{+3}:Se^{-2}}$

8.5 Results and Conclusions

Reasonable agreement was obtained between the model-calculated phase diagram shown in Figure 8.1 and the phase equilibrium available in the literature shown in Figure 8.2. The optimized parameters are listed in the Table 8.3. Further work needs to be done in order to get better agreement of phase equilibrium for all the phases.

Table 8.1. Experimental compositions in the Cu-In-Se system at 773K.

Phases	**Composition, at. % Se**	**Composition, at. % Cu**
α-CIS/β_R-CIS/IONIC_LIQ	0.5294/0.553/0.9852	0.1963/0.149/0.00142
IONIC_LIQ/α-CIS	0.5234/0.9904 0.5195/0.9926 0.5141/0.99285	0.2052/0.001896 0.2152/0.001942 0.2250/0.003625
α-CIS /β-Cu_2Se /IONIC_LIQ	0.5096/0.3794/0.994	0.2354/0.6157/0.00592
α-CIS /β-Cu_2Se /CU_FCC	0.5017/0.33646/0.0054	0.23895/0.6562/0.9061
α-CIS / /CU_FCC	0.5003/0/0.00296	0.2371/0.7/0.904
α-CIS / δ (Cu_7Se_3) /η(Cu_2In_1)	0.4988/0/0.0064	0.2353/0.7/0.6388
α-CIS / IN_4SE_3/η(Cu_2In_1)	0.4983/0.4286/0.001	0.2326/0/0.6225
α-CIS /IN_1SE_1_A/IN_4SE_3	0.5012/0.5/0.4286	0.2278/0/0
α-CIS / IN_1SE_1_A/β_H-CIS	0.5052/0.5/0.5141	0.22156/0/0.1388
α-CIS /β_R-CIS /β_H-CIS	0.5101/0.52795/0.523	0.2123/0.1649/0.161
IONIC_LIQ/γ- In_2Se_3/γ-CIS	0.961/0.6/0.5942	0/0/0.0332
IONIC_LIQ/γ-CIS /β_R-CIS	0.978/0.5932/0.589	0.02/0.0557/0.095
In6Se7/γ-CIS//β_R-CIS	0.538/0.5675/0.5537	0/0.0592/0.088
In6Se7/γ-CIS/ In_9Se_{11}	0.538/0.5720/0.55	0/0.052/0
In_5Se_7/γ-CIS/ In_9Se_{11}	0.5933/0.5744/0.55	0/0.0465/0
In_5Se_7/γ-CIS/β-In_2Se_3	0.5933/0.5819/0.6	0/0.0368/0

Table 8.2. Summary of the Enthalpies and Entropy [2, 3, 4]

Defect Type	ΔH^{EX} (ΔH_f)	ΔS^{EX} (ΔS_f)	$\Delta G_f = \Delta H_f - T\Delta S_f$ (Relative to defect-free CIS)	When T=773K (J mol $^{-1}$)
Va_{Cu}	57891.2	0	57891.2	57891.2
In_{Cu}	322261	0	322261	322261
Cu_{In}	148588	0	148588	148588
Va_{Se}	289456	20.6607	289456 – T*20.6607	273485.3

Table 8.3. Summary of the Optimized Parameters

Phases and Functions	Parameters
α-CIS ($CuInSe_2$)	${}^{\circ}G^{\alpha}_{Cu:In:Se}$ = CIS_A ${}^{\circ}G^{\alpha}_{Cu:Cu:Se}$ =CIS_A-GIN_S#+148588 ${}^{\circ}G^{\alpha}_{Va:In:Se}$ =CIS_A-GCUFCC#+57891.2 ${}^{\circ}G^{\alpha}_{In:In:Se}$ = CIS_A-GCUFCC#+GIN_S#+322261 ${}^{\circ}G^{\alpha}_{Cu:In:Va}$ = CIS_A-GSE_S#+289456 – T*20.6607 ${}^{\circ}G^{\alpha}_{Va:Cu:Se} = {}^{\circ}G^{\alpha}_{Cu:Cu:Se} + {}^{\circ}G^{\alpha}_{Va:In:Se} - {}^{\circ}G^{\alpha}_{Cu:In:Se}$ ${}^{\circ}G^{\alpha}_{In:Cu:Se} = {}^{\circ}G^{\alpha}_{Cu:Cu:Se} + {}^{\circ}G^{\alpha}_{In:In:Se} - {}^{\circ}G^{\alpha}_{Cu:In:Se}$ ${}^{\circ}G^{\alpha}_{Cu:Cu:Va} = {}^{\circ}G^{\alpha}_{Cu:Cu:Se} + {}^{\circ}G^{\alpha}_{Cu:In:Va} - {}^{\circ}G^{\alpha}_{Cu:In:Se}$ ${}^{\circ}G^{\alpha}_{Va:In:Va} = {}^{\circ}G^{\alpha}_{Cu:In:Va} + {}^{\circ}G^{\alpha}_{Va:In:Se} - {}^{\circ}G^{\alpha}_{Cu:In:Se}$ ${}^{\circ}G^{\alpha}_{In:In:Va} = {}^{\circ}G^{\alpha}_{Cu:In:Va} + {}^{\circ}G^{\alpha}_{In:In:Se} - {}^{\circ}G^{\alpha}_{Cu:In:Se}$ ${}^{\alpha}L^{0}_{Cu,In:*:*}$ =LCI ${}^{\alpha}L^{0}_{Cu,Va:*:*}$ =LCV ${}^{\alpha}L^{0}_{*:Cu,In:*}$ =LIC ${}^{\alpha}L^{0}_{*:*:Se,Va}$ =LSV
β_R-CIS ($Cu_1In_3Se_5$)	${}^{\circ}G^{\beta_R}_{Cu:In:Se} = 2.5\times{}^{\circ}G^{\alpha}_{Cu:In:Se}$. ${}^{\circ}G^{\beta_R}_{Cu:Cu:Se} = 2.5\times{}^{\circ}G^{\alpha}_{Cu:Cu:Se}$ ${}^{\circ}G^{\beta_R}_{Va:In:Se} = 2.5\times{}^{\circ}G^{\alpha}_{Va:In:Se}$ ${}^{\circ}G^{\beta_R}_{In:In:Se} = 2.5\times{}^{\circ}G^{\alpha}_{In:In:Se}$

	${}^{\circ}G^{\beta_R}_{Cu:In:Va} = 2.5\times {}^{\circ}G^{\alpha}_{Cu:In:Va}$ ${}^{\beta_R}L^{0}_{Cu,In:*:*} = 2.5\times LCI + V_{11}$ ${}^{\beta_R}L^{0}_{Cu,Va:*:*} = 2.5\times LCV + V_{12}$ ${}^{\beta_R}L^{0}_{*:Cu,In:*} = 2.5\times LIC + V_{13}$ ${}^{\beta_R}L^{0}_{*:*:Se,Va} = 2.5\times LSV + V_{14}$

Table 8.3 (Continued)

Phases and Functions	Parameters
β_H-CIS ($Cu_2In_4Se_7$)	${}^{\circ}G^{\beta_H}_{Cu:In:Se} = 3.5\times {}^{\circ}G^{\alpha}_{Cu:In:Se}$. ${}^{\circ}G^{\beta_H}_{Cu:Cu:Se} = 3.5\times {}^{\circ}G^{\alpha}_{Cu:Cu:Se}$ ${}^{\circ}G^{\beta_H}_{Va:In:Se} = 3.5\times {}^{\circ}G^{\alpha}_{Va:In:Se}$ ${}^{\circ}G^{\beta_H}_{In:In:Se} = 3.5\times {}^{\circ}G^{\alpha}_{In:In:Se}$ ${}^{\circ}G^{\beta_H}_{Cu:In:Va} = 3.5\times {}^{\circ}G^{\alpha}_{Cu:In:Va}$ ${}^{\beta_H}L^{0}_{Cu,In:*:*} = 3.5\times LCI + V_{21}$ ${}^{\beta_H}L^{0}_{Cu,Va:*:*} = 3.5\times LCV + V_{22}$ ${}^{\beta_H}L^{0}_{*:Cu,In:*} = 3.5\times LIC + V_{23}$ ${}^{\beta_H}L^{0}_{*:*:Se,Va} = 3.5\times LSV + V_{24}$
γ-CIS ($Cu_1In_5Se_8$)	${}^{\circ}G^{\gamma}_{Cu:In:Se} = 4\times {}^{\circ}G^{\alpha}_{Cu:In:Se}$. ${}^{\circ}G^{\gamma}_{Cu:Cu:Se} = 4\times {}^{\circ}G^{\alpha}_{Cu:Cu:Se}$ ${}^{\circ}G^{\gamma}_{Va:In:Se} = 4\times {}^{\circ}G^{\alpha}_{Va:In:Se}$ ${}^{\circ}G^{\gamma}_{In:In:Se} = 4\times {}^{\circ}G^{\alpha}_{In:In:Se}$ ${}^{\circ}G^{\gamma}_{Cu:In:Va} = 4\times {}^{\circ}G^{\alpha}_{Cu:In:Va}$ ${}^{\gamma}L^{0}_{Cu,In:*:*} = 4\times LCI + V_{31}$ ${}^{\gamma}L^{0}_{Cu,Va:*:*} = 4\times LCV + V_{32}$ ${}^{\gamma}L^{0}_{*:Cu,In:*} = 4\times LIC + V_{33}$ ${}^{\gamma}L^{0}_{*:*:Se,Va} = 4\times LSV + V_{34}$
η (Cu_2In_1)	Except all the parameters from Cu-In binary system, the following ternary interaction parameters are added: ${}^{\eta}L^{0}_{Cu,In,Se:*} = -1029637$ ${}^{\eta}L^{0}_{*:Cu,In,Se} = -1029637$

Table 8.3 (Continued)

Phases and Functions	Parameters
β-Cu_2Se	Except all the parameters from Cu-Se binary system, the following ternary interaction parameters are added: ${}^{\beta-Cu_2Se}L^{0}_{Cu,In,Va:Se:Cu}$=-20000
δ (Cu_7In_3)	Except all the parameters from Cu-In binary system, the following ternary interaction parameters are added: ${}^{\delta}L^{0}_{Cu,In,Se:*}$=-90000 ${}^{\delta}L^{0}_{*:Cu,In,Se}$=-90000
Fcc (Cu)	Except all the parameters from Cu-In and Cu-Se binary system, the following ternary interaction parameters are added: ${}^{CuFcc}L^{0}_{Cu,In,Se}$=-90000
Ionic_Liq	Except all the parameters from Cu-In and Cu-Se binary system, the following ternary interaction parameters are added: ${}^{Ionic\_Liq}L^{0}_{Cu^{+1},Cu^{+2},In^{+3}:Se^{-2}}$=-46015 ${}^{Ionic\_Liq}L^{1}_{Cu^{+1},Cu^{+2},In^{+3}:Se^{-2}}$=9015
Functions	CIS_A=GCUFCC#+2*GSE_S#+GIN_S#-205380-10.08*T LCI =-15036 LCV=-8745 LIC=-60657 LSV =-48548 V_{11} = 350000 V_{12}= 0 V_{13}= 200000 V_{14}=20000 V_{21} = 400000 V_{22}= 900 V_{23}= 550000 V_{24}=30000 V_{31}= 50000 V_{32}= -90000 V_{33}= 180000 V_{34}=280000

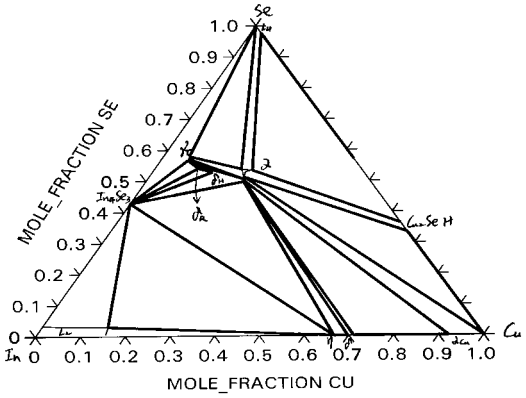

Figure 8.1 Calculated Cu-In-Se 773 K isothermal section.

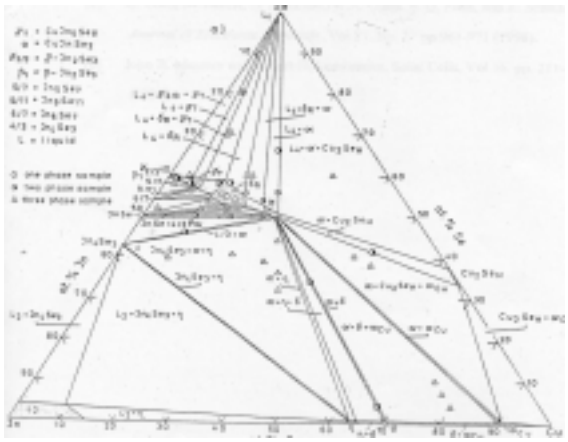

Figure 8.2 Experimental Cu-In-Se 773 K isothermal section.

8.6 References

[1] T. Gödecke, T. Haalboom, and F. Ernst, *Zeitschrift für Metallkunde*, Vol. 91, No. 8 pp. 622-662 (2000).

[2] B.S. Stanbery, Ph.D. Dissertation, University of Florida (2001).

[3] S. B. Zhang, Su-Huai Wei, and Alex Zunger, *Physical Review B*, Vol. 57, No. 16 pp. 9642 – 9656 (1998).

[4] S. B. Zhang, Su-Huai Wei, and Alex Zunger, *Physical Review Letters*, Vol. 78, No. 21, pp. 4059–4062 (1997).

[5] Q. Chen, M. Hillert, B. Sundman, W.A. Oates, S. G. Fries, and R. Schmid-Fetzer, *J. Electronic Mat.*, Vol. 27, No. 3, pp. 961-971 (1998).

[6] John B. Mooney and Robert H. Lamoreaux, *Solar Cells*, Vol. 16, pp. 211-220 (1986).

PART 9

Development of Alternative Buffer Layers

Abstract

The buffer layer materials of CdS, (Cd,Zn)S, ZnS, or $In(OH)_xS_y$ was deposited on the soda-lime glass substrates, $Cu(In,Ga)Se_2$ (CIGS), or $Cu(In,Ga)(Se,S)_2$ (CIGSS) thin films by the Chemical-Bath-Deposition (CBD) process. The impurities in the deposited films and their atomic concentration were characterized by the X-ray Photoelectron Spectroscopy (XPS) and Auger Electron Spectroscopy (AES) analyses. In addition, the AES was used to depth profile the samples. The band-gap energy of the deposited $In(OH)_xS_y$ thin films was determined from the optical absorption data. Both the CIGS and CIGSS samples deposited with the CdS, (Cd,Zn)S, ZnS, or $In(OH)_xS_y$ buffer layers by the CBD process were fabricated into solar cells. The current-voltage (I-V) characteristics of these cells with the alternative buffer layers were measured, and the results were compared to the cells deposited with CBD CdS buffer layers. The results show comparable performance among these cells, and further optimization of the deposition conditions should improve the performance of the cells deposited with the alternative buffer layers.

Section Contents

9.1 Brief Overview

9.1.1 Participants

Faculty Adviser: Prof. Sheng S. Li

Research Assistants: Chia-Hua Huang

9.1.2 Objectives

The objective of this research task is to develop and optimize the chemical-bath-deposited (CBD) CdS and CdS-free buffer layers for CIS solar cells.

9.2 Introduction

In a typical CIGS-based solar cell a very thin CdS buffer layer (< 500Å) is usually deposited between the ZnO window layer and the CIGS absorber layer in order to achieve high conversion efficiency. Among various buffer layer materials such as CdS, (Cd,Zn)S, ZnS, $Zn(O,S,OH)_x$, ZnO, ZnSe, $In_x(OH,S)_y$, In_2S_3, $In(OH)_3$, SnO_2, $Sn(S,O)_2$, ZnSe, or ZrO_2 deposited by CBD, ALE, MOCVD, or other deposition processes, the best performance CIGS solar cell with a total-area conversion efficiency of 18.8% [1] and other high-efficiency (> 17%) CIGS solar cells [2 and 3] were obtained by using the CBD CdS buffer layers. However, the role of CBD CdS buffer layer on the CIGS cell performance is not well understood. In view of the ability of depositing large area and uniform films, the non-vacuum low-temperature CBD process is very advantageous for manufacturing low-cost photovoltaic devices. Although a dry vacuum process has advantages for in-line manufacturing, the CBD process provides a simple, flexible, and cost-effective means for the deposition of buffer layers on the CIS-based solar cells. It has been reported that Cd-partial electrolyte treatment [4] modifies the CIGS surface favorably as evidence by the improvement in performance of CIGS solar cells [5]. Unfortunately, the basic mechanisms responsible for the cell performance are still not clear.

Using wider band-gap materials to replace the CdS ($E_g \approx 2.4$eV) buffer layer could improve the quantum efficiency of the CIGS cell at shorter wavelengths, resulting in an increase of the short- circuit current. The (Cd,Zn)S buffer layer has a band-gap energy greater than 2.4eV, and can provide a better lattice match to the CIGS absorber layer. The toxicity of cadmium (Cd) and the desirability of using a wider band-gap material to achieve a higher spectral response in the blue region have motivated the search for other alternative buffer layer materials. Using ZnS ($E_g \approx 3.6$eV) and $In(OH)_xS_y$ ($E_g \approx 2.54$eV [6]) buffer layers for the CIGS solar cells have achieved high active-area conversion efficiencies of 16.9% [7] and 15.7% [8], respectively. Thus, both ZnS and $In(OH)_xS_y$ thin films are promising candidates for the Cd- free buffer layers among the reported alternative materials.

9.3 Processing

9.3.1 The Chemical Bath Deposition (CBD) Conditions

In the deposition of solid thin films in a chemical bath by the CBD process the nucleation centers are regularly formed by the absorption of metal hydroxo species on the surface of the substrate. The initial layer of the thin film is formed through the replacement of hydroxo group by the sulphide ions, and subsequently the solid film is grown by the condensation of metal and sulphide ions onto the top of the initial layer.

The aqueous solution consisting of 2.4×10^{-4}M $CdCl_2$, 2.38×10^{-3}M NH_2CSNH_2, 7.43×10^{-4}M NH_4Cl, and 6.61×10^{-4}M NH_4OH at a bath temperature in the range of 80 to 85°C was applied for the deposition of CdS films. The CBD $In(OH)_xS_y$ films were deposited using a freshly prepared aqueous solution of 0.005M indium chloride and 0.15M thioacetamide at 70°C with deposition times varied between 15 and 25 minutes and with a pH value of 1.8. In order to avoid nucleation centers in the bath for the deposition of $In(OH)_xS_y$, the insoluble particles present in the stock solution of thioacetamide were eliminated by filtration. The complexing agent, acetic acid, was added into the bath during the deposition of $In(OH)_xS_y$ as a new deposition condition to improve the film quality. The deposition of (Cd,Zn)S buffer layers was carried out with 1.2×10^{-3}M $CdCl_2$, 6.27×10^{-4}M $ZnCl_2$, 1.2×10^{-2}M thiourea, 5.27×10^{-4}M NH_3, and 1.39×10^{-3}M NH_4Cl, and the bath temperature was maintained at around 85°C. For the CBD ZnS films the deposition bath was prepared with an aqueous solution of 2.5×10^{-2}M $ZnSO_4$, 3.5×10^{-2}M thiourea, 1M NH_3, and 3M hydrazine at a bath temperature varied between 70 and 80°C.

Two competitive processes, the heterogeneous process of the solid film deposited on the substrate and the homogeneous process of precipitation in the reaction bath, took place simultaneously in the chemical bath during the CBD process. In order to remove the possible precipitation, which may be attached on the surface of the films, the substrates were well rinsed with DI water after the deposition and blown dry with nitrogen stream.

9.3.2 Device Fabrication

The CdS, (Cd,Zn)S, ZnS, or $In(OH)_xS_y$ buffer layers were deposited on the CIGS and CIGSS samples provided by Institute of Energy Conversion (IEC) of the University of Delaware, ISET, or Siemens Solar Industries. The high/low resistivity ZnO bilayer films were then deposited by either MOCVD or sputtering technique on these samples. Ni/Al grids as contact pads were finally deposited to obtain the finished cells.

9.4 Characterization of CdS, (Cd,Zn)S, ZnS, and $In(OH)_xS_y$ Buffer Layers

9.4.1 Compositional Analysis

The near surface composition of the CdS, (Cd,Zn)S, ZnS, and $In(OH)_xS_y$ films deposited on the soda-lime glass substrates or CIGS samples were characterized by the X-ray Photoelectron Spectroscopy (XPS), and the results are shown in Figure 9.1. The XPS analysis was conducted by using a Physical Electronics 5100 ESCA equipped with a Mg Kα X-ray source and a hemispherical analyzer. Depth profiling was performed with an argon ion source

operating at the beam energy of 4 KeV. The charging effects were taken into account by referring the measured spectra to the binding energy peak of C 1s at 285 eV. Carbon was initially present for all films deposited by the CBD process described in section 9.2.1but became undetectable during sputter depth profiling, indicating that little carbon was incorporated in the films. Besides carbon elements of metal (Cd, Zn, or In), sulfur, and oxygen were also identified in the deposited films.

Before and after sputtering the CBD CdS films the binding energy peaks of Cd $3d_{5/2}$ and S $2p_{3/2}$ at about 405.3eV and 161.5eV were obtained, respectively. The result shows that the sulfur peak is in good agreement with the reported data (S-Cd: 161.7eV [9]). The binding energies of Cd-S (405.3eV [9]), Cd-O (405.2eV [9]), and Cd-OH (405.0eV [9]) are too close to identify the exact compounds presented in the film from the measured Cd peak at 405.3eV. Two peaks at 529.48eV and 531.09eV obtained from the deconvolution of O 1s binding energy curve demonstrate that the film consists of chemical bonds Cd-O (529.2eV [9]) and Cd-OH (530.9-532eV [9]). The estimated atomic concentration ratios of [Cd]/[S] and [S]/[O] are approximately 1.6 and 5.4, respectively. For the (Cd,Zn)S film the atomic concentration was estimated from the peak area of each element, Cd, Zn, S, and O, in the film. The XPS result indicated that a large amount of oxygen (around 40%) and a small amount of zinc (around 2%) were incorporated in the (Cd,Zn)S film. Because the precipitation of CdS is easier and faster than that of ZnS during the CBD process, the deposited (Cd,Zn)S film only had a very small quantity of zinc even though the concentration of zinc source was an order of magnitude higher than that of cadmium source in the deposition bath.

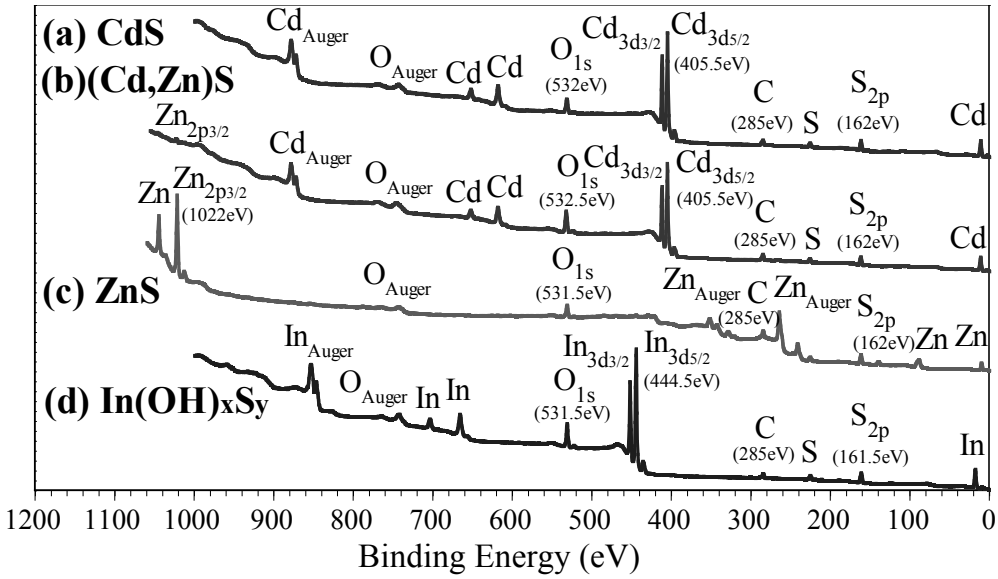

Figure 9.1 XPS spectra of CdS, (Cd,Zn)S, ZnS, or $In(OH)_xS_y$ thin films deposited on CIGS thin films by the CBD process.

For the ZnS film, the deconvolution of Zn $2p_{3/2}$ binding-energy spectrum from 1018eV to 1026eV revealed only one peak at 1022.0eV. This is consistent with the energy peaks of possible compounds ZnS and/or ZnO at 1022.0eV and 1021.8eV-1022.5eV [9], respectively. No evidence of $ZnSO_4$ was found from the Zn $2p_{3/2}$ peak, where the binding energy peak of $ZnSO_4$

is 1023.1eV. The oxygen 1s photoelectron binding energy spectra were fitted with Gaussian-Lorentzian curves both before and after sputtering the film. The XPS spectra can be represented by two peaks at about 530.6-530.1eV and 531.6eV, which correspond to the chemical bonds of Zn-O (530.4eV [9]) and metal-hydroxide compound (530.9-532eV [9]), respectively. Thus the results suggest that the CBD ZnS films might be a mixture of ZnS, ZnO, and $Zn(OH)_2$. The estimated atomic concentration ratio of Zn, S, and O was about 5:3:2 after sputtering the film for 4 minutes.

For the $In(OH)_xS_y$ films deposited by CBD with acetic acid in the bath, a binding energy peak of S $2p_{3/2}$ was found at about 161.24eV (see Figure 9.2), which can be assigned to the sulfide compound. In Figure 9.2 a very weak binding energy peak at around 168.96eV suggests that the indium sulfate (169-171eV [9]) was also present. After sputtering the film for 4 minutes no peak was found between 167ev and 173eV. We conclude that the sulfate compound only exists at the surface of the film. From Figure 9.3 the montage of binding energy distribution curves between 526eV and 544eV, it is evident that the shape of these curves changes for the oxygen 1s peak during the depth profile. As shown in the inset of Figure 9.3(a), before sputtering the XPS spectra can be represented by two peaks at 531.4eV and 529.5eV, suggesting that the oxygen is present in the form of In-OH (531.8eV [9]) and In-O (529.8eV [9]). As exhibited in the inset of Figure 9.3(b), likewise two fitted peaks at 531.5eV and 530.0eV are present in the curve after sputtering the film. This suggests that the film has more indium hydroxide than indium oxide in the near surface region. The estimated atomic concentration ratios of In, O, and S were found to be around 49.9%: 26.5%: 23.6% after sputtering for 4 minutes.

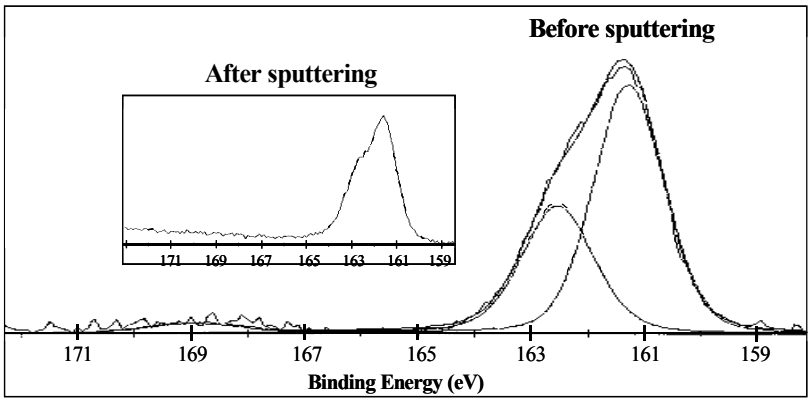

Figure 9.2 The XPS spectra of $In(OH)_xS_y$ films.

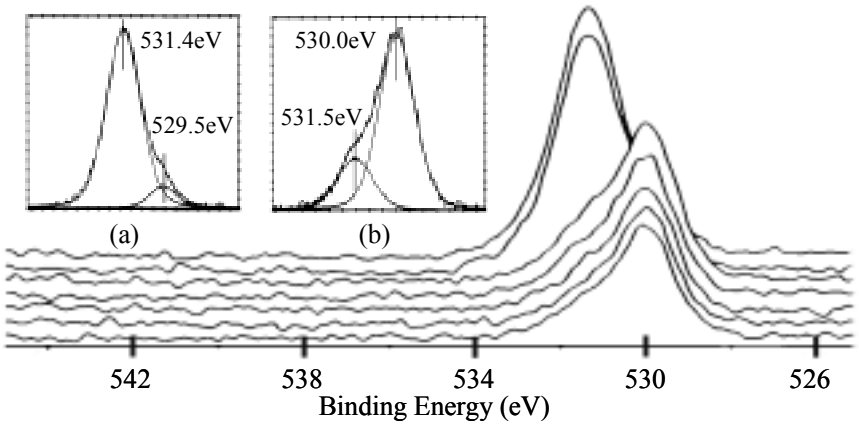

Figure 9.3 Montage of photoelectron binding energy spectra for a depth profile of an $In(OH)_xS_y$ film (View with surface curve in the background). The oxygen 1s photolectron binding energy spectra are (a) as-received surface, and (b) after sputtering for 4 minutes.

To determine whether the carbon was only present at the surface or incorporated throughout the film, Auger Electron Spectroscopy (AES) sputter depth profiles were performed. Figure 9.4 shows differential Auger spectra taken for the initial $In(OH)_xS_y$ thin film and compared to those taken after 3 and 5 minutes of sputtering. The results indicate that the carbon is only at the surface and likely derived from the ambient. The spectra in Figure 9.4 also show that after 5 minutes sputtering time, some regions of the glass were exposed as evidenced by the appearance of Ca and Si signals. An AES depth profile for the $In(OH)_xS_y$/CIGS sample is shown in Figure 9.5. The results indicate that the buffer layer barely covered the CIGS layer. Although intermixing between the $In(OH)_xS_y$ and the CIGS layers is suggested from the depth profile, this result is probably best attributed to the roughness of CIGS surface. Interdiffusion between the $In(OH)_xS_y$ buffer layer and the CIGS absorber layer is not expected to occur during the low temperature CBD process. An Ordered Vacancy Compound (OVC) such as $Cu(In,Ga)_3Se_5$, however, may be present at the interface between the $In(OH)_xS_y$ and $Cu(In,Ga)Se_2$ layers, and its high density of lattice vacancies might be more conductive to such interdiffusion. But evidence of this could not be resolved by these experiments. However, an observation of intermixing at the interface between CdS and CIGS involving the elements of S, Se, and In was reported recently [10]. Furthermore after the completed cell processing a strong intermixing between absorber (CIGS), buffer (CdS), and TCO (ZnO) material in the interface region was found [11].

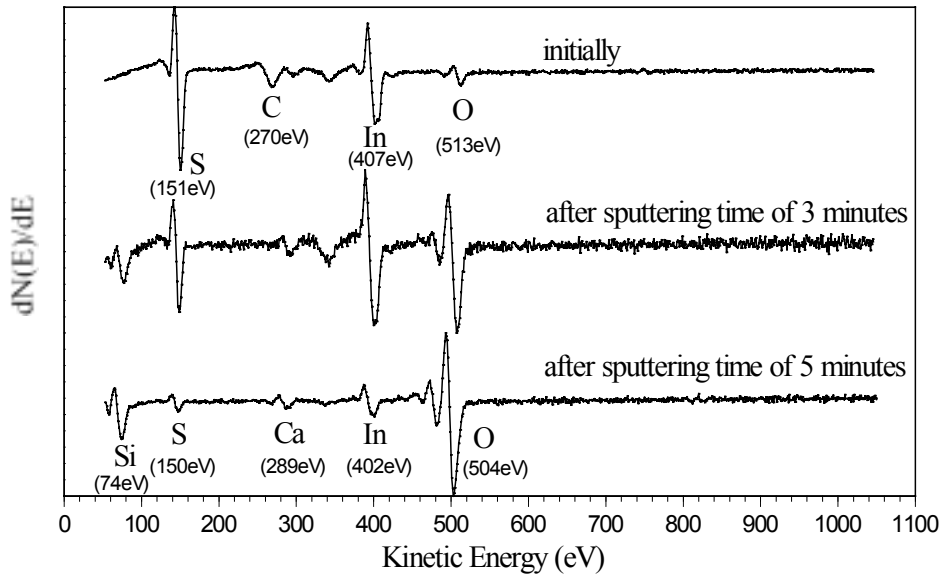

Figure 9.4 Differential Auger spectra of the $In(OH)_xS_y$ thin film deposited on the glass substrate.

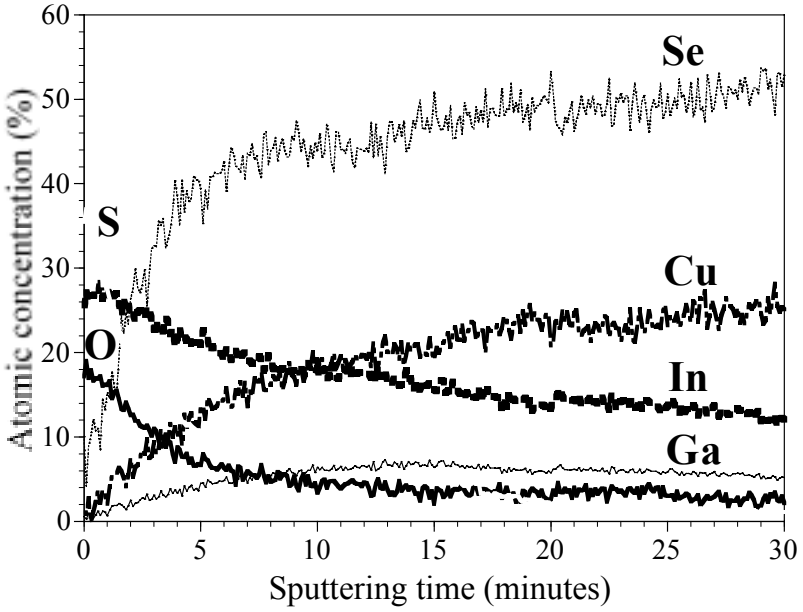

Figure 9.5 The Auger depth profile of the $In(OH)_xS_y$ thin film deposited on the CIGS cell by CBD process.

9.4.2 Optical Properties

The spectral dependence of the transmittance for the $In(OH)_xS_y$ films grown on soda-lime glass substrates was measured using a spectrophotometer, and the results are shown in the inset of Figure 9.6. The $In(OH)_xS_y$ films with shorter deposition time have higher transmittance at

shorter wavelength, which will result in an increase of short-circuit current in the CIGS cells. The buffer layers grown with longer deposition time, however, could provide a better shield effect against sputtering damage during the ZnO deposition step and thereby reduce the interface recombination. Thus, the buffer layer thickness needs to be optimized for solar cell performance. The band-gap energy of $In(OH)_xS_y$ was determined from the optical absorption data. To obtain the direct transition, $(\alpha h\nu)^2$ was plotted against $h\nu$ for the $In(OH)_xS_y$ films as illustrated in Figure 9.6. A band-gap energy of 9.54eV was obtained from the intercept of this plot. The band gap energy of $In(OH)_xS_y$, which depends on the films stoichiometry, lies between 2eV and 3.7eV, the band-gap energies of In_2S_3 and In_2O_3, respectively [12].

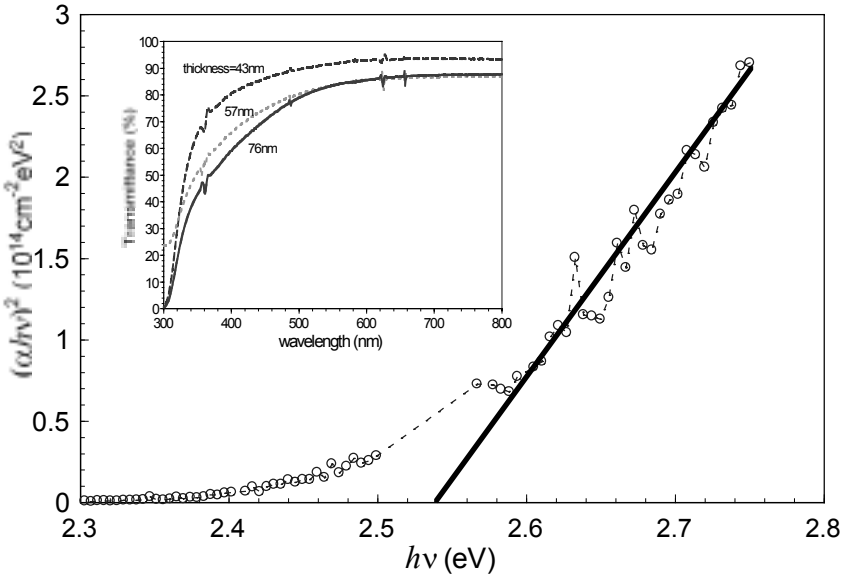

Figure 9.6 $(\alpha h\nu)^2$ versus $h\nu$ plot for the $In(OH)_xS_y$ thin film deposited on the glass substrate by the CBD process.

9.5 J-V Characterization of CIGS-based Solar Cells with CdS, (Cd,Zn)S, ZnS, or $In(OH)_xS_y$ Buffer Layers

9.5.1 The CIGS-based Cells with CdS or (Cd,Zn)S Buffer Layers

The J-V characteristics of CIGSS solar cells with CdS or (Cd,Zn)S buffer layers deposited by our baseline CBD process are shown in Figure 9.7, where the CIGSS absorbers are provided by Siemens Solar Industries. Evidently the CIGSS solar cell with CdS buffer layer has the best conversion efficiency. On the contrary the performance of the other cells deposited with (Cd,Zn)S, ZnS, or $In(OH)_xS_y$ buffer layers yields a lower conversion efficiency than that of the CdS/CIGSS cell. From the results of this study further optimization of the alternative buffer layers is needed, which includes the optimization of the deposition conditions to improve the film quality and the investigation of the effects of post-deposition annealing and light soaking on the devices.

In addition, the CdS buffer layers were also deposited by using the UF baseline CBD

process [13] with a deposition time of 30 or 40 minutes on the same sets of CIGS samples provided by IEC. The CdS/CIGS cell with a deposition time of 30 minutes has a better performance with V_{OC} =0.51V, J_{SC} =30.5mA/cm^2, F.F. =63.8%, and conversion efficiency η =9.99%, and the results are listed in Table 9.1. Apparently, the effect of annealing considerably improves the performance of these cells with either thinner or thicker buffer layers. Also the performance of the CIGS cells can be further enhanced by optimizing the thickness of the CdS buffer layers via the variation of the deposition time.

Table 9.1 The performance of CIGS Cells with CBD CdS buffer layers

	Deposition time	As deposited	Annealing 5 min.
Conversion Efficiency η	40minutes	8.87%	9.91%
	30minutes	8.41%	9.99%
Fill Factor (F.F)	40minutes	61.7%	61.9%
	30minutes	60.8%	63.8%
Open-circuit Voltage VOC	40minutes	0.4745V	0.5017V
	30minutes	0.4697V	0.5136V
Short-circuit Current Density JSC	40minutes	30.31 mA/cm2	31.88 mA/cm2
	30minutes	29.47 mA/cm2	30.51 mA/cm2

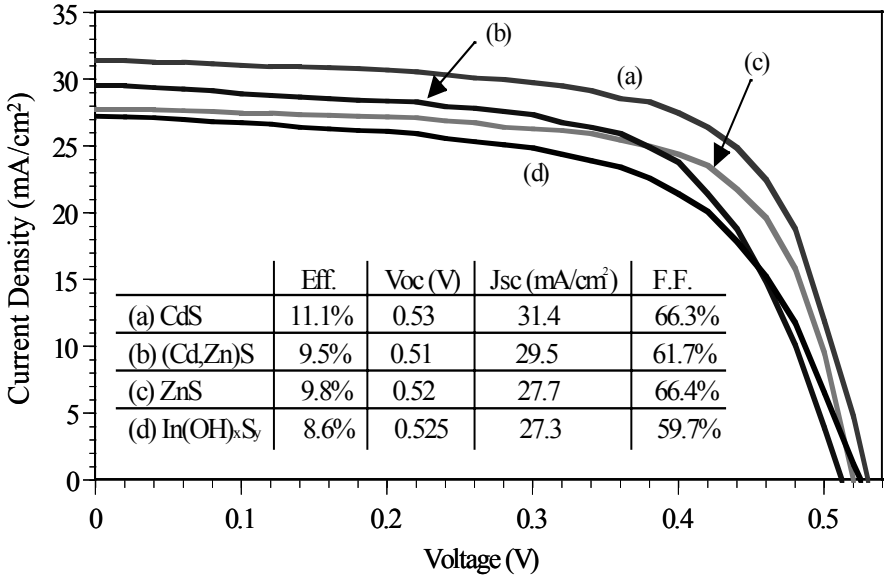

Figure 9.7 The J-V characteristics of the CIGSS cells with CdS, (Cd,Zn)S, ZnS, or $In(OH)_xS_y$ buffer layers.

9.5.2 The CIGS-based Cells with ZnS Buffer Layers

Figure 9.8 illustrates the effect of ZnS buffer layer thickness on the performance of Siemens CIGSS solar cells. By increasing the ZnS buffer layer thickness the absorption of

incident light in the ZnS layer increases, and thus the short- circuit current of the cell decreases. Due to the high resistivity of ZnS buffer layer a thick buffer layer can cause a high series resistance in the solar cell and results in poor fill factor as shown in Figure 9.8. With a higher band gap of ZnS than that of CdS, the ZnS/CIGSS cell should have a higher short-circuit current than the CdS/CIGSS cell because of the higher quantum efficiency at the shorter wavelength region. However, the highest short-circuit current obtained in this study for the ZnS/CIGSS cell was only 27.74 mA/cm^2 (see Figure 9.7), whereas for the CdS/CIGSS cell a short-circuit current of 31.4 mA/cm^2 was obtained. Thus, further optimization of ZnS layer thickness and deposition condition is needed in order to achieve the potential of ZnS buffer layers for the CIS-based cells. The performance of the CIGS solar cells fabricated from the same set of ISET CIGS samples with our ZnS or ISET CdS buffer layers is shown in Figure 9.9. The ZnS/CIGS cell has a higher short-circuit current as expected but the cell suffers a comparably low open-circuit voltage.

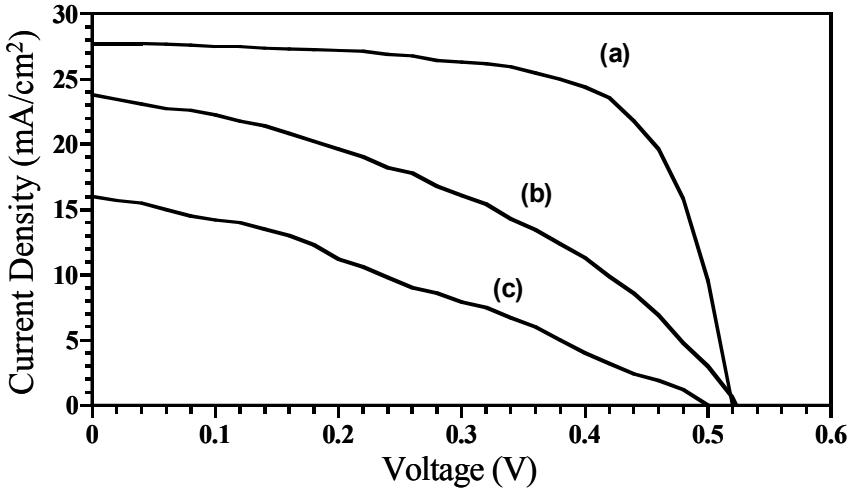

Figure 9.8 The J-V characteristics of CIGSS solar cells using different thickness of CBD ZnS buffer layers deposited for (a) 10min, (b) 20min, and (c) 25min at 70°C.

9.5.3 The CIGS-based Cells with $In(OH)_xS_y$ Buffer Layers

In order to obtain an optimum CBD process procedure for the deposition of $In(OH)_xS_y$ buffer layers, three different sequences of adding chemicals $InCl_3$ and CH_3CSNH_2, which might result in the modification of CIGS surface, were applied to the CIGS samples. It was found that the CIGS sample dipped in the DI water for a few seconds prior to the start of the deposition, which might have a pre-cleaning effect on the CIGS surface, showed the best device performance from this experiment. The results are shown in the Table 9.2.

Each I-V measurement for the CIGS cells comprised a sweep in the I_{SC} to V_{OC} direction followed immediately by a sweep from V_{OC} to I_{SC} direction. The dark- and photo- I-V curves of the $In(OH)_xS_y$/CIGS heterojunction cell before and after annealing at 200°C in the air for 20 minutes are shown in the Figure 9.10. As illustrated a hysteresis loop was observed in the photo-I-V curves of the $In(OH)_xS_y$/CIGS cells before and after annealing. On the contrary, no evidence of a hysteresis loop in the photo-I-V curves of the CdS/CIGS cells was found in this study.

Initially the device without annealing showed the inflected I-V curve. As shown in Figure 9.10 and Figure 9.11, the fill factor (F.F.), J_{SC}, V_{OC}, and hence the conversion efficiency were dramatically improved after annealing time of 20 minutes. The cells, however, showed degradation when the total annealing time was increased to 40 minutes. In order to improve the cell performance, it is necessary to optimize the annealing conditions.

Comparing the performance of CdS/CIGS cells and $In(OH)_xS_y$/CIGS cells, we have found that the latter has a much higher open-circuit voltage, a comparable short-circuit current density, and a very poor fill factor (V_{OC} =0.57V, J_{SC} =29.1mA/cm^2, F.F. =44.6%, and a low conversion efficiency η =7.39%) as shown in Figure 9.12, while the CdS/CIGS cell yielded a conversion efficiency of 9.99%, V_{OC}=0.51V, J_{SC}=30.5mA/cm^2, and F.F.=63.8%. The possible reason why the $In(OH)_xS_y$/CIGS cell has a higher V_{OC} is that the net acceptor concentration in the CIGS layer is increased and hence the depletion width is reduced. The CBD alternative buffer layer process might influence the charged states at the surface or at the grain boundaries of the CIGS layer and hence modify the electrical properties of the absorber layer as well [8]. However, the $In(OH)_xS_y$/CIGS cell has a lower J_{SC} due to the lower quantum efficiency than the CdS/CIGS cell in the long wavelength region [8].

By adding the complexing agent of acetic acid into the chemical bath, a more adherent, reproducible, homogeneous, and higher quality $In(OH)_xS_y$ film [14] has been deposited on the glass substrates and on Siemens CIGSS samples. The performance of one CIGSS cell deposited with $In(OH)_xS_y$ buffer layer using acetic acid and the performance of the CIGSS cells deposited with other buffer layers are shown in Figure 9.7. The result reveals that we can take advantage of the $In(OH)_xS_y$ buffer layer deposited by the new deposition method to improve the cell performance.

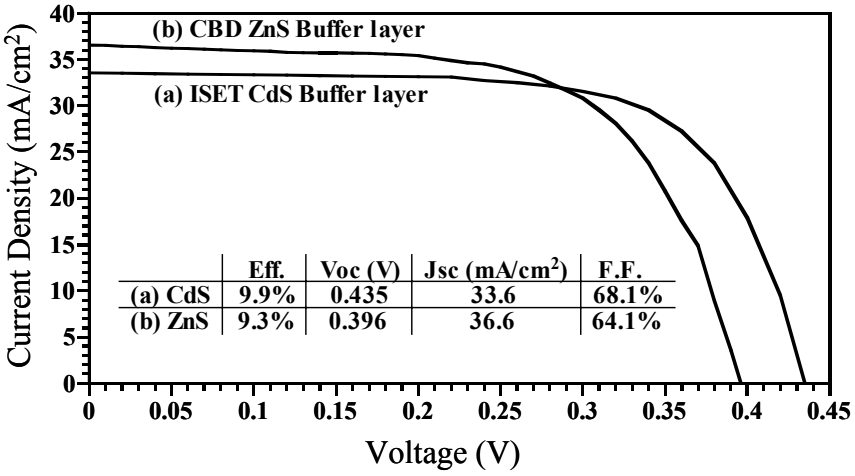

Figure 9.9 The J-V characteristics of CIGS cells with CdS buffer layer deposited at ISET or the ZnS buffer layer deposited at UF.

Table 9.2 The Performance of the CIGS solar cells with CBD $In_x(OH,S)_y$ buffer layers using different procedures of adding chemicals

	Conversion Efficiency (η)	Fill Factor (F.F)	Open-circuit Voltage (V_{OC})	Short-circuit Current Density (J_{SC})
Cell- 1	7.39 %	44.6 %	0.57 V	29.1 mA/cm^2
Cell- 2	5.73 %	38.2 %	0.52 V	28.9 mA/cm^2
Cell- 3	5.23 %	38.3 %	0.51 V	27.0 mA/cm^2

For the CBD process: cell- 1 was first immersed in DI water, and then both $InCl_3$ and CH_3CSNH_2 were added into the bath simultaneously; cell- 2 was first immersed in the solution of CH_3CSNH_2, and then $InCl_3$ was added into the bath; cell- 3 was first immersed in the solution of $InCl_3$, and then CH_3CSNH_2 was added into the bath.

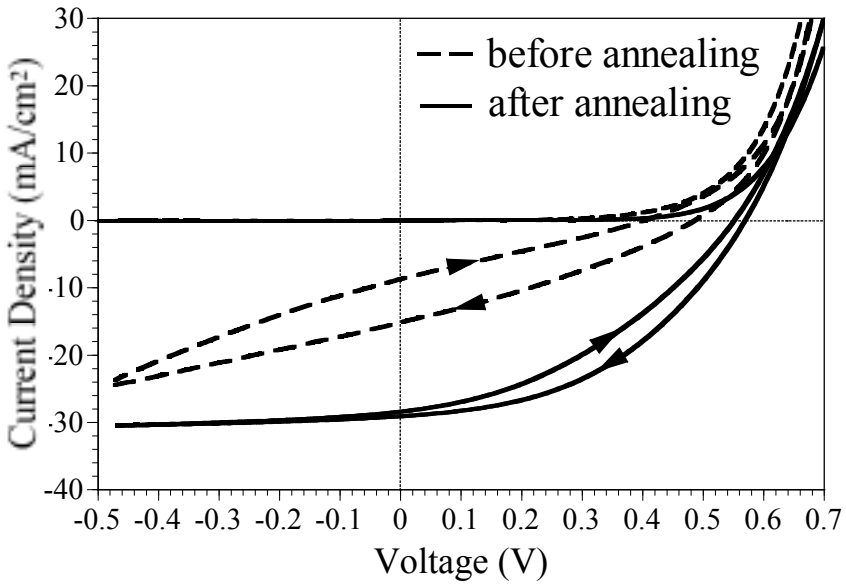

Figure 9.10 The J-V characteristics of the CIGS cell deposited with CBD $In(OH)_xS_y$ buffer layer before and after annealing.

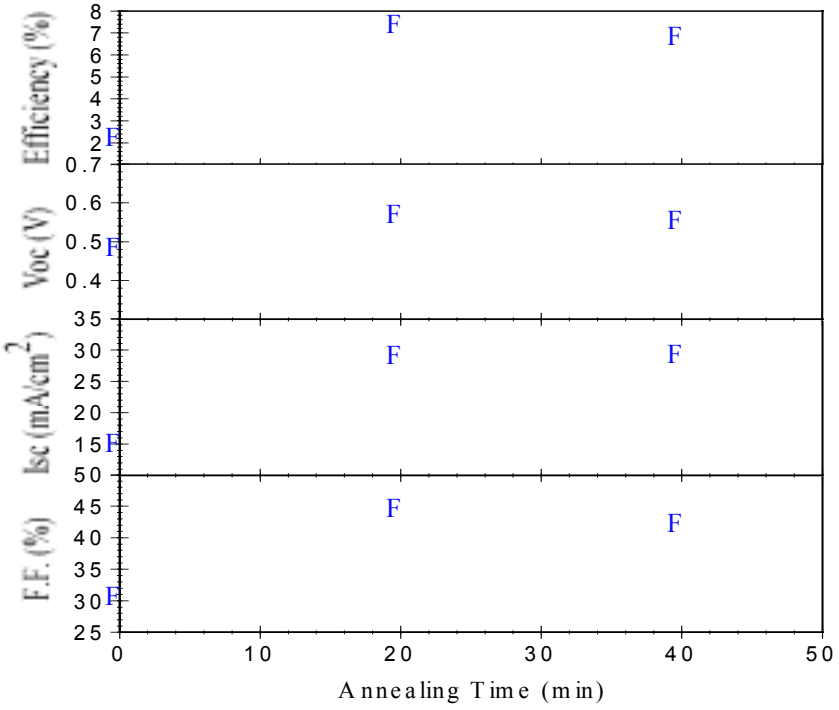

Figure 9.11 The performance of the CIGS solar cells deposited with CBD $In(OH)_xS_y$ buffer layers as a function of annealing time.

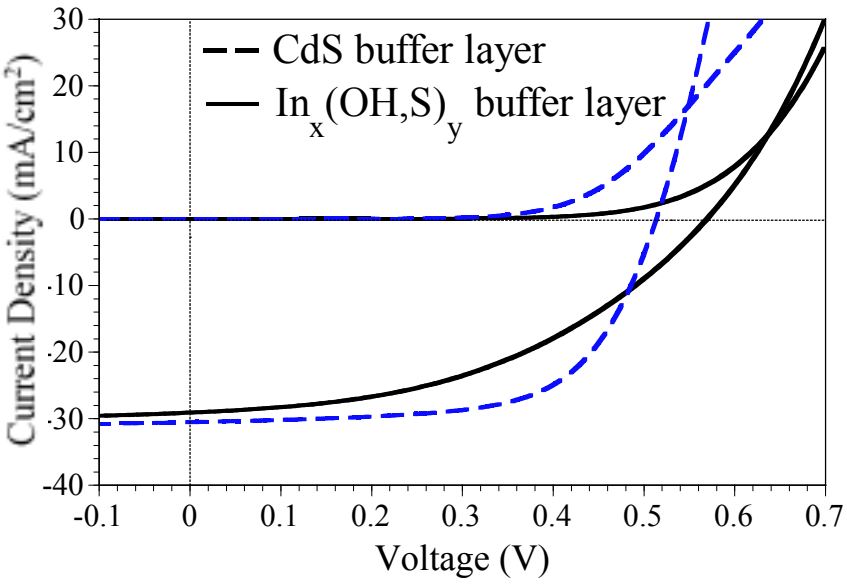

Figure 9.12 J-V characteristics of the CIGS cells with CBD- CdS or CBD-$In(OH)_xS_y$ buffer layer (CdS/CIGS solar cell: Eff.=9.99%, V_{OC}=0.51V, J_{SC}=30.5mA/cm^2, F.F.=63.8%; $In(OH)_xS_y$ /CIGS solar cell: Eff.=7.39%, V_{OC}=0.57V, J_{SC}=29.1mA/cm^2, F.F.=44.6%).

9.6 Summary and Conclusions

A study of the electrical and optical properties of the CBD buffer layers on the soda-lime glass substrates and on the absorber layers was conducted. The XPS results indicated that CdS, (Cd,Zn)S, ZnS, and $In(OH)_xS_y$ films deposited by the CBD method were not completely pure. A small amount of carbon was found to incorporate in the first few atomic layers of the films. Also oxygen in the form of metal oxide and/or metal hydroxide was incorporated into the films during the deposition process. A better quality $In(OH)_xS_y$ buffer layer has been achieved by adding the acetic acid into the reaction bath. Annealing has been found to be a key factor for improving the conversion efficiency of CIS-based cells deposited with alternative buffer layers. Among the CIS-based solar cells with CdS, (Cd,Zn)S, ZnS, or $In(OH)_xS_y$ buffer layers studied in this work, the CdS/CIGSS cell gave the best performance. From the J-V characteristics obtained for the CIS-based solar cells with the alternative buffer layers, the deposition conditions of CBD process are merited to further optimize in order to realize the potential advantages of these buffer layers. Future study of the CIS-based solar cells with alternative buffer layers will focus on optimizing annealing conditions and on investigating the light soaking effects.

9.7 References

[1] M.A. Contreras, B. Egaas, K. Ramanathan, J. Hiltner, A. Swartzlander, H. Hasoon, and R. Noufi, "Progress Toward 20% Efficiency in Cu(In,Ga)Se_2 Polycrystalline Thin-film Solar Cels," *Prog. Photovolt: Res. App*., Vol. 7, pp. 311-316 (1999).

[2] T. Negami, Y. Hashimoto, and S. Nishiwaki, " Cu(In,Ga)Se_2 thin-film solar cells with an efficiency of 18%," *Solar Energy Materials and Solar Cells*, Vol. 67, pp. 331-335 (2001).

[3] E. Niemi, J. Hedstrom, T. Martinsson, K. Granath, L. Stolt, J. Skarp, D. Hariskos, M. Ruckh, H.W. Schock: "Small- and Large-area CIGS Modules by Co-evaporation," *Conf. Rec. of the 25th IEEE PVSC*, pp. 801-804 (1996).

[4] J. Kessler, K.O. Velthaus, M. Ruckh, R. Laichinger, H.W. Schock, D. Lincot, R. Ortega and J. Vedel, *6th Photovoltaic Science and Engineering Conference (PVSEC-6) Proceedings, New Delhi, India*, pp. 1005-1010 (1992).

[5] K. Ramanathan, R.N. Bhattacharya, J. Granata, J. Webb, D. Niles, M.A. Contreras, H. Wiesner, F.S. Hasoon, and R. Noufi, *Conference record of the 26th IEEE PVSC*, p. 319 (1997).

[6] C.H. Huang, Sheng S. Li, W.N. Shafarman, C.-H. Chang, J.W. Johson, L. Reith, S. Kim, B.J. Stanbery, and T.J. Anderson: “Study of Cd-free Buffer Layers Using $In_x(OH,S)_y$ on CIGS solar cells,” *Technical Digest of the 11th International Photovoltaic Science and Engineering Conference*, p. 855 (1999).

[7] T. Nakada, K. Furumi, and A. Kunioka, "High-Efficiency Cadmium-Free Cu(In,Ga)Se_2 Thin-Film Solar Cells with Chemically Deposited ZnS Buffer Layers," *IEEE Transactions on Electron Devices*, Vol. 46, pp. 2093-2097 (1999).

[8] D. Hariskos, M. Ruckh, U. Rühle, T. Walter, H.W. Schock, J. Hedström, and L. Stolt, *Solar Energy Materials and Solar Cells*, Vol. 41/42, pp. 345-353 (1996).

[9] J.F. Moulder, W.F. Stickle, P.E. Sobol, and K.D. Bomben, *Handbook of X-ray Photoelecttron Spectroscopy*, pp. 45, 61, and 213-242 (1995).

[10] C. Heske, D. Eich, R. Fink, E. Umbach, T. van Buuren, C. Bostedt, L.J. Terminello, S. Kakar, M.M. Grush, T.A. Callcott, F.J. Himpsel, D.L. Ederer, R.C.C. Perera, W. Riedl, and F. Karg, *Applied Physics Letters*, Vol. 74, pp. 1451-1453, (1999).

[11] I. Luck, U. Störkel, W. Bohne, A. Ennaoui, M. Schmidt, H.W. Schock, and D. Bräunig, “Influence of buffer layer and TCO deposition on the bulk properties of chalcopyrites,” *Thin Solid Films*, Vol. 387, pp. 100-103 (2001).

[12] R. Bayon, C. Guillen, M.A. Martinez, M.T. Gutierrez, and J. Herrero, *J. Electrochem. Soc.*, Vol. 145, pp. 2775-2779 (1998).

[13] C. -H. Chang, A. A. Morrone, B. J. Stanbery, C. McCreary, M. Huang, C. H. Huang, S. S. Li, and T. J. Anderson, "Growth and Characterization of CdS Buffer Layers by CBD and MOCVD," *AIP Conference Proceedings (NCPV Program Review Meeting)*, No. 462, pp. 114-119 (1998).

[14] R. Bayon, C. Maffiotte, and J. Herrero, "Chemical Bath Deposition of Indium Hydroxy Sulphide Thin Films: Process and XPS Characterization," *Thin Solid Films*, Vol. 353, pp. 100-107 (1999).

PART 10

Mass Flux Modeling in Thermal Effusion Sources for Molecular-Beam Epitaxy Applications

Abstract

A comprehensive model is derived to describe the flux received by a substrate through a molecular beam produced in conical or cylindrical thermal effusion sources with a free evaporating surface. The model appropriately describes the dependence of the flux to the melt height and temperature. The approach integrates different techniques previously documented in the literature and introduces significant enhancements that improve the accuracy of the model while reducing the numerical computation cost. Improved computational efficiency is obtained by the introduction of analytical solutions to the integrals that have been previously solved by numerical methods, and by the adoption of a table look-up and interpolation method for calculating fluxes at any melt-height and any temperature. The entries of the look-up table are calculated only once for a given crucible geometry using a finite number of reference melt heights. Fast flux calculations are then possible permitting the utilization of the model in real-time control applications.

The model is illustrated with a conical crucible source. The results are generic for any material and only depend on the geometry of the crucible and the orientation of the substrate with respect to the source. The calculated flux distribution at different melt heights demonstrate the growth of a region around the center of the substrate over which the flux remains relatively constant as the melt height decreases because the collimating effect of the walls becomes more pronounced. Thus at lower filling levels better film uniformity can be achieved but at the expense of lower deposition rates.

Section Contents

10.1 Brief Overview

10.1.1 Participants

Faculty Adviser: Prof. Oscar D. Crisalle

Research Assistants: Serkan Kincal

10.1.2 Objectives

The objectives of this project are to develop a comprehensive model for the mass flux produced by a thermal effusion source as a function of radial and vertical direction. (Note: Include here all the objectives we have stated in our previous quarterly progress reports).

10.2 Introduction

Molecular beam epitaxy (MBE) is an ultra-high vacuum process with the ability to produce very high quality films for semiconductor applications. As the technology evolves, the requirement of tight thickness and composition uniformity is becoming increasingly important because the performance of newly designed devices may be significantly altered by monolayer changes in thickness [1]. Furthermore, as the high purity raw materials required for MBE growth become more costly, the run-to-run repeatability of the process becomes increasingly crucial.

The behavior of thermal effusion sources used in such systems is highly non-linear due to the exponential relationship between the rate of evaporation and temperature. Particularly Langmuir type sources [2] where there is a free evaporating surface present an even more significant challenge because their modeling involves extensive numerical methods that cannot be used in real time for model based control strategies.

This report describes the numerical modeling of the flux distribution from a single thermal effusion source with a free evaporating surface onto a stationary substrate. The effusion sources considered are of general conical shape, and include cylindrical shapes as a limiting case. The resulting models can be specialized to sources of different dimensions in a multi-source reactor to obtain a complete model useful for controller design purposes.

10.3 Modeling Strategy

10.3.1 Basis of the model

All flux distribution calculations detailed in the following sections are based on the differential form of the cosine law of effusion. Figure 2.1 shows a schematic.

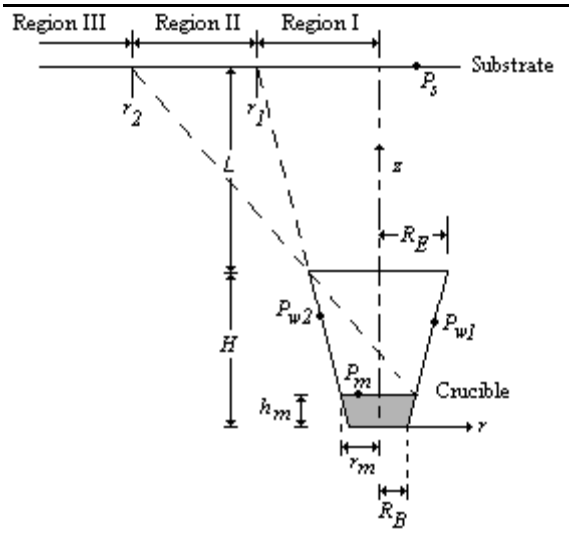

Figure 10.1. Schematic of the source being considered.

10.3.2 Flux distribution from the crucible

There are two sources of flux inside the crucible. Although most of the flux originates from the melt surface, there is also a considerable contribution from the crucible walls as some portion of the flux from the melt surface is reflected off the walls and leaves the crucible. This is defined as the collimating effect of the crucible walls, and is known to be more pronounced at lower melt height. The two sections that follow outline how the fluxes from the melt surface and from the crucible walls are calculated.

10.3.2.1 Flux from the melt surface

Assuming that the melt surface is at a constant temperature and that the vapor leaving the surface is in equilibrium with the melt, the number of atoms leaving the melt per unit area per second is given by the Knudsen effusion equation

$$F_m(T) = 3.51\,10^{22}\,\frac{P_v(T)}{\sqrt{MT}} \tag{10.1}$$

where M is the molecular weight of the evaporating species, and where the vapor pressure can be estimated by Antoine′s equation

$$P_v(T) = \exp\left(A + \frac{B}{T}\right). \tag{10.2}$$

where A and B are material specific constants.

10.3.2.2 Flux originating from the crucible walls

Any point on the crucible walls receives flux from two separate sources. The total flux incident on such a point, $F_c(z)$, is the sum of two terms: the first term, $F_{mc}(z)$ considers the emissions from the melt surface, and the second term, $F_{cc}(z)$ expresses the flux reflected from the melt surface from the rest of the walls, *i.e.*,

$$F_c(z) = F_{mc}(z) + F_{cc}(z) \quad (10.3)$$

It should be noted here that due to the symmetry of the crucible, the flux from the walls changes only in the z direction, defined as the height of the point on the wall with respect to the bottom of the crucible as shown in Figure 10.1

10.3.2.2.1 Flux from the melt to the crucible walls

The flux from the melt to the crucible walls corresponds to the case where the emitting point P' is chosen as P_m (Figure 10.1) and the target point P is selected as P_{w1}. The final flux equation is

$$F_{mc}(z) = \frac{F_m \tilde{m}(z - h_m)}{2(mz + R_B)} \int_0^{r_m} \frac{A_{mc}(B_{mc} - A_{mc}^2)}{(B_{mc}^2 - A_{mc}^2)^{3/2}} dr' \quad (10.4)$$

where for convenience of notation the dimensionless groups A_{mc} and B_{mc} are defined as

$$A_{mc}(r') = \frac{r'}{r_m} \quad (10.5)$$

$$B_{mc}(r') = \frac{(mz + R_B)^2 + r'^2 + (z - h_m)^2}{2r_m(mz + R_B)} \quad (10.6)$$

both m and $\tilde{m}$ being geometrical constants of the crucible defined by

$$m = \frac{R_E - R_B}{H} \quad (10.7)$$

$$\tilde{m} = \frac{1}{\sqrt{m^2 + 1}} \quad (10.8)$$

and where all the remaining variables have been defined in Figure 10.1.

10.3.2.2.2 Flux from the crucible walls to the crucible walls

Using the same approach as in the previous section but with the coordinates and unit normal vectors now corresponding to P_{w1} (P) and P_{w2} (P'), the flux expression is derived to be

$$F_{cc}(z) = \frac{\tilde{m}}{2(mz + R_B)} \int_{h_m}^{H} F_c(z') \frac{(C_{cc} + 2)\sqrt{C_{cc}^3 + 2C_{cc}} - C_{cc}^2 - 3C_{cc}}{(C_{cc} + 2)\sqrt{C_{cc}^2 + 2C_{cc}}} dz' \quad (10.9)$$

The expressions for the fluxes $F_{mc}(z)$ and $F_{cc}(z)$ given by (10.4) and (10.9) can be substituted into (10.3) to yield an equation for $F_c(z)$. Unfortunately the equation is implicit on the unknown because $F_c(z)$ also appears in the integrand of (10.9). A solution can be found via an iterative procedure where successive approximations $F_{cc}^{(i)}(z)$ to the solution $F_c(z)$ are obtained using the scheme

$$F_c^{(i)}(z) = F_{mc}(z) + F_{cc}^{(i-1)}(z) \quad (10.10)$$

where i denotes the i^{th} iteration. The flux $F_{mc}(z)$ is determined from (10.4) and $F_{cc}^{(i-1)}(z)$ is obtained from (10.9) using the approximation $F_c^{(i)}(z')$ instead of $F_c(z')$ in the integrand. The scheme is initiated with the estimate

$$F_{cc}^{(0)}(z) = 0 \tag{10.11}$$

and terminates after M iterations when

$$\max\left|\frac{F_c^{(M)}(z) - F_c^{(M-1)}(z)}{F_c^{(M)}}\right| \le \varepsilon \tag{10.12}$$

where ε is a user-defined tolerance that specifies the desired degree of accuracy.

This final step concludes the characterization of the flux distribution from the crucible source. If the height coordinate z is subdivided into N small finite increments Δz, then the procedure described results in a vector of flux values with elements $F_c(i\Delta z)$, $i = 1, 2, \ldots, N$. Naturally the greater the number of discrete elements (*i.e.*, the smaller the mesh size), the more accurate the results at the expense of computational cost. Now these values can be used in calculating the distribution of flux on the substrate, as outlined in the following sections.

10.3.3 Deposition on the substrate

The physical principles behind determining the flux incident on any point on a substrate located at a distance of L above the crucible lip (see Figure 10.1) are identical to those that are used in characterizing the flux distribution from the crucible. However, additional complexity comes from the fact that some regions on the substrate are exposed to a limited portion of the melt surface and/or the crucible walls, their view being obstructed by the crucible walls. Therefore the integration limits depend on the location of the point on the substrate. For this reason the regions of integration of the flux equations that are derived are variables that depend on the position on the substrate.

10.3.3.1 Flux equations for the substrate

The flux incident on the substrate $F_s(r)$ may originate from the two different sources within the crucible, namely the flux from the melt surface $F_{ms}(r)$, and that from the crucible walls $F_{cs}(r)$, *i.e.*,

$$F_s(r) = F_{ms}(r) + F_{cs}(r)\,. \tag{10.13}$$

Due to the symmetry of the crucible with respect to the substrate orientation, the deposition rate at a point on the substrate depends only on the radial distance of the point to the center of the crucible. Let R_{ms} be the area of the melt surface contributing to the flux to a point on the substrate. Clearly R_{ms} depends on the radial position r.

To calculate $F_{ms}(r)$ the points P and P' are respectively chosen to be P_s and P_m (Figure 10.1) so that the cosine law of effusion leads to

$$F_{ms}(r) = \frac{F_m(L+H-h_m)}{2\pi r'^2 r_m^2} \iint_{R_{ms}} \frac{A_{ms}}{(B_{ms} - A_{ms}\cos\phi')^2}\, dr'd\phi' \tag{10.14}$$

where

$$A_{ms}(r') = \frac{r'}{r_m} \tag{10.15}$$

$$B_{ms}(r') = \frac{r^2 + r'^2 + (L+H-h_m)^2}{2rr_m}\,. \tag{10.16}$$

An identical procedure is applied to derive $F_{cs}(r)$ but by choosing P and P' respectively as P_s and P_{w2} and defining R_{cs} (for the crucible wall surface) in an analogous manner to R_{ms} in (10.14)

$$F_{cs}(r) = \frac{1}{2\pi r_m} \iint_{R_{cs}} F_c(z') \frac{G_{cs}(D_{cs} - A_{cs}\cos\phi')}{(B_{cs} - A_{cs}\cos\phi')^2} dz' d\phi' \tag{10.17}$$

where

$$B_{cs}(z') = \frac{r^2 + (mz' + R_B)^2 + (L + H - h_m)^2}{2(mz' + R_B) r_m} \tag{10.18}$$

$$G_{cs}(z') = \frac{L + H - z'}{mz' + R_B} \tag{10.19}$$

$$A_{cs} = \frac{r}{r_m} \tag{10.20}$$

$$D_{cs} = \frac{mL + R_E}{r_m} \tag{10.21}$$

Substitution of (10.14) and (10.17) into (10.13) gives the complete expression for the flux, $F_s(r)$ incident on the substrate as a function of the radial position. The definition of the regions R_{ms} and R_{cs} depend on the radial position, making the integration limits dependent on the position on the substrate.

10.3.3.2 Definition of the substrate regions

Any point on the substrate surface can be classified into one of three different groups depending on its exposure to the melt surface and the crucible walls. Region I is defined by extending the walls of the crucible to intersect the plane of the substrate (see Figure 10.1). Any point lying on Region I has complete exposure to both the walls and the melt surface. Furthermore, all points in Region I have a radial coordinate satisfying $r \le r_1$, where

$$r_1 = H + L \tag{10.22}$$

Another critical limit for exposure is defined by drawing a straight line from the edge of the melt surface through the opposite side on the crucible lip until it intersects the substrate (see Figure 10.1). This intersection point has the radial coordinate

$$r_2 = \frac{mh_m + R_E + R_B}{H - h_m} L + R_E \,. \tag{10.23}$$

Then Region II is the annular area defined by r_1 and r_2, so that any point in this region satisfies $r_1 < r \le r_2$. In this region there is partial exposure of the substrate points to both the melt surface and the crucible walls. The outmost region, Region III, constitutes the rest of the substrate and its points are characterized by the coordinates $r > r_2$. In this region the points on the substrate do not see the melt surface at all because the crucible walls obstruct the line of sight. Thus only the crucible walls contribute flux to points in Region III.

In Region II some portions of the melt surface and the crucible walls do not contribute to the flux incident on the substrate due to geometric hindrance. To determine the correct definition of the integration regions, a projection of the perimeter of the top of the crucible is made onto the

plane of the melt surface through the point of interest on the substrate. The resulting projection is a circle of radius

$$\beta = \frac{R_E}{L}(L + H - h_m) \tag{10.24}$$

centered at a distance

$$\alpha = \frac{r}{L}(h_m - H) \tag{10.25}$$

away from the center of the melt surface. Further analysis in Region II indicates that this region should be subdivided into three sub-regions, over which the definitions of R_{ms} and R_{cs} for the integration are different. The limits that define these sub-regions are given by

$$r_{1,1} = \frac{R_E(L + H - h_m)}{H - h_m} \tag{10.26}$$

$$r_{1,2} = \frac{L}{H - h_m}\sqrt{r_m^2 + \beta^2}\ . \tag{10.27}$$

Therefore, a substrate point lying on Region IIa has radial coordinates $r_1 < r < r_{1,1}$, a point in Region IIb satisfies $r_{1,1} < r < r_{1,2}$, and finally in Region IIc $r_{1,2} < r < r_2$. A summary on the radial boundaries of all regions of relevance is given on Table 10.1.

Table 10.1 Three different regions and their sub-regions on the substrate

Region	Inner Limit	Outer Limit	Melt Exposure	Wall Exposure
I	0	r_1	complete	complete
IIa	r_1	$r_{1,1}$	partial	partial
IIb	$r_{1,1}$	$r_{1,2}$		
IIc	$r_{1,2}$	r_2		
III	r_2	∞	none	partial

For reasons that will become apparent in the expression of the integration limits over the melt surface for points lying in Region II, it is more convenient to express the entire area as a sum of two regions, namely

$$R_{ms} = R_{ms1} + R_{ms2}\ . \tag{10.28}$$

This new definition splits (10.14) into the sum of two integrals one over R_{ms1} and the other over R_{ms2}, each of which have different integration limits.

Since there is complete exposure of points in Region I to both the melt surface and the crucible walls, the integration is carried out over the entire surfaces. In this simple case there is no need to split R_{ms} in (10.14) into two sub-regions as in (10.28); However, to conserve generality of the formula, the region R_{ms2} is nevertheless kept as a zero area, indicated by the corresponding limits of integration appear in Table 10.2.

A distinction between the three subregions of Region II is made to account for the three different modes in which the projection of the upper perimeter of the crucible intersects the melt surface, requiring slightly different definitions for the regions R_{ms1} and R_{ms2} in each case, hence calling for different integration limits. In all the cases the exposure to the walls is identical, making the limits of integration that define R_{cs} identical in all three subregions. All integration limits are tabulated in Table 10.2 which uses a number of constants that are summarized in Table

10.3 for convenience.

In Region III there is no exposure to the melt surface, therefore both R_{ms1} and R_{ms2} are void regions. The portions of the crucible walls that are closest to the melt surface also begin to lose line-of-sight to the point on the substrate. Therefore the lower limit of the region R_{cs} in terms of z' is now defined by a constant that is above h_m as

$$c = \frac{R_E L + R_E H - Hr + R_B L}{R_E - r - Lm} . \tag{10.29}$$

Table 10.2. Definitions of the upper (max) and lower (min) limits of integration for the flux integrals appearing in (10.14) and (10.17). The variables appearing in this table are defined in Tables 10.1 and 10.3.

	Melt Surface								Crucible Walls			
	R_{ms2}				R_{ms1}				R_{cs}			
	r'		ϕ'		r'		ϕ'		z'		ϕ'	
Region	min	Max	min	max	min	max	min	max	min	max	min	max
I	0	r_m	0	π	0	0	0	0	h_m	H	0	π
Iia	0	r'_+	0	Φ_1	0	r_m	Φ_1	π	h_m	H	Φ_1	π
Iib	r'_-	r'_+	Φ_2	Φ_1	r'_-	r_m	Φ_1	π	h_m	H	Φ_1	π
Iic	r'_-	r_m	Φ_1	π	0	0	0	0	h_m	H	Φ_1	π
III	0	0	0	0	0	0	0	0	c	H	Φ_1	π

Table 10.3 Variables used in Table 10.2.

$\Phi_1 = \arccos\left(\frac{r_m^2 + \alpha^2 - \beta^2}{2 r_m \alpha}\right)$	$\Phi_2 = \arccos\left(\frac{1}{\alpha}\sqrt{\alpha^2 - \beta^2}\right)$
$r'_- = \alpha\cos\phi' - \sqrt{\beta^2 - \alpha\sin^2\phi'}$	$r'_+ = \alpha\cos\phi' + \sqrt{\beta^2 - \alpha\sin^2\phi'}$
$c = \frac{R_E L + R_E H - Hr + R_B L}{R_E - r - Lm}$	

10.4 Example

10.4.1 Description of the simulated system

The source modeled has the physical dimensions of $R_B = 0.26$ cm, $R_E = 1.44$ cm, and $H = 9.00$ cm. The source to substrate distance is $L = 14$ cm and the fill level was varied from a completely full crucible ($h_m = 9.00$ cm) to an almost empty condition ($h_m = 1.00$ cm). The mesh size on the crucible was fixed at $\Delta z = 0.005$ cm after optimizing this value for an acceptable accuracy with a reasonable computation time. This implies that when the source has a filling level of 4.50 cm the height of the exposed walls is 4.50 cm, which would then correspond to $N = 900$ discrete elements of height 0.005 cm on the crucible walls for which the flux $F_c(z)$ needs to be evaluated. In all of the calculations the evaporation rate from the melt surface F_m is set at unity without the loss of generality since the final results can be scaled to any evaporation rate by simply multiplying by the desired value of F_m.

10.4.2 Flux distribution from the crucible walls

The flux $F_{mc}(z)$ incident on the walls of the crucible from the melt surface is calculated using (10.4) for a melt height of 4.50 cm and the result is plotted in Figure 10.2. The iteration scheme (10.12) is executed with a tolerance $\varepsilon = 0.005$, and converges after 21 iterations to the flux $F_c(z)$ and $F_{cc}(z)$, also shown in Figure 10.2.

10.4.3 Deposition on the substrate

The flux $F_s(r)$ incident on the substrate is calculated via (10.13) after integrating (10.14) and (10.17) over the regions whose limits are defined in Table 10.2. These calculations are then repeated at 9 different filling levels ranging from $h_m = 1.00$ cm to $h_m = 9.00$ cm. The results are plotted in Figure 10.3.

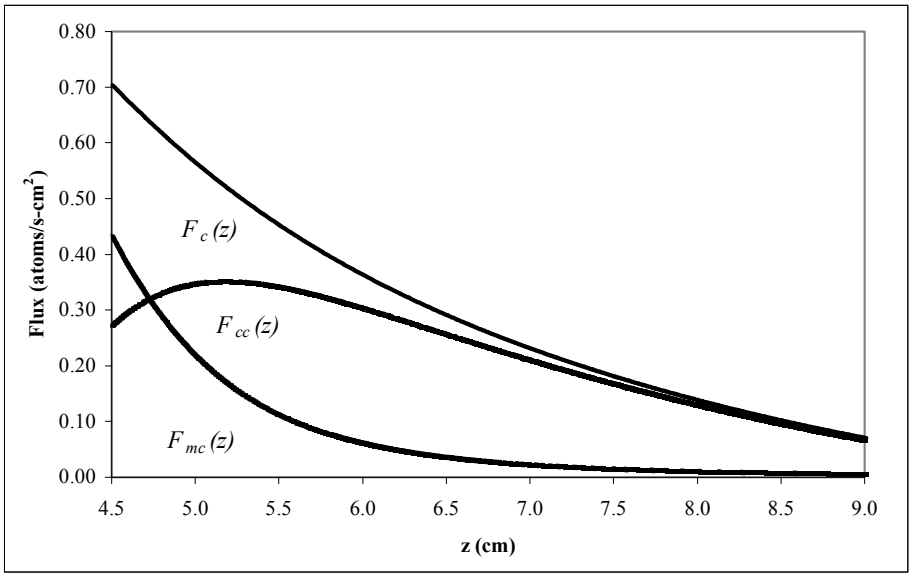

Figure 10.2. Distribution of the flux $F_c(z)$ from the crucible walls as a function of position for a melt height $h_m = 4.5$ cm. The contributing fluxes from the melt $F_{mc}(z)$ and the other positions on the walls $F_{cc}(z)$ are also shown.

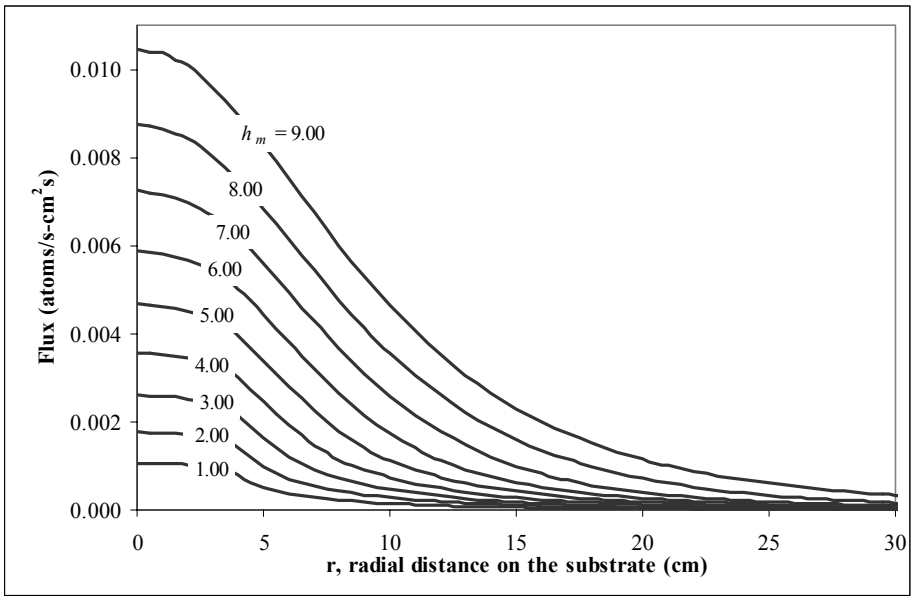

Figure 10.3. Deposition flux $F_s(r)$ on the substrate at nine different melt levels. The results are normalized to unity evaporation rate from the melt.

10.4.4 Interpolation for intermediate filling levels

The calculations that have been shown so far take too long to be done in real time for control purposes. It is however possible to interpolate the deposition profile at any intermediate filling level using the 9 deposition profiles of Figure 10.4 as a reference. A possible choice is to use bi-cubic interpolation to obtain the results shown in Figure 10.4. The two thick lines encapsulating the thinner line (the profile at an intermediate filing level of $h_m = 5.20$ cm calculated using (10.13)) are the deposition profiles at melt heights of $h_m = 4.50$ cm and $h_m = 5.50$ cm, two of the nine profiles that are reported in Figure 10.3. The black circles denote the interpolation of the intermediate data from the reference deposition profiles for comparison with the calculated profile.

The deposition profile is linear with respect to the evaporation rate from the melt surface. Therefore the reference results can be extended to the evaporation rate at any temperature by simply multiplying the entire profile by the actual evaporation rate determined through (10.1)

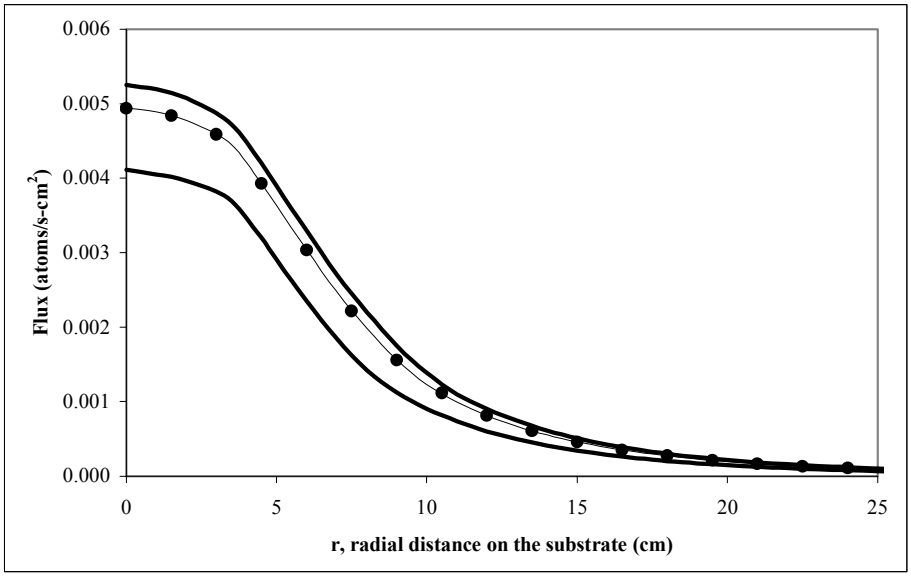

Figure 10.4. Interpolation of an intermediate filling level $h_m = 5.20$ cm from the reference data shown in Figure 10.3. The interpolated values are shown by the dots, the thin line is the calculated profile at $h_m = 5.20$ cm. The results are normalized to unity evaporation rate from the melt.

10.5 Conclusions

The flux distribution appearing in Figure 10.2 shows that there is significant flux leaving the walls of the crucible compared to the melt surface in an effusion source with a free evaporating surface. This implies that the collimating effects of the walls cannot be ignored. Furthermore, Figure 10.3 shows that deposition rate varies significantly with the melt height and position on the substrate, making it impossible to use a single value for the flux to estimate the entire flux distribution. These two requirements conflict with the need to have real-time deposition profiles as the calculations involved are numerically intensive. As demonstrated in Figure 10.4, this problem is resolved without conceding any accuracy in flux distribution because intermediate flux distributions can be estimated very quickly by interpolation from a set of deposition profiles at a series of reference heights. This is the most important contribution of this work since it permits the rapid evaluation of fluxes.

Figure 10.3 illustrates that as the melt level decreases, a region forms around the center of the substrate where the deposition rates are approximately constant at a given melt height. This is important from an operational point of view since it implies the existence of an optimum melt level depending on the substrate size and the desired level of uniformity through the film. If the particular growth process requires high levels of uniformity over large surface areas, the growth should be carried out at low melt heights at the expense of lower rates of deposition. This is due to the fact that the collimating effects of the walls become more pronounced as more and more walls are exposed with decreasing melt levels.

The procedure outlined in this paper applies to a single source. However almost all current MBE processes use more than one source for growth. Since the deposition profile for any source

can be reconstructed from a series of calculations made at reference heights, the addition of consecutive sources to the model does not increase the computational requirements. This is due to the fact that once the reference look-up tables have been formed for each source, deposition profiles are accessed almost instantaneously by interpolation.

10.6 References

[1] R. Pankajavalli, M. Ider, B. J. Stanbery, and T. J. Anderson, “Phase Diagram for Ternary Cu-In-Se Mixtures”, *Journal of Materials Science*, Vol. 1, pp. 30-33 (2002).

[2] S. Kincal and O. D. Crisalle, "Thermal Effusion Source Modeling for Control in Molecular Beam Epitaxy Applications", *Proceedings of the American Control Conference,* Chicago, pp. 4401-4405 (2000).

PART 11

Modeling the Substrate Temperature Distribution in the UF PMEE Reactor

Abstract

A two-dimensional model of the heat transfer was developed for a rotating platen/substrates in a molecular beam epitaxy reactor. Time-varying view factors were calculated and employed to solve the problem dynamically accounting for the fact that the platen rotates at a given angular speed. The correlation between actual temperature on the substrates and the thermocouple reading due to the indirect measurement was modeled. The poor thermal contact between the platen and the substrates was simulated embedding a thin thermal break-region. The modeling study shows that the existence of the contact resistance improves the temperature uniformity in the substrate region. The effects of rotation speed and rotation direction were also investigated. The modeling results predict the temperature distribution in the substrate regions to be fairly uniform under certain conditions. Fairly good agreement with experimental validation result was obtained without using any model-fitting parameter.

Section Contents

11.1 Brief Overview

11.1.1 Participants

Faculty Adviser: Prof. Timothy J. Anderson and Prof. Oscar D. Crisalle

Research Assistants: Suku Kim and Serkan Kincal

11.1.2 Objectives

The objective of this project is to develop a thermal model for obtaining the temperature distribution on the platen and the substrate regions.

11.2 Introduction

The uniformity of the temperature distribution on the substrate is crucial to the growth of thin films in many semiconductor processes. The uniformity issue becomes more critical as the substrate size is larger, or position of the heating source is localized so that the heat distribution is not constant through time and location e.g. substrates on a moving platen. In addition, measuring the temperature distribution is another important issue in determining the uniformity. The measurement spots are too limited to obtain the entire distribution over larger region in many cases. Direct measurement is very hard in some situation e.g. moving substrates. As an effort to resolve those problems, numerical modeling can be an efficient approach.

Our research group uses a modified molecular beam epitaxy reactor for depositing $CuInSe_2$ thin films as an absorber layer of solar cells. The system is equipped with a rotating tungsten platen on which nine substrates can be loaded. Rotational movement of the platen delivers each substrate to the deposition zones and heating zone sequentially and periodically. As a result, the platen and the substrates are locally heated and cooled down with certain periodicity. The rotational movement of the platen and the various heating sources result in certain temperature gradient through position on the platen and the substrate regions. This problem should be dynamically solved due to the periodical variation of all the conditions with respect to time. In addition, a direct measurement of any single spot on the substrate is virtually impossible due to the rotational movement of the platen. In other words, the thermocouple cannot be attached to the substrates. These factors, combined together, create certain complexities on the problem. A two-dimensional model of the heat transfer on the platen and the substrates was developed based on heat balance equations adopting time-varying view factor functions.

11.3 Modeling Equations and Strategy

Under such a low pressure condition (~10^{-8}torr), the convection term can be neglected; hence, the heat balance equations for the domain (platen and substrates) is,

$$\rho C_p \frac{\partial T}{\partial t} = k\nabla^2 T + q_{rad} \tag{11.1}$$

where q_{rad} is the heat flux by radiation, T is temperature, ρ is density, C_p is specific heat, and k is thermal conductivity.

As explained above, the problem requires a dynamic solution that considers the periodic effects on the heat distribution coming from the rotation of the platen even though final solution is a steady state one i.e. quasi-steady state solution. It could be achieved by adopting the time-varying view factors with respect of the heating sources. This made it possible to keep the domain fixed. In other words, all the heating and the cooling sources were considered to be rotating instead of considering the platen to be rotating that is the real situation. For each heating or cooling source, the dimensionless view factors between a pair of surface elements dA_1 and dA_2 that face each other can be calculated from the following equation [1],

$$F_{12} = \frac{1}{\pi A_1} \iint \frac{\cos\theta_1 \cos\theta_2}{r_{12}^{\,2}} dA_1 dA_2 \tag{11.2}$$

and the surface elements dA_1 and dA_2 are joined by a straight line r_{12}. The line makes the angle θ_1 with the normal vector to dA_1, and the angle θ_2 with the normal vector to dA_2. If the domain 1 (platen and substrates) is divided to small regions, the view factor, the fraction of radiation leaving a heating source that is directly intercepted by each divided region, can be also calculated for each small region by the same equation. When the divided region approaches to an infinitesimally small one i.e. a spot, the equation 11.2 becomes

$$F_{12} = \frac{1}{\pi} \int \frac{\cos\theta_1 \cos\theta_2}{r_{12}^{\,2}} dA_2 \tag{11.3}$$

since the integrated value is kept constant within the infinitesimally small area. The view factors were calculated over the entire region and stored in a table file as a function of the position (x, y). Therefore, there are four different table files for the heating and the cooling sources. In the simulation, the dimensionless view factor on a specific position is obtained by interpolating the values in the corresponding table file. When the simulation program reads the data, the values periodically vary with time. Time variable is converted to corresponding position parameters in the simulation. Figure 11.1 depicts some of the view factors on the platen and their variation with respect to time.

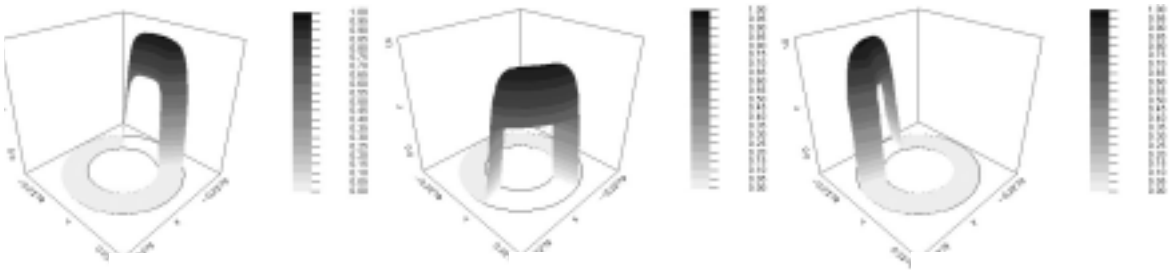

(a)

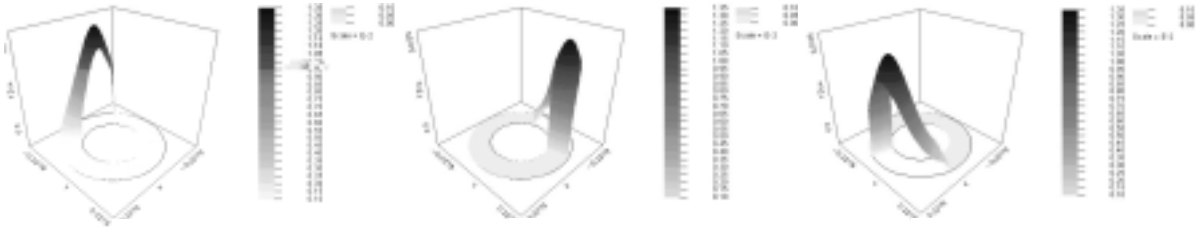

(b)

Figure 11.1. Time-varying view factors at 20 rpm; (a) for the main heater and (b) for the copper effusion cell.

The fact that the measurement of temperature is indirect and only of single point, gives limited information on the uniformity issue and consequently creates additional difficulties in modeling. Single thermocouple (C-type) is located in the middle of the gap between the heater and the moving platen; hence, it reads some average temperature of the heater and the platen. It does not give full information about temperature distribution on the substrates, which makes the experimental validation difficult. The view factors on the thermocouple were calculated by the same scheme used for the platen. Another heat balance equation is embedded for the thermocouple. Those two heat balance equations are simultaneously calculated with the time-varying view factors in the simulation so that the correlation between the thermocouple reading and the actual temperature on the substrates can be obtained.

The substrates are just sitting on the platen during the operation i.e. the thermal contact between the substrates and the platen is poor; hence, a thin thermal break-region of very low thermal conductivity is embedded to simulate the contact resistance. The effect of the thermal break-region on the temperature uniformity will be discussed later.

Significant simplification was obtained by assuming a black body radiation, an assumption that is not likely to produce significant errors since the distance between the objects simulated is much smaller than the objects' dimensions. A finite element solver was used for solving the differential equations.

11.4 Result and Discussion

Figure 11.2 depicts the final temperature profile that is a quasi-steady state solution. It shows that the hottest spot on the entire region is formed when the substrate exits the heating zone, i.e. right after heating period. The coldest spot is formed when the substrate enters the heating zone, right after cooling period. The results are exactly as expected. Figure 11.3 plots the quasi-steady state temperature gradient along the centerline of the substrate/platen. It clearly displays that there is a temperature gradient on the domain with respect to position/time variation. Because the substrate is in more centered position to the main heater and its thermal conductivity is lower (glass), the temperature of the substrate region is overall higher than that of the tungsten platen region.

In addition, sudden change of temperature appears when it passes through the boundary between two regions. It can be explained from the different thermal conductivities and the existence of the thermal break-region (or thermal barrier). This result is common for any poor thermal contact and simulated in this modeling by embedding a thin thermal break-region that has very low thermal conductivity. Figure 11.4 shows the difference that is made by the thermal break-region. The poor thermal contact clearly improves the temperature uniformity on the substrate since most of the abrupt temperature change occurs in the thermal-break region, and it certainly flatten the temperature around the edge of the substrate region.

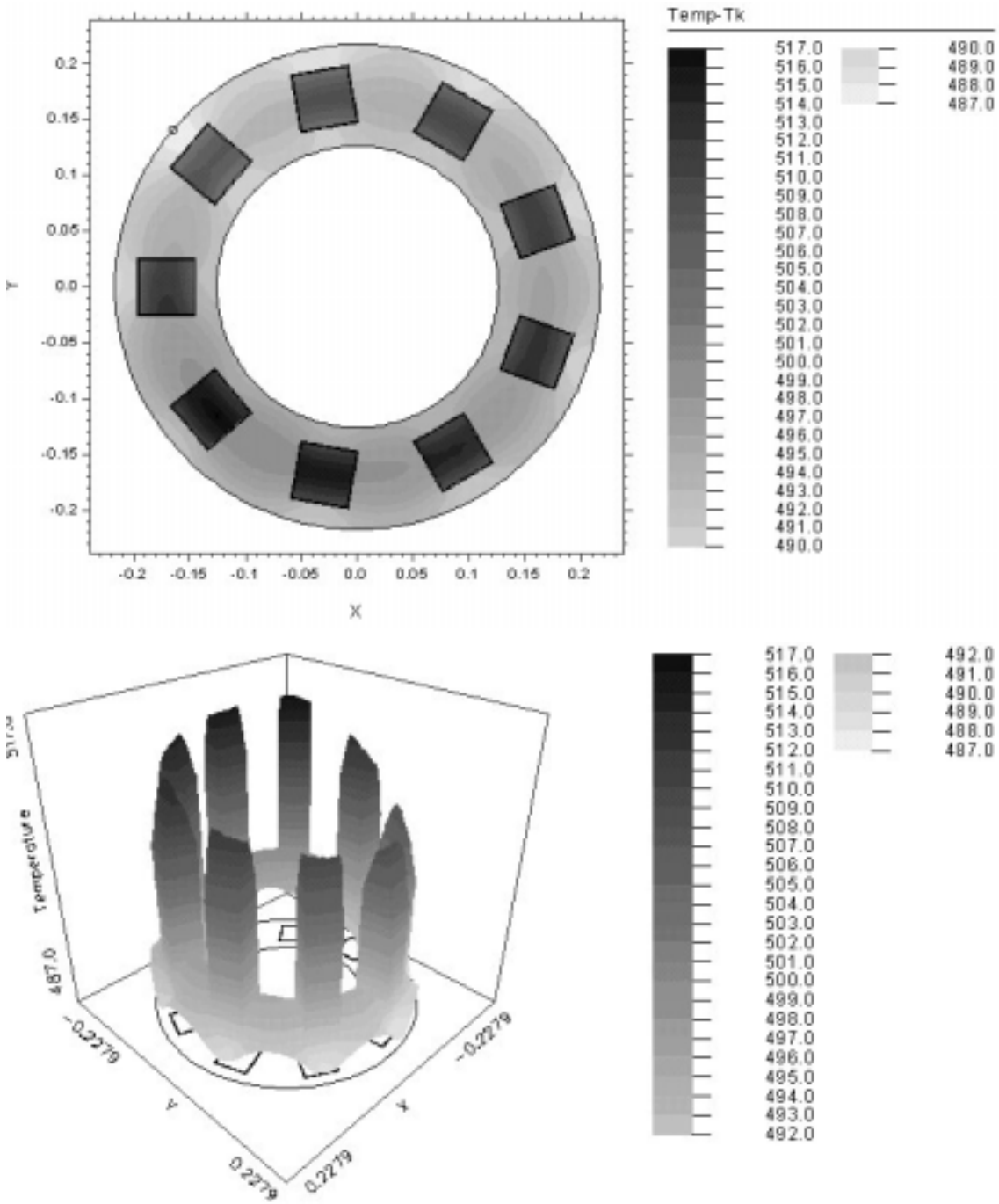

Figure 11.2. Quasi-steady state temperature profile on the platen/substrates; thermocouple reading = 710°C, rotation speed = 20 rpm.

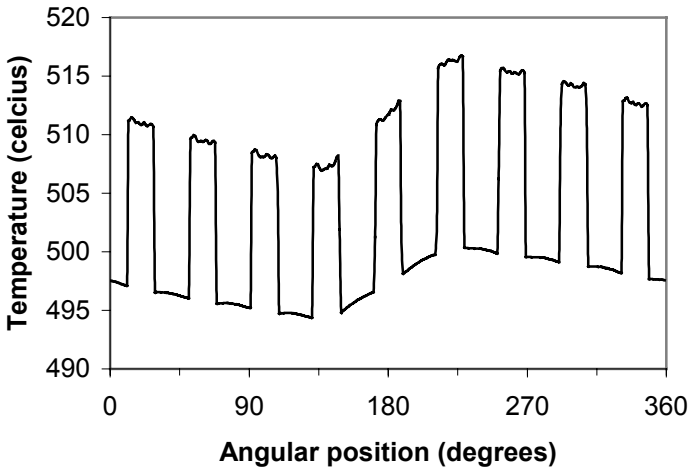

Figure 11.3. Temperature profile along the angular position.

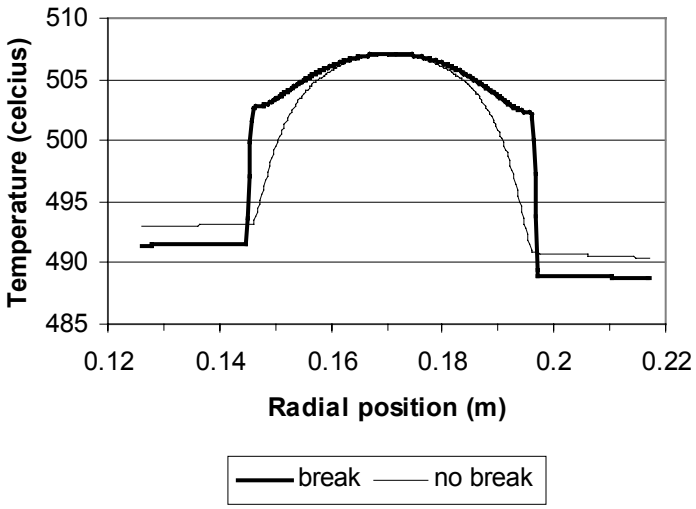

Figure 11.4. Temperature profile along the radial position at 140° with and without a thermal-break region.

The thermal-break region also affects the pattern of the temperature profile in the substrate region (Fig. 11.5). It is observed that pattern of the temperature distribution is somewhat parallel to the direction of the rotation with the thermal-break region. Due to the design of the heater and the platen, the view factor change with radial direction is larger than that with angular direction (Fig. 11.5(a)). The thermal-break region makes that effect remain through a revolution by reducing the heat conduction between the substrate region and the platen region. Without the thermal-break region, the heat conduction becomes significant so that the pattern of the temperature profile within a substrate region becomes symmetrical about the center of a substrate region.

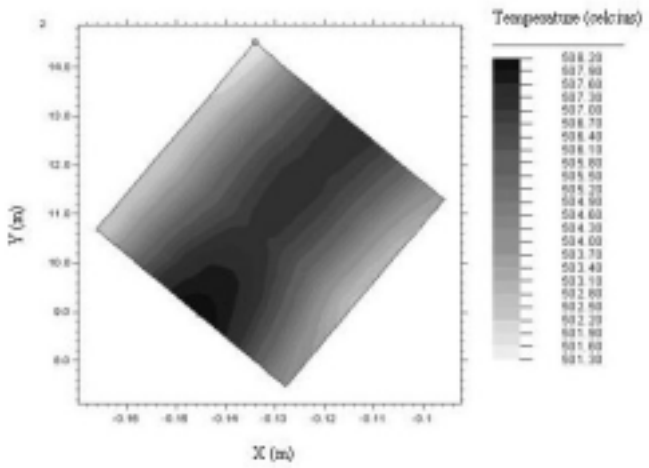

(a) With a thermal-break region

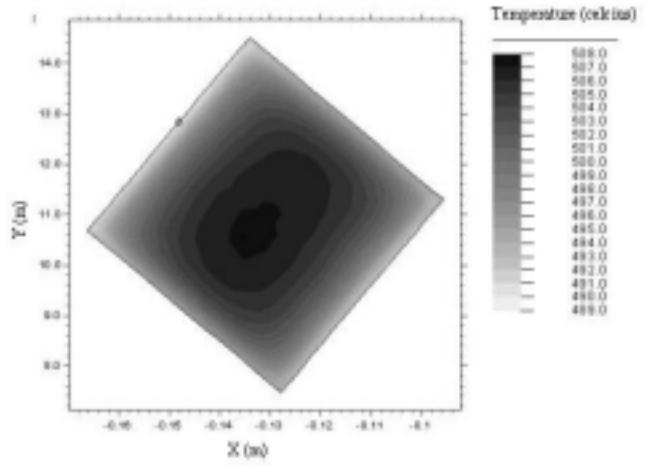

(b) Without a thermal-break region

Figure 11.5. The effect of the thermal-break region on the pattern of temperature profile within a substrate at 140°.

Lower rotation speed (12 rpm) creates higher temperature gradient through a revolution and higher temperature non-uniformity on the substrate region. In other words, the difference between the maximum and the minimum temperature within a substrate region is larger in case of the lower rotation speed. Correspondingly, the highest temperature on the substrates is higher when the platen rotates slower. It can be inferred that the rotation speed should be kept above certain value to obtain acceptably uniform temperature distribution. To obtain higher peak temperature, the rotation speed needs to be lower.

The rotation direction, in this case, does not make any noticeable difference except that the temperature profile is now symmetrically reversed with respect to the radial direction since the effect of the main heater is dominant in the heat transfer, compared to the other heating sources.

The model predicts that the maximum temperature difference within the substrate region is at most 10^{o}C, and the temperature variation experienced by any single substrate throughout a complete revolution is no greater than 15^{o}C when the peak temperature on the entire domain region is approximately 520^{o}C and the corresponding thermocouple reading is 700^{o}C. Such temperature variations are relatively small with respect to the peak temperature, therefore, the substrate temperature can be considered to be fairly uniform with the thermal break-region. The uniformity is also maintained under lower temperature conditions.

The thermal modeling results were validated by comparison to the temperatures measured through a calibration experiment using selected eutectic films that visually melt above certain temperatures. The method is comparing the peak temperatures since the eutectic films respond to the highest temperature on the substrates. Fairly good agreement was obtained considering no model-fitting parameter. However, using eutectic films is not very precise technique to calibrate the temperature and does not give enough information about the temperature distribution; hence, further experimental validation is needed.

11.5 References

[1] R.B. Bird, W.E. Stewart and E.N. Ligthtfoot, *Transport Phenomena*, John Wiley & Sons, New York, p. 440 (1960).

PART 12

Growth and Characterization of Polycrystalline $CuInSe_2$ Films

Abstract

The results of efforts to grow epitaxial and polycrystalline CIS thin films are described in this section. CIS epitaxial films have been grown on single-crystal GaAs substrates under conditions that enhance the influence of surface effects on the resulting films and their properties. There is a pronounced morphological contrast between indium-rich and copper-rich films. In addition, epilayers with nominally identical compositions and morphologies can exhibit fundamentally different ordering of the lattice in either the equilibrium chalcopyrite (CH) or the metastable CuAu (CA) structures.

The polycrystalline CIS thin films grown in the University of Florida PMEE system reveal features that seem to lend experimental support to the hypothesis of a vapor-liquid-solid growth mechanism. Droplet-like structures reproducibly appear on the surface of as-grown Cu-rich polycrystalline CIS films when certain conditions are fulfilled, namely when a Cu-rich composition is attained and using a sufficiently high Se flux during the growth and cooling-stages. Other features of the samples and corresponding process suggest that the droplet structure is closely related to the presence of a Cu-Se liquid phase during growth process. The results are significantly affected by the substrate type, temperature, as well as by the final thickness of the film. Finally, progress in developing a process for deposition of precursor films that are used for rapid thermal process is discussed.

Section Contents

12.1 Brief Overview

12.1.1 Participants

Faculty Adviser: Prof. Tim Anderson and Prof. Oscar D. Crisalle

Research Assistants: Suku Kim, Serkan Kincal, and Billy J. Stanbery

12.1.2 Objectives

The objectives of this project are to investigate the growth mechanism of CIS thin films and to develop a process for growth of device-quality absorber layers. We are also developing a growth process and a corresponding design of layer structure for precursor films that are used for rapid thermal processing.

12.2 Epitaxial Growth of CIS Thin Films

12.2.1 Experiment

The films were grown in a custom rotating-disk reactor designed to implement the Plasma Migration-Enhanced Epitaxy (PMEE) process variant of the Molecular Beam Epitaxy technique. Further details of the reactor configuration and the corresponding characteristic deposition schemes are described in elsewhere [1-3] and in Part 16 of this report. For the epitaxial growth of CIS thin films on GaAs wafers, polished GaAs substrates oriented 2^o off the (001) direction towards to the nearest [110] direction were etched in a 5:1:1 solution of H_2SO_4:H_2O_2:H_2O at room temperature for 1 minute, then rinsed sequentially in H_2O and in methanol immediately prior to mounting into the PMEE system's load lock system. The substrate was then heated *in-situ* to a temperature greater than 600°C for 10 minutes and then exposed to a direct selenium source flux for about 1 minute, at which point the $CuInSe_2$ film growth was initiated. The steady-state substrate temperature during film growth was 550±50°C. Absolute total flux calibration was employed to set the Se/(Cu+In) molar flux ratio to 5, and the total incident molar flux of metals (Cu+In) was adjusted to provide the equivalent of 1 unit cell of chalcopyrite $CuInSe_2$ per cycle. The rotation rate of the substrate platen was 20 rpm (3 sec/cycle). For a total growth time of ~60 minutes, the film thickness was nominally equal to 0.3 μm.

12.2.2 Results and discussion

As reported previously [1-3], the PMEE reactor has been successfully employed for growing epitaxial films of the ternary $CuInSe_2$ compound on (001) GaAs. The material is ordered in a CuAu crystallographic structure rather than in the compound's equilibrium chalcopyrite structure. This was the first reported observation of CuAu crystallographic polytype of $CuInSe_2$ during growth.

Evidence for the CuAu epitaxial structure was provided by XRD, TEM-TED, and Raman scattering data. Figure 12.1 shows the resulting θ-2θ scans of the X-ray diffraction study. It features an unusually prominent series of diffraction peaks that we tentatively assign to the (002), (004), (006), and (008) reflections of the CuAu structure. Detailed characterization results

can be found in the previous publication [2]. Each epitaxial $CuInSe_2$ film grown on single-crystal GaAs substrates exhibited a *film+island* growth morphology characteristic of the Stranski-Krastonov growth mode, but we observe a pronounced morphological dichotomy between indium-rich and copper-rich films (Figure 12.2) was observed. A quasi-periodic self-assembled array of similarly sized islands in the case of copper excess, and a spatially disordered distribution with variable island sizes in the case of indium excess. Further discussion for the different surface morphology is described in publications from our group [3]. The overall result confirms a recent theoretical prediction that the CuAu crystallographic polytype, although metastable, can coexist with the equilibrium chalcopyrite structure of $CuInSe_2$.

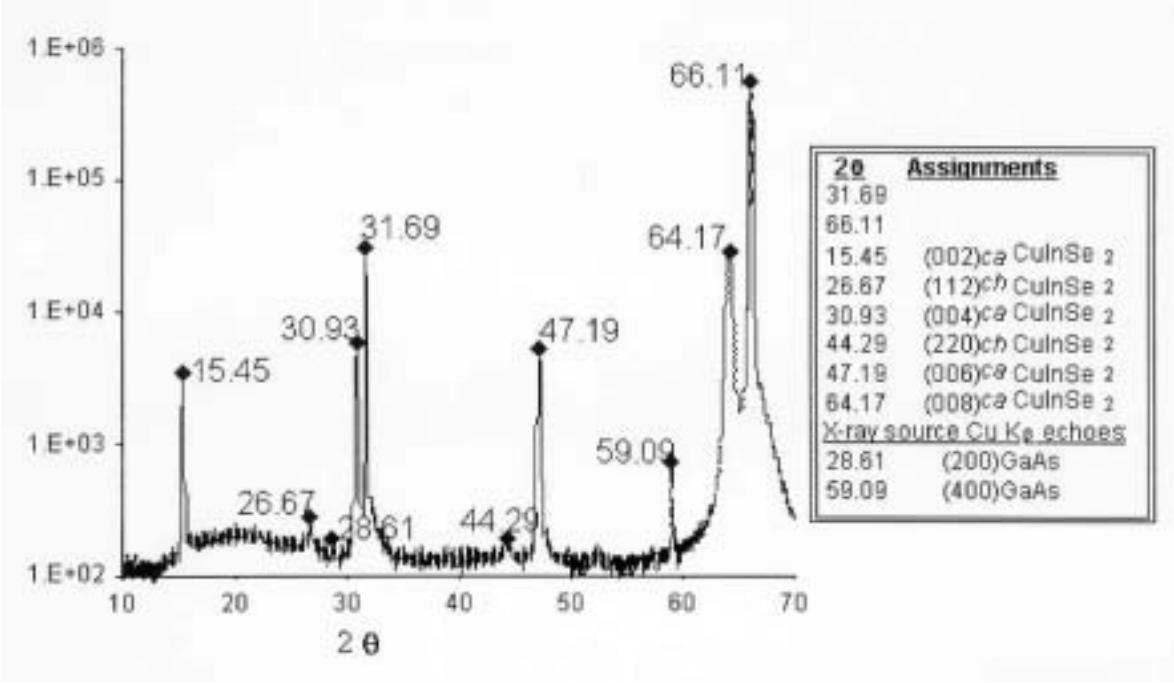

Figure 12.1. XRD spectrum of indium-rich CuInSe2 grown epitaxially on (001) GaAs by PMEE.

Figure 12.3 displays (from right to left) theoretical dynamical electron diffraction patterns along the [010] direction of the CH and CA structures, the experimental transmission electron diffraction (TED) pattern, and experimental TEM dark-field cross-sectional images taken using either the (001) diffraction spot (top) or (-10-1) diffraction spot (bottom). The latter two images display the spatial distribution of the two phases, since the theoretical diffraction pattern modeling shows only a very weak (001) spot for the CH structure (due to double-diffraction) and no intensity at all for the CA structure in the (-10-1) position. It is apparent from these images that the epilayer nucleates initially in the CH structure but converts to the CA structure as growth continues. The presence of the underlying CH–$CuInSe_2$ also explains the weak peaks from this structure evident in the XRD spectrum shown in the preceding section.

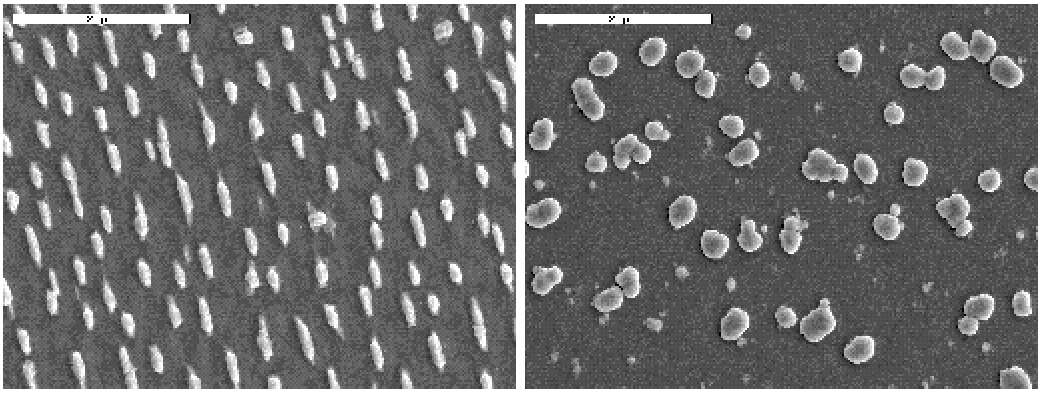

Figure 12.2. Se–SEM images of Cu-rich (left) and In-rich (right) islands.

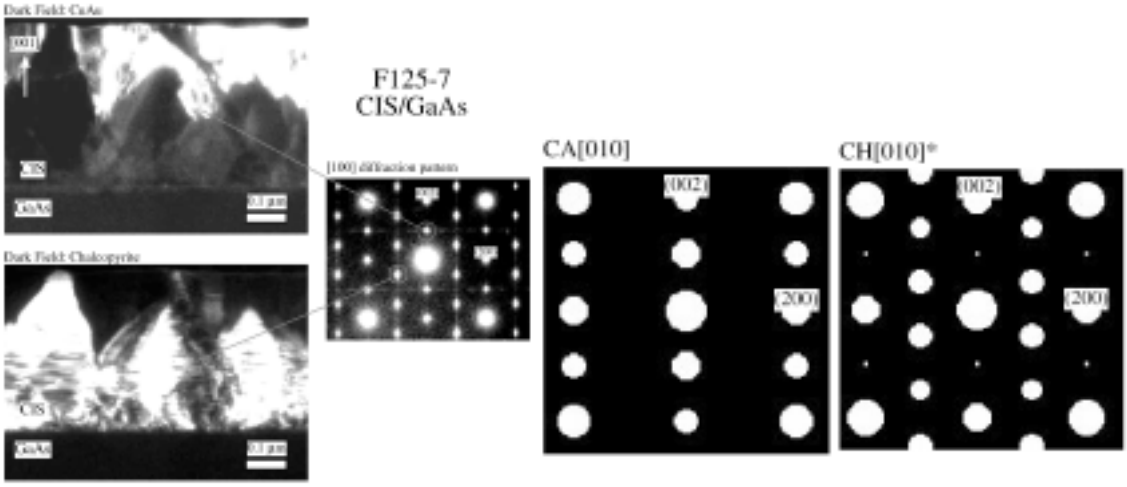

Figure 12.3. TEM-DF cross-sections, TED pattern along [101], and the theoretical TED patterns.

Epitaxial growth of $CuInSe_2$ was also attempted on various other substrates (such as single-crystal GaAs, ZnTe, and SrF) using the newly installed selenium plasma cracker available in the PMEE reactor. An epitaxial structure of $CuInSe_2$ was achieved on (001) GaAs and on (111) ZnTe substrates using the plasma cracker as a selenium-flux source. Figure 12.4 exhibits a series of diffraction peaks of seemingly CuAu + Chalcopyrite structure. Similar peaks to Figure 12.1 appear in the XRD spectrum. Figure 12.5 displays the diffraction peaks of the epitaxially grown sample on the (111) ZnTe substrate. Additional near-future studies are planned to further probe the characteristic features of films deposited using the plasma cracker and to elucidate the effect of using different substrates.

Investigation on the role of sodium on ordering and surface morphology of expitaxially grown $CuInSe_2$ is described elsewhere in detail [3], and brief summary is given here. The results shows that under our growth conditions minute quantities of sodium inhibit the incorporation of excess indium into the growing film. Especially, the addition of sodium to indium-rich $CuInSe_2$ epilayers during the initial stages of epitaxial growth both suppresses the formation of metastable

CuAu-$CuInSe_2$ crystal polytypes and dramatically changes the film morphology. The result is consistent with our previous hypothesis [4] that sodium acts as a surfactant during the growth of $CuInSe_2$ by destabilizing the (In_{Cu} + $2V_{Cu}$) cation neutral-defect-complex (NDC) in the near-surface transition layer and rejecting excess indium from the growing film.

It was observed that classic chalcopyrite epitaxial films on (001) GaAs were obtained at higher growth temperature rather than those used for obtaining the CuAu structure. This suggests that there may be a specific temperature range required for the formation of the metastable CuAu structure during growth. Additional studies are planned to investigate the effects of platen rotation (speed and direction), substrate temperature, sodium addition, and of substrate type.

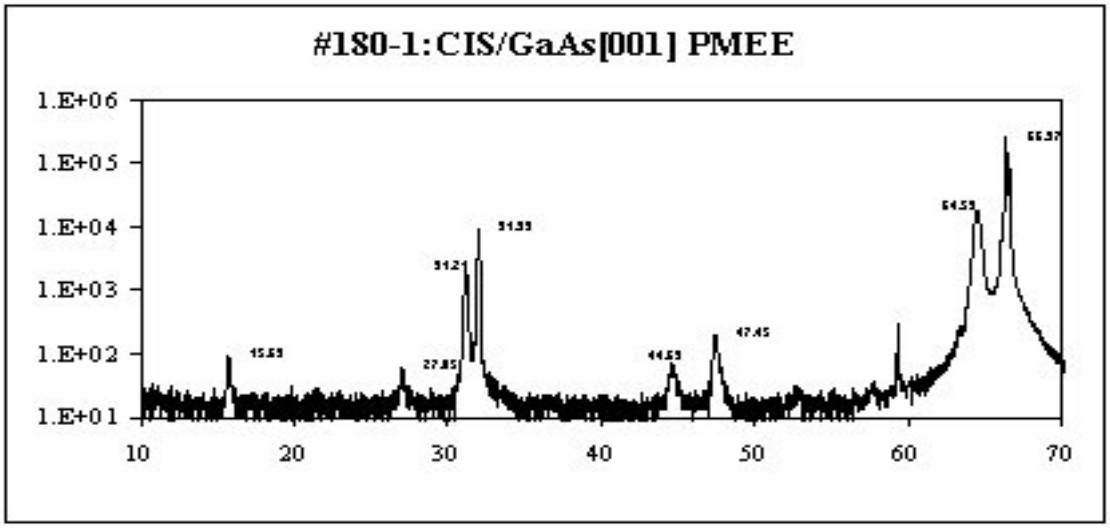

Figure 12.4. XRD spectrum of CuInSe2 grown epitaxially on (001) GaAs by PMEE.

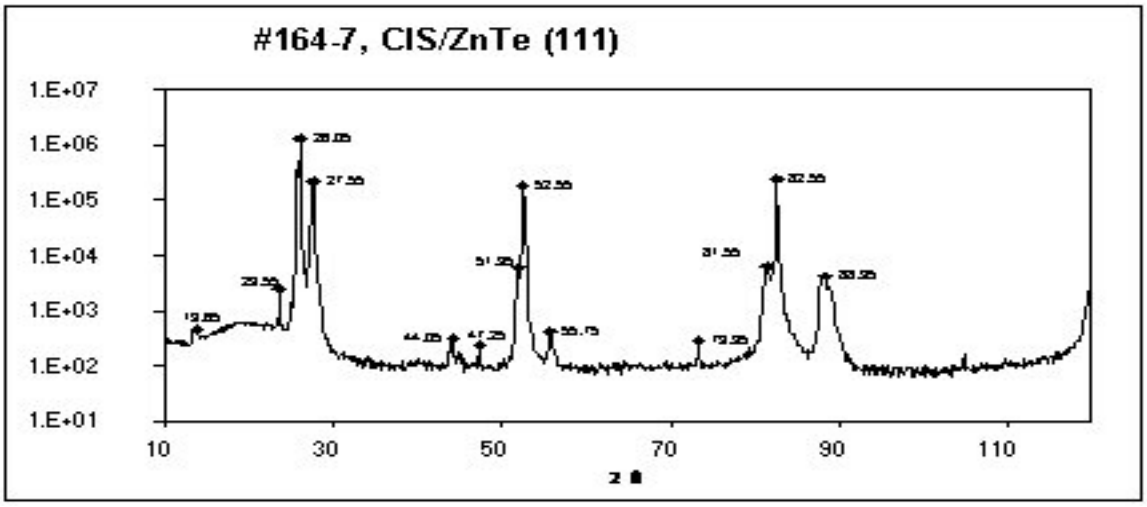

Figure 12.5. XRD spectrum of CuInSe2 grown epitaxially on (111) ZnTe by PMEE.

12.3 Deposition of Precursor Layers

One of the objectives of this program was to explore an alternative pathway using binary precursor layers and the rapid thermal processing. According to the CIS ternary phase diagram, the best candidate phases for these precursor layers are (i) a slightly selenium-rich CuSe and (ii) a slightly selenium-poor InSe. The reason is that these binary compositions they have the lowest melting temperatures among the possible phases, 523^{o}C and 550^{o}C, respectively. Thus, this precursor structure has been investigated.

The primary growth parameters are the substrate temperature and the flux rates. For the Cu-Se layer, we could reproducibly produce a copper-rich phase such as $Cu_{2-x}Se$, Cu_2Se, or CuSe by adjusting the flux ratio between copper and selenium. However, a selenium-rich phase has not been achieved. The highest Se content was the 50:50(%) CuSe film, as measured by inductively coupled plasma (ICP). X-ray diffraction analysis indicates that it is β/γ-CuSe phase. An alternative cracking temperature or plasma cracker condition will be explored.

For the InSe bilayer, selenium-rich phases (In_2Se_3 and In_6Se_7) could be easily obtained under normal conditions. Considering selenium loss during the RTP, it is desirable to produce an overall composition with excess Se. The precursor layers tested consisted of CuSe and In_6Se_7, which yields an excess selenium composition (>52%). XRD measurements of the CuSe films indicate that the material is a homogeneous phase. As for the In-Se phases, using an XRD method we cannot exclude the possibility of a mixed phase of In_2Se_3, In_6Se_7 or InSe from the XRD results because of the difficulty in distinguishing peaks. The composition data obtained by ICP analysis assisted in identifying the phases.

12.4 Experimental Evidence for a Liquid Phase During the Growth

Growth of this binary structures gave an interesting experimental result that seems to be related to the vapor-liquid-solid (V-L-S) growth mechanism. Cu-rich CIS thin films have been grown under various temperature conditions and composition ratios. Certain surface morphology is reproducibly obtained when both conditions of Cu-rich and sufficient selenium flux are fulfilled. Droplet-shaped islands are formed on the surface of Cu-rich CIS thin films (see Figure 12.6). According to characterization results via AES and EDS, the islands (*droplet regions*) have a different composition from the other region (*plane region*). The composition of the droplet regions is more Cu-rich than that of the plane region. When the overall composition of the films is slightly Cu-rich, only the droplet region has a Cu-rich composition, while the plane region is slightly Cu-poor or almost stoichiometric (Cu/In ≤1). This suggests that there is a lateral phase segregation in the growth plane during the growth process.

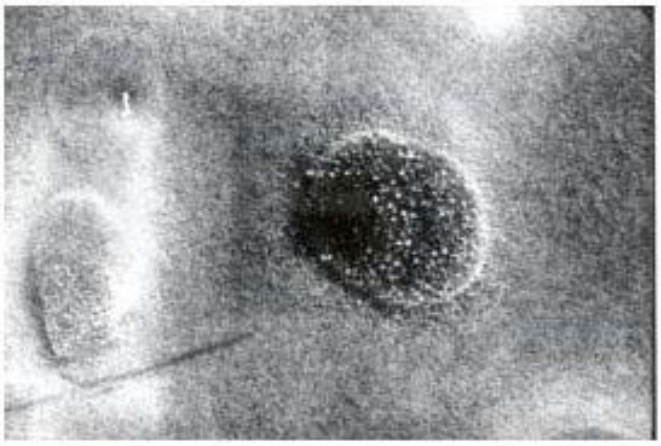

Figure 12.6. Droplet structures on an as-grown Cu-rich $CuInSe_2$ film.

Observation by SEM revealed that the grain size of the droplet region is larger than that of the plane region. XRD analysis shows that the structure has a Cu-rich secondary phase, $Cu_{2-x}Se$. The droplet structure remains even after etching out the secondary phase with a KCN solution, which means that the larger grains as well as the Cu-rich secondary phase are $CuInSe_2$.

A hypothesis is that the droplet structure is produced by the presence of a liquid phase which induces a superior grain-growth mechanism. The shape of the structure is very similar to that of liquid droplets. The Cu-rich composition in the droplet region indicates that the region was covered by the Cu-rich secondary phase that has a lower melting point than that of $CuInSe_2$. The difference in grain size between the droplet region and the plane region becomes larger when an annealing step is introduced at the end of the deposition, probably because the annealing step enhances surface migration (Figure 12.7).

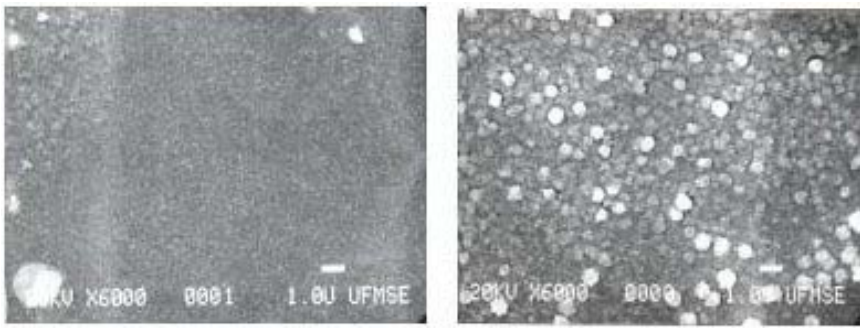

Figure 12.7. Comparison of the grain size in (a) plane region and (b) droplet region.

The droplet structure did not form when the selenium composition was below 50%, even though the film is Cu-rich. Cu-Se secondary phases such as Cu_2Se and $Cu_{2-x}Se$ have high melting point compared to the selenium-rich Cu-Se (523^{o}C). It can be easily inferred that the deficiency in selenium the prevented formation of the low melting phases; hence, no liquid phase could form during the growth process. These observations and the analysis results consistently

suggest that the droplets are caused by the presence of the Cu-Se secondary phase, and that it enhances the grain growth. The shape of the droplets observed becomes similar to that of a liquid droplet at high growth temperature or under a high-temperature annealing process (see Figure 12.8).

Figure 12.8. Droplet structures on an as-grown Cu-rich $CuInSe_2$ film with annealing.

Regarding the V-L-S hypothesis proposed above, there are still some questions that need to be answered. Firstly, the substrate temperature of $400\pm30^{o}C$ is too low to melt the secondary phases since the lowest melting temperature of the secondary phases is $523\ ^{o}C$ (CuSe). The issue may be resolved by appealing to results reported in the literature that show, for other materials than the ones considered in our studies, that the thermodynamics and kinetics on the surface can be quite different from that of bulk state in thin-films [5]. It is possible for some species to condense as a liquid or semi-liquid phase at temperatures approximately equal to 2/3 of the melting point (in degrees K) of its bulk state. Applying this observation to our films, the 2/3-rule yields a melting point of 236°C, making the hypothesis plausible.

A second issue is to resolve why so far this evidence has been obtained only in our PMEE system and not in other growth systems. The answer may lie in the fact that the PMEE reactor has a series of unique features. Our PMEE system features a rotating platen that sequentially exposes the substrates to one flux-source at the time; therefore, the exposure of the substrate to each source flux intermittent and periodic rather than constant. The platen also drives the substrates over a fluxless relaxation zone which is designed for enhancing surface migration effects. We hypothesize that these features make the reaction occur closer to a thermodynamic and kinetic equilibrium point that in the case of the typical co-deposition typically used for CIS growth. Some of the key differences between PMEE growth and typical co-deposition systems are explored in more detail in Part 16 of this report.

As for the phase segregation effect, namely that the liquid phase exists on the solid phase, it is commonly observed that the liquid phase tends to agglomerate forming droplets to make the system more thermodynamically stable. A similar mechanism is likely to occur in the V-L-S growth model since the surface is covered by the liquid phase. The reason why this effect has not been observed in typical co-deposition systems may be that the surface of the growing films

receives a constant flux during the growth process. In such systems, the kinetic and thermodynamic state must be far from equilibrium, and the agglomeration of the liquid phase may be prevented or minimized by the constant arrival of the molecules on the surface.

It has been observed that occurrence of the droplet morphology is a function of the substrate type. The structure clearly formed on Mo-coated SCG but it did not appear on the bare-glass substrate. Based on work on phase-segregation in Al-Ge deposition, Adams[6] suggest that phase segregation is lateral during the initial stages of growth, and it later becomes transverse as the film grows thicker. This transformation occurs to make the system more stable thermodynamically. Our conjecture is that a similar thermodynamic model may be developed for CIS thin-film growth mechanisms, and in our future work will aim to gain a better understanding the fundamental physics underlying this process.

12.5 References

[1] B.J. Stanbery, C.H. Huang, C.H. Chang, S.S. Li and T.J. Anderson, "Characterization and Processing of CuInSe2 Solar Cells", *Proceedings of 2nd World Conference on Photovoltaic Solar Energy Conversion*, Vol. 1, pp. 529-532 (1998).

[2] B.J. Stanbery, C.-H. Chang, S. Kim, S. Kincal, G. Lippold, S.P. Ahrenkiel, L. Li, T.J. Anderson, M.M. Al-Jassim, "Epitaxial Growth of CuAu-Ordered $CuInSe_2$ Structural Polytypes by Migration Enhanced Epitaxy", in *Self Organized Processes in Semiconductor Alloys*, MRS Symposium Proceedings, Vol. 583, pp. 195-200 (2000).

[3] B.J. Stanbery, S. Kincal, S. Kim, T.J. Anderson, O.D. Crisalle, S.P. Ahrenkiel, and G. Lippold, "Role of Sodium In The Control of Defect Structures in CIS", *Proceedings 28th IEEE PVSC*, Anchorage, September (2000).

[4] B.J. Stanbery, C.H. Chang and T.J. Anderson, "Engineered Phase Inhomogeneity for CIS Deice Optimization", *Inst. Phys. Conf. Ser.* No. 152, pp. 915-922, ICTMC-11.

[5] E.I. Givargizov, *Oriented Crystallization on Amorphous Substrates*, Plenum Publishing Corp., New York, (1991).

[6] C.D. Adams, M. Atzmon, Y.T. Cheng, and D.J. Srolovitz, "Phase separation during co-deposition of Al-Ge thin films", *J. Mater. Res.* Vol. 7**,** 653 (1992).

PART 13

Progress on CIS and CGS Single-Crystal Growth

Abstract

Morphological and compositional characterization were performed for two CIS thin films grown on GaAs substrates in the University of Florida PMEE reactor under ration of copper to indium mass flow rates. Characterizations were performed by SEM, AFM, EDS and AES. Each film showed two regions with different morphologies. Using different source-flux ratios and different substrate temperature appears to affect the growth mechanism or crystal quality of the final CIS films. Additional experiments will be performed in the near future to more fully assess the effect of the source flux ratio on the growth mechanism and crystal quality.

Section Contents

13.1 Brief Overview

13.1.1 Participants

Faculty Adviser: Prof. Timothy J. Anderson

Research Assistant: Seokhyun Yoon

13.1.2 Objectives

As a first step in the process of characterizing the electrical properties of CIS and CGS single crystals, the differences in the morphology and the composition between two $CuInSe_2$ (CIS) films of different compositions were studied, including the effect of using different substrate temperatures and different rations of elemental-source fluxes.

13.2 Introduction

Past work on single crystals and thin films CIS showed that CIS can be made as p- or n-type, depending on the growth or annealing conditions [1,2]. The conductivity type was proposed to be dominated by the presence of intrinsic defects, such as Cu, In, and Se vacancies, interstitials, and other antisite defects [3]. The electrical transport properties, such as carrier mobility, were proposed to be affected by the defects through the scattering of holes or electrons by defects [4]. Therefore, it is very important to study the defect structure of CIS or CGS with the goal of better understanding the behavior of solar cells and attaining improvements in their performance. It has also recently been discovered that high efficiency CIS cells can be fabricated only on soda-lime glass, and it is believed that out-diffusing Na ions may favorably influence CIS grain growth or its electrical conductivity [5]. It has also been proposed that Na-related defects can increase conductivity through the increase of effective carrier density and the reduction of compensation [6,7]. We are motivated to study single-crystal films to remove the confounding effects of grain boundaries which exist in the polycrystalline thin film.

This report includes the results of characterization of CIS thin films grown on GaAs a substrate which was assumed to be single crystals. Two CIS thin films grown under different source-flux ratios were investigated by high resolution Scanning Electron Microscopy (HR-SEM), Atomic Force Microscopy (AFM), Energy Dispersive Spectroscopy (EDS) and Auger Electron Spectroscopy (AES). The characterization analysis suggests details of the growth mechanism for each experimental condition.

13.3 Experiments

13.3.1 Growth conditions

Two CIS thin films grown on (1 0 0) GaAs substrates were utilized to assess the differences in morphology and composition resulting from the use of different Cu/In source flux ratios. The University of Florida Migration Enhanced Epitaxy (MEE) reactor was used to grow

CIS thin films. The MEE reactor is a variant of a standard MBE (Molecular Beam Epitaxy) system, with the difference that the substrate in MEE is exposed to cationic and anionic fluxes sequentially rather than simultaneously. Another distinguishing feature is that the MEE reactor introduces relaxation steps without flux between each exposure; thus, the atoms of each element on the substrate may have time to migrate horizontally and therefore and enhance epitaxial growth. Previous MEE systems used source shutters to control and alternate the fluxes. In contrast, the substrate is rotated in the MEE system and shutter wear is thus reduced while throughput is increased. Furthermore, a condensation shield has been designed to eliminate source interaction. A schematic diagram of the configuration of the reactor is shown in Figure 13.1.

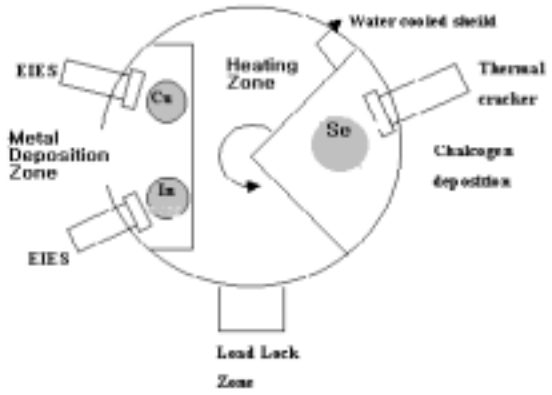

Figure 13.1. Configuration of the MEE reactor (top view).

Inside the reactor there is a substrate platen located near the top, where up to 9 substrates can be placed. The substrate platen can be rotated in either direction. The inside of the reactor is also divided into four zones (see Figure 13.1), namely, a heating zone, a metal deposition zone, a load-lock zone, and a chalcogen deposition zone. The back of the substrated is heated when the substrate on the platen passes below the radiation heater. The substrate next enters the metal deposition zone where copper atoms from an effusion cell first impinge on the substrate and then, as the substrate is transported by the rotational platen to another location, In atoms emanating form another effusion cell are deposited. Before the substrate enters the chalcogen deposition zone, it passes the load lock zone, where the sample can be loaded and a relaxation process occurs. In the chalcogen deposition zone, Se or S is deposited from effusion sources working as pyrocrackers. Then the substrate again enters the heater zone and the cycle is repeated. The system may reach a pseudo steady state after several rotations and each atomic layer can be deposited sequentially and the atoms are allowed to migrate along the surface to form expitaxial layers.

Two CIS thin films with different metal source fluxes were investigated in this study under the experimental conditions shown in Table 13.1. The table shows that sample CIS161 grown under In-rich condition in the source fluxes, and CIS163 is grown under Cu-rich condition in source flux. Other parameters of relevance include a substrate temperature of 550 C, a platen rotation of 20 RPM, a Se-crucible Temperature of 145C, and a Se cracker temperature of 350 C.

Table 13.1. Growth condition of CIS thin film 161 and 163

Sample ID	Cu flux (Angstrom/sec)	Cu flux : In flux	Rotation direction
CIS161	9.9	1 : 1.43	CCW
CIS163	9.9	1 : 0.96	CW

13.3.2 Morphological analysis

Samples CIS161 and CIS163 were investigated by high resolution SEM. For CIS161, we could observe a white semi-continuous pattern on the surface with dark background region at low magnification as in Figure 13.2.a. However, we could see particle-like islands on the surface of CIS 163 as in Figure 13.2.b.

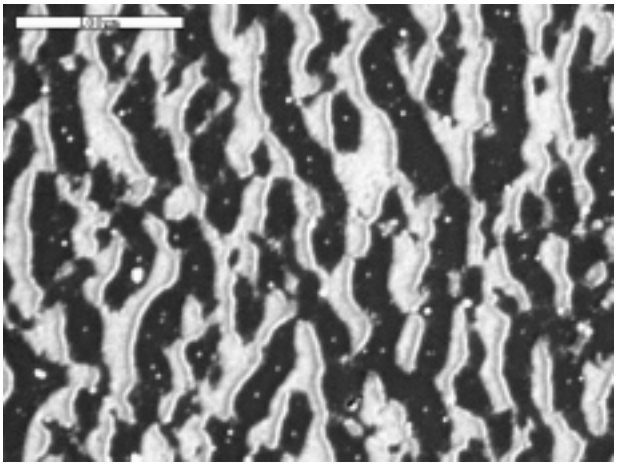

Figure 13.2.a. Sample CIS161 (330X).

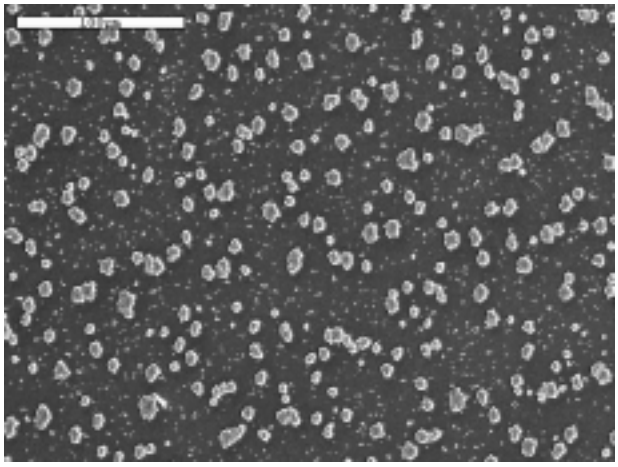

Figure 13.2.b. Sample CIS163 (330X).

Regarding the dark background region, we could not observe any further grain-like structure in any of the samples. However, in two island-like bright region in each sample, some grain structures were identified under high magnification, as shown in Figures 13.3.a. and 13.3.b. It appears that the size of the grains in sample CIS161 was between 600 nm and 800 nm. We could not see clearly the boundary of each grain for CIS163, and the grains seemed to be much smaller.

To observe the structure of the island structures in three dimensions and with higher lateral and vertical resolution, we investigated the surface of each sample by AFM. Figures 13.4.a and 13.4.b. are AFM images of CIS161. Whereas Figure 13.4.a. is the image obtained by the deflection of the AFM tip, Figure 13.4.b. is a real height change of the surface of sample CIS161. As can be seen in Figure 13.4.b., the island regions are surrounded by barrier-like structures about 2 μm above the dark background region, and the inside of the island is about 1 μm above the background region. If we consider the three dimensional image, it is more pronounced in Figure 13.5. Hence, it appears that there might have been some kind of evaporation process inside the island regions. Through observations at higher resolutions, we could see many grain structures inside the island region, with sizes ranging from 50 nm to 500 nm, as shown in Figures 13.6.a. and 13.6.b. There were no further structure changes observed in the dark background region under higher resolution as in the case by HR-SEM.

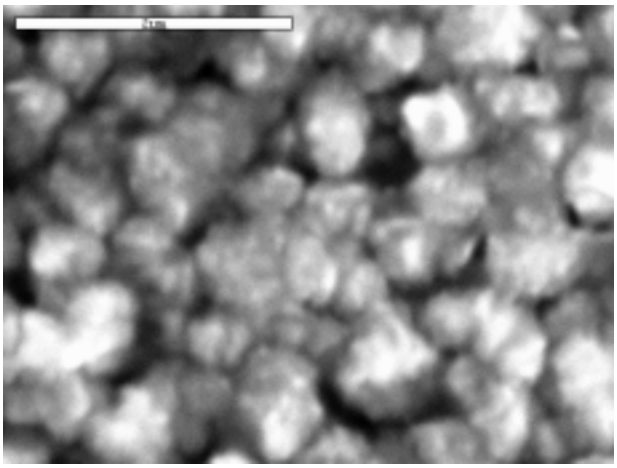

Figure 13.3.a. Sample CIS161, island region (27,000X).

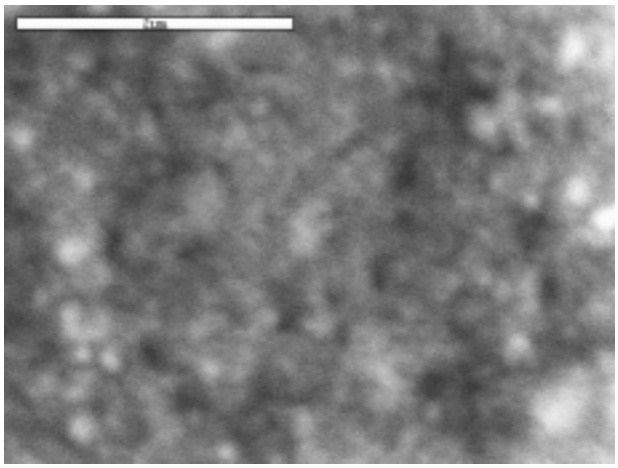

Figure 13.3.b. Sample CIS163, island region (27,000X).

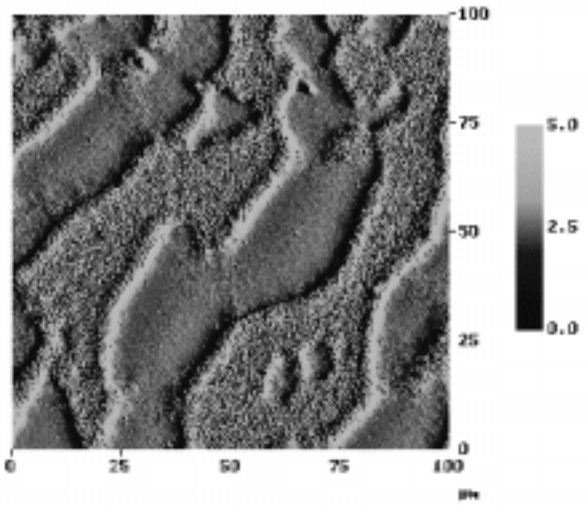

Figure 13.4.a. Deflection view of sample CIS161 by AFM.

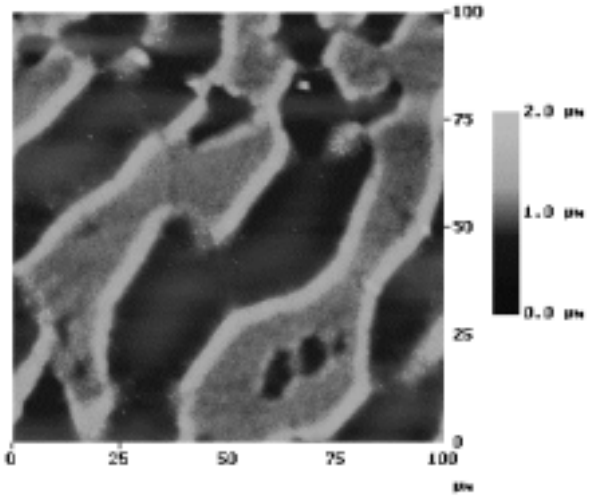

Figure 13.4.b. Height image of sample CIS161 by AFM.

For sample CIS163 we observed large islands with a height of about 800 nm and with a diameter of about 7 μm, as shown in Figure 13.7.a. We could also observe small islands with dimensions of less than 1 μm. Under higher resolution we observed many smaller grains inside the large island structure, with sizes ranging from 20 nm to 200 nm. There were no further small grain-like structures found in the dark background region, as in the case of sample CIS161.

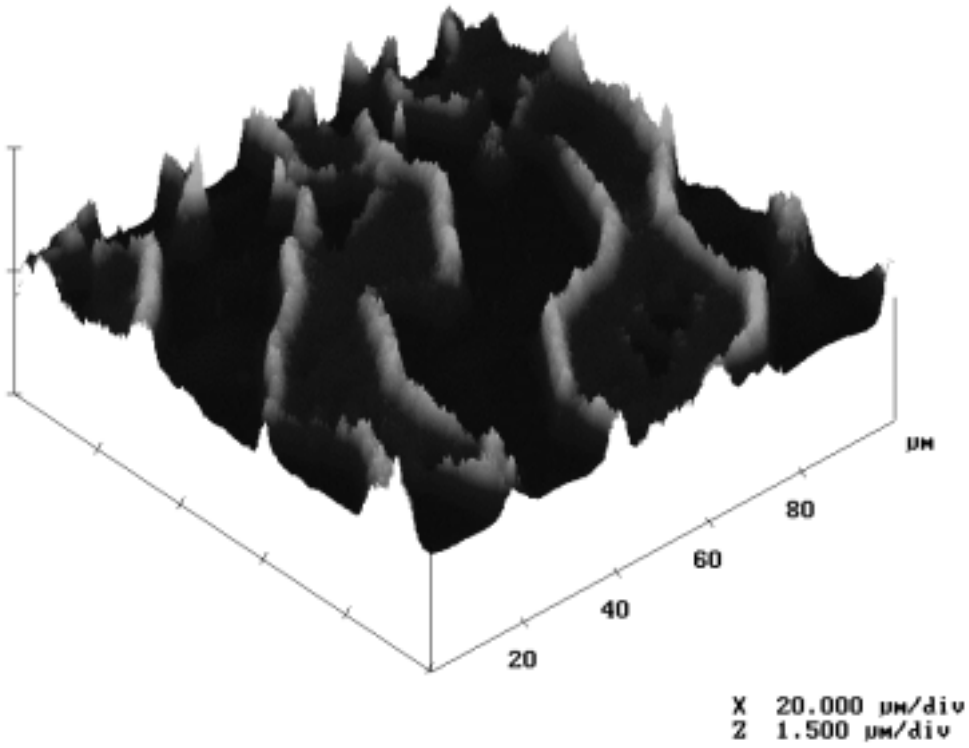

Figure 13.5. Three dimensional view of the surface of sample CIS161.

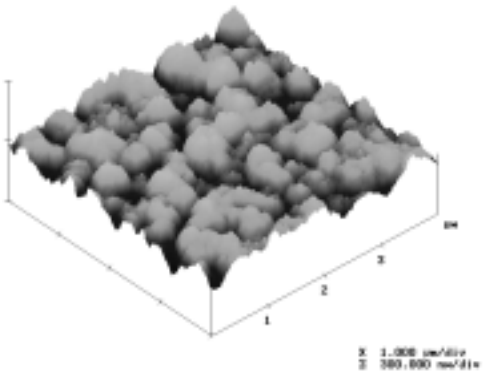

Figure 13.6.a. 3-D view of CIS161 : Scan area = 4 μm x 4 μm.

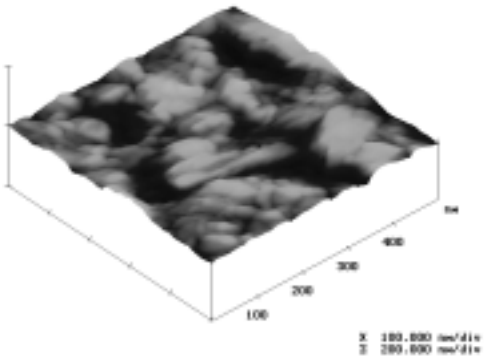

Figure 13.6.b. 3-D view of CIS161 : Scan area = 500 nm x 500 nm.

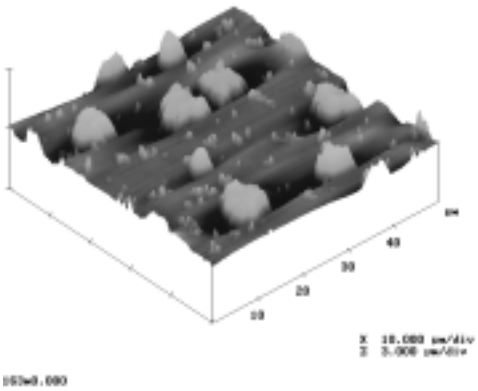

Figure 13.7.a. 3-D view of CIS163 : Scan area = 50 μm x 50 μm.

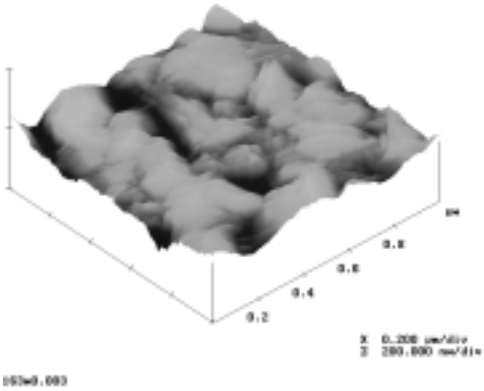

Figure 13.7.b. 3-D view of CIS163 : Scan area = 1 μm x 1 μm.

13.3.3 Compositional analysis

As discussed in Section 13.3.2., there were differences in the morphologies between the bright island-like region and the dark background region. Usually such morphological differences result from phase or compositional difference. To probe this issue EDS analysis was performed for samples CIS161 and CIS163. As shown in Table 13.2., there was no difference in bulk composition between the island (bright) region and dark region for sample CIS161. Although for sample CIS163 it seems that the dark region has a slight Cu-rich composition, the difference must be neglected given the available resolution of the EDS technique.

Table 13.2. Bulk composition for two regions of CIS161 by EDS.

Sample ID	Cu, In, Se atomic composition in dark region	Cu, In, Se atomic composition in island (bright) region
CIS161	24.08% : 28.08% : 47.84%	24.00% : 27.88% : 48.12%
CIS163	25.82% : 26.93% : 47.25%	25.25% : 27.43% : 47.32%

We could nevertheless see large differences in surface composition between the two regions via AES analysis, as reported in Table 13.3. The composition of the dark region is highly Cu-rich for both samples, whereas the Cu to In ratio for the island region is almost unity for both samples. Therefore, it appears that in the dark region a Chalcopyrite CIS crystal structure was not formed due to a high deviation from the required stoichiometry. This may be the reason why we could not observe any further grain structures under higher resolution. Both regions showed a higher Cu-rich composition after sputtering, as reported in Table 13.4.

Table 13.3. Surface composition of CIS161 and CIS163 by AES

ID	Cu : In : Se in dark region	Cu : In	Cu : In : Se in bright region,	Cu : In
CIS161	26.71% : 19.13% : 54.16%	1.40 : 1	20.91% : 19.66% : 59.43%	1.06 : 1
CIS163	24.27% : 13.24% : 62.49%	1.83 : 1	16.22% : 15.68% : 68.10%	1.03 : 1

Table 13.4. Composition of CIS161 and CIS163 by AES after sputtering for 5 minutes

ID	Cu : In : Se in dark region	Cu : In	Cu : In : Se in bright region,	Cu : In
CIS161	19.89% : 16.54% : 63.57%	1.20 : 1	23.63% : 18.50% : 57.87%	1.28 : 1
CIS163	32.88% : 18.05% : 49.08%	1.82 : 1	28.41% : 16.19% : 55.40%	1.75 : 1

13.4 Discussion and future work

We found different morphologies for two CIS thin films under different Cu to In source flux-ratios. Sample CIS161 grown under an In-rich source flux showed an In-rich bulk composition, and presented semi-continuous island regions where many grain structures exist. Sample CIS163 had a less In-rich bulk composition, and presented many particle-like islands with smaller grains (compared to those of sample CIS161). Hence, it appears that different Cu to In flux-ratios result in different growth mechanism. However, there is another possibility that must be considered, namely, as the rotation direction for the growth of CIS161 was counterclockwise, Cu and In are deposited when the substrate temperature is near its maximum; as a consequence, the metal atoms might have increased mobility and this might result in larger grain size than that of CIS163.

In the future we plan to use diffraction mode Transmission Electron Microscopy (TEM) analysis to characterize the crystal quality and the phase differences observed between the two distinct regions that were realized through growth. A comprehensive experimental matrix will be carried out to characterize the crystal growth process taking into consideration several ratios of elemental-fluxes and including both clockwise and counterclockwise rotational directions.

13.5 References

[1] V. Shahidi, I. Shih, T. Araki and C. H. Champness, *J. Electron. Mater.* 14, 297 (1985).

[2] S. Isomura, H. Kaneko, S. Tomioka, I. Nakatani and K. Masumoto, Japan. *J. Appl. Phys.* 19, 23 (1980).

[3] H. Newman, *Crystal Res. Technol.* 18, 483 (1983).

[4] D. J. Schroeder, E. Arushanov and E. Bucher, *Solar Energy Materials and Solar Cells*, 61, 417 (2000).

[5] J. Hedstrom, H. Ohisen, M. Bodegard, A. Kylner, L. Stolt, D. Hariskos and M. Ruckh, *Proc. 23rd IEEE Photovoltaic Specialists Conf.*, Louisville, 364 (1993).

[6] D. Schroeder and A. A. Rockett, *J. Appl. Phys.* 82, 4982 (1997).

[7] Su-Huai Wei, S. B. Zhang and A. Zunger, *J. Appl. Phys.* 85, 7214 (1999).

PART 14

Simulation of CIS-Based Solar Cells

Abstract

The AMPS (Analysis of Microelectronic and Photonic Structures) one-dimensional device simulation program was used to simulate the ZnO/CdS/CIS-based solar cells performance parameters for different CdS buffer layer and absorber layer thickness. We have performed numerical simulation of the ZnO/CdS/CIS-based solar cells taking into account the effects of acceptor-like defects and doping concentration in the CdS buffer layer. In addition, we performed numerical simulation of the ZnO/$Cd_{1-x}Zn_xS$/CIS-based solar cells. Simulation of the current-voltage (JV) and spectral response (QE) characteristics has been carried out on these cells.

Section Contents

14.1 Brief Overview

14.1.1 Participants

Faculty Adviser: Prof. Sheng S. Li

Research Assistants: Jiyon Song

14.1.2 Objectives

The objective of this research task is to develop theoretical models and perform numerical simulations to characterize the performance of CIS-based solar cells deposited with different buffer layers and to compare the results with experimental data. The goal is to produce a simulation model to guide the design of high-efficiency CIS and CIGS cells with optimized cell parameters, and to gain a better understanding of the basic physics underlying the cell's performance.

14.2 Numerical simulation of ZnO/CdS/CIS-based solar cells with different CdS buffer layer and absorber layer thickness

14.2.1 The effect of CdS layer thickness on the CdS/CIS and CdS/CIGS cells

The AMPS (Analysis of Microelectronic and Photonic Structures) One-Dimensional (1-D) Device Simulation Program was used to simulate the CdS/CIS solar cell performance parameters for different CdS buffer layer thickness. Simulation of the current-voltage (JV) and spectral response (QE) curves has been made. For the CdS/CIS cells, increasing the CdS buffer layer thickness will increase the absorption of the shorter wavelength incident light in the CdS layer, and hence the short-circuit current of the cell decreases. In addition, using a thicker CdS buffer layer will increase the series resistance of CIS solar cells, and causes a poor fill factor in the cell (see Table 14.1 and Figure 14.1) [1]. However, for the CdS/CIGS cells, increasing the CdS buffer layer thickness from 20 nm to 60 nm showed improvements in device performance, but the efficiency starts to decrease when the buffer layer thickness increases to 90 nm (see Table 14.2 and Figure 14.2). In general, very thin CdS films (< 50 nm) are commonly used in the CIS solar cells. Since light absorbed in the CdS layer usually does not contribute much to the collection of photocurrent, it is desirable that this layer be kept at the minimum thickness possible. The minimum thickness should allow for the CdS conformal coverage of the substrate without formation of defects that could shunt the cell.

The band gap energy of the CIS absorber layer can be increased by the incorporation of Ga to form a CIGS absorber layer to increase the band gap energy, matching it more closely to the solar spectrum. This results in a tradeoff of higher open-circuit voltage and lower short-circuit current, which should be advantageous for the manufacture of CIGS photovoltaic modules. A higher band gap energy reduces the current losses due to free carrier absorption in ZnO or other transparent conducting materials. When the band gap energy of the CIGS absorber layer is increased by the incorporation of Ga or S, the loss in the conversion efficiency due to the

decrease of light generated current with increasing voltage becomes important. A high-efficiency CIGS solar cell with conversion efficiency of approximately 18% has been reported recently [2]. Figure 14.3 and Figure 14.4 show the simulation results of the current-voltage (JV) and spectral response (QE) curves for the CdS/CIS and CdS/CIGS cells.

From these simulation studies conducted, it is concluded that using thicker CdS buffer layer in the CIS cells causes a poor fill factor in the cell. However, for the CdS buffer layer in the CIGS cells, increasing the CdS buffer layer thickness from 20 nm to 60 nm shows improvement in device performance, but the efficiency starts to decrease when the buffer layer thickness increases to 90 nm. We also see a higher efficiency realized in the CdS/CIGS cells than in the CdS/CIS cells.

Table 14.1. Simulation results for the CdS/CIS cells

CdS Thickness (nm)	V_{oc} (V)	J_{sc} (mA/cm^2)	Fill Factor	Efficiency (%)
20	0.453	39.235	0.763	13.569
30	0.450	38.952	0.762	13.365
40	0.448	38.693	0.758	13.147
50	0.446	38.453	0.746	12.786
60	0.444	38.214	0.684	11.605
80	0.441	37.567	0.270	4.478

Table 14.2. Simulation results for the CdS/CIGS cells

CdS Thickness (nm)	V_{oc} (V)	J_{sc} (mA/cm^2)	Fill Factor	Efficiency (%)
20	0.706	33.600	0.612	14.523
30	0.699	33.625	0.682	16.040
40	0.695	33.651	0.729	17.053
50	0.694	33.676	0.745	17.417
60	0.693	33.683	0.748	17.459
90	0.692	33.209	0.741	17.027

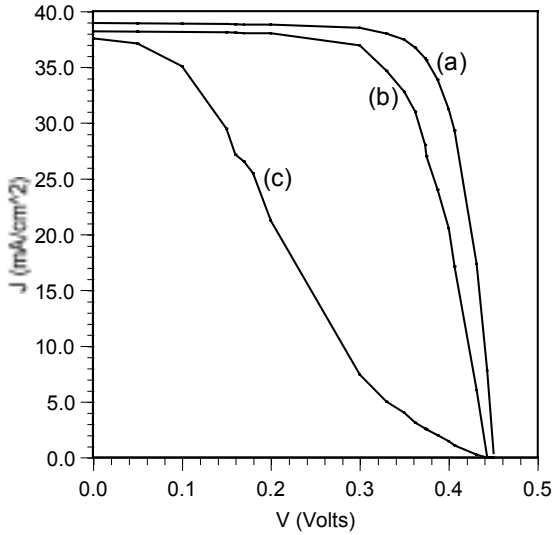

Figure 14.1. Light J-V of the CIS solar cell using different thickness of the CdS buffer layer simulated by AMPS-1D for (a) 30 nm, (b) 60 nm, and (c) 80 nm.

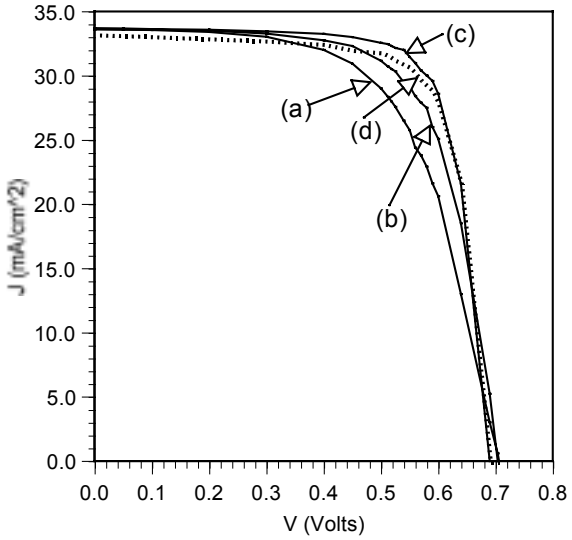

Figure 14.2. Light J-V of the CIGS solar cell using different thickness of the CdS buffer layer simulated by AMPS-1D for (a) 20 nm, (b) 30 nm, (c) 60 nm, and (d) 90 nm.

14.2.2 The effect of CIS layer thickness on the cell performance

The AMPS (Analysis of Microelectronic and Photonic Structures) One-Dimensional (1-D) Device Simulation Program was used to simulate the CdS/CIS solar cell performance parameters for different CIS absorber layer thickness. The cell performance is shown to be unaffected by reducing the film thickness in the CIS absorber layer as shown in Table 14.3. Thinner absorber layers reduce the total amount of material used and allow faster process throughput. If absorber layer becomes too thin, such that the minority carrier diffusion length becomes comparable to the thickness, then V_{OC} may be reduced by the back surface recombination at the Mo/CIGS interface.

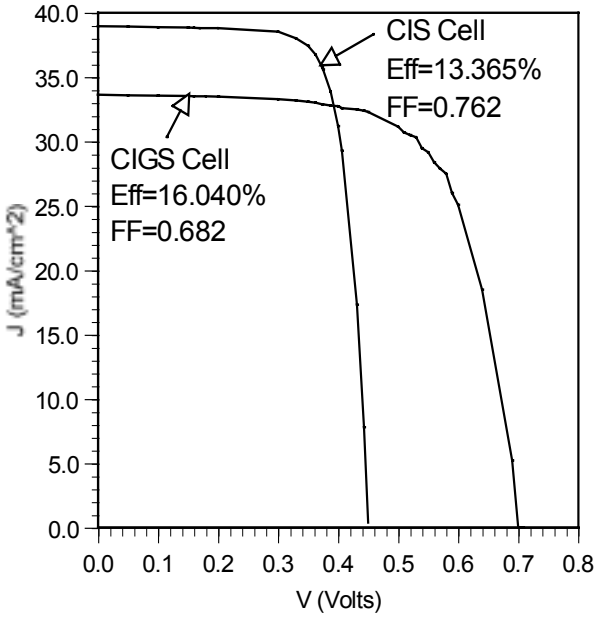

Figure 14.3. Light J-V of the CIS and CIGS solar cells simulated by AMPS-1D for 30 nm thickness of CdS buffer layer.

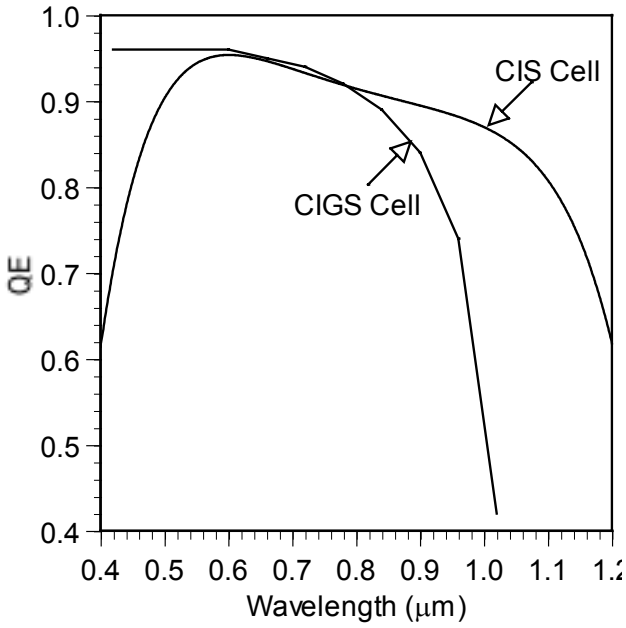

Figure 14.4. Spectral response (QE) curves of the CIS and CIGS solar cells simulated by AMPS-1D.

Table 14.3. The effect of CIS layer thickness on the CdS/CIS cell performance

CIS Thickness (nm)	V_{oc} (V)	J_{sc} (mA/cm^2)	Fill Factor	Efficiency (%)
3570	0.451	39.698	0.763	13.673
3070	0.451	39.383	0.763	13.543
2570	0.450	38.952	0.762	13.365
2070	0.450	38.332	0.760	13.109
1570	0.449	37.371	0.758	12.714
1070	0.447	35.717	0.754	12.033

The results presented indicate that reducing the thickness of the CIS layer does not affect too much on the cell performance. The minimum thickness is limited by the optical absorption coefficient of the CIS layer or the ability to incorporate optical confinement from a device perspective.

14.3 Numerical simulation of the ZnO/CdS/CIS-based cells taking into account the effects of acceptor-like defects and doping concentration in the CdS buffer layer

We have performed numerical simulation of the ZnO/CdS/CIS solar cells using the AMPS-1D program. We divided the CIS absorber into nine sections for simulation purposes. We have incorporated two main defects in the simulation. One is a shallow- level defect with activation energy of E_V+0.03 eV, which exists in each section of the CIS layer. The other defect has an

activation energy of E_C-0.34 eV, and it only exists in the first section of the CIS layer next to the CdS layer. This initial uniform band-gap solar cell model has a conversion efficiency of 13.353 %, a V_{OC}=0.452 V, a J_{SC}=38.873 mA/cm^2, and an F.F.=0.761.

The CdS layer plays a critical role in fabricating the high efficiency solar cells. From our previous simulation studies we have found that using a thicker CdS buffer layer in the CIS cells causes a poor fill factor. To characterize the effects of donor-like and acceptor-like defects in the CdS layer, we simulated the presence of both of these defects in the middle of the band gap to make them effective in recombination, and we varied their concentration. The results have shown that a donor-like defect in the CdS layer has no effect on the cell performance. The resulting simulated cells have a conversion efficiency of 13.353 %, a V_{OC}=0.452 V, a J_{SC}=38.873 mA/cm^2, and a F.F.=0.761 for the donor-like defect densities varying from 1×10^{15} cm^{-3} to 1×10^{18} cm^{-3}. In contrast, the acceptor-like defects in the CdS layer have a significant influence on the cell performance. Table 14.4 shows the results of their effect on the cell performance. This trend was also seen in the CdS and interface layers in the CIGS cells reported by the Penn State simulation studies [3].

The effect of doping concentration in the CdS layer is shown in Table 14.5. The results reveal that the performance changes with varying doping concentrations in the CdS layer. The doping in the CdS layer acts to reduce the concentration of trapped electrons, changing the cell performance.

The crystal structure of the CIS and the consequences of a lattice mismatch between the CdS and ZnO is an important issue. The simulation studies show that there is a significant different between the lattice constants of ZnO and CdS. The simulation results produced a 14.049 % conversion efficiency (V_{OC}=0.461 V, J_{SC}=39.856 mA/cm^2, and F.F.=0.765) of ZnO/CIS cell without the CdS layer. NREL has developed a process to fabricate the ZnO/CIS cells with a 13.5 % conversion efficiency without any buffer layers.

The results presented indicate that donor-like defects in the CdS layer of the CIS cells have no effect on the cell performance, while acceptor-like defects do influence the cell performance. The doping concentration in the CdS layer in the CIS cell influences the cell performance, increasing the conversion efficiency with increasing doping concentration. We also notice a 14.049 % conversion efficiency in a ZnO/CIS cell without the CdS layer.

14.4 Numerical simulation of ZnO/$Cd_{1-x}Zn_xS$/CIS-based solar cells

We have performed numerical simulation of the ZnO/$Cd_{1-x}Zn_xS$/CIS cells by using the AMPS-1D simulation program. For a simple CIS solar cell model, we have used a ZnO (50 nm) layer, a $Cd_{1-x}Zn_xS$ (30 nm) layer, and the CIS absorber (2570 nm) layer from the top layer. The key parameters for the simulation are band gap energy, electron affinity, and optical absorption coefficients. Simulation of the current-voltage (IV) characteristics has been carried out on these cells.

The $Cd_{1-x}Zn_xS$ buffer layer gives a better match of lattice spacing and electron affinity between the $Cd_{1-x}Zn_xS$ and $CuInSe_2$ layers. The replacement of CdS with a higher band gap $Cd_{1-x}Zn_xS$ leads to the increase in quantum efficiency in the short wavelength region, a zero-band offset, a decrease in window absorption losses, and increases in the short- circuit current and open- circuit voltage. Increasing the Zn content in the CdS from x=0 to 1.0 gives a decrease of

the electron affinity from 4.5 eV (CdS) to 3.9 eV (ZnS) and increases of the band gap energy from 2.42 eV (CdS) to 3.60 eV (ZnS). Theoretical calculations show that the optimal Zn content is in the range of 15 – 17 % for lattice spacing and electron affinity matching to the $CuInSe_2$. Experiments have been performed on the $Cd_{1-x}Zn_xS/CuInSe_2$ cells with conversion efficiency, η, exceeding 9 %.

Table 14.4. The effect of acceptor-like defects in the CdS layer

Acceptor-like Defect Density (cm^{-3})	V_{oc} (V)	J_{sc} (mA/cm^2)	Fill Factor	Efficiency (%)
1×10^{15}	0.451	38.873	0.761	13.350
1×10^{16}	0.451	38.872	0.760	13.329
5×10^{16}	0.448	38.870	0.759	13.234
1×10^{17}	0.446	38.867	0.756	13.109

Table 14.5. The effect of doping concentration in the CdS layer

Doping Concentration (cm^{-3})	V_{oc} (V)	J_{sc} (mA/cm^2)	Fill Factor	Efficiency (%)
1×10^{15}	0.448	38.869	0.758	13.197
1×10^{16}	0.448	38.870	0.759	13.221
1×10^{17}	0.454	38.875	0.762	13.458
1×10^{18}	0.549	38.920	0.788	16.841

Using the 18.3 % Zn and 38.5 % Zn contents, i.e. E_g=2.595 eV for the $Cd_{0.817}Zn_{0.183}S$ and E_g=2.811 eV for the $Cd_{0.615}Zn_{0.385}S$, we have calculated the V_{oc}, J_{sc}, F.F., and conversion efficiency for the CdZnS/CIGS cells. We have used the optical absorption coefficients with photon energy from the experimental data by chemical bath deposition (CBD) of $Cd_{1-x}Zn_xS$ as input parameters for the simulation [4].

Table 14.6 Simulation results for the CdS/CIS, $Cd_{0.817}Zn_{0.183}S$/CIS and $Cd_{0.615}Zn_{0.385}S$/CIS cells. The replacement of CdS with higher band gap $Cd_{1-x}Zn_xS$ leads to the increase in short-circuit current, open- circuit voltage, and conversion efficiency compared to the CdS/CIS cells.

Table 14.6. The simulation results for the $Cd_{1-x}Zn_xS$/CIS cells with different Zn contents

Zn content	V_{oc} (V)	J_{sc} (mA/cm^2)	F.F.	Efficiency (%)
0.0 %	0.438	38.947	0.763	13.027
18.3 %	0.451	39.133	0.762	13.432
38.5 %	0.451	39.540	0.762	13.582

For the CdS/CIS cells values of the electron affinity different $\Delta E_c = \chi_2$ (CdS) - χ_1 ($CuInSe_2$) lie between 0.20 and 0.30 eV. The use of $Cd_{1-x}Zn_xS$ in place of CdS reduces the value of ΔE_c to slightly less than 0.1 eV. Table 14.7 shows the $Cd_{1-x}Zn_xS$/CIS simulation results as a function of ΔE_c for the case of fixed χ_1 (CIS) = 4.3 eV and χ_2 ($Cd_{1-x}Zn_xS$) varied from 4.3 eV to 4.5 eV.

Table 14.7. The $Cd_{1-x}Zn_xS$/CIS simulation results with different electron affinity (χ_2) values

Electron affinity (χ_2)	V_{oc} (V)	J_{sc} (mA/cm^2)	F.F.	Efficiency (%)
4.3 eV	0.451	39.133	0.762	13.432
4.4 eV	0.449	39.132	0.763	13.417
4.5 eV	0.438	39.128	0.763	13.093

It is important to have $\chi_1 = \chi_2$ in order to obtain high V_{oc}. Eliminating the difference in the electron affinity between $CuInSe_2$ (χ = 4.3 eV) and CdS (χ = 4.5 eV) with the addition of Zn to the CdS an efficiency increase to about 13 – 14 % could be achieved.

14.5 Summary and Conclusions

From the simulation studies conducted in this task, it is concluded that using thicker CdS buffer layer in the CIS cells causes a poor fill factor in the cell. However, for the CdS buffer layer in the CIGS cells, increasing the CdS buffer layer thickness from 20 nm to 60 nm shows improvement in device performance, but the efficiency starts to decrease when the buffer layer thickness increases to 90 nm. We also see a higher efficiency realized in the CdS/CIGS cells than in the CdS/CIS cells. It is also concluded that reducing the thickness of the CIS layer does not affect too much on the cell performance. The minimum thickness is limited by the optical absorption coefficient of the CIS or the ability to incorporate optical confinement from a device perspective. The simulation results indicate that donor-like defects in the CdS layer of the CIS cells have no effect on the cell performance, while acceptor-like defects do influence the cell performance. The doping concentration in the CdS layer in the CIS cell influences on the cell performance, increasing the conversion efficiency with increasing doping concentration. We also notice a 14.049 % conversion efficiency in a ZnO/CIS cell without the CdS buffer layer. The replacement of CdS with higher band gap $Cd_{1-x}Zn_xS$ leads to increases in the short-circuit current, open- circuit voltage, and conversion efficiency compared to CdS/CIS cells.

14.6 References

[1] C.H. Huang, Sheng S. Li, L. Rieth, A. Halani, Lei Li, S. Kim, Jiyon Song, T.J. Anderson, and P.H. Holloway, "A Comparative Study of Chemical-bath-deposited CdS, (Cd,Zn)S, ZnS, and $In(OH)_xS_y$ Buffer Layers for CIS-based Solar Cells," *Proc. 28th IEEE photovoltaic Specialists Conference*, pp. 696-699, Anchorage, September (2000).

[2] M.A. Contreras, B. Egaas, K. Ramanathan, J. Hiltner, A. Swartzlander, H. Hasoon, and R. Noufi "Progress Toward 20% Efficiency in $Cu(In,Ga)Se_2$ Polycrystalline Thin-film solar cells," *Prog. Photovolt:Res. App.,* Vol. 7*,* pp 311-316 (1999).

[3] J. Cuiffi, H. Zhu, and S.J. Fonash, The Pennsylvania State University, *Report for the second quarterly report (January – March, 1999) for the program EPRI NREL CIS AMPS.*

[4] J.M. Dona and J. Herrero, "Chemical bath co-deposited CdS-ZnS film characterization," *Thin Solid Films,* Vol 268, pp. 5-12 (1995).

PART 15

Construction of a Computer-Controlled I-V and QE Measurement System

Abstract

A computer-controlled current-versus-voltage (I-V) measurement system for measuring the conversion efficiency and for characterizing the electrical parameters of the CIS-based solar cells was constructed. The measurement apparatus consists of a halogen lamp as the solar simulator, a temperature-controlled test chuck, a programmable power supply as the variable load, electronic instruments for measuring the terminal voltage and current of the test cells, and a computer program for the control of the measurement procedure and for the data acquisition. The I-V curve of the test cell is measured from the forward bias to the reverse bias using the voltage mode with a resolution of 1mV. A computer-controlled spectral response measurement system using a monochromator for wavelength selection to measure the spectral response and quantum efficiency (QE) of the CIS-based solar cells was constructed. The measurement system scanning the spectral range from 400 nm to 1400 nm with 10 nm increment step has the capability of applying white light bias and voltage bias to the test cell, and during the measurement the entire area of the test cell is covered with a uniform and sufficient illumination-level monochromatic light. A computer program based on the LabVIEW software was utilized for the control of the measurement procedure and for the data acquisition.

Section Contents

15.1 Overview

15.1.1 Participants

Faculty Adviser: Prof. Sheng S. Li

Research Assistants: Chia-Hua Huang

15.1.2 Objectives

The objective of this task is to establish the capabilities for the characterization of CIS-based solar cells fabricated at the University of Florida by using the I-V and quantum efficiency (QE) measurements.

15.2 Introduction

Analysis of I-V characteristics is one of the most crucial diagnostic tools utilized to characterize solar cells. The electrical parameters including the conversion efficiency η, open-circuit voltage V_{OC}, short-circuit current density J_{SC}, fill factor F.F., series resistance R_S, shunt resistance R_{SH}, diode ideality factor n, and saturation current density J_0 of a solar cell can be determined from the measured dark- and photo- I-V curves. These parameters are important for understanding and the optimization of the performance of solar cells. A comparison of the electrical performance of solar cells is meaningful only when the photo- I-V measurements are performed with a certain uniform standard, namely the Standard Reporting Conditions (SRC) specifying the total radiation level, device temperature, and reference spectral radiance distribution. The typical SRC for terrestrial solar cells are a total irradiance of 100 mW/cm^2, a reference spectrum of AM1.5 Global (ASTM Standard E892), and a cell junction temperature of 25°C. The apparatus used for the construction of our I-V measurement system and measurement procedure are based on the standard test method for electrical performance of photovoltaic cells using reference cells under simulated sunlight.

Measurements of the spectral response in terms of the wavelength dependence of the photo-generated current for a solar cell as the characterization and diagnostic techniques are extremely important for quality control in cell fabrication, cell design, and understanding the diffusion mechanisms and separation of the individual photocurrent loss mechanisms. The external quantum efficiency (QE), which is defined as the ratio of the generated electron-hole pairs per incident photon, of the solar cell can be calculated from the measured absolute spectral response curve.

15.3 The I-V Measurement Instrumentation and Procedures

15.3.1 The I-V Measurement Instrumentation

15.3.1.1 Solar Simulator and Irradiance Control

The reference cell method, which basically uses the reference cell to adjust the illumination level of the solar simulator, is employed in the performance measurement of CIS and CIGS solar cells. The solar simulator intensity is adjusted by changing the distance between the solar simulator and the test plane so that the measured short-circuit current of the reference cell is equal to its calibrated value at the standard measurement intensity of 100 mW/cm^2. The ELH (tungsten-halogen bulb) lamp with an integral dichroic rear reflector is utilized as the solar simulator in the experimental setup. The ELH lamp is classified as a class C solar simulator by using the ASTM standard procedure E927 due to a lack of energy below the wavelength of 0.5 μm and too much energy in the wavelength range of 0.6-0.7 μm when comparing with global reference spectrum AM1.5G. Using the reference cell method for the efficiency measurements there are always the spectral mismatch errors introduced by the solar simulator and the reference cell due to the difference of the spectrum between the solar simulator and the real solar irradiance at sea level as well as the difference of the spectral response between the reference cell and the test cell. Although we do not intend to directly correct the measured I-V data with the spectral mismatch correction parameter M [1], using a CIGS solar cell calibrated against a primary reference cell and the global reference spectrum by NREL to set the illumination level of the solar simulator can be served as a first order correction for the spectral mismatch in the photo- I-V measurement system.

15.3.1.2 The Measurement Platform and Temperature Control

The open-circuit voltage of the CIS or CIGS solar cells decreases with increasing temperature at an irradiance power density of 100 mW/cm^2 from the solar simulator. In order to have the measurement under the standard reporting conditions (SRC) with temperature at 25°C for the cell junction and the illumination intensity of the solar simulator at 100mW/cm^2, the temperature of the test cell is maintained at 25±1°C by using a thermoelectric cooler assembly with a temperature controller during the photo-I-V measurement. Because the CIS and CIGS solar cells are deposited on the glass substrates, a temperature gradient of 3-5°C exists between the top and bottom surfaces of the solar cell under a solar simulator intensity of 100 mW/cm^2 at the test plane. A thermocouple is used to monitor the top surface temperature of the test cell during the measurement. Therefore the temperature controller of the cooling system is set at about 20°C to keep the reading of the thermocouple and hence the temperature of the test cell at 25±1°C.

15.3.1.3 The Current- Voltage (I-V) Measurements

The four-terminal contacts (also known as the Kelvin connections) are used for the connection between the test cell and the measurement system. Not only the measurement wiring resistance but also the contact resistance between the probe tips and the contact pads of the solar cell can be neglected for the efficiency measurements by using the four-terminal contact method

to achieve a more accurate efficiency measurement for the solar cells. Four micromanipulators with tungsten probe tips whose radii are in the range from 0.6 to 25 μm are utilized to adjust the position of the probe tips for contacting the small contact pads of the test cell. The voltage and current probes for both the top and bottom contacts should be placed as close as possible to avoid a high voltage drop between the two probes, and the resistance between the voltage and current probes is hence minimized (less than 5Ω).

As illustrated in Figure 15.1, the semi-automated I-V measurement system, which is controlled by a personal computer with the data acquisition and data analysis software *LabVIEW*, is composed of a programmable bipolar power supply served as the variable load, an electrometer for measuring the terminal current, and a digital multimeter for measuring the terminal voltage of the test cell. The measuring range for current measurements by the electrometer is from 1fA to 20mA. Although the upper limit of the electrometer is only 20mA, the photo-generated current of the CIS cell under test is typically smaller than 20mA due to the small area (nominally 0.429cm^2) of the CIS cells fabricated in a laboratory scale. With the sensitivity in the low-current measurements the electrometer with a current resolution of 0.1fA is particularly ideal for the dark- I-V measurement.

15.3.1.4 The Data Acquisition and Analysis

A computer program is written in the *LabVIEW* software program for data acquisition from the electrometer, multimeter, and power supply as well as controlling the programmable power supply to complete a full sweep of the I-V curve in each measurement via interface of GPIB.

15.3.2 The I-V Measurement Procedures

For photo- I-V measurements, the illumination intensity of the solar simulator is first set by using the reference cell method depicted above. The test cell is exposed under this condition and biased at around the maximum power point for about 10 minutes (i.e., light soaking effect). The I-V curve is then swept from the forward bias to the reverse bias using the voltage mode with a resolution of 1mV.

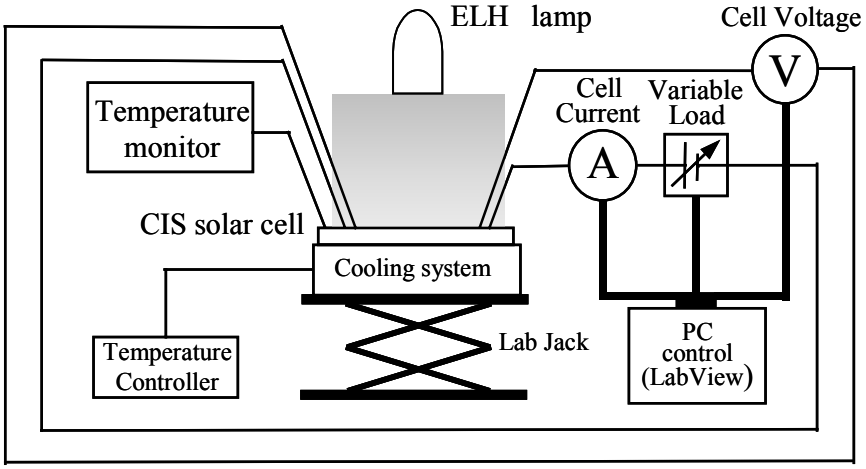

Figure 15.1 Apparatus and block diagram of I-V measurement system for the CIS-based cells.

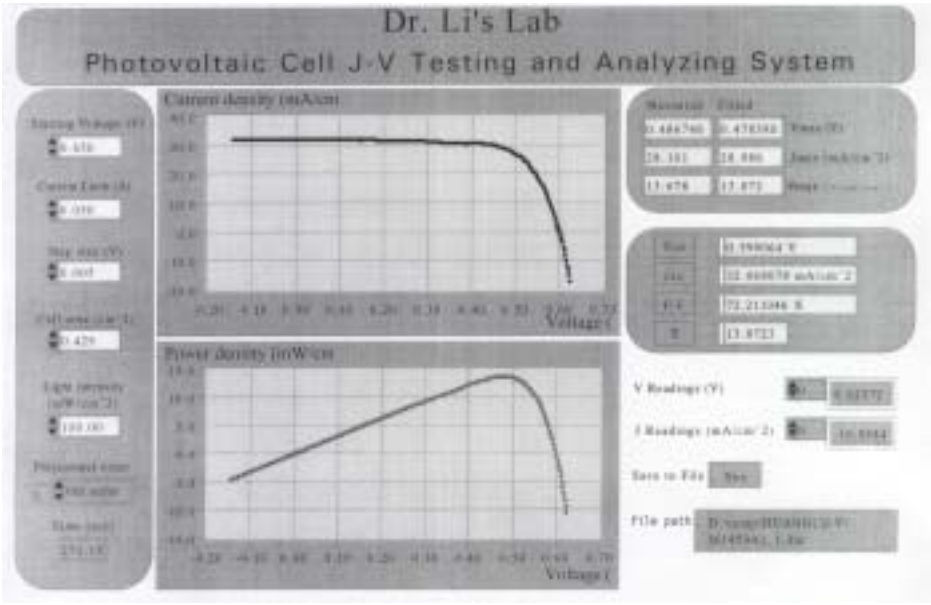

Figure 15.2 The J-V measurement and analysis for solar cells using the *LabVIEW* program. (The tested solar cell in this illustration is a CIGS solar cell fabricated by NREL.)

15.3.3 Analysis of the Measured I-V Curves

Using the *LabVIEW* data acquisition software (see Figure 15.2) the basic parameters such as V_{OC}, J_{SC}, fill factor F.F., output voltage at maximum power point V_{MAX}, output current density at maximum power point J_{MAX}, maximum power point P_{MAX}, and conversion efficiency η of test cells can be directly obtained from the measured photo-I-V curves. The open-circuit voltage V_{OC} is determined from a linear fit to the I-V curve near zero output current, and similarly J_{SC} is determined from a linear regression to the I-V points near zero output voltage. The maximum power point P_{MAX} is obtained from an *at least fifth-order polynomial fit* to the data points of the output power versus voltage with the constraints in which the P_{MAX} must be greater than 85% of the measured maximum power and the V_{MAX} must be greater than 85% of the measured V_{MAX}.

15.4 The Spectral Response Measurement Instrumentation and Procedures

15.4.1 The Spectral Response Measurement Instrumentation

Two types of measurement systems, i.e., the filter wheel and grating monochromator systems, are commonly used to measure the spectral response of the solar cells. The grating monochromator system has the basic feature of the flexibility to select wavelength, but has disadvantages of low light intensity, poor beam uniformity, and small beam size. While the filter wheel system has the features of higher light intensity, better beam uniformity, and larger beam size, but has the drawback of limited and fixed wavelengths in spectral response measurements. With the small area of the CIS-based solar cells fabricated at UF, we have constructed a spectral response measurement system using a grating monochromator to analyze the spectral response and quantum efficiency of our solar cells. The measurement system scanning the spectral range

from 400 nm to 1400 nm with 10 nm as an increment step has the capability of applying white light bias and voltage bias to the test cell when the measurement is performed.

15.4.1.1 The Monochromator and Monochromatic Light Source

As illustrated in Figure 15.3, a 30-Watt tungsten-halogen lamp is coupled with the monochromator as a light source to produce a monochromatic light with a narrow bandwith of about 10 nm in the wavelength range from 350 nm to 2500 nm and with a resulting beam size of around 9mm×14mm on the test plane. With the considerations of the possible spatial non-uniformity of the test cell to the spectral response, significant errors arising from the test cell and reference detector with different size or shape under a non-uniform monochromatic light [2], and the potential disadvantages, namely the low light intensity, uneven light distribution, and small beam size, directly inheriting from a typical monochromator measurement system, the geometric location and selection of the optical components including the lenses, mirror, and optical diffuser are specially arranged with caution so that the entire area of the cell on the test plane is covered with a uniform and adequate illumination-level monochromatic light. The entrance slit width of the monochromator is opened to its maximum to increase the throughput of light intensity at the expense of the resulting image resolution from the output of the monochromator. The exit slit width of the monochromator is opened to around 2.8mm to keep the bandwidth of the monochromatic light at about or less than 10 nm for the wavelength from 400 nm to 1400 nm. The divergent monochromatic beam from the exit of the monochromator is collimated through the condenser lens, reflected onto the test plane via the high-reflection broadband flat mirror, and homogenized by a high-transmission (>85%) optical diffuser to make the monochromatic light more uniform without substantially sacrificing the light intensity.

Since there is no real-time calibration and the data of the incident power density on the test plane are stored before the photocurrent measurement, care must be taken for the stability of the light source used for the monochromator. A stable well-regulated power supply is served as the power source for the light source of the tungsten-halogen lamp. Two order sorting filters are utilized to block the undesired harmonic terms from the monochromator. One with the cut-on wavelength of around 610nm and the other with the cut-on wavelength of about 830 nm are applied for the ranges of wavelength from 630 nm to 1000 nm and from 1000 nm to 1400 nm, respectively. It is not necessary to use the order sorting filter for the range of wavelength from 400 nm to 630 nm because the silicon detector, which only responses to the wavelength above 360 nm, is used as the reference detector in the measurement system.

15.4.1.2 The Monochromatic Light Chopper

An optical chopper used together with a lock-in amplifier in the spectral response measurement system can discriminate the chopped ac signal from the undesirable noise and strong dc signal from the bias light, and hence increases the signal-to-noise ratio in the spectral response measurement system. However, errors can occur for the inadequate use of chopped light method when the test cell and reference detector are of different size and/or shape [3]. These errors can be minimized by locating the chopper blade in the narrowest location of the monochromatic beam pathway [3]. Therefore, we put the chopper right next to the exit of the monochromator in the measurement system to reduce the errors. In order to avoid the interference of the harmonics from the power lines of the bias light, a chopping frequency of

150Hz is utilized in the measurement.

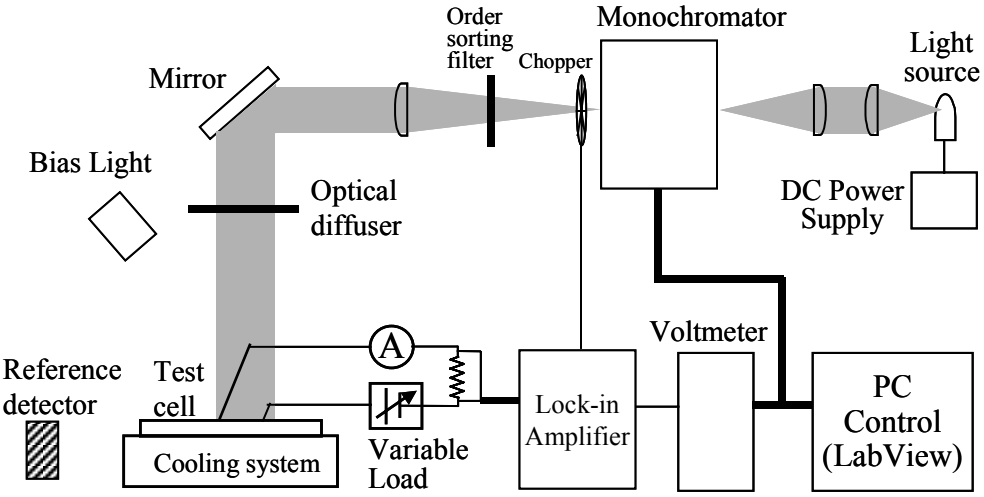

Figure 15.3 The block diagram of a spectral response measurement system for the CIS-based solar cells.

15.4.1.3 The Bias Light Source

Besides the monochromatic light a bias light is typically used in the spectral response measurement not only to approximate the standard operating conditions but also to compensate to effects, which might be attributed to trapping mechanisms of the test cell, about the non-linearity of the photo-generated current in the cell to the illumination level. An ELH lamp is used as the bias light source in the measurement system. The light intensity of the ELH lamp is adjusted during the spectral response measurement, which is one hundred times greater than that of the monochromatic light, to provide with sufficient illumination level such that the short-circuit current is within 70%-100% of the I_{SC} measured from the photo- I-V measurement with respect to the SRC. A screen is placed between the chopper and lens to eliminate the undesired noise, whose magnitude can be comparable to the measured ac signal due to the high illumination-level bias light, resulting form the stray light reflected from the components and the possible direct illumination from the bias light through the chopper onto the test cell.

15.4.1.4 The Spectral Detector and Synchronous Detection Instrumentation

The NIST traceable calibrated silicon and germanium photodetectors together with a lock-in amplifier are employed to measure the incident power density of the frequency-chopped monochromatic light beam on the test plane in the measurement system. A zero-inductance four-terminal resistor of 2Ω is used as the current-voltage converter to convert the ac photocurrent generated from the photodetectors or the tested cell into the photovoltage, which is then fed into the lock-in amplifier. The monochromatic signal through the chopper becomes a trapezoidal waveform. For absolute photocurrent measurement of the detectors, the signal measured from the lock-in amplifier must be multiplied by a waveform correction factor (i.e. multiplicative constant) because the lock-in amplifier typically measure the amplitude of fundamental component of the trapezoidal waveform (root-mean-square signal), which is not exactly the same as the peak amplitude. Since the signals for the reference detectors and test cell

are measured with similar electronic instruments, all multiplicative errors drop out and the absolute spectral response of the test cell can then be achieved.

15.4.2 The Spectral Response Measurement Procedures

The monochromator, which is controlled by a computer program written in *LabVIEW* software via the interface of GPIB, scans the spectral range from 400 nm to 1400 nm with 10 nm as an incremental step. The incident power density on the test plane is first measured by the photodetectors and the data are stored in the hard disk of the computer. The spectral response measurement is operated at the short-circuit mode by adjusting the variable load in the circuit loop to set the measurement at short-circuit condition with the terminal voltage of the test cell within ±5mV. The light intensity of the light-bias lamp is adjusted such that the short-circuit current is within 70%-100% of the I_{SC} measured from the photo- I-V measurement with respect to the standard reporting conditions (100 mW/cm^2, 25°C, and reference spectrum). The ac photocurrent $I_{test\ cell}(\lambda)$ of the test cell is converted into photovoltage with a zero-inductance four-terminal precision resistance and is measured by using a lock-in amplifier. Subsequently the spectral response is calculated from the data stored in the computer previously and the measured photocurrent of the test cell. The external quantum efficiency as a function of wavelength can be converted from the spectral response using the following expression:

$$QE(\lambda) = \frac{h \cdot c \cdot I_{test\ cell}(\lambda)}{q \cdot \lambda \cdot \text{power density}_{detector}(W/cm^2) \cdot \text{Area}_{test\ cell}(cm^2)} \times 100\%$$

where h, c, q, and λ are the Plank constant, speed of light, electronic charge, and the photon wavelength, respectively. Figure 15.4 shows the spectral response and external quantum efficiency of a UF CIS solar cell taken by this measurement system.

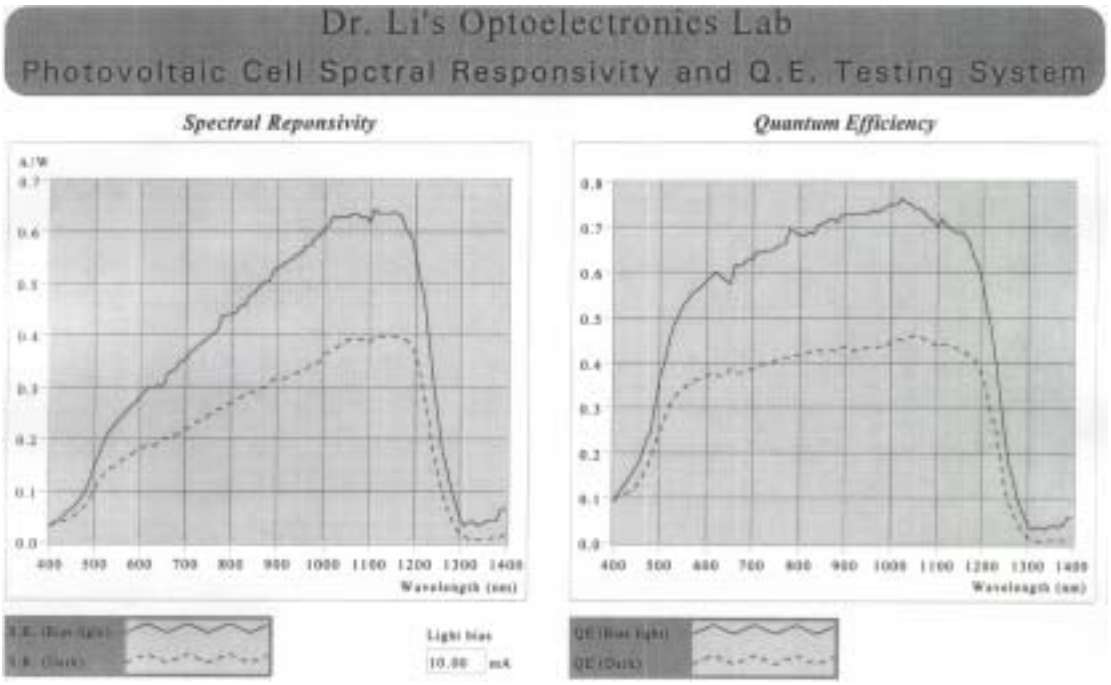

Figure 15.4 The spectral response and quantum efficiency measurements for solar cells using *LabVIEW* program. (The test cell in this illustration is a UF CIS solar cell.)

15.5 References

[1] C.R. Osterwald, *Solar Cells*, Vol. 18, p. 269 (1986).

[2] A. Schönecker and K. Bücher, "Influence of non-uniform illumination on spectral response and efficiency measurements of large area solar cells," *Conference Record of 22nd IEEE PVSC*, pp. 203-208 (1991).

[3] G. Sala, J. Olivan, and J.C. Zamorano, *Proceedings of the 11th E.C. Photovoltaic Solar Energy Conference*, pp. 341-343 (1992).

PART 16

Operation and Maintenance of the UF PMEE Growth System

Abstract

The plasma-enhanced migration-enhanced epitaxial reactor (PMEE) available at the University of Florida is used for the deposition of a wide variety of thin CIS films, supporting device manufacturing based on polycrystalline co-deposited CIS, as well as are variety of studies such as single-crystal growth, nucleation effects, and bi-layers precursor design for RTP studies. The custom designed reactor provides for this flexibility. Significant effort is spent on operating and maintaining the UF PMEE reactor, a few significant operational hurdles had to be overcome during the period of this contract, including performance problems related to the load luck pump system and the substrate temperature sensors. Furthermore a new source was purchased for deposition of Ga in addition to the existing sources. Finally four new graduate assistants were trained to take over operations after the graduation of the current students responsible for the operation of the reactor to ensure continuity in the project.

Section Contents

16.1 Brief Overview

16.1.1 Participants

Faculty Adviser: Prof. Timothy J. Anderson and Prof. Oscar D. Crisalle

Research Assistants: Suku Kim and Serkan Kincal

16.1.2 Objectives

The objective of this section is to report on the operation and maintenance of the PMEE reactor. This effort requires quite a significant time investment and is essential to the success of the other parts of the project because the reactor produces the most important layer for the production of the solar cell. The section will begin with an overview of the reactor itself, outlining its description as well as capabilities. Some issues that prevented regular operation of the reactor and required a significant time investment for obtaining a solution will be mentioned in the following section. Finally improvements and additions to the current status of the reactor will be reported.

16.2 System Description

Photovoltaics research group in the University of Florida has been developing and employing the plasma-enhanced migration enhanced epitaxy (PMEE) reactor to produce $CuInSe_2$-based absorber layer for solar cell application. The system has some novel and unique features compared to other facilities for production of CIS thin films. It is basically a variant of molecular beam epitaxy (MBE) system in adopting ultra high vacuum environment and effusion cells to generate the molecular beams of the elemental sources (Cu, In, Se, and S). In addition to the capabilities of typical MBE, it is capable of processing nine samples by adopting a large rotating platen. Square substrates of 2"×2", 2" diameter wafers (Si or GaAs) and 1cm×1cm of square substrates can be loaded onto the platen. Another unique feature of the system is the sequential deposition of each source through a revolution of the platen rather than simultaneous co-deposition of all the sources. The details of these features will be described in the following.

As a modified MBE system, it creates an ultra high vacuum environment and molecular beam fluxes of the elemental sources. The pumping unit consists of three mechanical pumps, one large capacity diffusion pump, a turbo molecular pump (TMP), and a liquid nitrogen-based cryogenic pump inside the system. The base pressure can be maintained as low as 8×10^{-9} Torr with the cryogenic pump to be turned on. The pressure during deposition is in the range of 10^{-8}-10^{-7} Torr depending on the source fluxes. The pressure can go as high as 10^{-5} Torr range when inert gas is introduced to the system to generate plasma. At standby mode, the system pressure is maintained as low as 5×10^{-7} Torr by the turbo molecular pump and a back up mechanical pump.

Inside of the system is divided into four different zones, seen from top view (Figure 16.1). It consists of heater zone, metal deposition zone, load-lock zone, and chalcogen deposition zone (as counter-clockwise direction). As described above, the system adopts a

rotating platen that delivers the substrates to all the zones sequentially and periodically. A radiation heater is located in the heater zone; hence, the substrates and the platen are heated up while they pass through the heater zone. In other zones, the substrates are slowly cooled down since there is no direct heating object. Some extent of non-uniformity of the temperature distribution on the platen and the substrates is expected due to the complex design as described above. Two effusion source cells are located in the metal deposition zone. Deposition of copper and indium occurs while the heated substrates pass through the metal deposition zone. Rotation of the platen continuously delivers the substrates to the cooling zone (or load-lock zone) where neither of deposition nor heating occurs. Finally, the substrates enter the chalcogen deposition zone and deposition of selenium or sulfur occurs. The same steps are repeated through rotational movement of the platen. The above description about the rotational movement and sequential deposition is for the case of counter-clockwise rotation of the platen. Direction of the rotation can be either clockwise or counter-clockwise so that the sequence of deposition may be reversed. Selenium deposition zone is isolated to minimize selenium deposition on the rest part of the system since selenium has the lowest vapor flux, and correspondingly create the highest flux; hence, it can cause some contamination of other sources and the ion gauges in the system. The substrates are loaded into or unloaded from the PMEE system through the load-lock zone. A separate chamber, the load-lock, is connected to the main chamber, which makes it possible to move the substrates in and out without venting the main chamber.

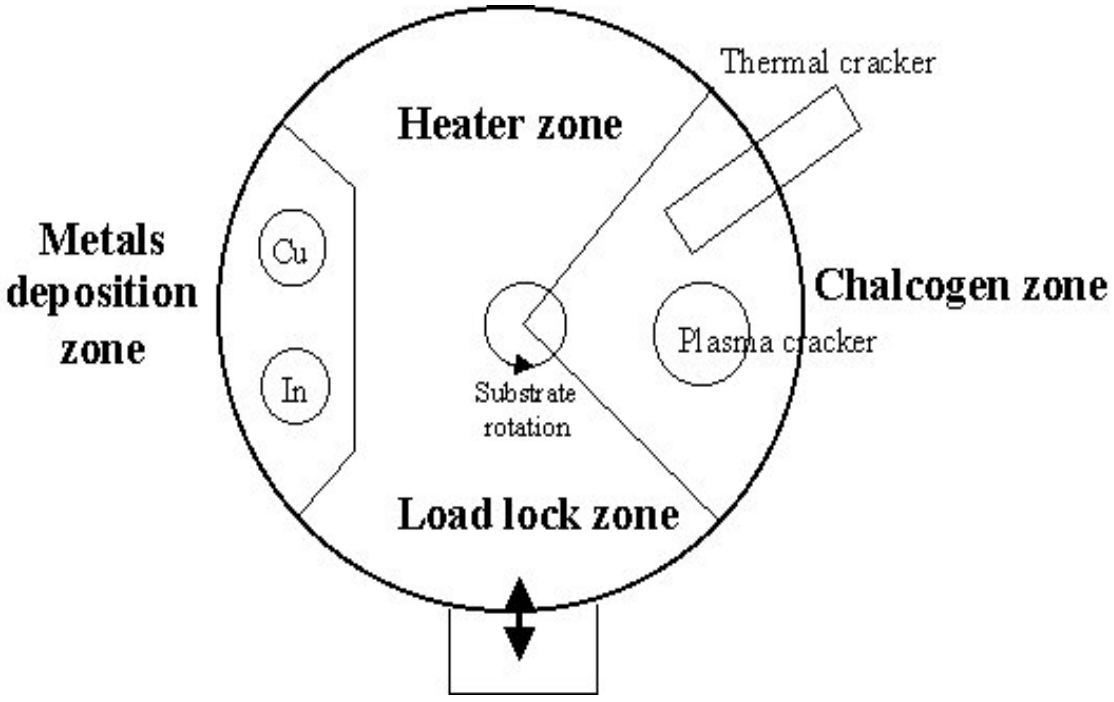

Figure 16.1. Schematic top view of the migration enhanced epitaxy reactor

Five effusion source heaters are operated in the system. Two thermal evaporation sources are to create Cu and In fluxes. Due to high melting temperature and high sticking coefficient of copper, a dual filament system was adopted in the source heater to ensure melting surface of the elemental copper, and prevent condensation around the exit. The source heater for

selenium has more advanced units that consist of a cracker and a crucible. It is known that selenium vapor flux is usually mixture of various molecular phases e.g. Se, Se_2, Se_6, and Se_8. The high molecular weight species may not easily react with other species on the substrate even under high temperature condition. The thermal cracker is to crack and activate the high molecular weight selenium phases. The temperature range for the cracker during deposition is usually from 350°C to 1000°C. Another unit of selenium source is located in the chalcogen deposition zone. It is for plasma cracking of selenium molecular flux. Electron cyclotron resonance (ECR) plasma is generated and maintained in the sapphire tube that works as a wave-guide and the passage of selenium molecular flux. This source cell can be used for both chalcogens, selenium and sulfur. Separate or simultaneous operation of these chalcogen source cells is possible so that both of sequential and simultaneous deposition can be conducted during deposition.

The fluxes from the copper and the indium sources are in-situ measured by employing the EIES sensors. A closed loop feed-back control is conducted along with the EIES sensors for the Cu and the In sources. The EIES sensors are calibrated by quartz crystal monitor (QCM) that is located right over the source cells whenever the source material is refilled. There is no instrument that measures the chalcogen (selenium and sulfur) flux rate in-situ; hence, the flux rate is calculated by depositing the chalcogens on a substrate at room temperature and measuring the thickness. For the chalcogen sources, a closed loop feed-back control based on temperature has been adopted. Whole control logic and operation were programmed in and conducted through a personal computer.

Along with the unique features of the system described above, the current growth system has both of advantages and limitations of its own compared to other deposition facilities. First, it has some advantages of MBE system, including ultra high vacuum environment and relatively precise control over the flux rates. The ultra high vacuum creates extremely clean condition and makes it possible to generate the molecular beam of each source so that the growth system can be used to grow epitaxial CIS thin films of high crystalline quality. Combined with the shutter operation and the rotational movement of the platen, an operation of atomic layer epitaxy is also possible. In addition, it can overcome to certain extent a disadvantage of the MBE, low productivity, by processing nine samples in one batch. Adopting the sequential deposition scheme gives more versatile environment for our research e.g. to study the effect of the rotation speed and the rotation direction.

There exist some disadvantages of this system as well. Due to the rotational movement of the platen/substrates, direct in-situ measurement of the substrate temperature is virtually impossible. The thermocouple is currently located in the gap between the platen and the heater and reading sort of average value of those two temperatures. The localized heater location creates certain non-uniformity of temperature distribution on the substrates. The growth rate is significantly limited by the chalcogen flux delivery. Even with high chalcogen flux rate ($[Se]/([Cu]+[In]) > 5$), it is hard to obtain sufficient chalcogen incorporation into a growing film under very high temperature condition since the chalcogen deposition zone is localized, and the high-vapor-pressure material is easily re-evaporated from the surface. As a result, the maximum flux rates of copper and indium are limited, which makes it difficult to achieve high growth rate.

16.3 Resolved problems

Many minor problems are encountered during the operation of the PMEE reactor and most are resolved through the course of normal operation without significant time investment such as changing fuses and refilling sources. However once in a while a problem is encountered that takes a significant period of time and prevents experiments to be done. These will be reported in some detail.

16.3.1 Substrate Temperature Measurement

The substrate temperature is measured by a thermocouple that is suspended in between the substrate heater and the rotating substrate platen. The small clearance between these two surfaces, approximately 6mm, makes the installation of the thermocouple a very significant issue. The C-type thermocouple is installed inside a 3mm outer diameter high-temperature ceramic tube, which is secured through a hole in the holding plate. The dimensions of this tube leave a clearance of approximately only 1.5mm on either side. Any movement of the tube towards the rotating platen causes the platen to get stuck and prevents the regular deposition of CIS.

This has been a constant problem with the reactor and requires at least three working days of down-time, excluding time to degas the system so that suitable operating pressures are achieved for growth because the system has to be pulled apart to get into the thermocouple. To solve this problem a new mechanism was designed for securing the thermocouple tube to the holding plate. To overcome problems related to the high temperatures that this mechanism is to face, the only Tantalum was used in the construction.

Since the installation of this new holding mechanism, no run was aborted due to the failure of the substrate thermocouple, making the reactor operation more efficient.

16.4 Improvements and Additions

In addition to the regular operation and maintenance, improvements and additions were made to the reactor for ensuring that the reactor is capable of providing more flexibility in growing films and thereby allowing the fulfillment overall project objectives. Another significant issue is the resolution of continuity in operation.

16.4.1 New Ga Source

In order to increase the efficiency of solar cells produced by the UF program as well as achieving all the objectives outlined by the current contract it was necessary to install a Ga source into the existing PMEE reactor.

The major problem is that the PMEE reactor has been custom designed and therefore requires extensive customizations to regular sources available from manufacturers. Furthermore there is very limited space inside the reactor in its present state to install an extra source. All of these problems were considered in deciding what configuration could be used for the deposition of Ga in the PMEE reactor.

Three different options were considered. The simplest solution was to use the existing dopant source for Ga. The advantage of this option is that it is very simple to implement and requires no modifications to the rector. However it was decided that the amount of Ga to be deposited would have been too small, not allowing for effective deposition incorporation of Ga into the film.

The second option considers the use the existing In source for the deposition of Ga. This option once again is very easy to implement without any modifications to the reactor however it does not allow for the co-deposition of Ga and In and there will be significant down-time when switching between the source materials.

The final option was to install and brand new source with all the related instrumentation, sensor, power supplies and controllers. This option requires a new hole to be built into the cryoshroud where the new source is to be installed as well as a significant financial investment to cover the cost of the equipment. However it overcomes all the problems of the previous options such as low deposition rates and the inability to co-deposit Ga and In.

In order to pursue this option several source manufacturers were contacted and it was decided to purchase a dual filament thermal effusion source from Applied EPI, MN. The power supplies were purchased from Eurotherm and a quartz crystal sensor and related accessories were purchased from Inficon. Detailed design of modifications to be made inside the reactor were made, the most significant being the new hole into the cryoshroud and a holding plate for the source and the shutter. Currently all orders have been placed and about half of the required parts have already been received. Once all parts are procured, the new source will be installed within a month and the reactor will be ready to deposit Ga in addition to Cu, In, Se, S and Na.

16.4.2 Training and Documentation

Since the UF PMEE reactor has been custom designed and built, no documentation set exists for the operating and maintenance procedures. Such documentation is crucial for the continuity of the project because it is the responsibility of a team of graduate students (2 to 4 at a time) to operate the reactor. Once the senior current members of the team graduate the newcomers do not have access to a comprehensive written report for the operation. For overcoming this problem a 200 page document was prepared. This document includes detailed description of individual system components grouped by functionality as well as detailed step-by-step procedures describing in detail operating, maintenance and emergency procedures. This manual is also complete with vendor contact information in case spare parts are required.

In addition to the preparation of the reactor operation manual, two new members of reactor team were successfully trained by the previous graduate student who designed and built the PMEE reactor. Towards the end of this reporting period, two more new members joined the group and are currently undergoing training so that when it is necessary there will be a smooth transition.

PART 17

Instrumentation and Control of the UF PMEE Growth System

Abstract

A new instrumentation and control interface for the plasma-enhanced migration-enhanced reactor available at the University of Florida has been designed and deploy to enable the implementation of advanced control strategies envisioned for the local sources as well as the supervisory control structure. This section of the report outlines the hardware and the software that has been purchased and installed the system to achieve these goals. The section concludes with the documentation of the success of initial attempts to set-up a supervisory control scheme, namely a ratio control algorithm for the control of the metal fluxes.

Section Contents

17.1 Overview

17.1.1 Participants

Faculty Adviser: Prof. Oscar D. Crisalle

Research Assistants: Serkan Kincal

17.1.2 Objectives

The original configuration of the PMEE reactor did not allow for the implementation of the proposed advanced control strategies. This was because each of the sources to be controlled had their own local control equipment without the presence of an interface that could interconnect the individual loops to implement the supervisory control structure. Furthermore these local controllers were simply dedicated PID equipment, making it impossible to implement any other type of control even on the local level.

Perhaps the most significant experimental accomplishment in this project to date has been the upgrading of the previous control hardware by installing a central computer with the appropriate hardware and software to be able to achieve the control objectives. Furthermore the efficiency of the entire system has been enhanced by the installation of this control interface.

In this section of the report, this new interface will be described followed by the demonstration, by experimental data, of the new control set-up as compared to the original configuration.

17.2 The Description of the Interface

17.2.1 Overview

The desired flexibility was met by the LabVIEW ver 5.0 software package available from National Instruments. The software was set-up on a 400 MHz Pentium II computer under Windows NT 4.0. Analog input capabilities were added by installing a high performance analog to digital conversion card, in particular the PCI-MIO16E-4. Analog outputs to drive the various source supplies installed on the system were provided by installing a digital to analog conversion card, namely the AT-AO-10. IEEE 488 serial communications were enabled through the installation of the AT-GPIB card also available from National Instruments.

Significant work was done in debugging configuration problems with the computer and the aforementioned components so as to ensure a stable platform for the development and implementation of the proposed control strategies. In summary this effort of upgrading the data acquisition and system communication hardware provides the following capabilities:

(i) 16 channels of analog input with software configurable gains ranging from 0-100 mV to 0-10 V

(ii) 10 channels of analog output selectable between 0-10 V or 4-20 mA

(iii)IEEE 488 communications with up to 16 instruments that are IEEE 488 enabled

(iv)2 ports for RS 232 communications with capable equipment

It is envisioned that the control related communications will be carried out through the A/D and D/A cards that have faster and more robust responses than the serial communications which in turn will be utilized to carry out secondary directives such as monitoring process variables that are not actually required by the controllers.

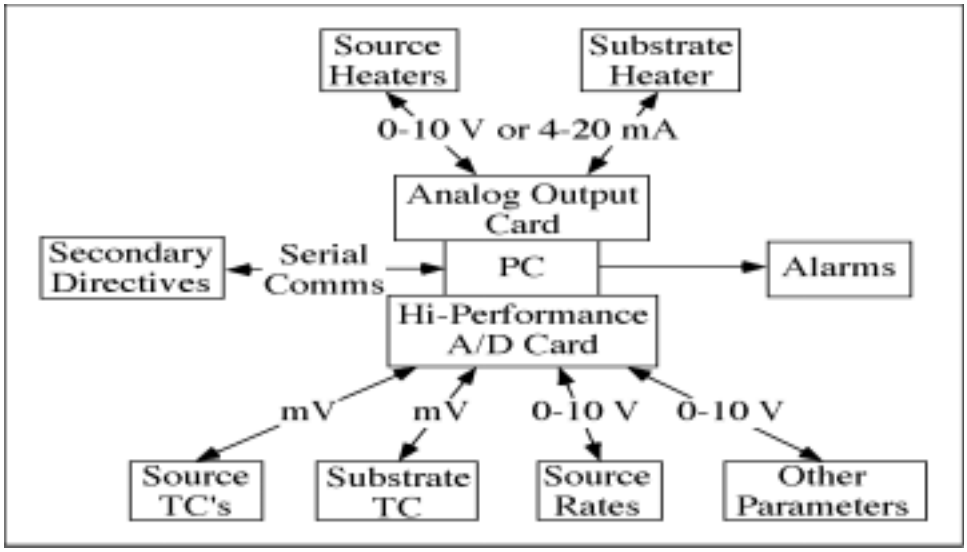

Figure 17.1. The flow-chart of the interface

17.2.2 Signal conditioning

The success of any controller scheme is limited by the quality of the input data. To ensure reliable measurements that are as noise free as possible, every signal that will be used for control purposes was tested systematically to characterize their noise content by spectral analysis.

The noise characterization experiments included scanning the frequency content of the signal of interest by an oscilloscope while certain power sources installed on the system were turned on. In some cases the noise analysis was done by acquiring signal at very high frequencies (i.e. 1000 Hz) and then evaluating the data using fast Fourier transform techniques. Most of the noise identified in the signals lies around the 60 Hz frequency range, which is the frequency of the alternating current that is supplied to the source filaments.

Wherever possible, the cables were routed away from the noise sources. However it was found necessary to also use analog or digital signal conditioning techniques before the noise fell below acceptable levels. It was determined necessary to amplify and filter the thermocouple signals, which are of the order of tens of mV, right at their source before the signals have to travel approximately 5 m to the shielded data acquisition box.

For this purpose a total of four analog signal conditioning modules, namely the CCT-01-0/100mV-0/10V, were purchased from Omega Engineering, Stamford, CT. These modules were installed as close to the reactor as possible. They take the cold-junction compensated thermocouple outputs and amplify and filter them to give an output in the range of 0 to 10 V which than becomes less susceptible to noise corruption as the signal travels to the computer.

A host of other signals that are generated by the system that are already in the 0 to 10 V range are filtered through digital filters that were designed according to the specifications dictated by their spectral analysis.

The functionality of the signal conditioning components were tested by comparing the frequency contents of the raw and the treated signals. As a result of this work, all the signals that will be significant for control purposes were brought the levels of acceptable noise content.

17.3 Software Development

The purpose of the controller developed at this point is to get a tight control over the local sources so that the supervisory control schemes that will be developed in the future can be implemented. On the other hand the ratio control that has been implemented with success can be called a very simple supervisory scheme.

The modular nature of the code, which has been developed in support of the current growth studies, will allow the implementation of the model based control strategies with ease. Once the module for any controller is developed, it will be substituted in for the module of the PID controller as the inputs and outputs are the same. The current PID controller will act as a baseline to which the future designs will be compared with in order to evaluate their performance. Furthermore the entire code can take set-points as inputs from another subprogram that implements the supervisory control. Aside from being open to future development, the modular nature of the code and the use of global variables make it possible for the different tasks to run independently from each other. Four independent tasks were identified, which were (i) data acquisition, (ii) control calculations, (iii) analog output, and (iv) data logging. These tasks are listed in order of decreasing importance to the integrity of the controller. If one of these tasks happens to fail during an experiment, the remaining ones are able to run without disturbance while the problematic tasks can be restarted by the operator to minimize the effects of a failure.

The data acquisition step is crucial to the performance of the controller whereas the controller is not affected at all by the process of data logging. To take this fact into account the four tasks were prioritized in terms of access to the resources of the computer. The net effect of this prioritization is to introduce an increase in the reliability of the control activities.

The stability and reliability of the new set-up was tested by running the program in a test mode, that is with dummy inputs and turned off heaters, over periods of longer than 24 hours. Once satisfied with the stability, the old controller was replaced by the new one. Out of the more than 50 runs that have been conducted since the installation of the new controller, there has been only one failure where the particular run had to be aborted.

17.4 Experimental Results

Experience with the reactor operation has demonstrated that the commercial controller installed on the system, namely an INFICON Sentinel III Deposition Controller, does not perform satisfactorily. Its main disadvantage is that it does not provide a consistent degree of metal flux control over the time span of a typical growth process. One of its limitations is that that the range of its tuning parameters is too limited, preventing it from operating successfully to

control the absolute flux of each source over the entire regime of interest. Furthermore the structure available for controlling the indium-to-copper flux ratio was very difficult to tune.

Software was developed on the LabVIEW environment to overcome the aforementioned difficulties. The controller used in this development was the commercially available proportional-integral-derivative controller provided as part of the control toolbox for LabVIEW. The deployment of this new controller resulted in a wider range for the PID controller parameters, which then made it possible to tune the individual source controllers and the ratio control to perform to the desired specifications.

The improvement obtained using the new flux-control resources is illustrated through the comparison of Figure 17.2 and Figure 17.3, which respectively show the performance of the original Sentinel controller and of the new LabVIEW based controller.

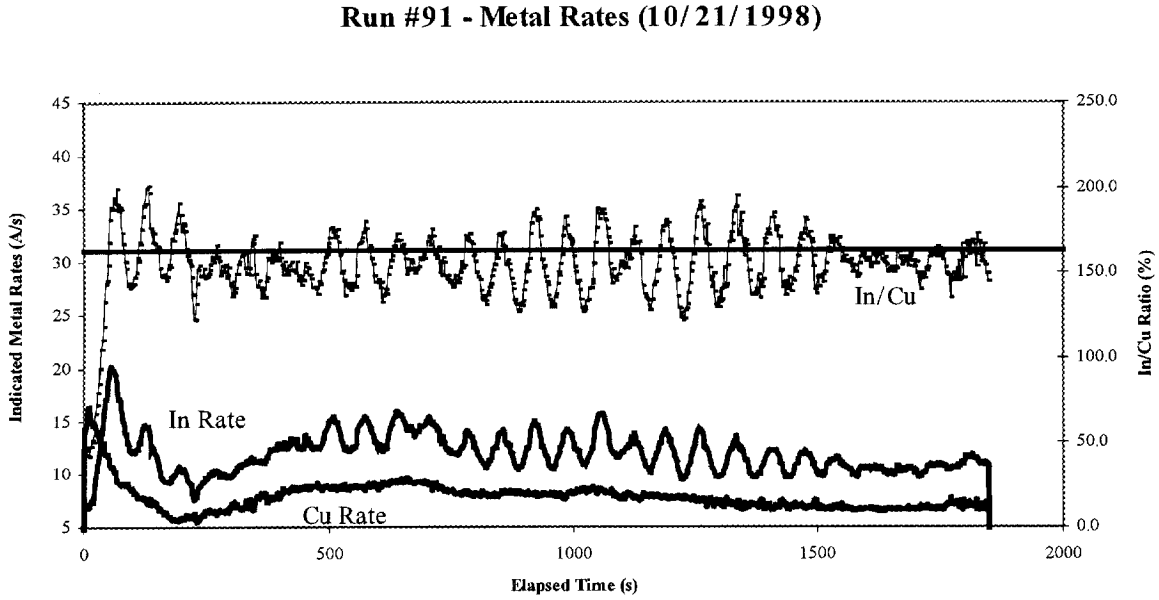

Figure 17.2. Metal flux-rate control achieved with the standard Sentinel III controller.

Both runs were done under ratio control, where a master controller controlled the Cu rate and a slave controller adjusted the rate of In. In both cases the Cu set-point was 9.8 A/s. The ratio set-points were 163% for the Sentinel-controller test (Figure 17.2 , Run #91) and 210% for the new LabVIEW-based controller test (Figure 17.3, Run #119). The plots in Figure 17.2 and Figure 17.3 have been drawn to the same scale to allow for a meaningful comparison.

The most obvious improvement attained by the new LabVIEW controller can be seen in the control of the Cu rate around its set-point value of 9.8 A/s. The initial surges in rate are inevitable because they are caused by inaccurate warm-up parameters and shutter transients. Figure 17.2 shows that the Sentinel controller takes quite a long time to stabilize after the inevitable original flux surge, and it suffers from an offset that eventually makes it fail to attain the specified Cu flux rate. In contrast, even when faced with a larger initial flux surge, the LabVIEW-based controller takes only about 300 seconds to attain the desired set-point without a significant offset.

The improvement of the In source control is demonstrated by the disappearance of the large

fluctuations, as shown in Figure 17.2. Due to this improved control the ratio of In to Cu is much more stable throughout the run. The LabVIEW controller produces lower fluctuations in the flux ratio, leading to an overall improved performance.

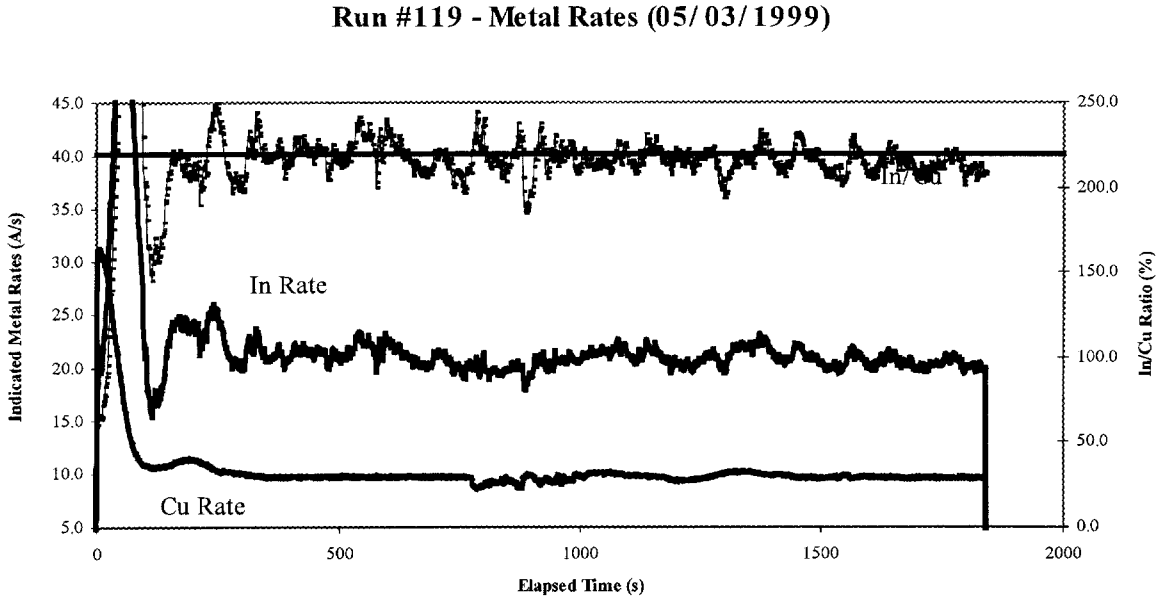

Figure 17.3. Metal flux-rate control achieved with the new LabVIEW controller.

All of these improvements are due to the fact that the new set-up allows for more flexibility on the controller parameters. Furthermore with the ability to signal-condition the temperature with very versatile digital filters that can be designed with great ease, the performance of the LabVIEW controller has been further improved. The filtering of the signals has also improved to a noticeable extent the operation of the standard Sentinel controller. In summary, the new instrumentation and data-acquisition interface has drastically improved the repeatability of growth of films of desired composition.

REPORT DOCUMENTATION PAGE

Form Approved
OMB NO. 0704-0188

1. AGENCY USE ONLY (Leave blank)	2. REPORT DATE	3. REPORT TYPE AND DATES COVERED
	June 2003	Final Report 8 July 1998–17 October 2001

4. TITLE AND SUBTITLE
Future CIS Manufacturing Technology Development,
Final Report, 8 July 1998–17 October 2001

5. FUNDING NUMBERS
PVP35001
XAF-8-17619-32

6. AUTHOR(S)
T.J. Anderson, O.D. Crisalle, S.S. Li, and P.H. Holloway

7. PERFORMING ORGANIZATION NAME(S) AND ADDRESS(ES)
University of Florida
P.O. Box 116005
Gainesville, Florida 32611

8. PERFORMING ORGANIZATION REPORT NUMBER

9. SPONSORING/MONITORING AGENCY NAME(S) AND ADDRESS(ES)
National Renewable Energy Laboratory
1617 Cole Blvd.
Golden, CO 80401-3393

10. SPONSORING/MONITORING AGENCY REPORT NUMBER
NREL/SR-520-33997

11. SUPPLEMENTARY NOTES
NREL Technical Monitor: Bolko von Roedern

12a. DISTRIBUTION/AVAILABILITY STATEMENT
National Technical Information Service
U.S. Department of Commerce
5285 Port Royal Road
Springfield, VA 22161

12b. DISTRIBUTION CODE

13. ABSTRACT *(Maximum 200 words):* The University of Florida served as the basis for educating 12 graduate students in the area of photovoltaics engineering and research with a focus on thin-film CIS manufacturing technologies. A critical assessment of the thermodynamic data and of the phase diagrams for the Cu-Se and In-Se binary systems were carried out. We investigated the use of two novel precursor structures that used stacked In-Se and Cu-Se binary layers instead of conventional elemental layers, followed by rapid thermal processing (RTP) to produce CIS films. We investigated the evolution of electrical and microstructural properties of sputter-deposited ZnO:Al thin films. An assessment of the thermodynamics of the pseudobinary Cu_2Se-Ga_2Se_3 system was done by using available experimental data, as well as an empirical method for estimating interactions in semiconductor solid solutions. Optimization studies were conducted to characterize the RTP of binary bilayer precursors for CIS synthesis using a newly acquired AG Associates Heatpulse furnace. Progress was made on the calculation of the 500ºC isothermal section of the phase diagram of the ternary Cu-In-Se system. Pursuit of developing alternative buffer layers for Cd-free CIS-based solar cells using a chemical-bath deposition (CBD) process has resulted in specific recipes for deposition. A rigorous model has been derived to predict the metal mass fluxes produced by conical thermal effusion sources. A two-dimensional model of the heat transfer was developed to model the substrate temperature distribution in the UF PMEE Reactor that features a rotating platen/substrates and effusion sources. We have grown and characterized polycrystalline CIS epitaxial films on single-crystal GaAs substrates under conditions that enhance the influence of surface effects on the resulting films and their properties. Progress was made on the study of CIS and CGS single-crystal growth, along with accompanying morphological and compositional characterizations. We have developed physical models and performed numerical simulations using AMP-1D program to predict the performance of the CIS-based solar cells constructed with different buffer layers (such as CdS and Cd-free materials) and to compare the results with experimental data. A new computer-controlled automated measurement system for the characterization of the solar cell performance parameters has been developed. The plasma-enhanced migration-enhanced epitaxial reactor (PMEE) is used for the deposition of a wide variety of thin CIS films. A new instrumentation and control interface for the plasma-enhanced migration-enhanced reactor has been designed and deployed to enable the implementation of advanced control strategies envisioned for the local sources, as well as the supervisory control structure.

14. SUBJECT TERMS: PV; manufacturing; thin film; sputter-deposited; rapid thermal processing (RTP); plasma-enhanced migration-enhanced epitaxial reactor (PMEE);

15. NUMBER OF PAGES

16. PRICE CODE

17. SECURITY CLASSIFICATION OF REPORT	18. SECURITY CLASSIFICATION OF THIS PAGE	19. SECURITY CLASSIFICATION OF ABSTRACT	20. LIMITATION OF ABSTRACT
Unclassified	Unclassified	Unclassified	UL